FAKULTÄT FÜR PHYSIK
Institut für Theoretische Festkörperphysik

Modelling complex mesoscopic growth processes via Kinetic Monte Carlo simulations: Applications to graphene growth and Solid Electrolyte Interphase (SEI)

Zur Erlangung des akademischen Grades eines
DOKTORS DER NATURWISSENSCHAFTEN (Dr. rer. nat.)

von der KIT-Fakultät für Physik des
Karlsruher Instituts für Technologie (KIT)
angenommene

DISSERTATION

von

Meysam Esmaeilpour

Tag der mündlichen Prüfung: 21.04.2023

1. Referent: Prof. Dr. W. Wenzel
2. Korreferent: Prof. Dr. M. Garst

Erklärung zur Selbstständigkeit

Ich versichere, dass ich diese Arbeit selbstständig verfasst habe und keine anderen als die angegebenen Quellen und Hilfsmittel benutzt habe, die wörtlich oder inhaltlich übernommenen Stellen als solche kenntlich gemacht und die Satzung des KIT zur Sicherung guter wissenschaftlicher Praxis in der gültigen Fassung vom 24.05.2018 beachtet habe.

Karlsruhe, den 15.03.2023, ____________________________
Meysam Esmaeilpour

Als Prüfungsexemplar genehmigt von

Karlsruhe, den 15.03.2023, ____________________________
Prof. Dr. W. Wenzel

Karlsruhe, den 15.03.2023, ____________________________
Prof. Dr. M. Garst

Contents

List of Figures

List of Tables

1. Introduction

1.1. The mesoscopic challenges

The term mesoscale represents an intermediate scale between the microscale and macroscale and is present in various physical systems, including materials, atmospheric phenomena, and even cosmology[1, 2]. At the mesoscale, a unique structure, called the mesostructure, is characterized by dynamic heterogeneity in both space and time, which is essential to the system's overall performance and behavior. In materials science, the mesoscale is particularly important as it governs many material properties and phenomena. In atmospheric science, the mesoscale describes the range of scales between turbulent eddies and global weather patterns. Similarly, in cosmology, the mesoscale refers to the range of scales between the smallest structures, such as stars and galaxies, and the largest structures, such as galaxy clusters and cosmic filaments. Mesoscopic science (mesoscience), which encompasses a wide range of scientific subjects, is the study of mesoscopic systems (see Figure 1.1). It deals with systems that are both too big and too small for macroscopic laws or quantum physics to adequately describe them. Among many other scientific disciplines, mesoscopic science involves physics, chemistry, biology, materials science, and engineering[3]. Its multiscale nature addresses systems that exist at various scales, from the molecular to the macroscopic[4]. In mesoscopic science, it is essential to comprehend how systems behave and interact at various scales in order to precisely predict and understand their behavior[5]. Materials, such as nanomaterials[6], and biological systems[7], such as proteins[8] and cells[9], are examples of multiscale systems in mesoscopic science. Mesoscopic research has its roots in the late 20th century, when technological advancements made it possible to create and study small-size systems[10]. Following that, mesoscopic science has evolved into a multidisciplinary field with a variety of applications in industries including electronics, materials science, biophysics, and nanotechnology[11]. The discovery of quantum transport in semiconductor nanostructures was one of the pivotal moments in the history of mesoscopic science[10] that resulted in understanding better the behavior of electrons in nanoscale systems[4]. The development of techniques to study the motion of ions and molecules through biological membranes was a key development in the field of biophysics[12]. Numerous prestigious awards have been given to researchers in honor of these and other significant contributions to the field of mesoscopic science. The National Medal of Science, the Wolf Prize in Physics, the Nobel Prize in Physics, and the Kavli Prize in Nanoscience are a few of the famous honors[4, 11]. These awards, which acknowledge the major achievements made by researchers in this field, are considered as some of the highest in the scientific community. An interdisciplinary approach that incorporates theoretical, experimental, and computational methods is necessary for mesoscopic research. Theoretical approaches give a foundation for understanding the governing principles and processes of mesoscopic systems. The validity of these ideas may then be established and tested by experiments, which provides crucial empirical data that supports the validity of theoretical models. One useful tool that computational approaches provide for studying mesoscopic systems in a virtual environment is mesoscopic simulation. With the help of this tool, researchers may simulate and analyze the behavior of complex systems under various conditions[13, 14, 15]. Considering the multiscale nature of mesoscopic science, numerous scientific problems and challenges are associated with the study in mesoscopic systmes, that some of them are listed here: 1) Length scale problem: mesoscopic systems frequently span multiple length scales, from the nanoscale to the macroscale. It is important to consider the interactions and effects at each length scale in order to fully understand how effectively these systems function.

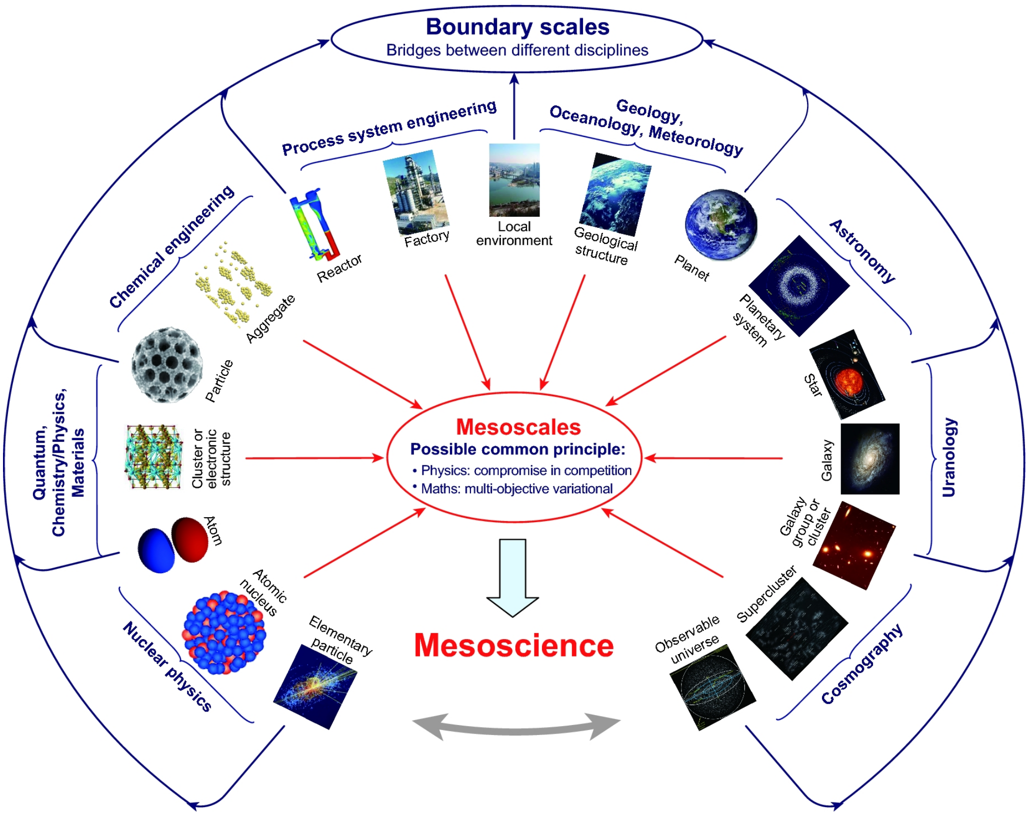

Figure 1.1.: All mesoscale phenomena: this represents a common challenge for the whole spectrum of science and technology. Reprinted from Ref.[16], used under Creative Commons CC-BY license.

For instance, quantum mechanical effects become more significant at the nanoscale, and it can be difficult to integrate them with classical mechanics[17]. 2) Complexity: the behavior of mesoscopic systems usually involves complex interactions between a number of components and physical processes, making it challenging to predict and understand. For instance, describing and understanding the connection between electrical transport and electrostatic interactions in mesoscopic electronics may be difficult.[10]. 3) Modelling and simulation: it might be hard to develop accurate models and simulations to estimate the behavior of mesoscopic systems, particularly when several physical phenomena and length scales are involved. For instance, it is frequently necessary to take both classical and quantum physics into account when modelling the behavior of nanoscale systems[18]. 4) Experimental measurements: developing novel experimental methods and measurement equipment could be required to evaluate the behavior of mesoscopic systems at various length scales. For instance, the small signal strength and sample size make it difficult to detect electronic transport in nanoscale systems[19]. 5) Environmental interactions: it can be problematic to predict and control the behavior of mesoscopic systems due to the way strongly their surroundings, such as temperature, pressure, and electromagnetic fields, can affect them. For instance, it might be difficult to ensure consistent experiment performance and reproducibility due to the sensitivity of nanoscale systems to external influences[20]. 6) Integration with macroscale systems: incorporating a mesoscale system into macroscale systems can present challenges due to compatibility and interface issues. Achieving reliable and efficient performance when integrating nanoscale electronic devices with macroscale systems may require the development of novel materials and processes[21]. These challenges of understanding and modeling complex systems refer to multiscale problems. The fact that interactions and events that take place at various scales can affect a system's behavior at one scale is one of the primary challenges in solving the multiscale problem. To overcome these difficulties, scientists are developing novel methods and approaches for investigating mesoscopic systems. To understand the structure and operation of mesoscopic systems at the nanoscale, for instance, cutting-edge imaging and spectroscopic techniques are being applied[22]. Additionally, mathematical and statistical models are employed to simulate and estimate how mesoscopic systems would behave in specific situations[23, 24, 25]. The study of mesoscopic systems often involves developing models and simulations to understand the behavior of these systems and the interactions between their various components[10]. This requires a multidisciplinary strategy that integrates knowledge and methods from several scientific disciplines. For instance, mesoscopic physics incorporates knowledge from materials science, chemistry, electrical engineering, and both classical and quantum physics. Researchers may employ a variety of techniques such as computer simulations, analytical techniques, and experiments, to explore the behavior of these complex systems. Mesoscopic research seeks to comprehend these complex systems better and to apply that knowledge to the development of novel materials, tools, and technology.[4]. Mesoscopic science has advanced substantially due to computational methods and simulations. The rapid technological advancement of computers has made it possible to create ever-more complex simulation tools and techniques, which has driven the use of these methods in mesoscopic science. These tools enable mesoscopic systems to be studied in a virtual setting, providing researchers with additional insight into the behavior and characteristics of systems without the constraints of experiments[13]. Some of the methods and techniques used in mesoscopic science include: Molecular Dynamics (MD) simulations involve analyzing the behavior of atomic-scale systems through the simulation of individual atom and molecule motion using classical mechanics[26]. This method has been used to study the behavior of biological molecules, including their structure and function[27]. In contrast, Continuum Mechanics simulations utilize mathematical models to describe the behavior of systems on a macroscale, such as fluids and solids[28]. This method has been applied to study the behavior of fluids in microfluidic devices[29]. Monte Carlo simulations are numerical simulation methods that model the behavior of a system using random sampling. These simulations have been employed to study the transport of electrons in mesoscopic systems such as quantum dots[30, 31]. Density functional theory (DFT) is a quantum mechanical method used to analyze the electronic structure and properties of materials. It has been used to investigate the electronic properties of nanoscale systems and their interactions with other materials in mesoscopic science[32, 33]. Non-equilibrium Green's functions (NEGF) is a method used to study the electron transport through mesoscopic systems like quantum dots and nanoscale transistors. NEGF can be employed to study the effect of interactions between electrons, including the scattering of electrons by impurities, and the transmission of electrons through the system[12]. Other methods and techniques used in mesoscopic science include the Finite Difference Method (FDM)[34], Finite Element Method (FEM)[35], or the Boltzmann transport equation (BTE)[36], and classical and quantum transport simulations[37]. The choice of computational method or technique depends on the specific problem and the type of system under study.

Despite all these efforts, there is often a gap between the length scales of atomistic and macroscopic simulations, creating a so-called "mesoscale gap"[38]. The mesoscale gap refers to the challenge in capturing the behavior of systems that exhibit multiple interacting length and time scales. This understanding is crucial for the development of new materials, technologies, and advancements in human health. There are currently two simulation approaches for mesoscale systems: atomistic simulations and continuum models. While atomistic simulations, such as Molecular Dynamics (MD) simulations, provide detailed representations of the behavior of individual atoms or molecules based on the principle of Newton's laws of motion[39], they are limited in their ability to cover the multiscale gap due to their high computational cost and inability to provide a macroscopic description of a system[40, 41]. To provide a more complete understanding of mesoscale systems, continuum models, such as finite element analysis or finite difference methods, are used in combination with atomistic simulations[41, 42, 43]. These models provide a macroscopic representation of the behavior of a system and treat it as a continuous entity using partial differential equations[43]. Continuum simulations are advantageous due to their computational efficiency and reduced complexity compared to atomistic simulations[44]. However, they have limitations in capturing the behavior of complex mesoscale systems[45], such as discontinuities, sharp interfaces, and large fluctuations in temperature or pressure[44]. While they provide a macroscopic representation of the behavior of mesoscale systems, they cannot offer a detailed understanding of individual atoms or molecules[43]. To overcome this limitation, researchers have developed multiscale simulation methods that integrate atomistic and macroscopic simulations[46]. These methods provide a more comprehensive understanding of mesoscale systems across different length and time scales, and have been used to study the behavior of materials in energy storage devices[47]. Among the developed methods, Kinetic Monte Carlo (KMC) simulations are a powerful tool in mesoscopic science for overcoming the multiscale gap. They provide a flexible and accurate solution by combining elements of both MD and continuum models. KMC simulations use a stochastic algorithm to simulate the dynamic behavior of the system, based on the transition rates between different configurations[48]. They can effectively capture the behavior of systems with multiple length and time scales, making them advantageous over traditional MD simulations and continuum models. KMC simulations are particularly useful at the mesoscale, where systems exhibit both macroscopic and molecular-level behavior, which is challenging to model using conventional methods. They provide a more complete and accurate picture of the system at this critical length scale[49]. KMC simulations are versatile and useful in various fields, as demonstrated by their successful application in: 1) Materials Science, where KMC simulations have been used to understand the behavior of materials at the mesoscale, including the growth of thin films[50], microstructure evolution in alloys[51], and formation of nanoscale structures[52]. 2) Chemistry, where KMC simulations have been used to study complex chemical reactions, such as the behavior of catalysts, nanoparticle formation[51], and reaction kinetics in heterogeneous systems[53]. 3) Biophysics, where KMC simulations have been used to understand the behavior of biological systems at the mesoscale, including ion channels in cell membranes[54], dynamics of biological membranes, and protein folding[55]. By modeling relevant events, such as diffusion of atoms, formation of bonds, and reactions of molecules and enzymes, KMC simulations provide a comprehensive understanding of complex systems at the mesoscale.

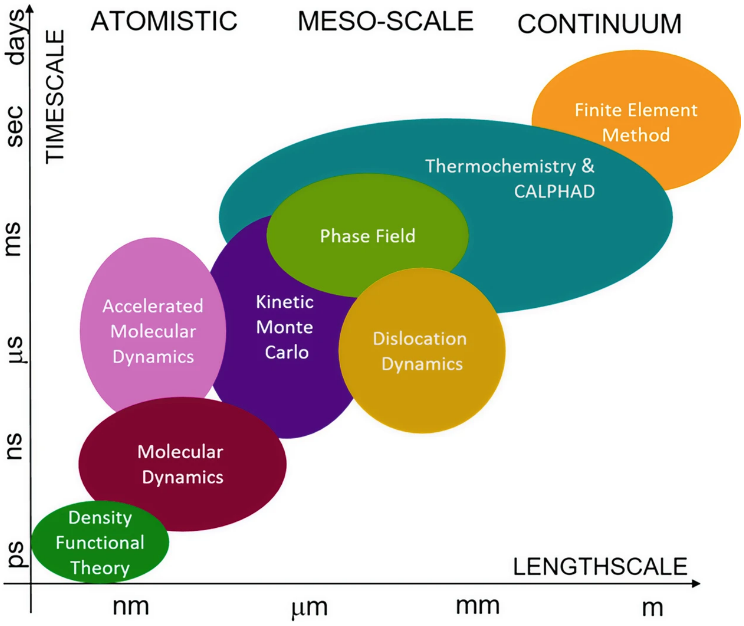

Figure 1.2.: Multiscale theoretical and computational methods used for materials model development and computer simulations. Reprinted with permission from Ref.[56], used under Creative Commons CC-BY license.

Figure 1.2 depicts a general overview of the length and time scales of various theoretical and computational methods is presented. Overall, KMC simulations offer a promising approach for overcoming the multiscale gap in mesoscopic science by combining the strengths of atomistic MD and continuum models. The ability of KMC simulations to effectively bridge the gap between different length and time scales has the potential to significantly advance our understanding of a wide range of systems and processes. With the increasing computational power and advances in algorithms, KMC simulations are poised to play an increasingly important role in the study of mesoscale systems.

Graphene and Solid Electrolyte Interphase (SEI) are two well-known mesoscopic systems that can be investigated with KMC simulations. KMC simulations have been used to examine a variety of graphene-related properties and processes, such as grain boundary creation and growth[57], thermal conductivity[58], and electronic transport[59].Similar to this, KMC simulations are used to study the creation and evolution of the SEI layer in lithium-ion batteries. KMC simulations were employed by Röder et al.[60] to investigate the formation of SEI and they found that the simulations accurately predicted the composition of SEI and its evolution over time. Similarly, Mathekar et al.[61] used KMC simulations to analyze the effect of SEI on the performance and stability of lithium-ion batteries, and they observed that the simulations offered valuable insight into how SEI affects the battery's rate capability and capacity fading. KMC simulations offer an efficient and cost-effective way to capture the atomic-level detail that is crucial for understanding the mesoscale behavior of both graphene and SEI. In this thesis, we employed KMC simulation to model and study the growth of graphene and SEI as two complex mesoscopic systems.

1.2. Graphene: A two-dimensional (2D) material

The history of graphene, a 2D material composed of carbon atoms arranged in a hexagonal lattice, can be traced back to 1947 when physicist Philip Russell Wallace predicted its existence as a single atomic layer of graphite[62]. However, it was not until 2004 that Andre Geim and Konstantin Novoselov at the University of Manchester isolated and characterized graphene[63], earning them the Nobel Prize in Physics in 2010 for their work on the material's unique properties. Geim and Novoselov used a simple technique of mechanical exfoliation to isolate individual graphene sheets[63]. Since its discovery[63], graphene has become one of the most attractive research topics globally, and 2D materials, crystalline materials made of one or a few layers of atoms with strong planar interatomic interactions, have gained attention due to their novel structures and outstanding features[64, 65, 66, 67, 68]. Graphene, with its unique covalently-bonded (sp^2 hybridized) carbon atoms arranged in a honeycomb lattice, possesses exceptional mechanical [69], electric[70], thermal[71], and optical properties[72, 73], making it a potential candidate for various applications in science and technology, such as field-effect transistors[74, 75, 76], flexible electronics[77, 78], photodetectors[79, 80, 81], energy storage[82, 83], sensors[84, 85], DNA sequencing[86, 87, 88], drug delivery[89, 90, 91], and composite materials[92]. Since the discovery of graphene, thousands of 2D materials with different physical properties have been predicted and exfoliated to mono-layer or multi-layers[93]. These materials include MoS_2 monolayer[94], hexagonal boron nitride[95, 96], black phosphorene[97], borophene[98, 99], silicene[100], germanane[101], stanene[102], antimonene[103], bismuthene[104], and tellurene[105]. These materials can be classified into four types based on their atomic structures and components: chalcogenides[106], graphene family[107, 108, 109] (Figure 1.3), Xenes[110], and 2D oxides[111]. The properties of 2D materials are strongly influenced by their structures, which are determined by their synthesis and growth processes. Two main methods are used to synthesize 2D materials: the top-down approach, which involves thinning a bulk material, and the bottom-up approach, which involves forming layers atom by atom. The top-down approach includes mechanical exfoliation[112], such as using sticky tape to peel off layered materials to form flakes, which is suitable for van der Waals materials and practical for lab studies but lacks control over the size and shape of the flakes. Liquid exfoliation is another top-down approach that uses mechanical force in an organic solvent to separate layered materials[113], but the resulting flakes may be less suitable for optoelectronic applications due to their high density. The bottom-up approach includes solution-based chemical synthesis, which encompasses various wet chemical techniques for producing 2D materials.

Nowadays, 2D materials are typically produced in flakes with a final size of less than 100 nm using different methods, such as mechanical and liquid exfoliation in the top-down approach, and solution-based chemical synthesis and chemical vapor deposition in the bottom-up approach. The bottom-up approaches have the potential to produce high quality 2D films, but in smaller amounts compared to the top-down approaches. Among the bottom-up approaches, chemical vapor deposition (CVD)[114] is a complex and expensive method (Figure 1.4 shows an the experimental CVD setup), but highly scalable and capable of producing large size films with high quality. The quality of the final product is highly sensitive to different parameters such as gas pressures, composition, temperature, reaction times, and thermodynamic and kinetic conditions such as heat transfer, mass transport, chemical reaction kinetics, adsorption, and nucleation[115]. Various theoretical and computational methods have been developed to fully understand the graphene growth process and exploit its remarkable properties alongside experimental efforts. DFT is one of the earliest and commonly used theoretical methods for predicting the electronic structure and energetics of graphene and other materials[116, 117], while tight-binding (TB)[118] is a simplified approach based on describing the electrons as moving through localized orbitals. Computational methods such as molecular dynamics (MD)[119], Monte Carlo (MC)[120] simulations, and KMC simulations are powerful tools for studying the dynamics and thermodynamics of materials, and modeling processes occurring over long timescales[121]. These methods, including DFT, TB, MD, MC, and KMC simulations, provide an in-depth understanding of the properties and behavior of graphene, contributing to the underlying physics of this important 2D material.

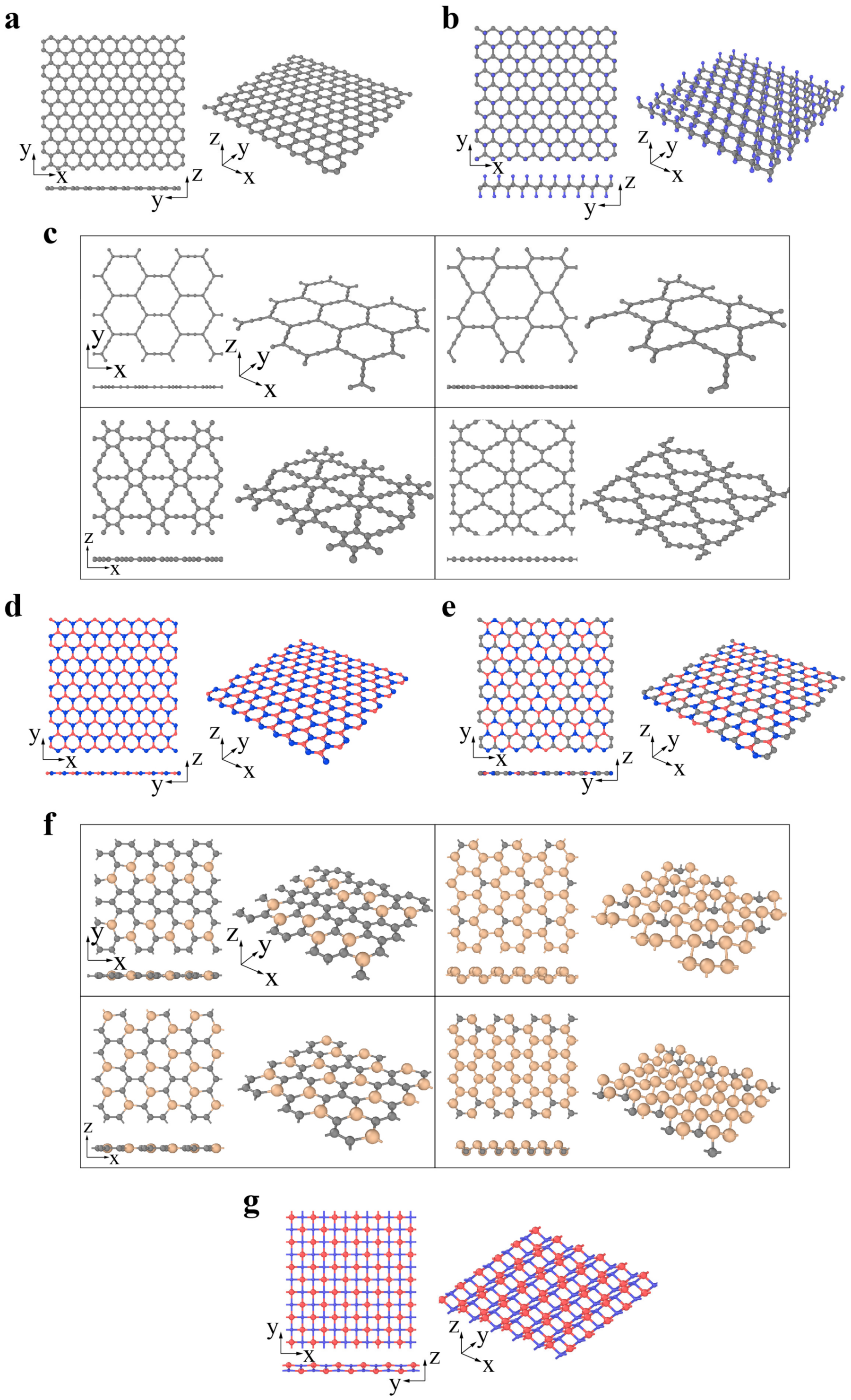

Figure 1.3.: The graphene family: (a) graphene (gray atom represents C), (b) CX (X = H, F, Cl; gray and blue atoms represent C and X, respectively), (c) graphyne (α-graphyne, β-graphyne, γ-graphyne and $6, 6, 12$-graphyne from left to right, top to bottom; gray atom represents C), (d) h-BN (red and blue atoms represent B and N, respectively), (e) BCN (Reprinted from [122]; red, gray and blue atoms represent B, C and N, respectively), (f) $Si_x\ C_{1-x}$ ($x = 2/10, 5/6, 2/6, 14/18$) from left to right, top to bottom; gray and yellow atoms represent C and Si, respectively) (Reprinted with permission from Ref.[107]), (g) TiC (Reprinted with permission from Ref.[108]; red and blue atoms represent C and Ti, respectively). Reprinted with permission from Ref.[109], used under Creative Commons CC-BY license.

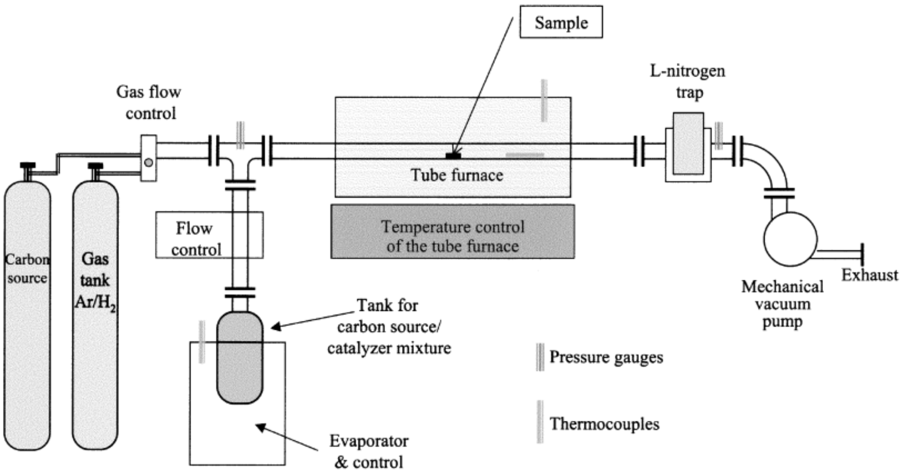

Figure 1.4.: Schematics of the experimental CVD setup using the floating catalyst method. The gas flow provides oxygen-free atmosphere for the pre-growth interval, and the carbon source-catalyst solution is evaporated from a separate bubbler. Temperature and pressure measurement and control is provided. Reprinted with permission from Ref.[123]. Copyright 2003 IEEE.

The motivation for using KMC simulations to study graphene growth on Cu(111) surface via chemical vapor deposition (CVD) is to overcome the limitations of other methods, such as DFT and molecular dynamics (MD), which are not capable of simulating the long timescales and large length scales involved in the growth process. KMC simulations provide a way to model the growth of graphene over longer timescales by using stochastic simulations that incorporate the kinetics of the chemical reactions and the thermodynamics of the system. This makes KMC simulations particularly well-suited to studying the growth of graphene on Cu(111) surface via CVD, as this process involves a complex interplay between chemical reactions, diffusion, and nucleation that occurs over long timescales. By using KMC simulations, researchers can gain insight into the growth mechanism of graphene on Cu(111) surface, as well as optimize the growth conditions to produce high-quality graphene with desirable properties. Compared to continuum modeling methods, KMC simulations offer a more detailed description of the processes occurring during graphene growth, and are computationally more efficient than atomistic simulations.

1.3. Solid Electrolyte Interphase (SEI)

The SEI is a critical element in lithium-ion batteries (Li-ion batteries - LIBs), providing a protective layer that prevents short circuits and ensures efficient and safe battery operation[124, 125, 126]. The SEI plays a vital role in the efficiency and safety of lithium-ion batteries, which are widely used in a variety of applications, including electric vehicles, consumer electronics, and energy storage systems[127]. Despite being an essential component of LIBs, the SEI is a complex system that has been challenging to study due to its dynamic nature and composition. The history of SEI research dates back to the 1970s[128], but it was not until the 1990s that researchers began to recognize its significance[129]. Since then, researchers have made considerable progress in understanding the SEI, leading to the development of high-performance lithium-ion batteries and recognition through prestigious awards. In 2019, John B. Goodenough, M. Stanley Whittingham, and Akira Yoshino were awarded the Nobel Prize in Chemistry for their work in developing the LIBs. Additionally, in 2020, Yang Shao-Horn was awarded the Royal Society of Chemistry's Tilden Prize for her work in understanding the SEI and developing new battery technologies. However, the lack of techniques capable of in situ or in operando probing of the SEI during battery cycling remains a challenge. Therefore, researchers have employed various experimental, theoretical, and computational methods to overcome these challenges and improve SEI understanding.

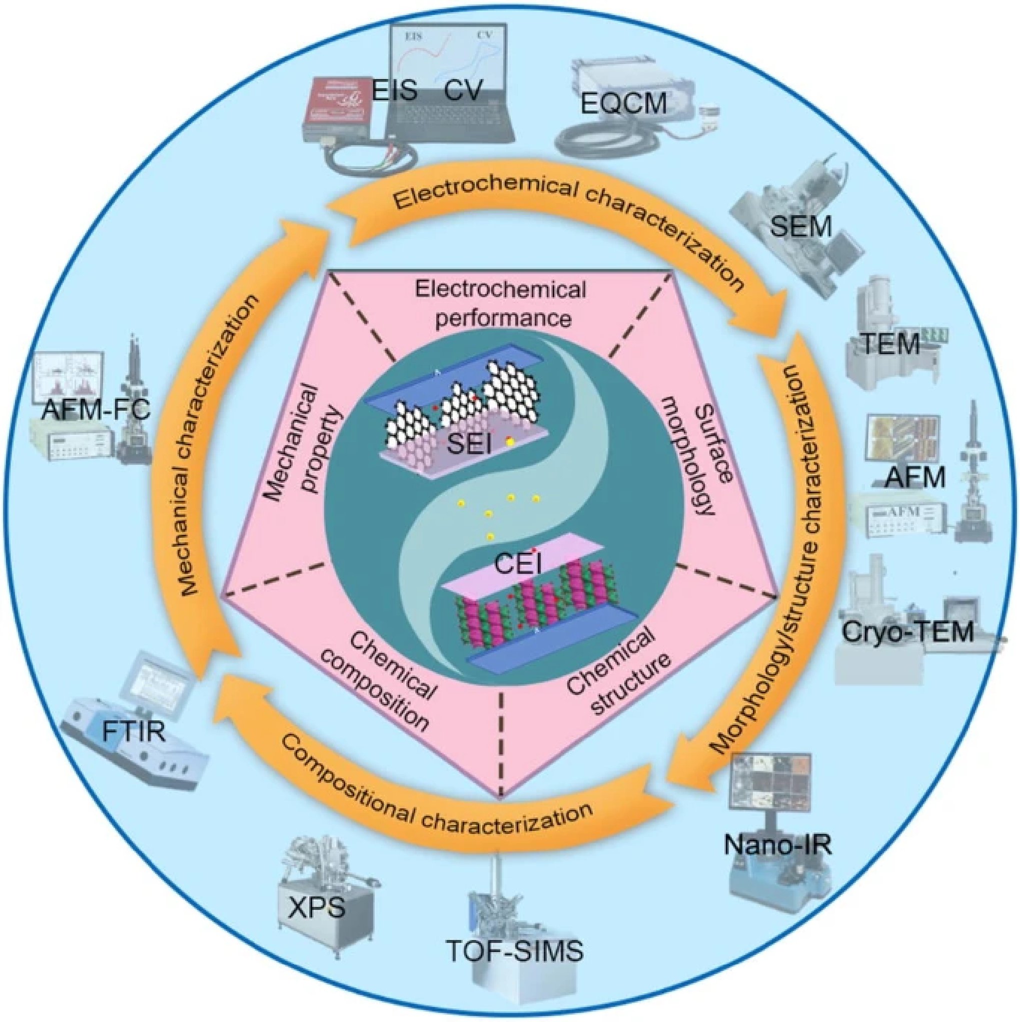

Figure 1.5.: SEI characterization, with a focus on state-of-the-art characterization techniques developed in recent years, includes methods to investigate electrochemical performance, surface morphology, chemical composition, and structural and mechanical characteristics. Reprinted with permission from Ref.[130] Copyright 2019, Shanghai University and Periodicals Agency of Shanghai University.

The SEI in Li-ion batteries can be studied using various experimental techniques, each with its own advantages and limitations(see Figure 1.5). Scanning Electron Microscopy (SEM) provides high-resolution images of the surface of the SEI[131], while X-ray Photoelectron Spectroscopy (XPS) can identify the chemical composition and electronic structure of the SEI[132]. Fourier Transform Infrared Spectroscopy (FTIR) can determine the molecular structure and chemical composition of the SEI[133], while Electrochemical Impedance Spectroscopy (EIS) measures the SEI's impedance and electrical properties[134]. Nuclear Magnetic Resonance (NMR) can identify the chemical species and types of chemical bonds present in the SEI[135]. However, each of these methods has limitations, and none can provide a complete understanding of the SEI's morphology, composition, and properties. Theoretical techniques have become an increasingly popular tool for investigating the SEI in Li-ion batteries. These methods can provide insights into the fundamental processes that occur within the SEI, which can aid in the design of more efficient and reliable batteries. One of the most widely used theoretical techniques is DFT, which can predict the electronic structure, ion transport, and chemical reactivity of the SEI. DFT calculations can determine the adsorption energies of electrolyte species on the SEI surface and the barriers to ion diffusion, among other properties. These calculations can also investigate the thermodynamics and kinetics of SEI formation and decomposition. However, DFT calculations can be computationally expensive and require a high level of expertise[136]. Another popular theoretical method is MD simulation, which can provide atomistic-scale insights into the structural and dynamical properties of the SEI. MD can simulate the SEI formation and the interfacial behavior between the SEI and the electrode, and investigate the transport properties of ions and solvent molecules in the SEI layer. However, MD simulations can also be computationally expensive and require a large number of atoms and long simulation times to achieve statistically significant results[137]. Continuum models are another class of theoretical methods that use mathematical models to describe the SEI's properties at a larger length scale. These models can provide insights into the transport properties of ions and solvent molecules in the SEI layer, and allow the investigation of the effects of SEI thickness and morphology on the electrochemical performance of Li-ion batteries. However, continuum models can oversimplify the complex structure of the SEI and result in lost aspects regarding its formation and dynamics[138]. Finally, KMC simulation is a powerful theoretical method that can simulate the SEI formation and the interfacial behavior between the SEI and the electrode, investigate the ion transport properties, and predict the SEI's evolution under different conditions. However, developing an appropriate KMC model can be challenging due to the complex and heterogeneous nature of the SEI. Each method has its own set of advantages and limitations, and the choice of method depends on the research question and the information required. By using theoretical methods in conjunction with experimental methods, researchers can gain a more complete understanding of the SEI formation and dynamics, leading to the design of better-performing Li-ion batteries.

KMC simulations have several advantages over other methods in studying the SEI growth in lithium-ion batteries. One of the primary motivations for using KMC simulations is that they can provide a detailed understanding of the growth mechanisms of the SEI layer at the atomic scale. KMC simulations can simulate the SEI growth over long timescales and under various conditions, providing insights into the evolution of the SEI layer over time. The other advantage of KMC simulations is that they are computationally efficient and can model large systems with reasonable accuracy.

1.4. Thesis outline

With the advancement of computational power and the development of more sophisticated algorithms, KMC simulations have become increasingly popular and accurate, enabling researchers to study complex systems, such as thin-film growth, surface reactions, and battery interfaces. In recent years, KMC simulations have been used to model the growth of two-dimensional materials, the formation of surface alloys, and the dynamics of the solid-electrolyte interphase in lithium-ion batteries. This thesis discusses two complex mesoscopic growth processes via KMC simulations.

- **Chapter 2**. presents a detailed explanation of the fundamentals of KMC simulations. It includes a historical overview of the method and its transition from MC to KMC simulations. The technical aspects of the method are explained, with a focus on the selection of transition rates, which is critical to the accuracy of the method. The chapter concludes with a review of various KMC algorithms and a discussion on the disparity problem in KMC timescales.

- **Chapter 3**. provides a detailed analysis of the CVD graphene growth mechanism on the Cu(111) surface via KMC simulations. The chapter identifies the specific reactions involved in the growth mechanism, investigates the impact of methane and hydrogen partial pressures as CVD control parameters and estimates the growth rate during steady-state growth. The chapter commences with an introduction to the problem and provides information about the reaction network of the mechanism. It also includes details of the KMC algorithm implemented for this complex mesoscopic growth process. It concludes by discussing the effects of CVD control parameters on graphene growth and its quality.

- **Chapter 4**. is dedicated to investigating the spatiotemporal evolution of organic and inorganic components of SEI formed during electrochemical processes. The chapter explores how a series of chemical reactions, diffusion, and aggregation impact SEI formation with nanometer resolution, while considering kinetic information specific to the electrolyte-anode chemistries. It commences with an introduction to the complexity of the SEI formation process, followed by information on the required reaction network. The chapter then describes the implementation of the KMC model in detail, which provides valuable insights into the complex mesoscopic SEI formation process.
- **Chapter 5**. summarizes the main findings of the study, highlighting the strengths of the constructed KMC model, identifying areas that require further improvement.

2. The Kinetic Monte Carlo Methods

2.1. Introduction

KMC simulations, as a type of stochastic Monte Carlo method, have proven to be an effective means of simulating the dynamic behavior of a diverse range of physical and chemical systems. These systems include catalysis[139], material fabrication[140], defect evolution in crystals[141], and diffusion[142, 143]. The KMC algorithm was first developed in 1960 and has been continually refined over the years. The earliest reported application of this method was in the study of radiation damage annealing in 1966 by Beeler [49]. KMC methods have demonstrated their capability to simulate longer timescales (ranging from milliseconds to hours) and spatial scales with relatively low computational expenses when compared to other computational methods [144, 145]. The algorithm describes the dynamic behavior of a system as it transitions from one state to another, providing a detailed understanding of the system's evolution over time. Due to their versatility and efficiency, KMC simulations have become a powerful tool in the field of computational modeling and have found a wide range of applications in diverse fields.

2.2. From Monte Carlo to Kinetic Monte Carlo

Monte Carlo (MC) methods are a set of algorithms that solve problems using random numbers. They emerged in the late 1940s and 1950s with the advent of electronic computers, and were named after the random nature of gambling at Monte Carlo, Monaco. The Metropolis algorithm, published by Nicholas Metropolis in 1953 [146], is one of the best-known MC methods. This algorithm describes the evolution of a system from one state to another based on the transitions between states described by a probability distribution. To generate new states, importance sampling is used to replace the old ones. This technique is applied to regions of importance with a low occurrence probability, generating samples of the region of interest with a lower probability by assigning a larger weight. The correct probability density distribution can be achieved through repeated replacements [147]. The Metropolis algorithm is highly adaptable and clear, making it one of the most credible MC methods. In 1975, Bortz, Kalos, and Lebowitz proposed an accelerated version of the MC method, known as the N-fold way algorithm or BKL algorithm [48]. In contrast to the Metropolis algorithm, where only some selected events are taken into account based on acceptance criteria, the N-fold approach considers all selected events on KMC steps. As MC simulations only record the number of steps from the first to the last, the KMC algorithm, developed from the Metropolis algorithm, required a way to deliver the temporal evolution of the system. The KMC algorithm describes the dynamic behavior of a system from one state to another by calculating the time required for the transition between states using the total transition rate of all possible transitions and a random number generated from a Poisson distribution [148]. This algorithm's efficiency lies in its ability to simulate longer timescales and spatial scales with relatively low computational expenses when compared to other computational methods. In conclusion, MC methods have become a powerful tool for solving problems using random numbers. The Metropolis algorithm and the N-fold way algorithm are two examples of these methods. The Metropolis algorithm remains a highly credible and adaptable method due to its clarity, while the KMC algorithm, developed from the Metropolis algorithm, provides a way to deliver the temporal evolution of a system. Through its ability to simulate longer timescales and spatial scales with relatively low computational expenses, the KMC algorithm has found applications in a wide range of fields. More detailed information on the KMC algorithm and its calculation can be found in section 2.6 of this chapter.

2.3. The timescale problem and infrequent event dynamics

Recent advancements in computational solid state physics and fluid dynamics have opened up new opportunities to investigate fundamental and longstanding questions through a diverse range of computational methods. Selecting the most suitable method for a particular problem is contingent upon the length and time scales needed to monitor the evolution of the system. Despite these developments, there are certain problems where the system requires larger time scales due to spending a significant portion of time vibrating within a potential basin of the potential energy surface (PES) before transitioning to another state[144, 49]. This vibration takes place on a picosecond scale and is several orders of magnitude faster than the state-to-state jumps. Due to this infrequent nature of the transitional jumps, they are considered rare or infrequent events. Assuming that the system is in a quasi-equilibrium state between these infrequent events, it has enough time to forget about its past path[144], a property known as the Markov property[149]. Molecular dynamics (MD) simulations have been widely used to study solid state and fluid transport problems, primarily focusing on the dynamic evolution of the system. This method integrates the classical equations of motion in time and requires selecting the interatomic potential for the atoms involved and setting boundary conditions for the system. Additionally, the precise integration of the equation of motion necessitates very short time steps (10^{-15} s) to account for atomic vibrations. As a result, the total simulation time is typically limited to less than one microsecond, even though the study case may take place over much longer time scales.

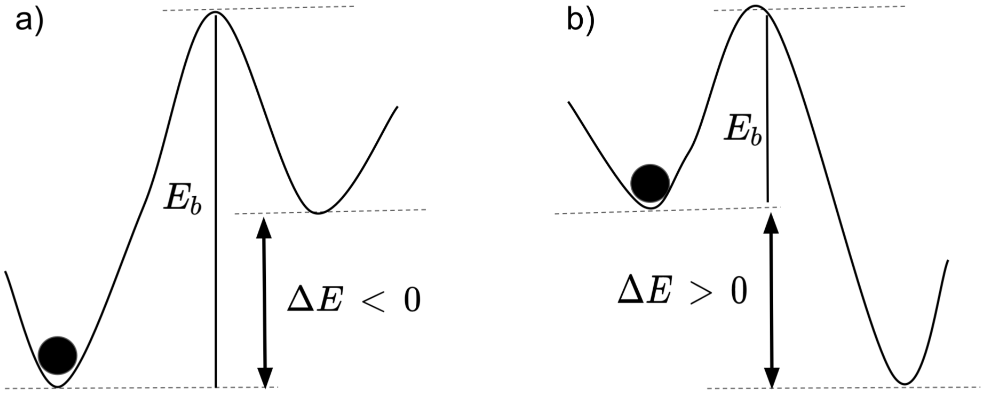

Figure 2.1.: Illustration of a barrier that leads to a higher-energy state (a) and one which leads to a lower state (b).

The fields of statistical mechanics and MC methods are valuable tools for simulating the evolution of a system, especially when the focus is on state-to-state jumps between infrequent events rather than on the vibrational motion of particles. The Kinetic Monte Carlo (KMC) simulation is based on the idea of determining the frequency of state-to-state transitions[145] and the corresponding transition rate constants, which depend on the activation energy barriers between states[144]. These rate constants describe the average fraction of systems in a quasi-equilibrated ensemble of systems that cross the energy barriers per unit time. Therefore, the time it takes for a system to transition between states depends on the activation energy barrier it must overcome to move from one energy basin to another[49]. Figure 2.1 provides an example of a transition from a low-energy state to a high-energy state (Δ E $<$ 0) and a positive energy difference transition (Δ E $>$ 0). The KMC method is unique in that it focuses on the statistics of overcoming energy barriers instead of tracking the vibrational motion of the particles. This allows access to longer time and length scales compared to other computational methods. Figure 2.2 illustrates a graphical representation of the time and length scales of the Density Functional Theory (DFT), Molecular Dynamics (MD), and KMC methods.

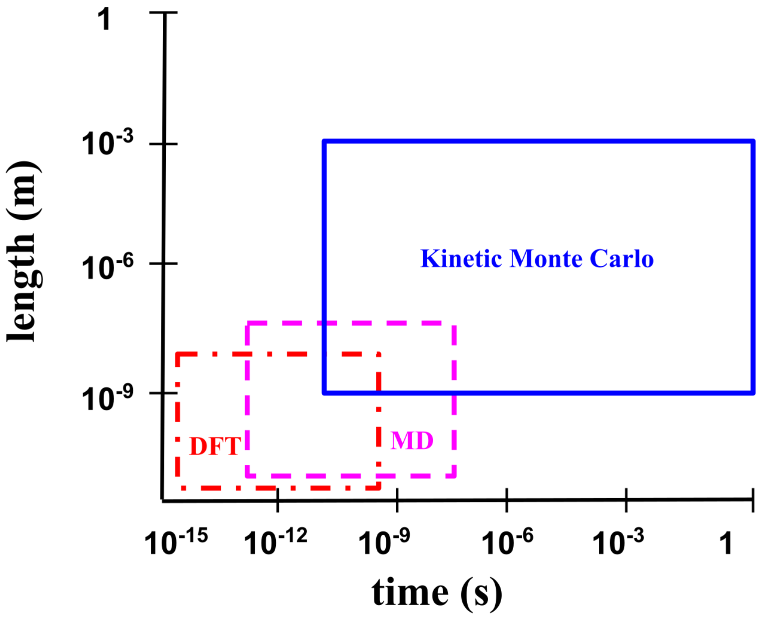

Figure 2.2.: Length and time scale of different modeling methods. DFT: Density Functional Theory, MD: Molecular Dynamics.

In order to develop a KMC model that accurately simulates the evolution of a system, several important factors need to be taken into consideration. The first important factor is ensuring the satisfaction of the Markov property. The Markov property is a fundamental concept in probability theory, which states that the future state of a system only depends on its present state, and not on any of its past states. In KMC simulations, the Markov property is crucial for accurately predicting the probability of state-to-state transitions. The second factor that must be considered is the satisfaction of microscopic reversibility. Microscopic reversibility is a principle of statistical mechanics which states that any process that can occur in one direction must also be able to occur in the opposite direction. In KMC simulations, microscopic reversibility is important for ensuring that the probability of a transition from state A to state B is equal to the probability of a transition from state B to state A. The third factor to consider is finding all relevant transition rates. The rate at which a system transitions from one state to another depends on the energy barrier that must be overcome to make the transition. It is important to accurately calculate all of the relevant transition rates in order to properly simulate the system's evolution. Finally, advancing the time of the system is an important factor to consider in KMC simulations. In order to accurately simulate the evolution of a system over a longer period of time, the simulation must be able to advance the system's time while accurately simulating the state-to-state transitions. By carefully considering and addressing each of these factors, an accurate and reliable KMC model can be developed for simulating the evolution of a system. We will discuss all these matters in the following chapter.

2.4. The Master equation

As it explains how the probability density function (PDF) changes over time, the Master equation can provide a thorough explanation of the system. It carries the PDF data for each system state at any given time. There are clusters of fast (frequent) vibrations and slow (infrequent or uncommon) transitions in such systems, which is their essential feature. One can argue that by the time the system escapes from the state n-1 to the state n, the memory of all the previous n-2 states has been lost because the time interval between two rare events is several orders of magnitude longer than fast vibrations. The following equality can be applied to restate it for any set of n consecutive times (i.e t_1, t_2...t_n) of the random variable X:

$$P_{1|n-1}(x_n, t_n|x_1, t_1; ...x_{n-1}, t_{n-1}) = P_{1|1}(x_n, t_n|x_{n-1}, t_{n-1}) \tag{2.1}$$

In Equation 2.1, the Markov property is represented by the conditional probability density at time t_n, given that the value x_{n-1} at time t_{n-1} is directly defined and independent of all the states preceding it. The transition probability, $P_{1|1}$, is a fundamental concept in Markov processes, and it represents the probability of transitioning from one state to another. Therefore, the behavior of a Markov process is completely characterized by two functions: $P_1(x_1,t_1)$ and $P_{1|1}(x_2,t_2|x_1,t_1)$. These two functions can be used to construct the entire list of probabilities P_n, which describe the probability of being in a certain state at a given time. The Master equation is another important concept in the study of Markov processes. It describes the time evolution of the probability of finding the system in a particular state i at time t[149]. This equation is a central tool in the analysis of Markov processes and provides a way to calculate the long-term behavior of the system.

$$\frac{dP_i(t)}{dt} = -\sum_{j \neq i} r_{i,j}^{KMC} P_i(t) + \sum_{j \neq i} r_{j,i}^{KMC} P_j(t) \tag{2.2}$$

The Master equation, represented by Equation 2.2, is a mathematical tool used to describe the time evolution of a system composed of different states. It calculates the sum of all possible incoming transitions from states j to states i, minus all possible outgoing transitions from states i to states j, using the probability of finding the system at states i (P_i(t)) and j (P_j(t)), multiplied by their transition probability per unit time ($r_{i,j}^{KMC}$) and ($r_{j,i}^{KMC}$), which indicate the i to j and j to i transitions, respectively. Solving this equation analytically can be challenging, especially for systems with more than two particles. Some methodologies have been developed to solve it analytically, such as the solution proposed by Kolokathis et al. for a system of spatially periodic states[150]. However, in most cases, an analytical solution of the Master equation is not achievable, and the evolution of the system can be simulated by using a KMC algorithm[144]. To ensure that the evolution of the system is accurately described within its thermodynamic limit, it is necessary to confirm that microscopic reversibility is met. This means that for any linked pair of states, a detailed balance condition must be fulfilled. The first part of Equation 2.2 must be equal to zero once the system reaches its equilibrium state (steady state), also known as steady state. In other words, the incoming and outgoing transitions must balance each other out, and the system must be in a state of detailed balance:

$$\sum_{j \neq i} r_{i,j}^{KMC} P_i^0 = \sum_{j \neq i} r_{j,i}^{KMC} P_j^0 \tag{2.3}$$

$$r_{i,j}^{KMC} P_i^0 = r_{j,i}^{KMC} P_j^0 \tag{2.4}$$

where, P_i^0 is the probability of finding the system in equilibrium at state i. Equation 2.4 indicates that there is a reverse event j → i for every elementary event i → j, where the average number of transitions from i to j is equal to the number of reverse transitions. Therefore, the microscopic reversibility of the system is being satisfied at equilibrium. But despite that, the detailed balance between states i and j expressed by Equation 2.4 must remain true while the system is not yet at equilibrium. To validate that the selected transitional rates obtain the dynamical evolution of the system within equilibrium accurately, we can take into account the Boltzmann relationship at equilibrium[144]:

$$P_i^0 \sim exp(-\frac{F_i(T)}{K_B T}) \tag{2.5}$$

This formula connects the population of state P_i^0 to the free energy of state i at temperature at temperature T (F_i(T)). Then the relationship between the kinetic rates $r_{i,j}^{KMC}$ and $r_{j,i}^{KMC}$ can be expressed by taking into account equations 2.4 and 2.5 as:

$$\frac{r_{i,j}^{KMC}}{r_{j,i}^{KMC}} = exp(-\frac{F_j(T) - F_i(T)}{K_B T}) \tag{2.6}$$

The equation establishes a connection between transition rates and the system's state at equilibrium, and it serves as an expression of the detailed balance condition that holds true for the system at all times[144].

2.5. Rate constants

To study the system's dynamic evolution using the KMC approach, all the potential events or transitions should be identified beforehand. This catalog of rates facilitates the KMC model to generate state-to-state trajectories that are comparable to those produced by MD simulations[49], which is an atomistic modeling technique. To determine all feasible pathways, statistical mechanics techniques such as transition state theory (TST)[144, 49, 151] can be employed.

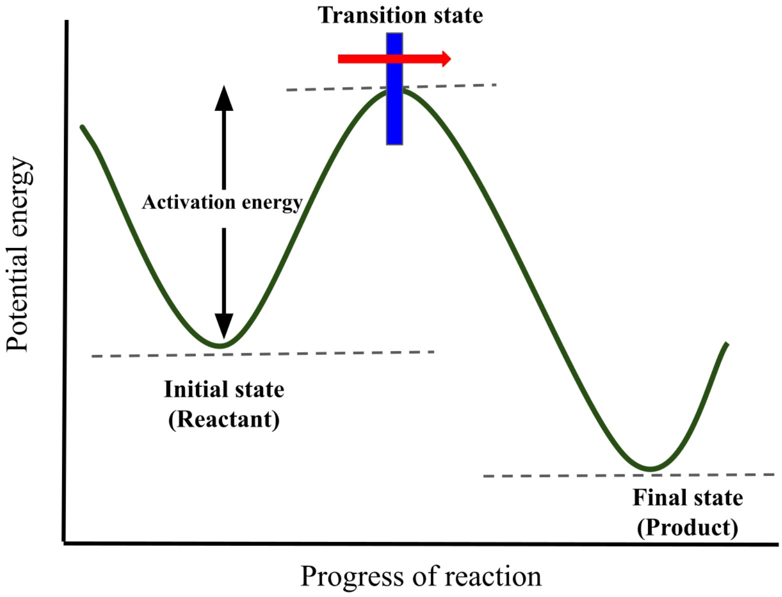

Figure 2.3.: Illustration of the transition state theory rate constant of escaping from the initial state to the final state. A thick blue line divides the surface area.

Although TST provides a good approximation for solid-state diffusive events, its primary purpose is to estimate the rate constant[49]. According to TST, the rate constant for transitioning from the initial state i to the final state j is determined by the outgoing flux through the dividing surface that separates the states at equilibrium, as demonstrated in Figure 2.3.

The TST rate constant, denoted by K^{TST}, can be determined by dividing the number of jumps passing through the dividing surface area by the number of trajectories in the initial state i at any given time. In order to ensure the Markov property is satisfied, a quasi-equilibrium state must be reached at each potential energy basin before transitioning to the next state[49]. TST assumes that each forward jump through the surface area is an independent event, and as a result, there is a possibility of jumping back before reaching the final or initial states. As a consequence, the TST rate constant tends to overestimate the actual rate. One approach to account for backward jumps is to establish the trajectories at the dividing surface area and integrate them over a short time period. This method can also account for multiple crossing events[49]. In 1935, Eyring derived the TST transition rate constant K^{TST}, which is expressed as follows[144, 152]:

$$K^{TST} = k\frac{K_B T}{h}\frac{Q^{\ddagger}}{Q_{reactants}}exp(-\frac{E_a}{K_B T}) \tag{2.7}$$

where,

- h = Planck's constant,
- k = factor used as a transmission coefficient for re-crossings of the barrier,
- E_a = Activation energy barrier,
- K_B = Boltzmann constant,
- T = temperature,
- $Q^{\ddagger}$ = molecular partition function for the transition state,
- $Q_{reactants}$ = molecular partition function for the reactants.

The free energy of the transition state in Equation 2.7 is composed of two factors, one related to the other degrees of freedom (excluding the reaction coordinate) and another related to the kinetic energy along with the reaction coordinate. To determine the activation energy barrier indicated in Equation 2.7, initial and final state information is required, and density functional theory (DFT) can be employed for this purpose[153, 154]. In order to account for backward jumps (i.e., re-crossing the transition state), Eyling introduced the pre-factor k, which decreases the rate (k $\leq$ 1)[152].

Additionally, the molecular partition function can be determined through the harmonic approximation of the potential, which is known as harmonic transition state theory (HTST). This method describes the molecular partition function as a product of electronic, vibrational, rotational, and transitional contributions[152, 153]:

$$Q = q_{elec}\, q_{vib}\, q_{rot}\, q_{tran} \tag{2.8}$$

In the context of the given situation, the symbol 'q' represents the sum of all contributions of a particular type, which can be computed through DFT calculations along with the saddle point energy[144]. Another method to determine the reaction rate constant involves the use of a pre-exponential factor added to an activation energy term. The expression for this approach is provided below[155]:

$$r^{KMC} = \nu\ exp[-\frac{E^{act}}{K_B T}] \tag{2.9}$$

where,

- r^{KMC} = transition rate,
- E^{act} = activation energy
- ν = pre-factor

It is often not accurate to assume that E_a and E^{act} are equal in equations 2.7 and 2.9, and the same goes for the pre-exponential factor in Equation 2.7 and ν in Equation 2.9. The reason for this is that the partition function in Equation 2.7 usually includes exponential factors that contribute to E^{act} but are not explicitly shown. The Arrhenius form given in 2.9 is suitable only for systems with temperature-dependent activation energy and pre-factor, which can lead to a temperature-dependent transition rate constant[155]. In this form, there are various ways of computing transition rates. One approach involves using Equation 2.9 to calculate the rate constant for any desired temperature and then applying linear regression to the plot of $ln(r)$ as a function of the inverse temperature $(1/T)$. By applying ln to both sides of Equation 2.9:

$$ln(r^{KMC}) = -\frac{E^{act}}{K_B T} + ln(\nu) \tag{2.10}$$

where $ln(\nu)$ and $-E^{act}/K_B$ are the coefficients b and a in the linear regression $y = ax + b$ respectively.

Another approach to computing the transition rate constant is to determine the factors in the partition functions that have the same exponential relation as the activation energy. This method is less precise than the previous approach but is more straightforward. Once the factors are determined, the transition rate constant can be calculated for any desired temperature. In this case, the pre-factor can be obtained by using the transition rate constant calculated as r_{cal}^{KMC}.

$$\nu = r_{cal}^{KMC}\ exp[\frac{E^{act}}{K_B T}] \tag{2.11}$$

Knowing about the efficiency of a KMC simulation in addressing the long-term evolution of systems containing infrequent events, it is time to discuss the KMC algorithms in detail.

2.6. KMC algorithms

After understanding the concept behind KMC simulations, which involves solving the Master equation for systems that include rare events, it is crucial to delve into the KMC algorithm itself. Essentially, a KMC trajectory is a sequence of jumps between different states of a system, where the time interval associated with each state transition can be calculated. Starting from an initial configuration, the KMC algorithm generates stochastic trajectories consisting of these state transitions, and averaging over these trajectories yields the time evolution of the corresponding probability according to the Master equation. In general, a KMC algorithm comprises three primary components at each step: identifying all possible events, selecting an event, and updating the system configuration. Based on the methodology for constructing the selection scheme, KMC algorithms can be classified into two categories: rejection-free KMC (rfKMC) and rejection KMC (rKMC).

A rejection-free KMC algorithm, also known as the KMC algorithm, is well-suited for simulating the time evolution of a system with known transition rate constants for all events. The following steps are involved in the KMC algorithm:

1. Set the time t=0 and choose the initial state i,
2. Collect all N_i possible transition rates from state i to state k in the system, r_{ik},

3. Compute the cumulative rate for the collected list as $R_{ik} = \sum_{j=1}^{k} r_{ij}$. The total rate is $R_{tot} = R_{i,N_i}$,
4. Generate two random numbers u,u′ within 0 and 1,
5. Search for the event k that satisfies $R_{i,k-1} < u \times R_{tot} \leq R_{i,k}$,
6. Execute the event k (update the state i → k),
7. Update the time using t+Δt where $\Delta t = R_{tot}^{-1}\, ln(1/u')$,
8. Repeat from the step 2.

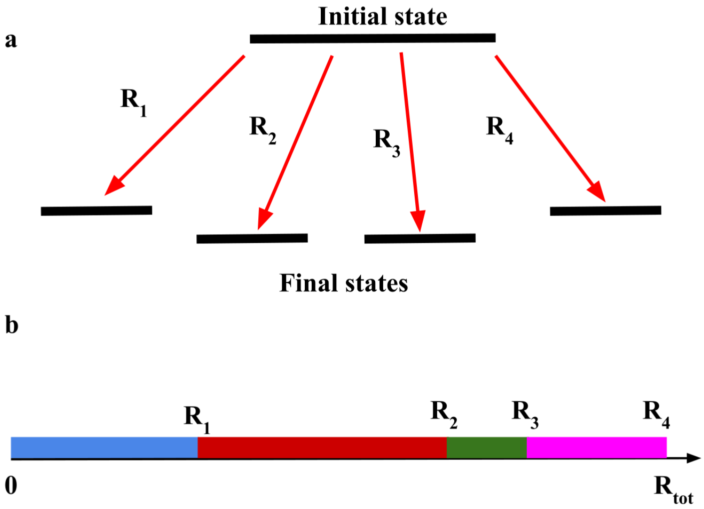

Figure 2.4.: Illustration of a) the rfKMC step in which all transition rates from the initial to final state are known, and b) the cumulative rate calculated from all possible transition rates.

A rKMC algorithm is another type of KMC algorithm that only requires the transition rates of possible events, rather than all of them. In this type of algorithm, not all possible events are considered, and instead, only a subset of the events is selected for simulation. The rKMC algorithm is based on the rejection principle, where the chosen event is compared with a random number generated between zero and one. If the selected event has a probability greater than the random number, then the event is accepted, and the system configuration is updated. Otherwise, the event is rejected, and the algorithm proceeds to the next iteration. The rKMC algorithm can be useful for simulating complex systems where the rate constants are not known in advance, or when it is computationally infeasible to calculate all of the transition rates. The general steps of an rKMC algorithm with the same transition rates are as follows:

1. Set the time t=0 and choose the initial state i,
2. Collect all N_i possible transition rates from state i to state k,
3. Select an event from the collected rates using uniform random sampling,
4. Accept the event with the probability of $f_{ik} = r_{ik}/r_0$ where r_0 is the single global upper bound for r_{ik},
5. Execute the event if it is accepted, (update the state i → k),
6. Generate a random number u within 0 and 1,
7. Update the time using t+Δt where $\Delta t = (N_i r_0)^{-1}\, ln(1/u)$,

8. Repeat from the step 2.

The efficiency of the rKMC algorithm is proportional to the ratio of the attempted events to the accepted events. Therefore, the algorithm's efficiency depends on the distribution of rates in each study case, where systems with a broader range of rates may have much lower efficiency than those with a narrower range of rates[156, 157]. Additionally, rare events can also impact the algorithm's efficiency by dividing the list of possible events into two categories: one with high transition rates and the other with small transition rates. Several KMC algorithms have been developed for various applications, such as the random selection method, the first reaction method, the direct method, among others[144, 158].

2.6.1. The random selection method

The random selection method (RSM) is a classic KMC algorithm that was developed to handle systems in which some MC events may not succeed[159]. It is also known as the null-event method and has been widely used in various applications. The Metropolis algorithm is one of the best-known examples of a random selection algorithm, which typically comprises three parts: determining the type of process, identifying the site where the selected event occurs, and calculating the time required for the event to occur. To implement this algorithm, the following steps are usually followed[155, 159, 160]:

1. Choose a site at which the event occurs using a random number,
2. Choose the event type for the selected site using a random number,
3. Check if the selected transition is possible at the nominated site. If so, update the system based on that event. Reject the event and return to the first step,
4. Calculate the time required for the transition,

In the random selection method, events are selected without any particular order in terms of the type of event or where it will occur. The efficiency of this method is determined by the ratio of successful events to unsuccessful ones, similar to the rKMC algorithm discussed earlier. Because selected events can be rejected during simulation, the method is also referred to as the null-event method[155, 159].

2.6.2. The first reaction method

The first reaction method (FRM), which is one of the algorithms in the rfKMC category, is based on selecting the event with the shortest time among all possible events. In this method, the list of potential transitions is traversed, and the required occurrence time for each of them is calculated. Then, the event with the smallest occurrence time is selected as the next event in the sequence. The occurrence time for any transition between two states, represented by i and j respectively, can be calculated as follows:

$$t_{i \to j} = t - \frac{1}{r_{ij}^{KMC}} \, ln(u) \tag{2.12}$$

where,

- t= the current simulation time,
- r_{ij}^{KMC}= the rate constant for the i to j transition,
- u= a random number from a uniform distribution,

The algorithm referred to as Discrete Event Simulation (DES), is another term for the FRM. This algorithm's efficiency relies on computing the occurrence time for all possible transitions and is proportional to the size of the collected events at each step. As a result, it can be computationally expensive and slow. To improve the method's efficiency regarding the time calculation process, it is possible to assume that executing the first event will not affect the occurrence time of the second transition. In other words, the random time for the second event remains the same until one of the following happens: 1) the second transition occurs, 2) the number of particles involved in the second transition changes due to another event, or 3) the transition rate of the second event changes under the influence of other system parameters, such as local temperature[155].

2.6.3. Direct method

The direct method, also known as Gillespine's algorithm, is another rfKMC algorithm that can handle the Master equation. Like the general rfKMC algorithm, it proceeds by collecting all possible events at each step, selecting one of them using a random number and the cumulative rate, updating the system configuration, and advancing the system time using another random number. Because the time increment of the system depends on the total rate of all possible events at each step, it may vary during simulation. Thus, this variant of the KMC method is called the variable step size method (VSSM) in the literature [161].

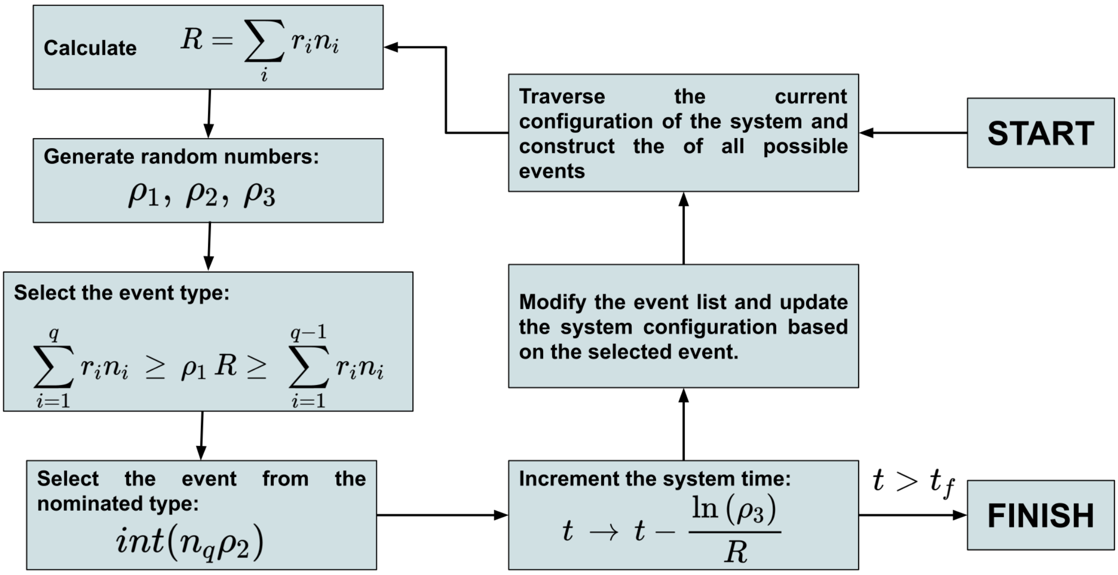

Figure 2.5.: Flowchart of the direct algorithm with a two-step event selection scheme. This algorithm requires three random numbers: two for the event selection and one for the time increment. The termination time is denoted by t_f in the flowchart.

The efficiency of this method depends on the number of event types and the update approach. To accelerate simulations for systems with a moderate number of event types, the two-step selection of the next event can be utilized. At the first step, KMC compares the random number with at most N partial sums over different event types, and at the second step, it selects among equally probable events of the selected type without comparing numbers. This selection scheme is computationally efficient, requiring at most N numerical comparisons for each step selection scheme, as illustrated in Figure 2.5.
However, this two-step selection scheme is impractical when the direct KMC algorithm involves a large number of event types. To address this issue, one possible solution is

to select the event in real space based on the local data representation. This enables a multi-step selection scheme for grouped events in real space, where the local region is first chosen using a random number, then the event type that can take place at that region is selected via another random number, and finally, one of the equally probable events within the selected type is picked. This selection scheme is independent of the number of event types, making it a useful development in the algorithm. Lastly, an important aspect of the direct method is the motivation behind the time increment. For an isolated species with a uniform transition probability r and a transition probability density f that provides the transition rates at time t, the theory of stochastic processes defines the process as a Poisson process when the probability of a transition is independent of the history of the transitions at all times, meaning the transition probability is a uniform function of time[162]. The change in f(t) over a short time *delta*t would be proportional to r, *delta*t, and f(t), as shown below:

$$df(t) = -rf(t)dt \Rightarrow \frac{df}{dt} = -rf \tag{2.13}$$

considering the boundary condition f(0) = r, the solution is:

$$f(t) = r\, e^{-rt} \tag{2.14}$$

One way to conceptualize the system is by considering it to be a vast Poisson process that shares similar characteristics as a single process. This analogy holds true for numerous processes that possess varying rates, denoted by r$_i$, and are present within the system. To express this idea mathematically, Equation 2.14 can be reconfigured to accommodate the larger scale of the system.

$$F(t) = R\, e^{-Rt} \tag{2.15}$$

Where, F(t) provides information for the transition probability density of the larger system with:

$$R = \sum_i r_i \tag{2.16}$$

To get the time increment equation, it is enough to calculate the inverse of its cumulative distribution function as the random number u and rearrange the equation:

$$e^{-Rt} = u \Rightarrow t = -\frac{ln(u)}{R} \tag{2.17}$$

2.7. Disparity problem in KMC timescale

As previously mentioned in this chapter, the KMC method was developed with the primary objective of studying the dynamic time evolution of systems over longer time and spatial scales. Compared to MD simulations, KMC simulations are faster since they focus on infrequent events such as transitions between different states rather than considering the vibrational degrees of freedom of the system which are more frequent. However, it should be noted that the infrequent events handled by KMC may also occur at different timescales. This can pose a problem in sampling the dynamics of the system properly since most of the simulation time is spent on short-term time events such as fast events. This is particularly true for KMC models dealing with surface reactions on metals, where the system contains a complex reaction network of slow surface reactions and fast surface diffusion. To overcome this issue, various approaches have been developed. One such approach is the tau-leap method[163], where multiple processes are carried out concurrently to accelerate the KMC simulation. The fundamental assumption of this method is the leap condition, which is satisfied when the surface populations are approximately constant in time. However, this method may not be practical for systems where surface reactions take place on microscopic lattices, and the site population can change substantially from zero to one species in just one KMC step. Therefore, this method is more suitable for coarse-grained lattices where the species concentration is roughly constant over time in each cell. Another approach is to separate the events into slow and fast processes and consider only the slow event dynamics stochastically at the KMC level while treating the fast event dynamics deterministically. This can be achieved by employing the Langevin equation[164, 165]. However, the main disadvantage of this type of model is that it requires manual setting of a constant timescale separation in advance. In recent times, most KMC approaches have been implemented using simple acceleration schemes. These schemes are based on decreasing the rate constants for the fast events in the system. In cases where it is confirmed that the output is not affected by scaling[166, 167, 168, 169], this rate scaling idea can be applied manually on systems with simple reaction networks. However, a different class of KMC algorithms has emerged that can deal with the scaling of fast processes automatically. This class of algorithms is based on the idea that fast processes, after a few iterations, become quasi-equilibrated, making it unnecessary to simulate these events further to describe the system dynamics accurately[170, 171]. One such algorithm is the accelerated superbasin (AS-KMC) method[170], which was introduced to investigate infrequent event dynamics more efficiently than standard KMC. The computational requirements of both approaches are almost the same. Thus, the AS-KMC method can be used for study cases including infrequent events without concern about manually scaling the rate constant to achieve reasonable results. However, the efficiency of this method depends on the complexity of the system. Increasing the total number of system configurations makes the full sampling of a single superbasin very slow, which is a disadvantage of this approach. To address this disadvantage, the Dybeck et al. method[171] took into account a series of user-defined processes rather than all processes and system configurations. This series of processes could be some species surface diffusion on the lattice, where rate constant scaling can be applied uniformly. Scaling for the included processes continues at every specified interval during sampling until a non-equilibrated process occurs. Then modified rate constants are reset to their initial values to enable the required sampling for the new superbasin. N'u nez et al.[172] and Hoffmann and Biligaard[173] later developed very similar KMC algorithms that are equipped with efficient sensitivity analysis and eliminate the reset scheme to advance sampling of systems with large timescale disparities. However, using this type of accelerated KMC algorithm may be problematic for cases with low coverage species close to each other on the lattice because it cannot keep track of all system configurations and confirm if required configurations within a superbasin are sampled. To solve this problem, the configurations of the nearest neighbor sites can be taken into account in the definition of the reaction series. However, this solution cannot be applied for low coverage species produced at far lattice points because that depends on diffusion before the reaction. Another recently developed accelerated KMC algorithm that can be used to study cases involving fast surface diffusion processes, in addition to elementary reactions such as those found in heterogeneous catalytic systems, known as the fast species redistribution (FSR) KMC method, was developed by Cao et al.[174]. To overcome the repetitive sampling of fast processes, the FSR-KMC method identifies different species and classifies them into two groups: fast and slow species. These species are labeled as fast or slow based on their ability to diffuse and participate in non-diffusive reactions. The FSR-KMC algorithm initializes the simulation prerequisites by labeling the involved reactions as slow and fast processes, where the long scale evolution of the system depends on the slow one and the fast one is used for the short-scale redistribution. The algorithm then traverses the lattice to collect all possible slow and fast reactions into separate lists. It selects one reaction among possible slow processes based on the standard KMC method (VSSM method), updates the configuration of the system, and starts the simulation. After the slow process is completed, the algorithm collects all fast species and their redistribution processes onto the lattice. It picks the fast species from the list one by one and considers the achievable lattice space to perform a redistribution process. This loop continues until all fast species are redistributed on the lattice. Although the FSR approach can be performed with optional steps, the kinetic behavior of fast species diffusion can be better described if the interval is set to 1. The proposed model was able to reproduce the kinetic results of several study cases with several orders of magnitude of acceleration in system time compared to the standard KMC and mean field models.

Many KMC algorithms, including the standard KMC, the accelerated KMC, and the fast species redistribution (FSR) KMC, have been covered in this chapter. We have also discussed each algorithm's advantages and disadvantages. Even while KMC simulations have shown promising results in the study of some problems, it is crucial to choose the method to use carefully based on the particular needs and constraints of the system being researched. Overall, the KMC simulation method is a useful supplement to experimental investigations and gives a powerful tool for investigating complex systems, such as growth processes, which we will address in the next chapters.

3. Modeling CVD growth of graphene on Cu (111) surface using Kinetic Monte Carlo simulation

3.1. Introduction

Graphene, the first two-dimensional (2D) material discovered by Novoselov and Geim [63], has garnered significant attention due to its exceptional physical, electrical, and mechanical properties, which make it a promising candidate for various scientific and industrial applications[175, 176, 177]. Consequently, developing efficient methods for the growth of graphene has become a challenging task. Currently, several techniques exist for producing graphene, including exfoliation [178], hydro-thermal reduction of graphene oxide[179], carbon dioxide reduction [180], chemical vapor deposition (CVD)[181], and plasma-enhanced chemical vapor deposition (PECVD)[182] [183, 184, 185, 186]. Among these methods, CVD is the most promising approach for producing high-quality, large-scale graphene sheets[187]. The CVD process for graphene growth is highly dependent on various synthetic parameters, such as the partial pressures of precursors, temperature, substrate surface, and carbon solubility in metal substrates[188, 189, 190]. The resulting growth quality of single-layer graphene varies significantly based on these factors. While various metals have been identified as suitable substrates for CVD procedures, copper has emerged as the most qualified metal for growing single-layer graphene[191]. Among the different facets of copper, the (111) surface has been found to be ideal for producing less polycrystalline graphene material[192, 193]. As a result, it is the preferred choice for the CVD growth of graphene.

The growth mechanism of graphene via chemical vapor deposition (CVD) has been extensively studied both theoretically and experimentally in both academic and industrial settingss[194]. However, there is still a need to further investigate the kinetics involved in the growth mechanism. Optimal process parameters are not yet well known despite understanding the elementary reactions involved in the growth mechanism. Alnuaimi et al.[195] studied the effects of growth pressure, temperature, and precursor gas ratio on CVD graphene synthesis, identifying high growth temperatures (1060 °C) as a key factor in reducing multilayer nucleation density by over 50%. They also found that low CH_4 and H_2 partial pressures and ratios were critical parameters for controlling flake size and quality growth. Seah et al.[196] investigated the graphene growth mechanism in CVD with various transition metals and conditions, suggesting that understanding the growth mechanism and kinetics is necessary to control growth. However, the controllable synthesis of large scale graphene flake via CVD remains challenging due to the complex growth process and its sensitivity to growth conditions[197]. The multiscale character of the graphene growth mechanism in CVD requires different computational methods, including ab-initio calculations[198], molecular dynamics (MD)[199], and kinetic Monte Carlo (KMC) simulations[200, 201, 202, 203, 204], to complement experimental observations appropriately. Recently, Popov et al.[205] proposed an analytical kinetic model combining kinetic nucleation theory and density functional theory (DFT) calculations to study graphene nucleation and growth in CVD on Cu(111) surface. They have investigated the graphene nucleation mechanism by highlighting the role of carbon and its dimer as feeding species and reproduced the experimentally observed characteristics of polycrystalline graphene. Temperature and precursor partial pressures were used as control parameters in the proposed model.

In recent years, the combination of kinetic Monte Carlo (KMC) models and first-principles calculations has emerged as a promising strategy to gain atomistic-level understanding of graphene growth mechanisms over large time and length scales compared to other modeling approaches. Multiscale models that integrate these methods have been developed, such as the work of Li et al.[200], who employed the Bortz-Kalos-Lebowitz (BKL) algorithm to identify the dominant kinetic pathways of graphene growth via chemical vapor deposition (CVD) on Cu(111). The authors constructed a list of chemical reactions involving CH_4 and H_2 gases, their dissociative adsorption on the surface, decomposition, hydrogenation and dehydrogenation reactions, and carbon-containing species′ surface diffusion and attachment/detachment to the edges. To accelerate KMC simulations, they applied a mean-field approximation to the (de)hydrogenation reactions, recording the number of hydrogen atoms and modifying the reaction rates accordingly. Their results revealed the stabilizing role of H_2 during simulations and identified the dominant feed species (i.e., C and C_2) in graphene growth pathways under different H_2 pressures on Cu(111) surfaces. Chen et al.[202] proposed an all-atom KMC model for studying the growth of graphene by considering a simplified reaction list containing carbon and its dimer reactions on the surface and edges. The reactions involved ring closure that resulted in the formation of hexagons on the edges, which is crucial for graphene growth. Instead of considering CH_4 and H_2 as growth precursors, they considered the deposition flux of carbon species and temperature as control parameters. The developed model predicted different morphologies of growing graphene. This study confirmed the findings of Wu et al.[206], where C_2 was identified as the dominant feeding species for graphene growth. They calculated the activation energy barriers of the involved reactions using first-principles calculations, similar to Li et al. In another study, Zhu et al.[207] developed a large-scale KMC method to study graphene growth up to several micrometers in size. They used a list of reactions that involved the attachment and detachment of hexagons as the elementary processes. Starting with an initial flake, the proposed KMC model grew the graphene flake by adding or removing hexagons as feeding species. The authors found a complementary relationship between graphene growth and etching, where the shape evolution of graphene islands during growth is exactly like a hole during etching, and the shape evolution of graphene islands during etching is exactly the same as a hole in growth.

Despite the numerous studies on modeling the growth of isolated graphene flakes through chemical vapor deposition (CVD) on Cu surfaces, many important questions regarding the interplay of kinetic pathways at the atomic scale of reactions involved in the growth mechanism still remain unanswered. Although previous studies have provided insight into the graphene growth mechanism, their restricted time and length scales were due to incomplete lists of reactions used in their KMC methods[208, 202, 121]. To overcome this limitation, multiscale models for graphene growth have been developed, consisting of two parts: 1) the reaction rates on the surface, for which activation energy barriers are obtained through quantum mechanical methods such as DFT[209] and 2) a KMC protocol to model the kinetics of graphene growth at the mesoscale, utilizing the activation energy barriers obtained from first-principle calculations. The accuracy of predictions for growth mechanism kinetics depends on the accuracy of the activation energy barriers for the elementary reactions involved.

In this chapter, we present a novel DFT-based KMC model, capable of handling a comprehensive list of reactions involved in the graphene CVD growth mechanism. The reactions include the dissociative adsorption of CH_4 and H_2 as precursors, edge attachment and detachment of all mobile species, ring closure at the edges, and hydrogenation and dehydrogenation of species attached to the edges. By considering the partial pressure of precursors as the CVD control parameters and all relevant reactions (55 in total), we investigate the growth pathways and the role of control parameters during graphene growth on a Cu(111) surface at a high temperature of 1300 K. Our model aims to offer valuable insights into the growth mechanism by distinguishing the role of specific reactions, observing the effects of selected CVD control parameters, and estimating the growth rate during steady-state growth. Furthermore, our model shows significant improvements in the quality of graphene by reducing the number of hydrogen-saturated edges and refining attachments.

3.2. Simulated CVD setup

The process and types of the different possible chemical reactions that occur in a CVD reactor are controlled by a lot of complicated factors, including the system setup, reactor configuration, gas feedstock, gas ratios, reactor pressure and precursor partial pressures, reaction temperature, growth time, temperature, etc[210] (see Figure 3.1). The CVD setup for graphene growth can be classified as hot-wall[211], cold-wall[212], and plasma enhanced[213] with different configurations depending on the mentioned factors on the process and final product quality[194].

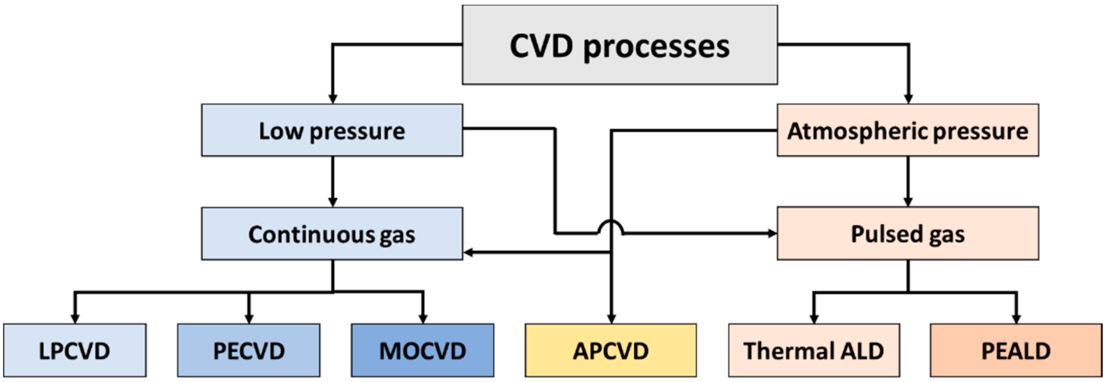

Figure 3.1.: Chemical vapor deposition (CVD) reactors and processesas: Low pressure CVD (LPCVD), plasma-enhanced CVD (PECVD), low pressure is the metal–organic CVD (MOCVD), atmospheric pressure CVD (APCVD), thermal atomic layer deposition (ALD), and Plasma-Enhanced Atomic Layer Deposition (PEALD). Reprinted from Ref.[214], used under Creative Commons CC-BY license.

We considered the CVD conditions depicted in Figure 3.2, where there is a chamber to carry out the process that contains a mixture of precursors, in this study, CH_4 and H_2 gases, at constant pressures P_{CH_4} and P_{H_2}. In general, gas mixtures contain a carrier gas, e.g., argon, in experiments; this gas does not participate in the chemical reactions involved in the growth mechanism based on experimental observations[215, 216], thus it was not considered in this study. The tube furnace, as previously reported[216, 190], is made up of a substrate and a catalyst, such as a copper plate that is coupled with the gas at temperatures ranging from 1000 to 1300 K to produce high-quality graphene via CVD. We considered the Cu(111) facet as the ideal surface to produce high-quality monolayer graphene at 1300 K.It is noteworthy that this temperature is quite close to the melting point of copper, which is approximately 1357 K. This indicates that the copper atoms present on the surface of the substrate are likely to exhibit high levels of mobility. Despite the fact that this cooper atom's mobility could influence the coalescence process according to the theoretical studies[217], we neglect all these effects on the CVD graphene growth process by considering the solid and rigid surface.

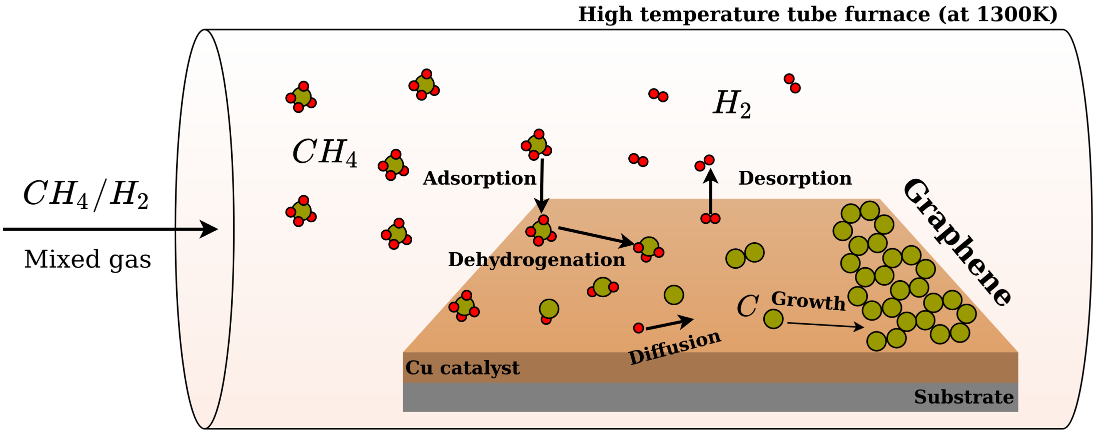

Figure 3.2.: An example of the chemical vapor deposition procedure used for graphene synthesis on Cu as the metal catalyst. The mixture of precursors enters the chamber under defined conditions, such as system temperature and partial pressure. The schematic shows a series reactions such as precursor adsorption and desorption, dehydrogenation, and surface diffusion processes.

3.3. Reaction network

In the initial stage of our multiscale model, we compiled a comprehensive list of reactions. The participating chemical species were CH_4(g), H_2(g), H, C, CH, CH_2, CH_3, C_2, C_2H, and C_2H_2 , as shown in Figure 3.3. These species, with the exception of the precursors and CH_3, were capable of surface diffusion, and most of the reactions in the list occurred in both forward and reverse directions.

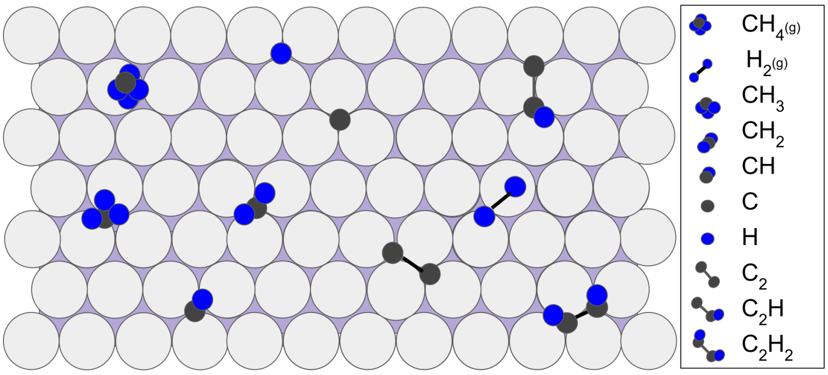

Figure 3.3.: Species on the Cu(111) surface. Cu, C, and H atoms are colored in grey, black and blue, respectively. The '(gas)' indicates Gaseous species.

The initial set of reactions starts with the dissociative adsorptions of CH_4 and H_2, leading to the appearance of CH_3 and hydrogen adatoms on the surface.

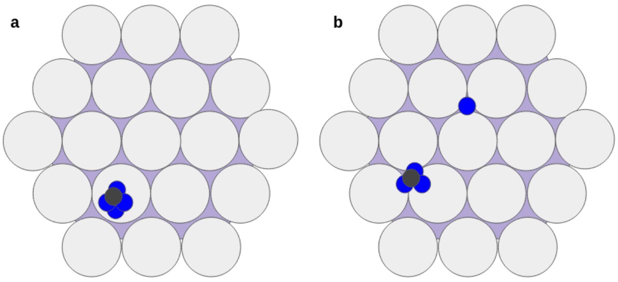

Figure 3.4.: Methane dissociative adsorption as: $CH_4 \rightleftharpoons CH_3 + H$. a) initial state b) final state in the forward direction. Cu, C, and H atoms are colored grey, black, and blue, respectively.

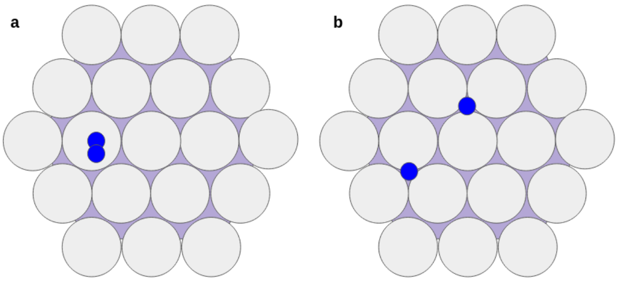

Figure 3.5.: H_2 dissociative adsorption as $H_2 \rightleftharpoons H + H$. a) initial state b) final state in the forward direction. Cu, and H atoms are colored grey, black, and blue, respectively.

A sequence of dehydrogenation reactions is necessary to yield a single carbon atom on the surface, which is a prerequisite for graphene growth. The initial reaction in this sequence involves the surface decomposition of CH_3 into CH_2 and a hydrogen adatom.

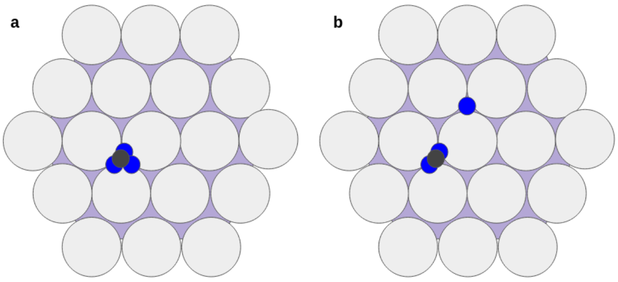

Figure 3.6.: CH_3 (de)hydrogenation as $CH_3 \rightleftharpoons CH_2 + H$. a) initial state b) final state in the forward direction. Cu, C, and H atoms are colored grey, black, and blue, respectively.

The subsequent reaction in the series requires the decomposition of CH_2 on the surface, giving rise to CH and an additional hydrogen atom, which can diffuse on the surface and contribute to hydrogenation reactions.

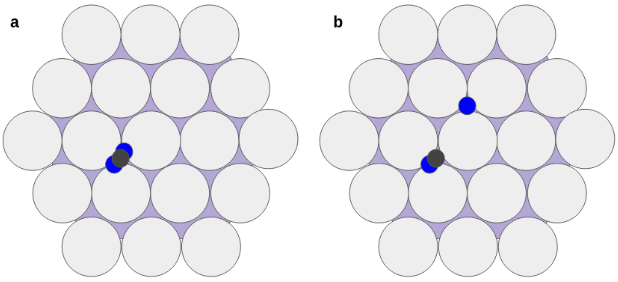

Figure 3.7.: CH_2 (de)hydrogenation as $CH_2 \rightleftharpoons CH + H$. a) initial state b) final state in the forward direction. Cu, C, and H atoms are grey, black, and blue, respectively.

CH molecules, like those of other surface species (except CH_3), can diffuse. This could result in a reaction with other CH molecules, forming C_2H_2:

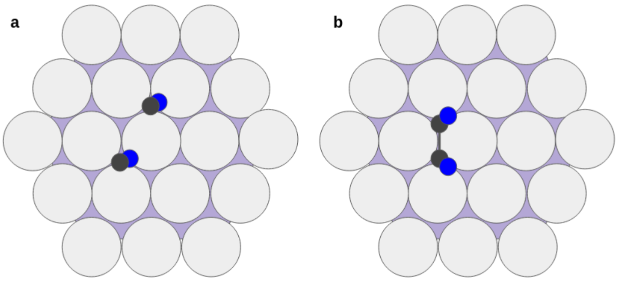

Figure 3.8.: C_2H_2 formation as $CH + CH \rightleftharpoons C_2H_2$. a) initial state b) final state in the forward direction. Cu, C, and H atoms are colored grey, black, and blue, respectively.

Meanwhile, the mobile C_2H_2 species can also undergo dehydrogenation, releasing H atoms and becoming detached from the surface as $C_2H_2(g)$. These processes mark the end of the first set of dehydrogenation reactions, starting from CH_4 and resulting in the formation of a single carbon atom on the surface.

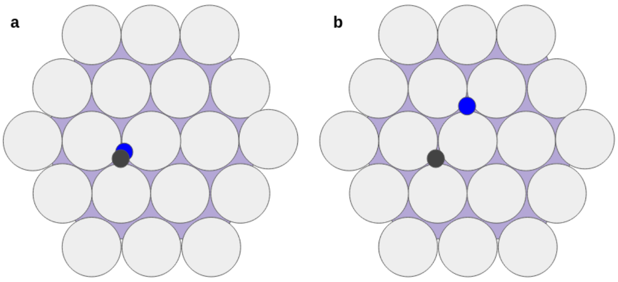

Figure 3.9.: CH (de)hydrogenation as $CH \rightleftharpoons C + H$. a) initial state b) final state in the forward direction. Cu, C, and H atoms are colored grey, black, and blue, respectively.

The single carbon can participate in two reactions, the first one is forming C_2H together with CH molecule as:

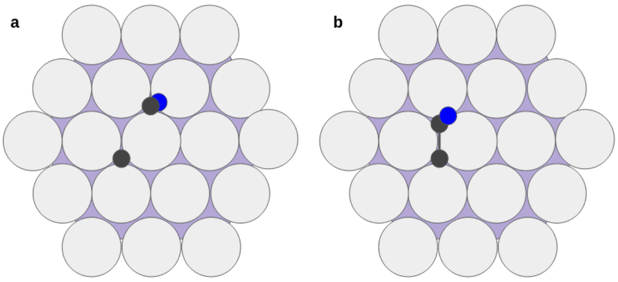

Figure 3.10.: C_2H formation as $C + CH \rightleftharpoons C_2H$. a) initial state b) final state in the forward direction. Cu, C, and H atoms are colored grey, black, and blue, respectively.

And the second one would be forming carbon dimer:

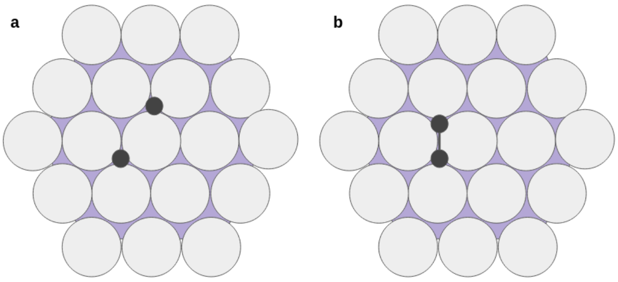

Figure 3.11.: C_2 formation as $C + C \rightleftharpoons C_2$. a) initial state b) final state in the forward direction. Cu, C, and H atoms are colored grey, black, and blue, respectively.

Due to its mobility, C_2 can engage in additional reactions, such as the reaction with a hydrogen adatom on the surface to form C_2H.

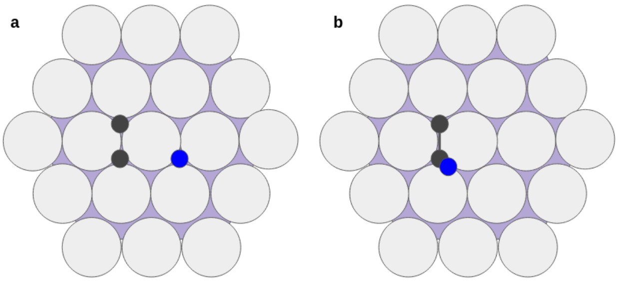

Figure 3.12.: C_2H formation as $C_2 + H \rightleftharpoons C_2H$. a) initial state b) final state in the forward direction. Cu, C, and H atoms are colored grey, black, and blue, respectively.

Subsequently, the C_2H species on the surface can react with another hydrogen adatom leading to the formation of C_2H_2.

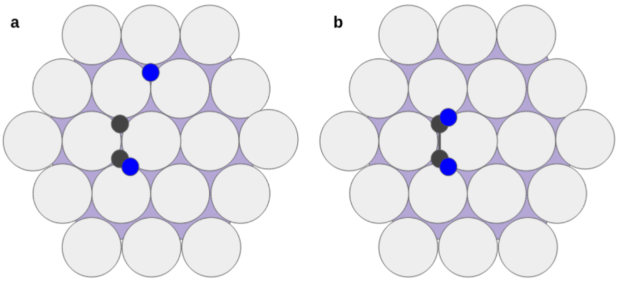

Figure 3.13.: C_2H formation as $C_2H + H \rightleftharpoons C_2H_2$. a) initial state b) final state in the forward direction. Cu, C, and H atoms are grey, black, and blue, respectively.

The next series of reactions are the attachments and detachments of mobile carbon-containing species to the graphene flake edges.

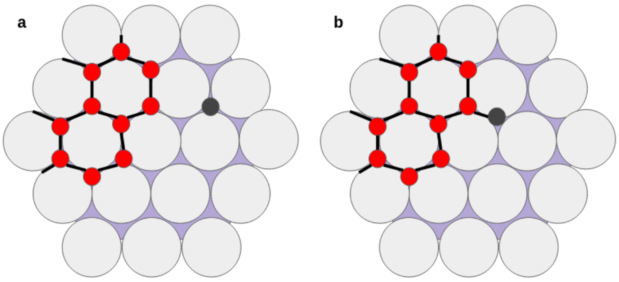

Figure 3.14.: C attachment/detachment to the edge as C + *edge* $\rightleftharpoons$ *edge*-C a) initial state b) final state in the forward direction. Cu, C, and H atoms are colored grey, black, and blue, respectively. Graphene flake is shown in red.

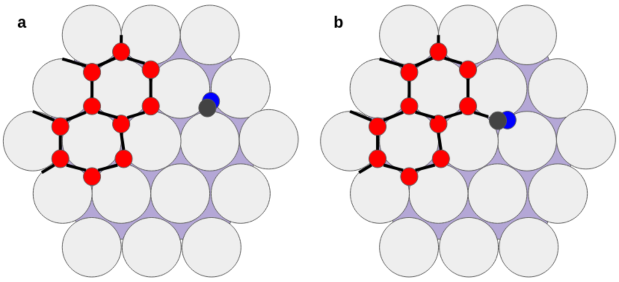

Figure 3.15.: CH attachment/detachment to the edge CH + *edge* $\rightleftharpoons$ *edge*-CH a) initial state b) final state in the forward direction. Cu, C, and H atoms are grey, black, and blue, respectively. Graphene flake is shown in red.

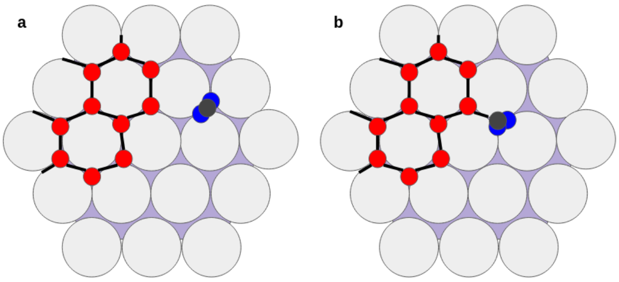

Figure 3.16.: CH_2 attachment/detachment to the edge CH_2 + *edge* $\rightleftharpoons$ *edge*-CH_2 a) initial state b) final state in the forward direction. Cu, C, and H atoms are colored grey, black, and blue, respectively. Graphene flake is shown in red

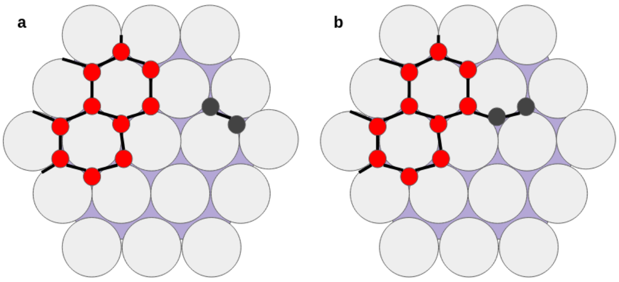

Figure 3.17.: C_2 attachment/detachment to the edge C_2 + *edge* $\rightleftharpoons$ *edge*-C_2 a) initial state b) final state in the forward direction. Cu, C, and H atoms are colored grey, black, and blue, respectively. Graphene flake is shown in red

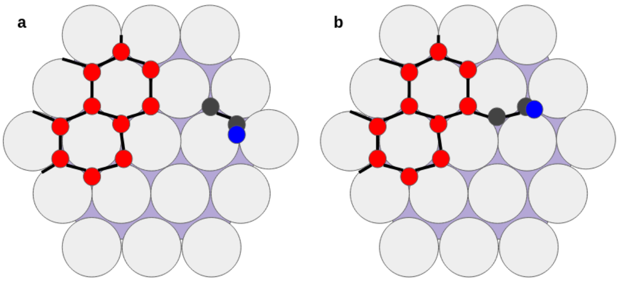

Figure 3.18.: C_2H attachment/detachment to the edge C_2H + *edge* $\rightleftharpoons$ *edge*-C_2H a) initial state b) final state in the forward direction. Cu, C, and H atoms are colored grey, black, and blue, respectively. Graphene flake is shown in red

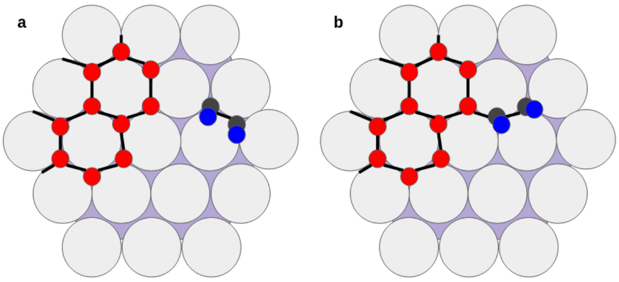

Figure 3.19.: C_2H_2 attachment/detachment to the edge $C_2H_2 + \mathit{edge} \rightleftharpoons \mathit{edge}\text{-}C_2H_2$ a) initial state b) final state in the forward direction. Cu, C, and H atoms are colored grey, black, and blue, respectively. Graphene flake is shown in red

Given the presence of hydrogen adatoms on the surface, we formulated a sequence of reactions to examine how the hydrogenation and dehydrogenation of attached species could contribute to the growth mechanism. The set of reactions includes forward and backward directions, corresponding to hydrogenation and dehydrogenation, respectively.

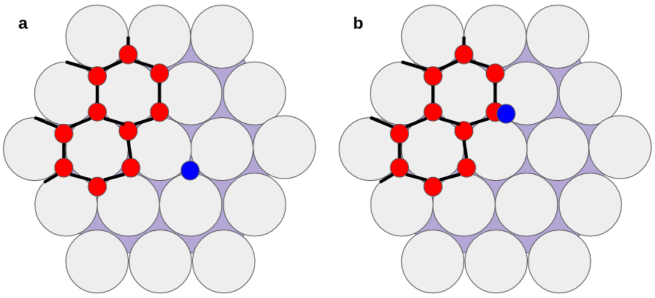

Figure 3.20.: Edge (de)hydrogenation H + *edge* $\rightleftharpoons$ *edge*-H a) initial state b) final state in the forward direction. Cu, and H atoms are colored grey, and blue respectively. Graphene flake is shown in red

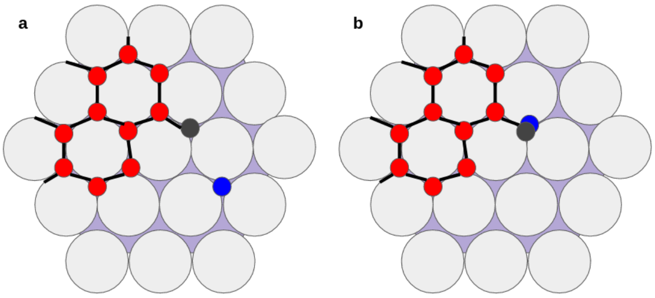

Figure 3.21.: C (de)hydrogenation at edge as *edge*-C + H $\rightleftharpoons$ *edge*-CH. a) initial state b) final state in the forward direction. Cu, and H atoms are colored grey, and blue respectively. Graphene flake is shown in red

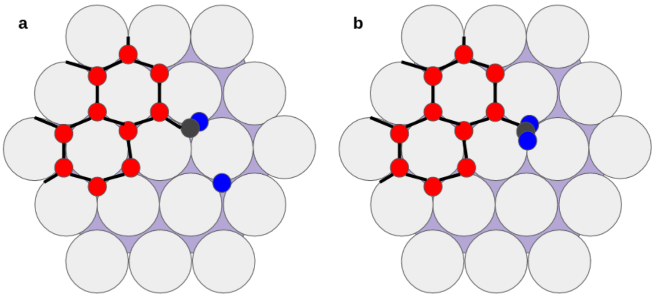

Figure 3.22.: CH (de)hydrogenation at edge as *edge*-CH + H $\rightleftharpoons$ *edge*-CH_2. a) initial state b) final state in the forward direction. Cu, and H atoms are colored grey, and blue respectively. Graphene flake is shown in red

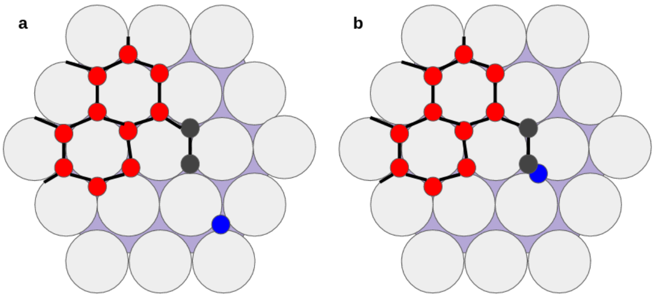

Figure 3.23.: C_2 (de)hydrogenation at edge as *edge*-C_2 + H $\rightleftharpoons$ *edge*-C_2H. a) initial state b) final state in the forward direction. Cu, and H atoms are colored grey, and blue respectively. Graphene flake is shown in red

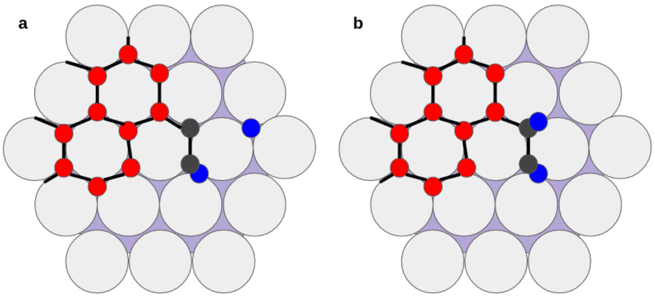

Figure 3.24.: C_2H (de)hydrogenation at edge as *edge*-C_2H + H $\rightleftharpoons$ *edge*-C_2H_2. a) initial state b) final state in the forward direction. Cu, and H atoms are colored grey, and blue respectively. Graphene flake is shown in red

The final set of reactions are crucial in enabling the formation of hexagonal structures on the edges, which is a key step in the growth mechanism. The first reaction in this series starts attaching a carbon to two existing carbons on neighboring edges of the flake. The same reaction can occur via attachment of C_2, resulting in the formation of a hexagon with a dangling carbon. The last reaction entails the closure of the ring by rotating a C_2 molecule that is already attached, with the addition of a single carbon to the neighboring edge.

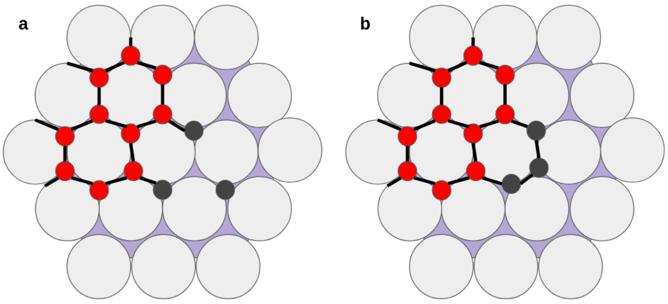

Figure 3.25.: Ring formation via C attachment. a) initial state b) final state in the forward direction. Cu, and H atoms are grey, and blue respectively. Graphene flake is shown in red

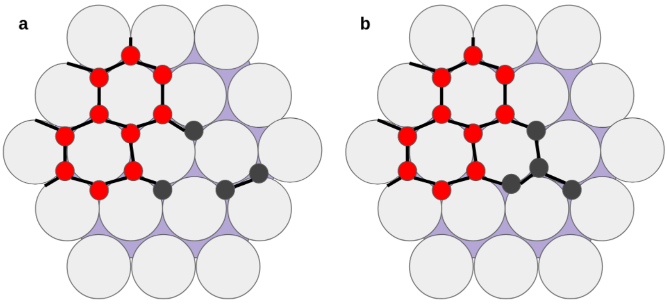

Figure 3.26.: C_2H (de)hydrogenation at edge. a) initial state b) final state in the forward direction. Cu, and H atoms are grey, and blue respectively. Graphene flake is shown in red

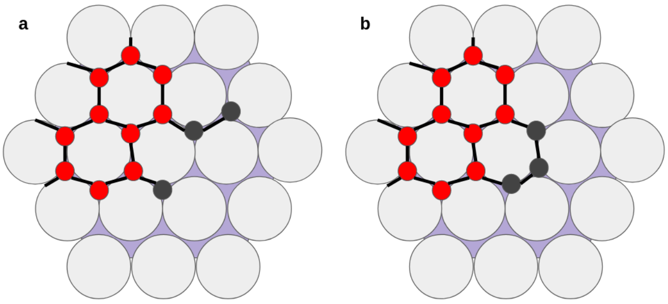

Figure 3.27.: Ring formation via dimer rotation. a) initial state b) final state in the forward direction. Cu, and H atoms are grey, and blue respectively. Graphene flake is shown in red

The series of illustrations do not depict the processes of surface diffusion, which involves changes in the position of species, as well as the desorption of CH_4, H_2, and C_2H_2 from the surface.

3.4. KMC model implementation

With a comprehensive set of reactions and the need to develop a multiscale model, this section provides an in-depth account of lattice construction, rate calculation, and the implementation of KMC algorithm capable of dealing with the chemical reactions involved in the CVD growth mechanism of graphene on Cu(111).

3.4.1. Lattice construction and rates used in KMC simulations

3.4.1.1. Lattice construction

The hcp (hexagonal close-packed) and fcc (face-centered cubic) adsorption sites of the Cu(111) facet are mapped into a honeycomb lattice (see Figure 3.28 for more details). Each point in the lattice is connected to three neighboring points of the other type. The lattice vectors have a length of 0.246 nm and the neighboring distance between points is 0.142 nm

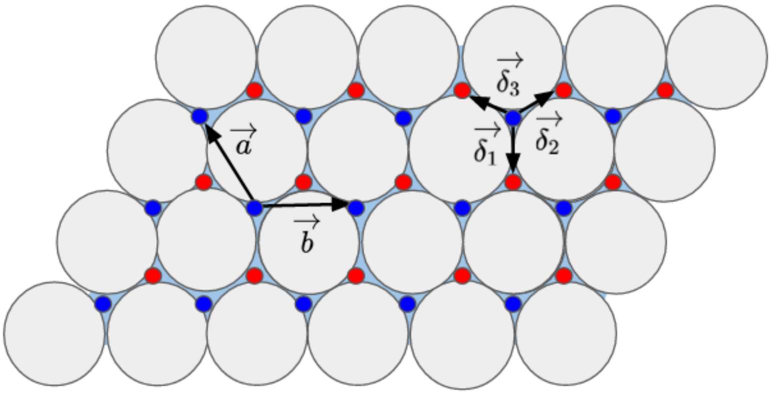

Figure 3.28.: Illustration of the honeycomb lattice formed via fcc and hcp adsorption sites in blue and red. $\vec{a}$ and $\vec{b}$ are lattice vectors and the nearest neighbor distances are $\vec{\delta_i}$ (i=1, 2, 3).

Eeach point on the honeycomb lattice, which is constructed from the Cu(111) facet hcp and fcc adsorption sites, is transformed into an object class. This object class is capable of carrying additional information besides coordinates, such as nearest neighbor sites, occupancy status, bonded species, and edge attachment status, as outlined in Table 3.1. As a result, the lattice can be represented as a list of site objects, which is critical for implementing the KMC protocol described later in this chapter.

Table 3.1.: Site class structure. All information assigned to each point on the lattice.

Coordinate	Coordinate of lattice point as a (x, y) pairs.
Species	Name of the species located at the lattice point (empty for not occupied sites).
Bond	Index of bonded species sites according to the lattice indexing format.
Neighbors	Indices of neighboring sites according to the lattice indexing format.
Status	With two categories of information: 1) Occupancy status: **True** for occupied site. **False** for empty site. 2) Time and coordinate of adsorption and edge attachment.
Flag	0: no edge attachment (free species on the surface). 1: edge attachment from one side (neighbor). 2: edge attachment from two sides (2 neighbors). 3: edge attachment from three sides (3 neighbors).

As outlined in Table 3.1, a site object can generally be constructed as follows:

$$(x, y) \Longrightarrow site(Coordinate\,(x, y),\ Species,\ Bond,\ Neighbours,\ Status,\ Flag)$$

assuming the honeycomb lattice illustrated in Figure 3.29 consisting of 28 lattice points, the site object of a single carbon species located at the 15th index site would be as follows:

$$site([x, y], "C", [\,], [9, 14, 16], [True, [t, [X, Y]], 0)$$

or site objects for a carbon dimer at lattice points with indices of 7 and 8 are as follows:

$$site([x, y], "C", [8], [6, 8, 13], [True, [t, [X, Y]], 0)$$

and

$$site([x, y], "C", [7], [7, 3, 9], [True, [t, [X, Y]], 0)$$

where t, X, and Y indicate the time and coordinates of adsorption, respectively.

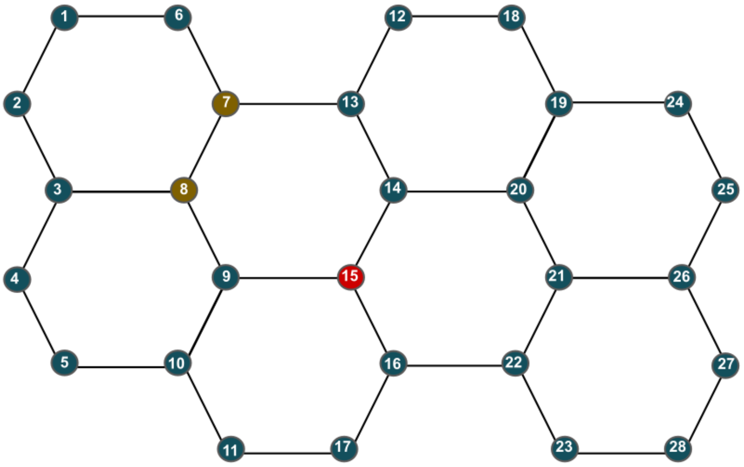

Figure 3.29.: An illustrated honeycomb lattice with 28 sites labeled with numbers as lattice indices.

3.4.1.2. Rates used in KMC simulations

The rates of all involved reactions, except dissociative adsorption of CH_4 and H_2 for a fixed temperature of 1300 K, are calculated using the transition state theory (TST)[218] and the following equation:

$$r_T = \frac{K_B T}{h} exp(-\frac{E_a}{K_B T}) \tag{3.1}$$

where K_B, H, and E_a are the Boltzmann constant, Planck constant, and activation energy barrier (in eV), and $K_B h/T$ is the pre-exponential factor(approximately 10^{13} S^{-1}). The ideal gas approximation approach introduced in Ref. [200] is used to calculate adsorption rates for H_2 and CH_4 (shown in Table 3.3).

$$r^{ad}_{H_2} = \frac{h^2}{(2\pi m_{H_2} K_B T)^{3/2}} \frac{P_{H_2} q^{vib}_{TS,H_2}}{q^{vib}_{gas,H_2} q^{rot}_{gas,H_2}} \; exp(-\frac{E_a}{K_B T}) \tag{3.2}$$

for H_2, where at at T=1300 K:

- $q^{vib}_{TS,H_2} = 54.96$, is H_2 vibrational partition function in the transition state.

- $q^{vib}_{gas,H_2} = 1.009$, is the gas phase H_2 vibrational partition function.
- $q^{rot}_{gas,H_2} = 7.466$, is the gas phase H_2 rotational partition function.
- P_{H_2} is the partial pressure of H_2 (in Torr).
- m_{H_2} is the mass of H_2 (in Torr).

After substituting the known values, the dissociative adsorption rate for H_2 would be:

$$r^{ad}_{H_2} = 5.9 \times 10^4 \times p\,(\mathrm{H_2})\,exp(-\frac{E_a}{K_B T}) \tag{3.3}$$

For CH_4, the dissociative adsorption rate can be written as:

$$r^{ad}_{CH_4} = \frac{h^2}{(2\pi m_{CH_4} K_B T)^{3/2}} \frac{P_{CH_4} q^{vib}_{TS,CH_4}}{q^{vib}_{gas,CH_4} q^{rot}_{gas,CH_4}}\, exp(-\frac{E_a}{K_B T}) \tag{3.4}$$

where, T=1300 K,

- $q^{vib}_{TS,CH_4} = 64532.53$, is CH_4 vibrational partition function in the transition state .
- $q^{vib}_{gas,CH_4} = 3.575$, is the gas phase CH_4 vibrational partition function.
- $q^{rot}_{gas,CH_4} = 352.13$, is the gas phase CH_4 rotational partition function.
- P_{CH_4} is the partial pressure of CH_4 (in Torr).
- m_{CH_4} is the mass of CH_4 (in Torr).

by substituting the values:

$$r^{ad}_{CH_4} = 1.8 \times 10^4 \times P_{CH_4} exp(-\frac{E_a}{K_B T}) \tag{3.5}$$

As the rates are determined per adsorption site, the overall adsorption rates of the lattice can be calculated using the product of the number of available free sites on the surface and the adsorption rate (r^{ad}) as $\mathrm{N}_{free} \times \mathrm{r}^{ad}$, where N_{free} is the number of free sites on the surface. This implies that the dissociative adsorption rates will not only vary for different pairs of CH_4 and H_2 pressures but also change depending on the number of surface sites available at a given time. Table 3.2 comprises 55 reactions that cover a range of processes, including dissociative adsorption of gases, attachment of different species to edges, (de)hydrogenation of attached species, and ring closures. The barriers and rate constants employed in KMC simulations are provided. All barriers are computed in Ref.[219], except for the ring closure reactions, which are sourced from Chen et al.[202].

Table 3.2.: All involved reactions in the KMC simulation. Activation energy barrier of reactions are taken from Ref.[219](reactions 1-29) and Ref.[202] (reactions 30-32).

Entry	Reaction	Type	Barrier(eV)	Rate(s^{-1})
1	$H_2 \rightleftharpoons H+H$	adsorption/desorption	0.37/0.92	–/7.35×10^{9}
2	$CH_4 \rightleftharpoons CH_3+H$	adsorption/desorption	1.48/0.90	–/8.78×10^{9}
3	$CH_3 \rightleftharpoons CH_2+H$	detachment/attachment	1.39/0.58	1.11×10^{8} /1.53×10^{11}
4	$CH_2 \rightleftharpoons CH+H$	detachment/attachment	0.99/0.55	3.93×10^{9} /1.99×10^{11}
5	$CH \rightleftharpoons C + H$	detachment/attachment	1.87/0.66	1.52×10^{6} /7.48×10^{10}
6	$C + C \rightleftharpoons C_2$	attachment/detachment	0.55/3.62	1.99×10^{11} /2.51×10^{-1}
7	$C + CH \rightleftharpoons C_2H$	attachment/detachment	0.48/2.95	3.73×10^{11} /9.92×10^{1}
8	$CH + CH \rightleftharpoons C_2H_2$	attachment/detachment	0.29/2.21	2.03×10^{12} /7.33×10^{4}
9	$C_2 + H \rightleftharpoons C_2H$	attachment/detachment	0.83/1.45	1.64×10^{10} /6.48×10^{7}
10	$C_2H + H \rightleftharpoons C_2H_2$	attachment/detachment	1.01/1.67	3.29×10^{9} /9.09×10^{6}
11	C_2H_2	desorption	1.59	1.86×10^{7}
12	C	diffusion	0.15	7.1×10^{12}
13	CH	diffusion	0.15	7.1×10^{12}
14	CH_2	diffusion	0.14	7.76×10^{12}
15	C_2	diffusion	0.48	3.73×10^{11}
16	C_2H	diffusion	0.31	1.07×10^{12}
17	C_2H_2	diffusion	0.36	1.09×10^{12}
18	H	diffusion	0.14	7.76×10^{12}
19	$C+edge \rightleftharpoons edge-C$	edge attachment/detachment	0.44/1.21	5.33×10^{11} /5.52×10^{8}
20	CH+edge	edge attachment/detachment	0.33/0.83	1.42×10^{12} /1.64×10^{10}
21	$CH_2+edge \rightleftharpoons edge-CH_2$	edge attachment/detachment	0.06/1.79	1.58×10^{13} /3.11×10^{6}
22	$C_2+edge \rightleftharpoons edge-C_2$	edge attachment/detachment	1.22/2.24	5.05×10^{8} /5.06×10^{4}
23	$C_2H+edge \rightleftharpoons edge-C_2H$	edge attachment/detachment	0.9/1.74	8.78×10^{9} /4.87×10^{6}
24	$C_2H_2+edge \rightleftharpoons edge-C_2H_2$	edge attachment/detachment	0.93/1.72	6.72×10^{9} /5.81×10^{6}
25	$H + edge \rightleftharpoons edge-H$	edge attachment/detachment	0.77/1.61	2.80×10^{10} /1.55×10^{7}
26	$edge-CH \rightleftharpoons edge-C+H$	(de)hydrogenation	1.76/0.71	4.07×10^{6} /4.79×10^{10}
27	$edge-CH_2 \rightleftharpoons edge-CH+H$	(de)hydrogenation	2.36/0.59	1.92×10^{4} /1.39×10^{11}
28	$edge-C_2H \rightleftharpoons edge-C_2+H$	(de)hydrogenation	1.57/1.08	2.22×10^{7} /1.76×10^{9}
29	$edge-C_2H_2 \rightleftharpoons edge-C_2H+H$	(de)hydrogenation	1.7/1.07	6.95×10^{6} /1.93×10^{9}
30	C	Ring (de)formation	2.29/0.54	3.59×10^{4} /2.18×10^{11}
31	C_2	Ring (de)formation	2.29/0.54	3.59×10^{4} /2.18×10^{11}
32	C_2	Rotation at edge	0.74	3.66×10^{10}

Note: The rates of dissociative adsorption of CH_4 and H_2 gases depend on their pressures and the number of available sites on the lattice(See Table 3.3).

Taking into account the Equation 3.3 and Equation 3.5, as well as the activation energy barriers for these reactions provided in Table 3.2, it is possible to determine the dissociative adsorption rates of CH_4 and H_2, which are dependent on both the precursor pressures and the number of free sites present on the surface. These rates are shown in Table 3.3.

Table 3.3.: Dissociative adsorption rates of CH_4 and H_2 (in s^{-1}) .

r_{H_2}	$2170 \times P_{H_2} \times N_{free}$
r_{CH_4}	$0.0329 \times P_{CH_4} \times N_{free}$

An event class is defined to create reaction objects that are capable of carrying important information such as reactants, products, reaction type, barrier, and rate constant, as shown in Table 3.4. This class is utilized to construct a list of events for the reference reaction list, which includes 55 event objects for the KMC protocol. The last attribute of this class allows constructing individual reactions of local regions among pairs of surface sites, which may be beneficial in implementing the KMC algorithm collection scheme, as we will discuss later in this chapter.

Table 3.4.: Event object structure.

Status	'n': free species reactions 'e': attachment reactions at edges 'h': hydrogenation reactions at edges 'd': dehydrogenation reactions at edges 'f': detachment reactions at edges
Type	Possible reaction type: Adsorption-Desorption-Attachment-Detachment Diffusion-Hydrogenation-Dehydrogenation
Reactant	Reaction's reactants
Product	Reaction's products
Barrier	Activation energy barrier of the reaction
Rate	Rate constant of the reaction
Reaction info	All involved species data and the reaction index

According to the Table 3.4, each event object can be constructed as:

$$reaction \Longrightarrow event(Status,\, Type,\, Reactant,\, Product,\, Barrier,\, Rate,\, Reaction\, info)$$

Once the requirements have been met and the lattice has been constructed as a collection of site objects and a list of event objects has been established to represent the reactions, the focus of the multiscale model shifts to the KMC protocol, which is discussed in the next section.

3.4.2. KMC algorithm development

Due to the presence of surface diffusion processes in Table 3.2 with higher rate constants than other reactions, conducting KMC simulations for this particular system would result in a computationally expensive process, as a significant amount of CPU time would be spent on sampling diffusion processes. In order to optimize the efficiency of the KMC simulation and reduce its computational burden, we have developed and compared two KMC algorithms equipped with acceleration schemes. The purpose of this comparison is to identify and select the most efficient algorithm for the entirety of the study. Chapter 2, section 2.7 discusses both models, namely, the automatic scaling KMC (AS-KMC) and the fast sampling with random redistribution KMC (FSR-KMC). These models are based on the standard Kinetic Monte Carlo (KMC) algorithm known as Bortz-Kalos-Lebowitz (BKL) algorithm[48]. AS-KMC is equipped with an automatic scaling scheme that was introduced by Chatterjee et al.[170], whereas FSR-KMC employs a random redistribution scheme that was proposed by Cao et al.[174]. Both models aim to improve the efficiency of the KMC simulation by reducing the computational burden associated with sampling diffusion processes. In our study, we utilize a lattice that spans an area of 100×100 nm^2 and contains a total of 388206 site objects. A ribbon or slab is positioned on the left-hand side of the lattice to represent the initial graphene flake. Subsequently, the growth kinetics of the domain are determined by considering the partial pressure of precursors and the temperature, which are used to define the elementary reactions (events) listed in Table 3.2 as KMC events. It is important to note that hydrogen atoms present in carbon-containing species are not taken into account on the lattice. Instead, lattice sites are used to represent the carbon atoms involved in these species.

In order to incorporate the scaling scheme of the AS-KMC algorithm, two user inputs are required, namely α and δ. Here, α represents the lowering factor, where α is greater than 1. The second input, δ, is used to define the uncertainty associated with the system and must satisfy the condition $0 < \delta < 1$. The confidence level is determined by $(1 - \delta)$, where it represents the probability of the system escaping its current state within a certain number of iterations. For example, if δ is set to 0.1, it implies that the system has a 90% chance of escaping its current state within a reduced number of iterations. With the help of these two coefficients, the minimum number of steps required to lower the rates can be computed, as per the methodology proposed in Ref. [170] via:

$$N_f = (\frac{\alpha - 1}{\delta}) \times ln(\frac{1}{\delta}) \tag{3.6}$$

The flowchart for the AS-KMC algorithm is presented in Figure 3.30, depicting several sequential steps including:

- **a**) the preparation step:
  - initialize the lattice: construct a honeycomb lattice (in nm^2) as a list of site class objects (Table 3.1).
  - take lowering factor α, and δ from user.
  - initialize the scaling step counter (SC = 0).
  - calculate the minimum number of sightings (N_f) required for lowering the rates.
- **b**) collection scheme: collect all possible processes.
- **c**) selection scheme: calculate the cumulative rate of all possible reactions and select an event from available reactions using a random number and the cumulative rate.
- **d**) scaling check: lowering the diffusion rate constants if the scaling step counter (SC) is equal or larger than the minimum sighting number (N_f).
- **e**) update scheme: execute the selected event based on its type. Update the configuration and advance the simulation time using another random number and the cumulative rate.

At the beginning of the simulation, the AS-KMC algorithm initializes the lattice and calculates the minimum sighting number (N_f) based on the given values of α and δ. Subsequently, the scaling counter (SC) is set to zero (SC=0), as shown in Figure 3.30-a. At each step of the simulation, KMC traverses the lattice to obtain a list of potential reactions based on the latest lattice configuration, as depicted in Figure 3.30-b. Following this, an event is chosen from the collected list, as shown in Figure 3.30-c. The algorithm then checks whether the selected event corresponds to a diffusion process. If the chosen event is a diffusion process, the scaling counter (SC) is incremented, and the necessity for scaling the diffusion rate constants is evaluated. If the scaling counter exceeds the minimum sighting number (N_f), then all diffusion rate constants are reduced by the scaling factor α, as illustrated in Figure 3.30-d. Depending on the type of the selected event, the lattice configuration is updated accordingly, and the simulation time is incremented. This is depicted in Figure 3.30-e. If no termination condition on simulation time or KMC steps is specified, the aforementioned cycle (from b to e) will continue until there are no further events available in the KMC list.

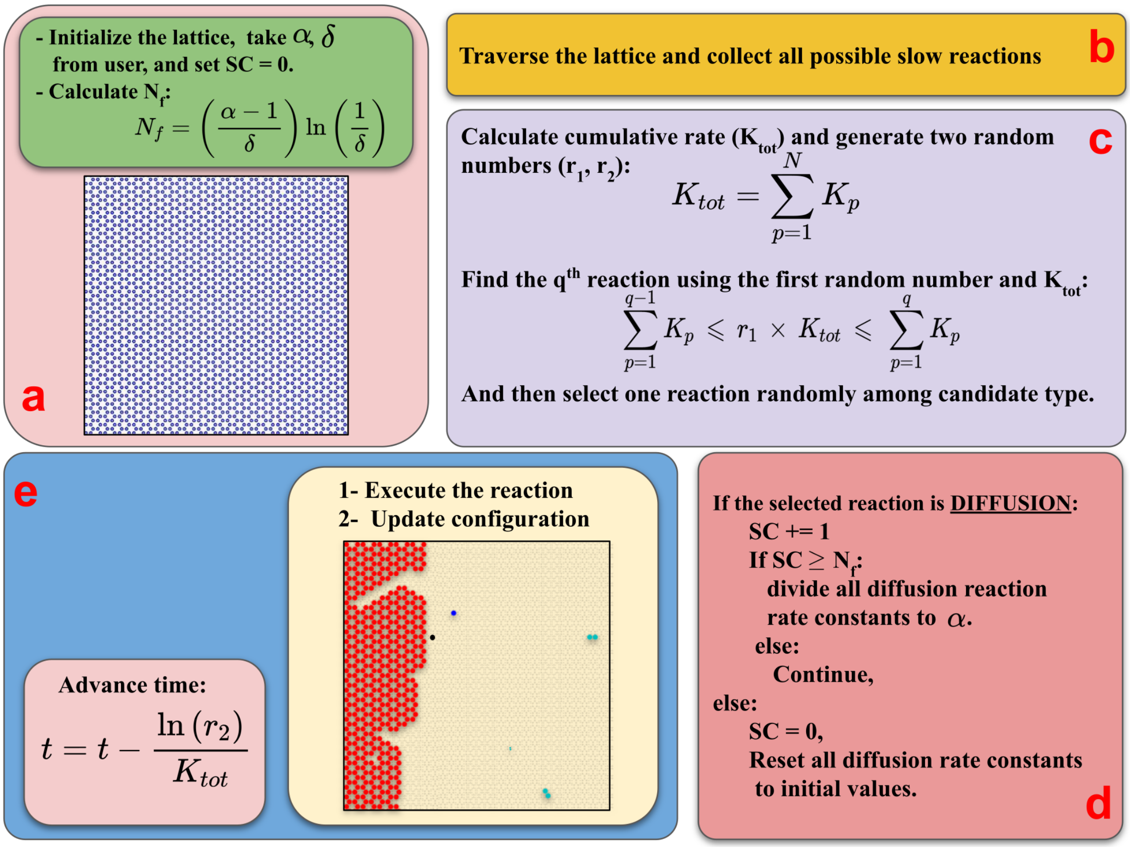

Figure 3.30.: Flowchart of the AS-KMC algorithm. Different parts of the algorithm are shown in boxes with letters.

To implement the FSR-KMC algorithm, we classify the events into two categories: fast and slow events. For this purpose, we classify surface diffusion as a fast event and all non-diffusion reactions as slow events. Then, we divide the species into two lists: "slow" and "fast" species, where each species can belong to both groups simultaneously. These two categories of events and species lists are utilized in the FSR-KMC algorithm's flowchart, which is presented in Figure 3.31. The algorithm can be described by the following steps:

- **a**) initialize the lattice: construct a honeycomb lattice (in nm^2) as a list of site class objects (Table 3.1).
- **b**) collection scheme: collect all possible non-diffusive processes.
- **c**) selection scheme: calculate the cumulative rate of all possible reactions and select an event from available reactions using a random number and the cumulative rate.
- **d**) update scheme: execute the selected event based on its type and update configuration and advance the simulation time using another random number and the cumulative rate.
- **e**) redistribution scheme: redistribute all mobile species on the lattice randomly.

At the beginning of the simulation, the lattice is initialized, and KMC traverses the lattice to collect possible non-diffusive reactions based on the current lattice configuration (Figure 3.31-b). Following the KMC protocol routine, one event is selected from the collected list (Figure 3.31-c). Depending on the type of the selected event, the lattice configuration is updated, and the simulation time is incremented accordingly (Figure 3.31-d). At the end of each step, all mobile species are randomly redistributed on the lattice. If there are no termination conditions for the simulation time or KMC steps, this cycle (from b to e) continues until no further event is available on the KMC list.

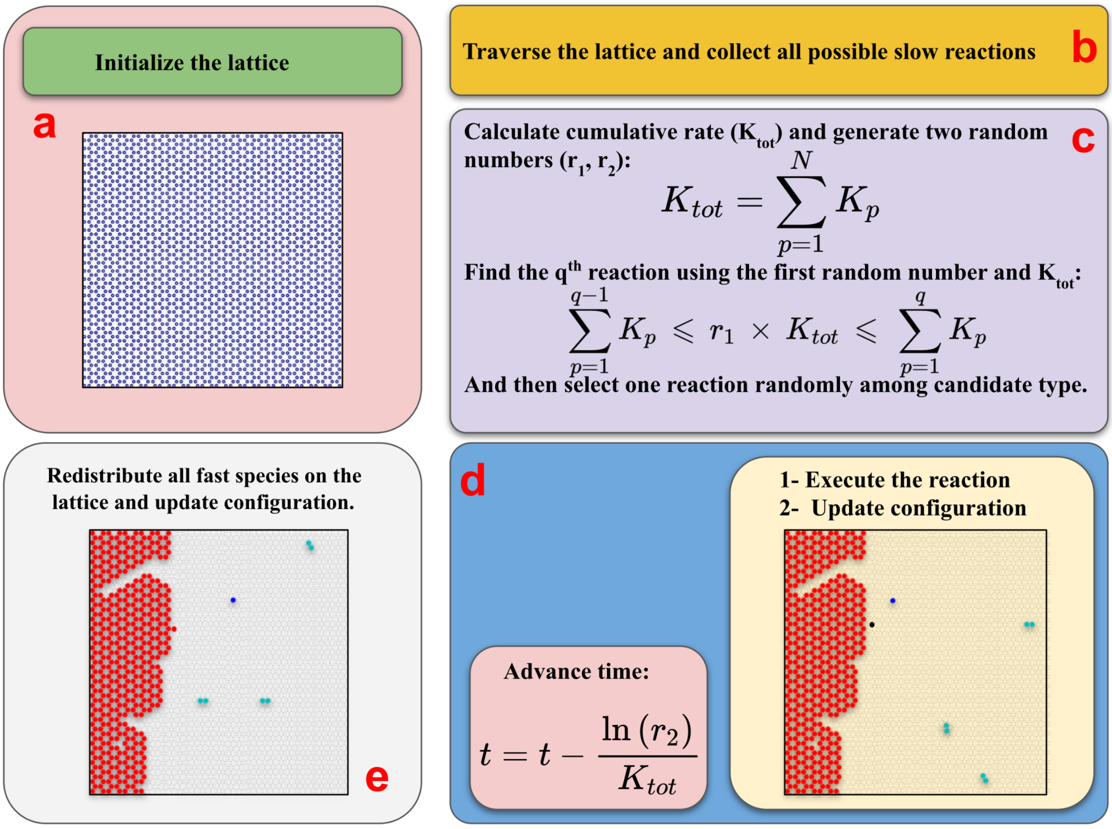

Figure 3.31.: Flowchart of the KMC algorithm. Different parts of the algorithm are shown in boxes with letters.

Following the implementation of AS-KMC and FSR-KMC protocols, we carried out initial stage simulations for both models. The simulations were performed under the same conditions with a 16×16 nm^2 lattice, where growth was not included. The system was subjected to P$_{CH_4}$ = 100 and P$_{H_2}$ = 0.01 Torr at a temperature of 1300 K. As AS-KMC requires two additional inputs from the user, we set the scaling factor α to 100 and varied δ from 0.3 to 0.7. We also calculated N$_f$ as the minimum sighting steps (refer to Table 3.5). These factors were evaluated to determine their possible effects on the results.

Table 3.5.: AS-KMC simulation requirements; δ and N$_f$, where N$_f$ is calculated according to Equation 3.6 for α = 100 for δ from 0.3 to 0.7.

δ	0.3	0.4	0.5	0.6	0.7
N$_f$	397	226	137	84	50

The evolution of the moving average concentration for all simulations is depicted in Figure 3.32. To assess the steady-state of the KMC simulations, we utilize the converged values of the moving average as a criterion for measuring quantities [173]. It can be observed that the steady-state is reached around 10^{-2} s for all simulations. In the AS-KMC protocol, different values of N$_f$ may affect the results as they lead to scaling the high rate constants at different intervals. Figure 3.32 a-e illustrate that the species concentrations exhibit the same trends for all AS-KMC simulations. The steady-state concentration of species is shown in Figure 3.33, which enables a comparison between AS-KMC and FSR-KMC results. It is worth noting that changing δ from 0.3 to 0.7 in the AS-KMC model does not have any discernible effect on the results. On the other hand, the achieved concentrations for the FSR-KMC simulation are almost the same as those of the AS-KMC simulations.

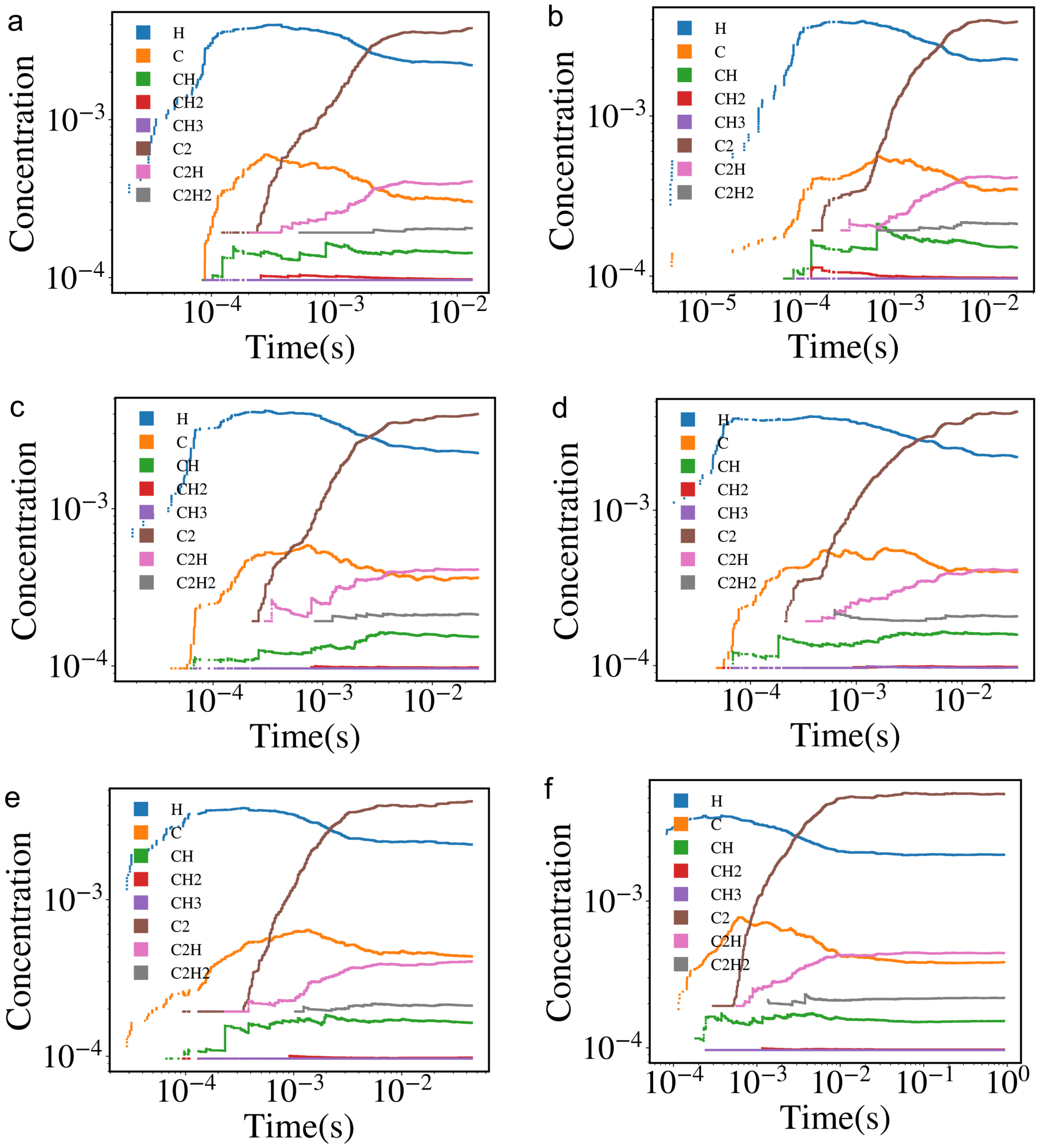

Figure 3.32.: Evolution of the moving average concentration of different species as a function of time for AS-KMC samples: $\delta = 0.3$ (a), $\delta = 0.4$ (b), $\delta = 0.5$ (c), $\delta = 0.6$ (d), $\delta = 0.7$ (e), and FSR-KMC sample (f). All simulations were performed for a 16×16 nm^2 lattice with the same conditions ($P_{CH_4} = 100$, $P_{H_2} = 0.01$ Torr, and T = 1300 K).

To ensure the proper sampling of different reactions, we have calculated the steady-state net occurrence rate (forward minus backward) of all involved reactions for each simulation time in all cases, as illustrated in Figure 3.34. The steady-state rates for all non-diffusion processes are almost identical for both AS-KMC and FSR-KMC cases, indicating that both models provide accurate sampling of non-diffusion processes. However, the diffusion processes show a slight difference between the two models due to the different values of N_f employed in the AS-KMC model. The largest N_f ($\delta = 0.3$) used in the AS-KMC model has less than 10 orders of magnitude difference with the FSR-KMC case. It is expected to observe different diffusion occurrences in simulations employing speed-up schemes in KMC

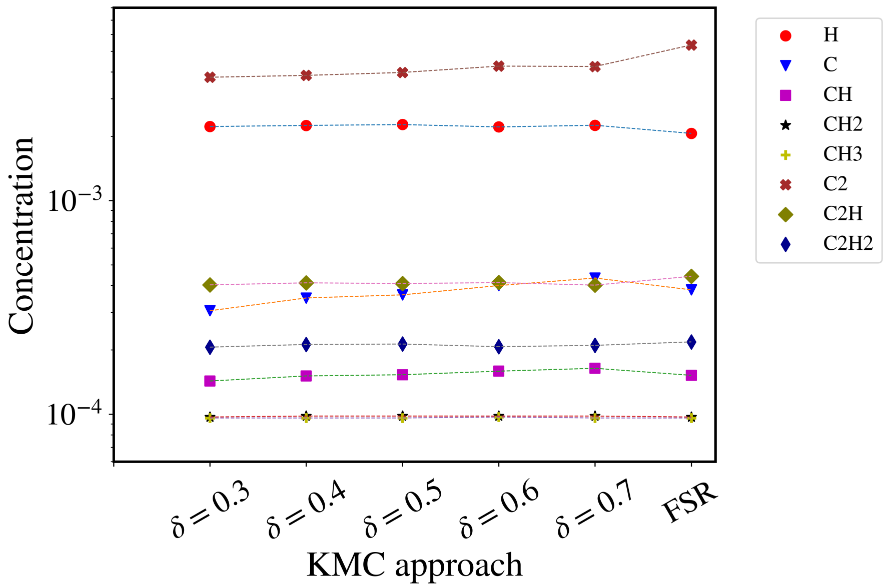

Figure 3.33.: Species steady-state concentration resulted from AS-KMC and FSR-KMC models for a 16×16 nm^2 lattice with conditions: P$_{CH_4}$ = 100, P$_{H_2}$ = 0.01 Torr and T = 1300 K.

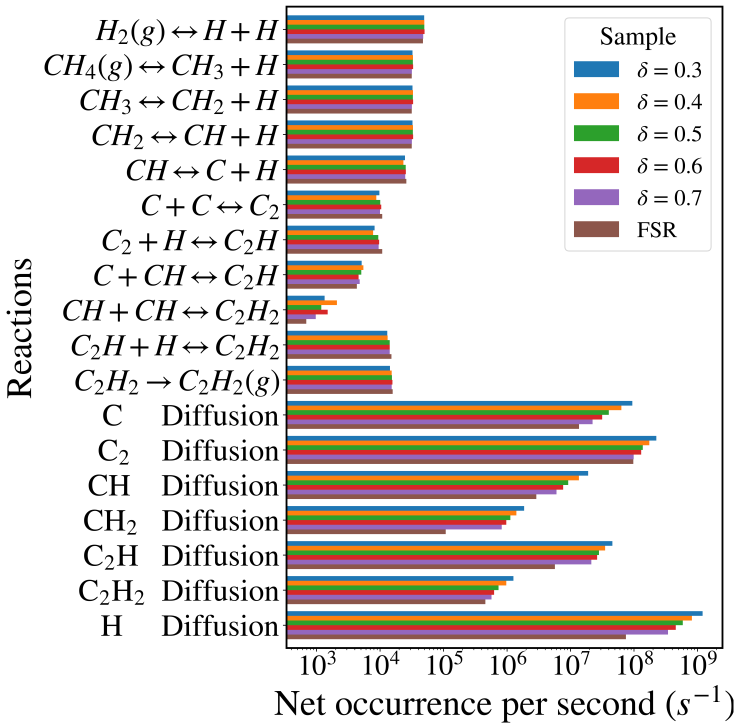

Figure 3.34.: Net occurrence per time of initial stage (reactions 1-18 from Table 3.2) AS-KMC and FSR-KMC simulations. Simulation are performed on a 16×16 nm^2 lattice under P$_{CH_4}$ = 100, P$_{H_2}$ = 0.01 Torr and T = 1300 K conditions. For AS-KMC simulations α = 100 and δ changes from 0.3 to 0.7.

simulations. However, these differences in diffusion processes do not have any significant impact on the output measured by the steady-state concentration of species, as shown in Figure 3.33. Therefore, considering the capability of both models in dealing with fast surface diffusion processes to study the graphene growth mechanism, we choose the FSR-KMC protocol, which requires less CPU hours than the AS-KMC protocol. In fact, for the same set of simulations performed with the same amount of CPU hours, the FSR-KMC simulation time is at least ten times shorter than that of the AS-KMC cases (see Figure 3.32).

3.4.2.1. Simulation samples

One of the primary objectives of this study is to investigate the influence of the partial pressures of CH_4 and H_2 on the growth of graphene using CVD. To achieve this goal, we created a list of precursor partial pressure pairs and generated corresponding samples for the study. We classified the samples into two primary profiles based on the CH_4 and H_2 partial pressures. The CH_4 partial pressure profile was created by varying the CH_4 pressure from 10 to 100 Torr while keeping the H_2 pressure constant at 0.01 Torr. Similarly, the H_2 partial pressure profile was created by varying the H_2 pressure from 10^{-3} to 8×10^{-2} Torr while keeping the CH_4 pressure constant at 10 Torr. These pressure values are tabulated in Table 3.6. We note that the CH_4 and H_2 partial pressures used in this study may not be directly comparable to experimental conditions due to the imperfections of the Cu substrate used in experiments, which provide stronger binding energy resulting in higher adsorption rates of precursors. To account for this effect, we used a range of partial pressures higher than the experimental values. This approach also made adsorption more frequent where other rate constants are much higher than adsorption, allowing us to speed up the kinetic Monte Carlo (KMC) simulations. To study different graphene growth pathways, we performed KMC simulations for the prepared pressure profiles, using an initial flake in the form of a ribbon (slab) located at the left side of a 100×100 nm^2 lattice, while the rest of the lattice was initially empty.

Table 3.6.: Pressure profile. Samples are named from S1 to S8 (pressures are in Torr).

Sample	P_{CH_4}	P_{H_2}
$S1$	100	0.01
$S2$	10	0.001
$S3$	60	0.01
$S4$	30	0.01
$S5$	10	0.005
$S6$	10	0.01
$S7$	10	0.05
$S8$	10	0.08

3.5. Results and discussion

We developed a KMC protocol that considered all possible reactions among the species involved in the process, including H, C, CH, CH_2, CH_3, CH_4, C_2H, and C_2H_2. Moreover, we also evaluated the effects of additional reactions, such as the (de)hydrogenation of species at the edges, on the quality of the growing graphene flake. By taking into account these reactions and barriers, we aimed to obtain a detailed understanding of the growth mechanism and the role of each reaction in the process. Our analysis allowed us to identify the key reactions that contribute to the graphene growth and the factors that influence the quality of the produced flakes.

3.5.1. Modulation of graphene growth by CH_4 partial pressure

We have implemented a KMC protocol to investigate the process of graphene growth on a Cu(111) surface in CVD using reaction rates obtained from DFT calculations.

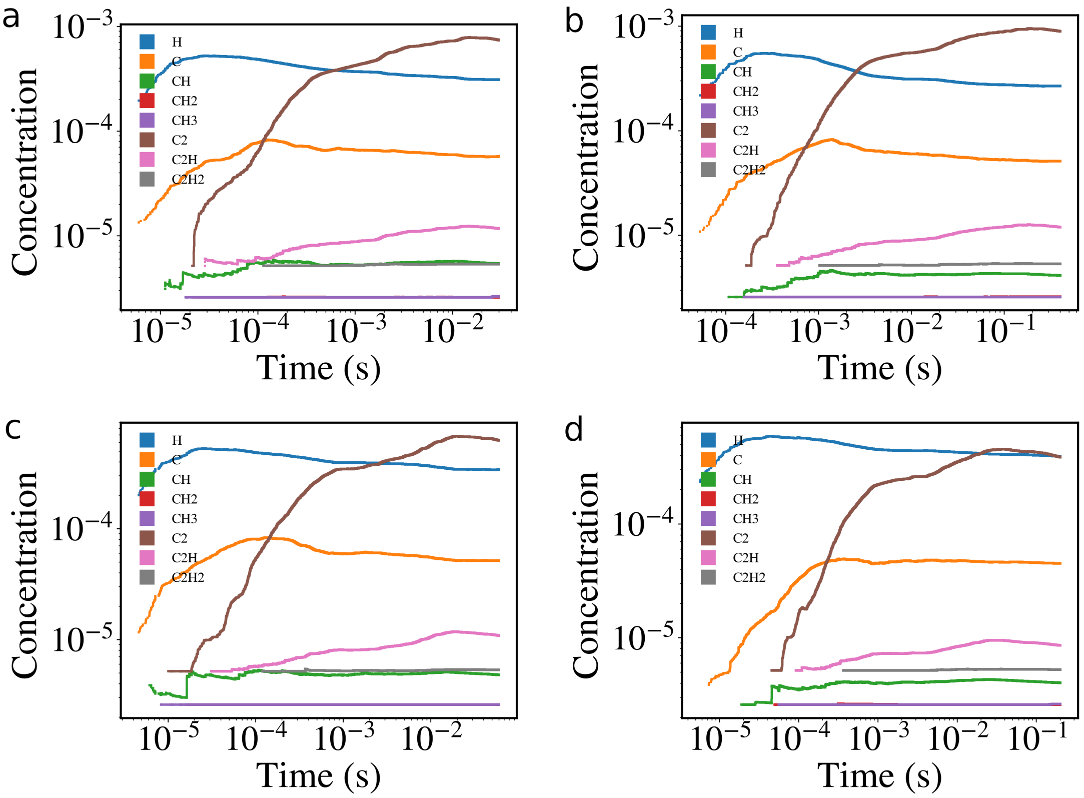

Figure 3.35.: Evolution of the moving average concentration of different species as a function of time for samples S1 (a), S2 (b), S3 (c), and S4 (d) (see Table 3.6).

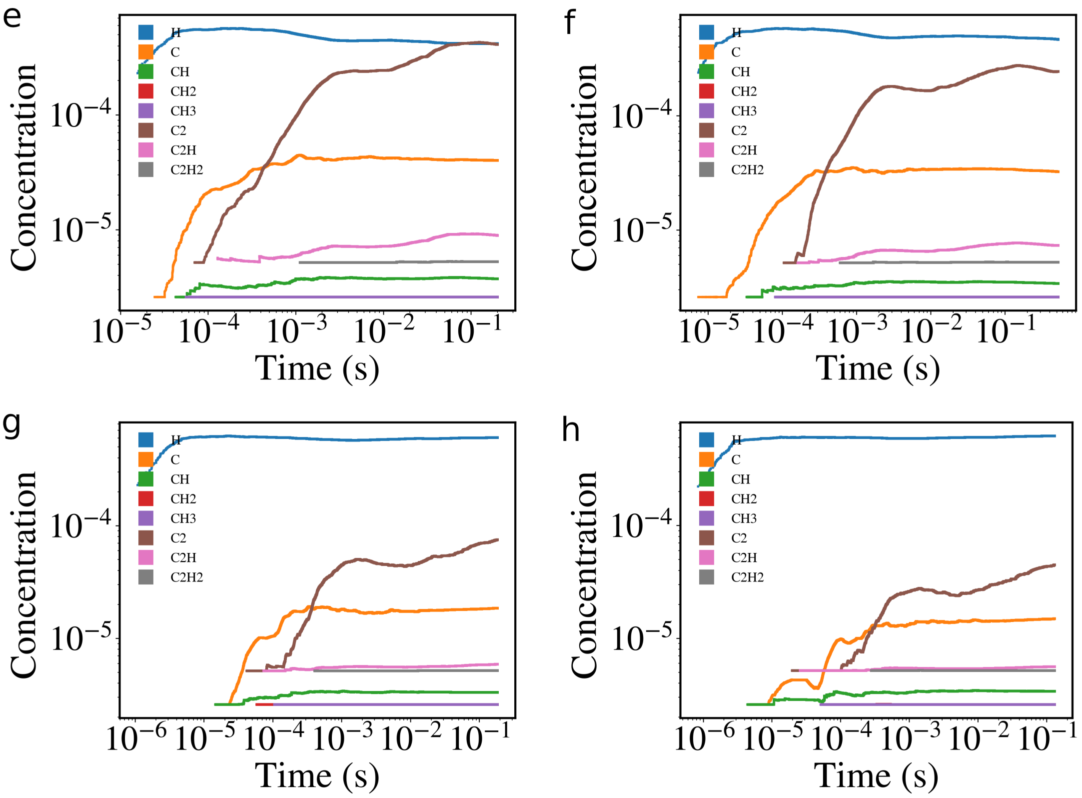

Figure 3.36.: Evolution of the moving average concentration of different species as a function of time for samples S5 (e), S6 (f), S7 (g), and S8 (h) (see Table 3.6).

By performing eight simulations with varying partial pressures of precursors (as shown in Table 3.6), we have demonstrated the impact of these control parameters on the CVD process. Non-equilibrium steady-state has been attained for all simulations at a time point of approximately 2×10^{-3} s, with concentrations of reactive species displaying fluctuations around their respective moving averages, which converged to a stable value [173]. The temporal evolution of the moving averages for all cases can be observed in Figures 3.35 and 3.36. Based on the data presented in Figures 3.35 and 3.36 a-h, we observed that the most abundant carbon-containing species in all simulations was carbon dimer, which exhibited the longest relaxation time of 2×10^{-3} (as evidenced by the brown curves in Figures 3.35 and 3.36 a-h). It is noteworthy that, despite the higher partial pressure of methane in all simulations, the concentration of H was typically higher than that of other carbon-containing species. This can be attributed to the fact that the dissociative adsorption rate of H_2 is much higher than that of CH_4. Upon examining the steady-state concentration of the relevant species in Figure 3.37, we found that increasing the partial pressure of CH_4 at a fixed H_2 partial pressure resulted in an increase in the concentration of carbon and its dimer (as shown in Figure 3.37 a). Conversely, increasing the H_2 partial pressure at a fixed CH_4 partial pressure led to an increase in the concentration of hydrogen adatom and a decrease in the concentration of carbon and carbon dimer. This result highlights the impact of the dissociative adsorption rates of CH_4 and H_2 on the different simulations, which is influenced by their respective pressures.

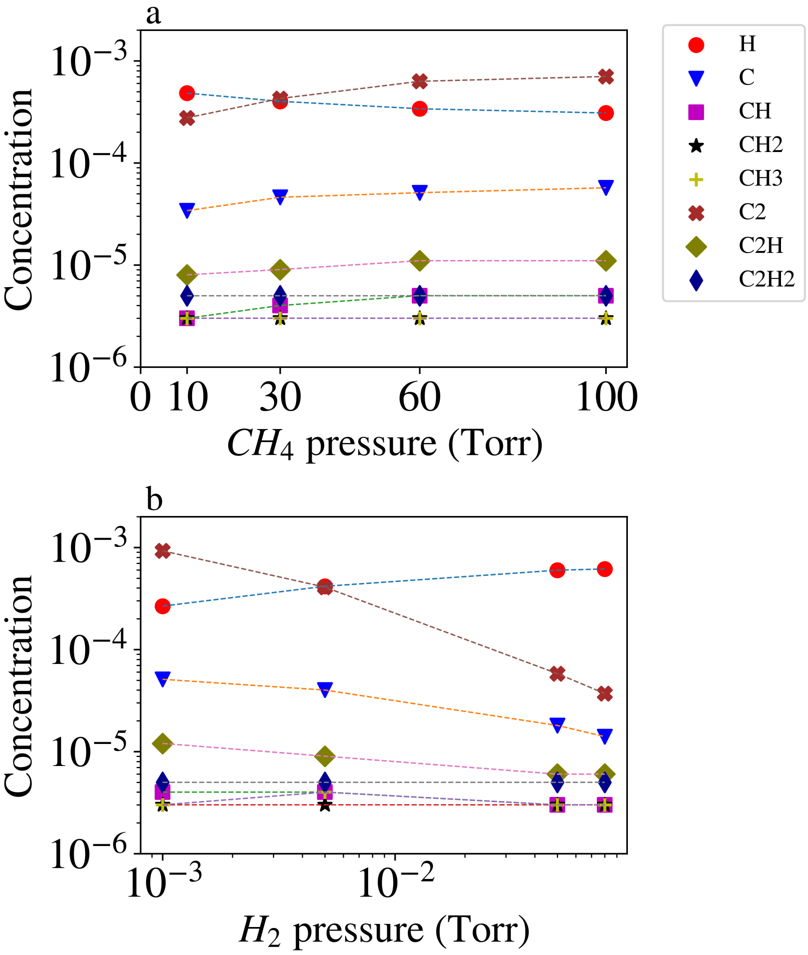

Figure 3.37.: a,b: Species concentration profile for all simulation. Species are shown using different markers and colors.

We have generated spatio-temporal evolution data of all samples through snapshots of KMC simulations taken at different times to monitor the growth of graphene on different samples. In the following, detailed analysis of the spatio-temporal evolution of all sample (refer to Table 3.6) are provided (Figures 3.38 to 3.45.

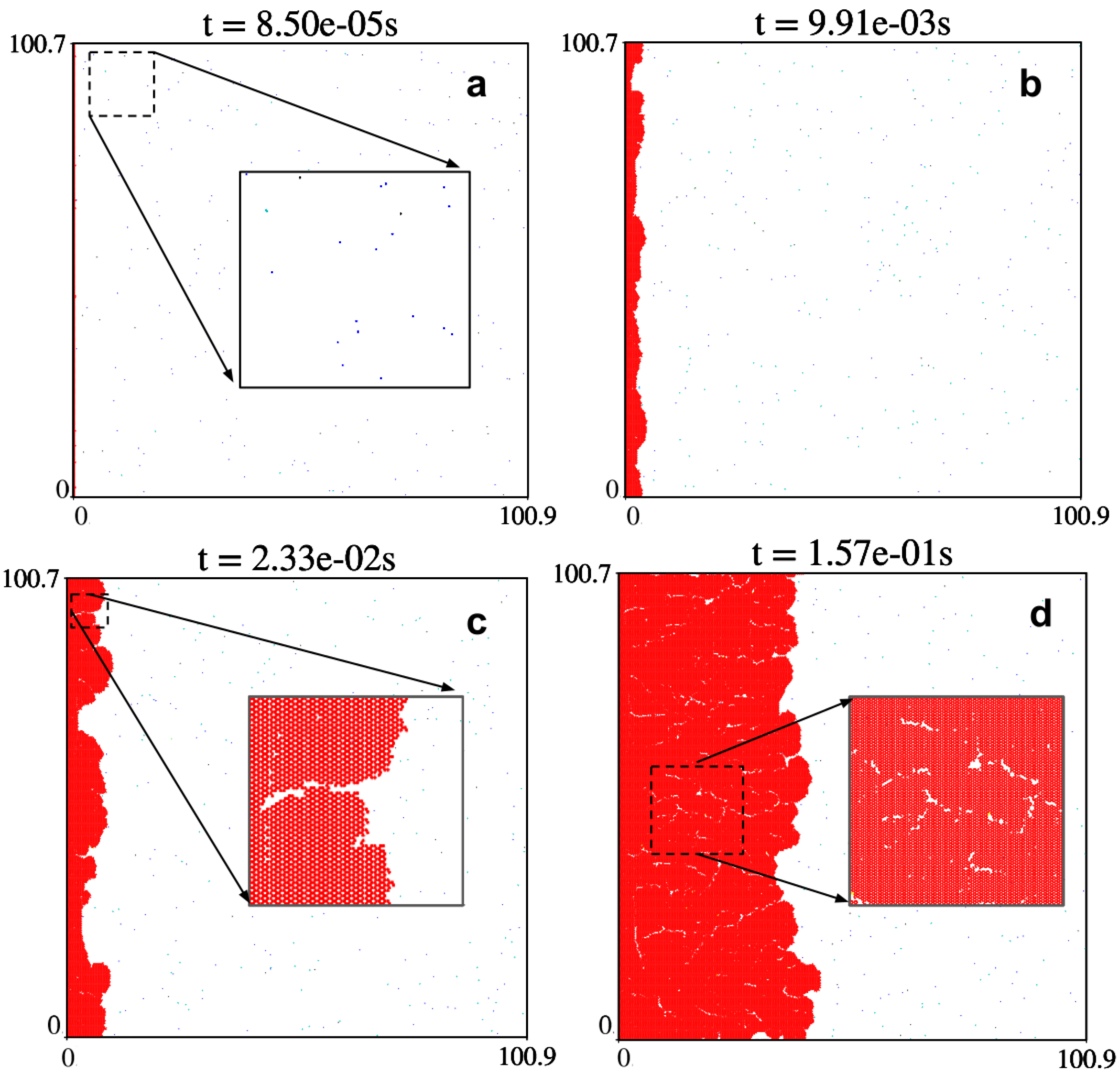

Figure 3.38.: KMC simulation of the CVD graphene growth on Cu(111) surface represented by 100×100 nm^2 lattice for P$_{CH_4}$ = 100 Torr, P$_{H_2}$ = 0.01 Torr, and T=1300K (sample S1 from Table 3.6). Each snapshot has a timestamp and shows different stages of the growth process (in red). a) The first stage of growth in which hydrogen and carbon-containing species reach the surface via dissociative adsorption of CH$_4$ and H$_2$, followed by further decomposition and (de)hydrogenations. b) As the concentration of species increases over time, around 2×10^{-3} system reaches a steady state and flakes begin to grow from the left hand side, where the initial flake is located. c) and d) Growth stage at t=2.33×10^{-2} S and t =1.57×10^{-1} S where the flake grows with cracks and irregular edges caused by vacancy defects and hydrogenation at the edges.

As with other samples, Figure 3.38 shows four different snapshots of the simulation at different times for the sample S1 (see Table 3.6). During the simulations, different species formed on the surface due to dissociative adsorption of CH$_4$ and H$_2$ followed by subsequent decomposition and other possible (de)hydrogenation reactions on the surface, resulting in the concentration of species increasing over time (Figure 3.38 a). After 2×10^{-3} s, the system reaches a steady state (see Figure 3.35a), and the flake starts to grow by attaching species to the edge (Figure 3.38 b). Since the initial and growing flake's width is around 100 nm, attachment processes can occur at different areas simultaneously, resulting in vacancy defects. The observed irregular edges and cracks on the growing flake (marked with black boxes in Figure 3.38 c-d) are attributed to edge hydrogenation.

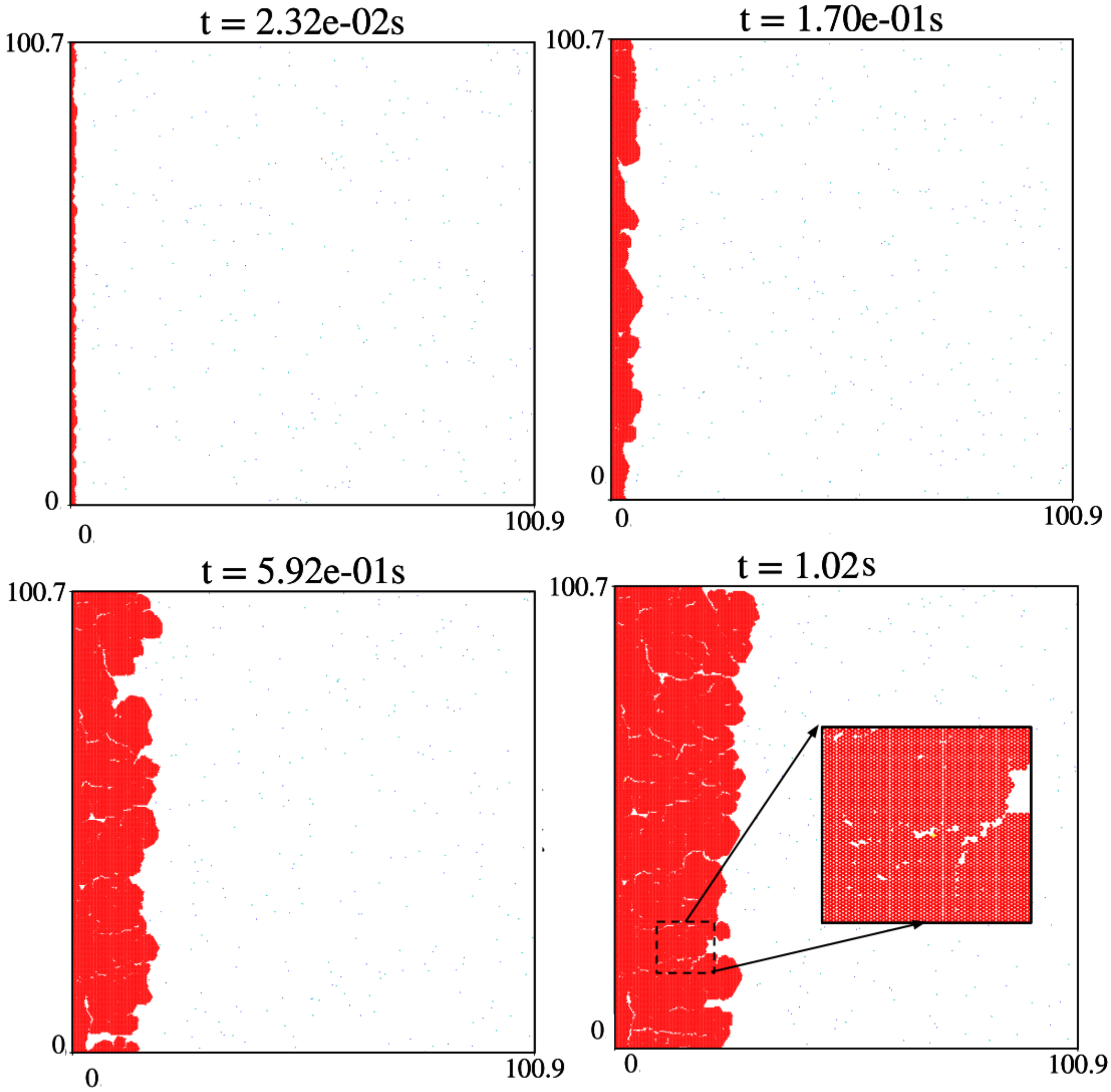

Figure 3.39.: KMC simulation of the CVD graphene growth on Cu(111) surface represented by 100×100 nm^2 lattice for P_{CH_4} = 10 Torr, P_{H_2} = 0.001 Torr, and T=1300K (sample S2 from Table 3.6). Each snapshot has a timestamp and shows different stages of the growth process (in red). The first stage of growth in which hydrogen and carbon-containing species reach the surface via dissociative adsorption of CH_4 and H_2, followed by further decomposition and (de)hydrogenations. As the concentration of species increases over time, around 2×10^{-3} system reaches a steady state and flakes begin to grow from the left hand side, where the initial flake is located. Growth stage at t=5.92×10^{-1} S and t=1.02 S where the flake grows with cracks and irregular edges caused by vacancy defects and hydrogenation at the edges are included.

The spatio-temporal evolution of sample S2 (as shown in Table 3.6) reveals a similar pattern to that observed in the previous simulation. However, the most notable difference is the simulation time, which is longer for this case. The simulation proceeds through the same series of steps, starting with precursor dissociation, followed by edge attachment and ring formation. However, the different pair of partial pressures used in this simulation resulted in a slower growth compared to sample S1. This is because the lower methane pressure in sample S2 resulted in a lower concentration of carbon-containing species available for growth over time. Moreover, the lower H_2 pressure in sample S2 allows for methane dissociative adsorption to occur, further reducing the concentration of carbon-containing species available for growth. Consequently, a longer simulation time was required for the growth of the graphene flake in sample S2.

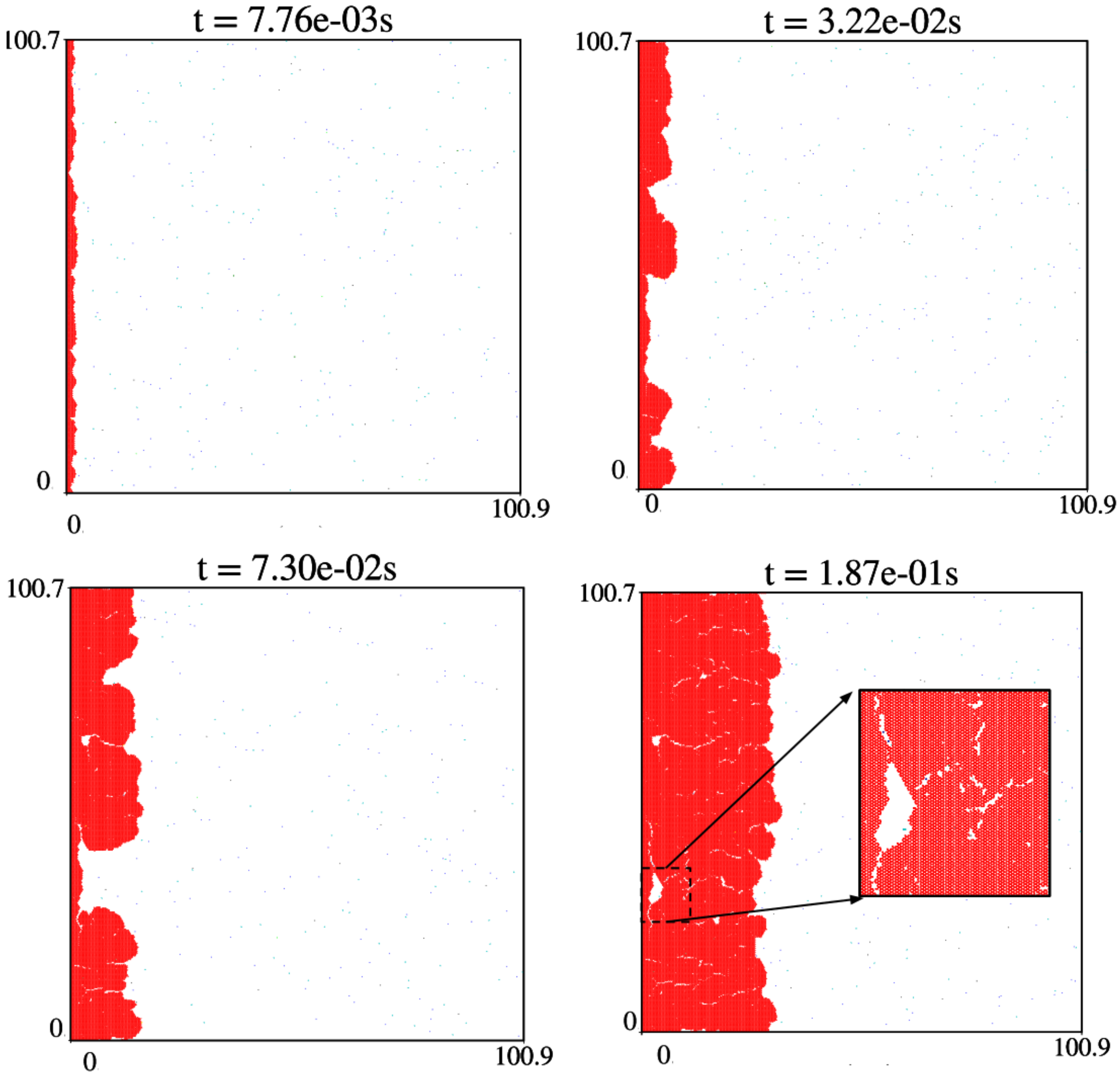

Figure 3.40.: KMC simulation of the CVD graphene growth on Cu(111) surface represented by 100×100 nm^2 lattice for $P_{CH_4} = 60$ Torr, $P_{H_2} = 0.01$ Torr, and T=1300K (sample S3 from Table 3.6). Each snapshot has a timestamp and shows different stages of the growth process (in red). The first stage of growth in which hydrogen and carbon-containing species reach the surface via dissociative adsorption of CH_4 and H_2, followed by further decomposition and (de)hydrogenations. As the concentration of species increases over time, around 2×10^{-3} system reaches a steady state and flakes begin to grow from the left hand side, where the initial flake is located. Growth stage at t=7.30×10^{-2} S and t=1.87×10^{-1} S where the flake grows with cracks and irregular edges caused by vacancy defects and hydrogenation at the edges are included.

In the case of the third sample (sample S3 from Table 3.6), the growth process exhibits a very similar pattern to that of the first sample, albeit with slight differences in the concentration of carbon-containing species during growth (see Figure 3.37. These differences are attributed to the methane partial pressure in the simulation, which affects the availability of carbon-containing species during the process.

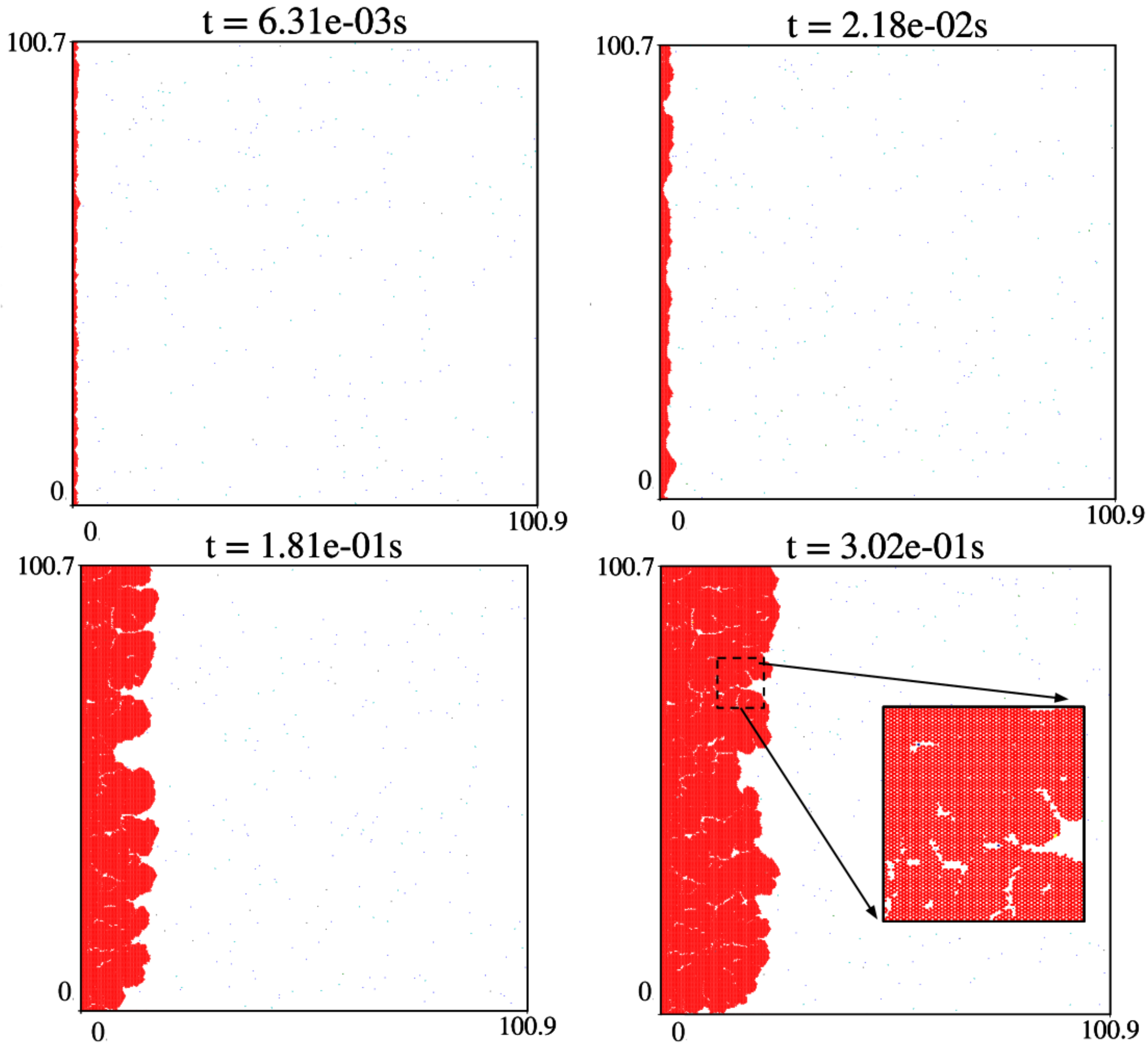

Figure 3.41.: KMC simulation of the CVD graphene growth on Cu(111) surface represented by 100×100 nm^2 lattice for P_{CH_4} = 30 Torr, P_{H_2} = 0.01 Torr, and T=1300K (sample S4 from Table 3.6). Each snapshot has a timestamp and shows different stages of the growth process (in red). The first stage of growth in which hydrogen and carbon-containing species reach the surface via dissociative adsorption of CH_4 and H_2, followed by further decomposition and (de)hydrogenations. As the concentration of species increases over time, around 2×10^{-3} system reaches a steady state and flakes begin to grow from the left hand side, where the initial flake is located. Growth stage at t=1.81×10^{-1} S and t=3.02×10^{-1} S where the flake grows with cracks and irregular edges caused by vacancy defects and hydrogenation at the edges are included.

The spatio-temporal evolution of sample S4 (as indicated in Table 3.6) exhibits a similar trend to samples S1 and S3, where the availability of carbon-containing species affects the growth process (see Figure 3.37). In contrast, sample S5 displays a different behavior, as reducing both partial pressures leads to smaller flake size. As compared to sample S2, which had the same methane partial pressure, an increase in H_2 partial pressure resulted in a lower level of dissociative adsorption of methane, which, in turn, reduced the amount of carbon species available on the surface (see Figure 3.37. It can be attributed to the varying dissociative adsorption rates of the precursors, which are dependent on their respective partial pressures (as indicated in Table 3.3).

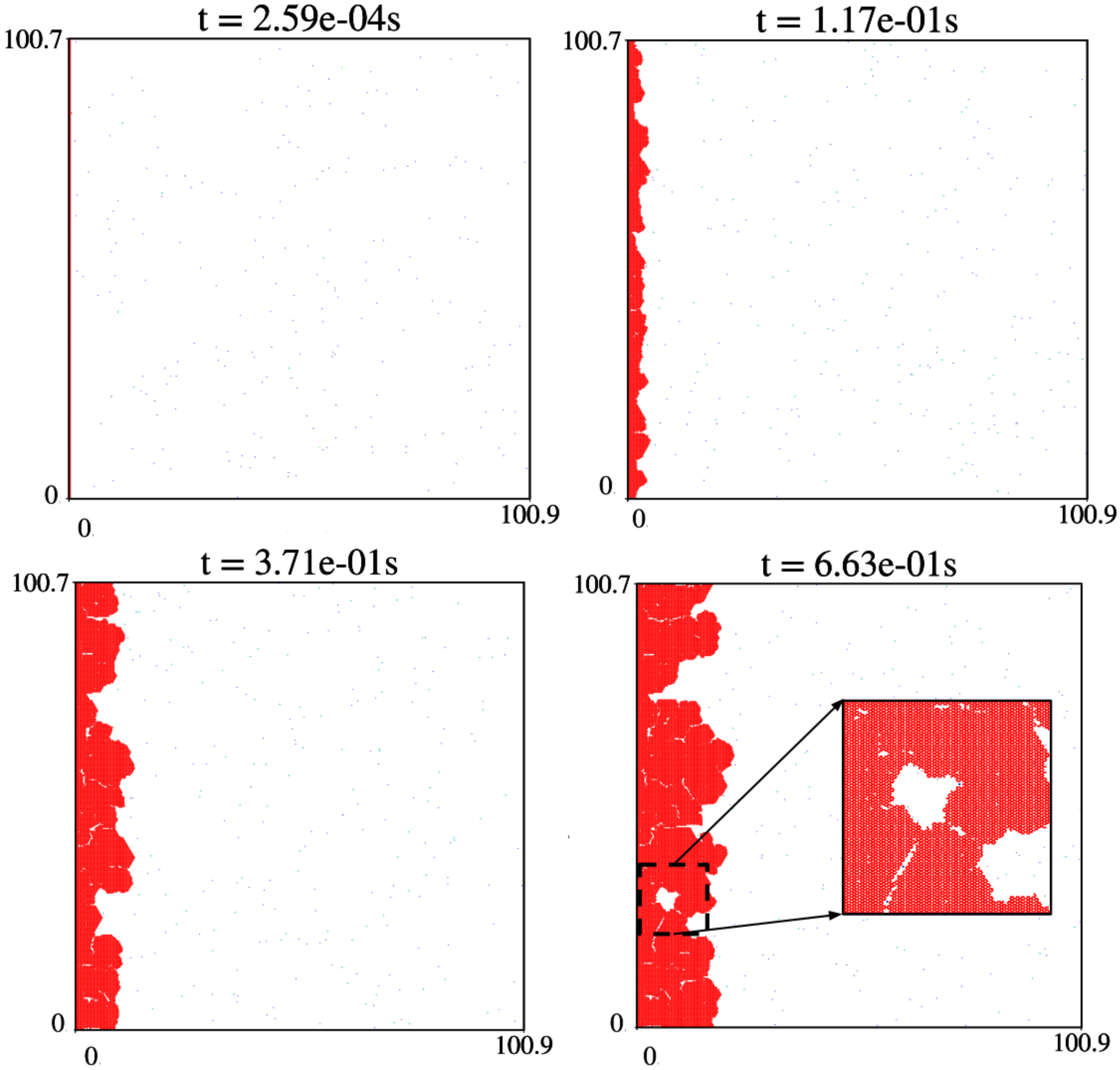

Figure 3.42.: KMC simulation of the CVD graphene growth on Cu(111) surface represented by 100×100 nm^2 lattice for P_{CH_4} = 10 Torr, P_{H_2} = 0.005 Torr, and T=1300K (sample S5 from Table 3.6). Each snapshot has a timestamp and shows different stages of the growth process (in red). The first stage of growth in which hydrogen and carbon-containing species reach the surface via dissociative adsorption of CH_4 and H_2, followed by further decomposition and (de)hydrogenations. As the concentration of species increases over time, around 2×10^{-3} system reaches a steady state and flakes begin to grow from the left hand side, where the initial flake is located. Growth stage at t=7.30×10^{-2} S and t=1.87×10^{-1} S where the flake grows with cracks and irregular edges caused by vacancy defects and hydrogenation at the edges are included.

Using the same reasoning, it can be inferred that the growth of the sixth sample (S6) with P_{CH_4}=10 Torr and P_{H_2}=0.01 Torr partial pressures required a longer period of time due to the dependence of the carbon-containing species concentration on the pair of pressures. The availability of the carbon species is critical for the growth of graphene, and the concentration of these species on the surface determines the rate of growth. Therefore, it can be deduced that the slower growth observed for sample S6 can be attributed to a lower concentration of carbon-containing species, which is directly linked to the pair of pressures.

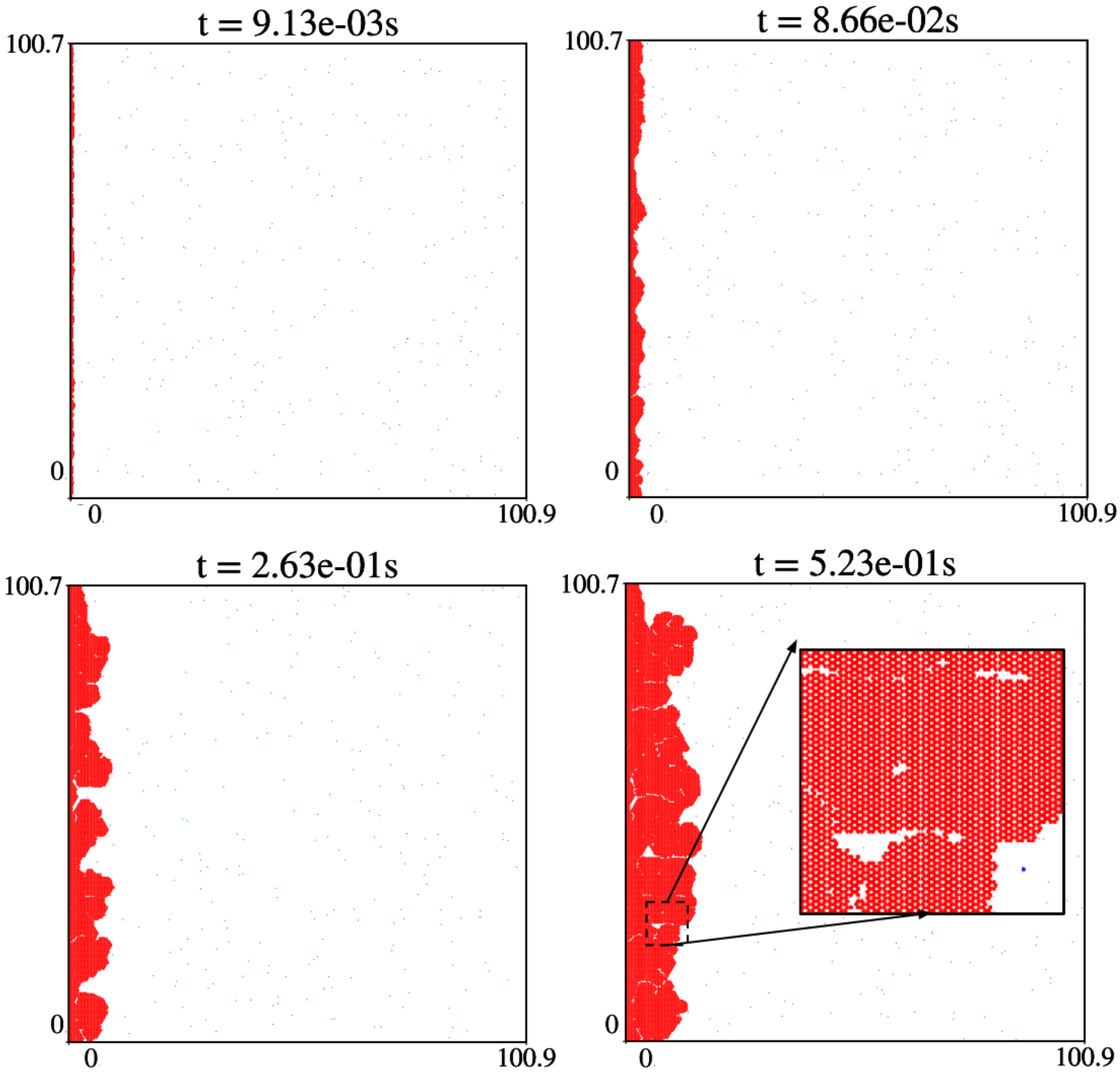

Figure 3.43.: KMC simulation of the CVD graphene growth on Cu(111) surface represented by 100×100 nm^2 lattice for P$_{CH_4}$ = 10 Torr, P$_{H_2}$ = 0.01 Torr, and T=1300K (sample S6 from Table 3.6). Each snapshot has a timestamp and shows different stages of the growth process (in red). The first stage of growth in which hydrogen and carbon-containing species reach the surface via dissociative adsorption of CH$_4$ and H$_2$, followed by further decomposition and (de)hydrogenations. As the concentration of species increases over time, around 2×10^{-3} system reaches a steady state and flakes begin to grow from the left hand side, where the initial flake is located. Growth stage at t=2.63×10^{-1} S and t=5.23×10^{-1} S where the flake grows with cracks and irregular edges caused by vacancy defects and hydrogenation at the edges are included.

Furthermore, it can be noted that the growth rate of the last two samples (S7 and S8 in Table 3.6) was severely compromised as a result of a higher H$_2$ partial pressure. This is because, in these samples, the methane partial pressure was kept constant at P$_{CH_4}$=10 Torr, while the H$_2$ partial pressure was increased. Consequently, a reduction in the availability of carbon-containing species on the surface was observed. The lower concentration of carbon species available for growth in these samples resulted in a slower growth rate compared to the other samples. These observations are consistent with the idea that the growth rate of graphene is strongly influenced by the partial pressures of precursor gases. Therefore, controlling the partial pressures of CH_4 and H_2 is critical for obtaining high-quality graphene samples with an efficient growth rate.

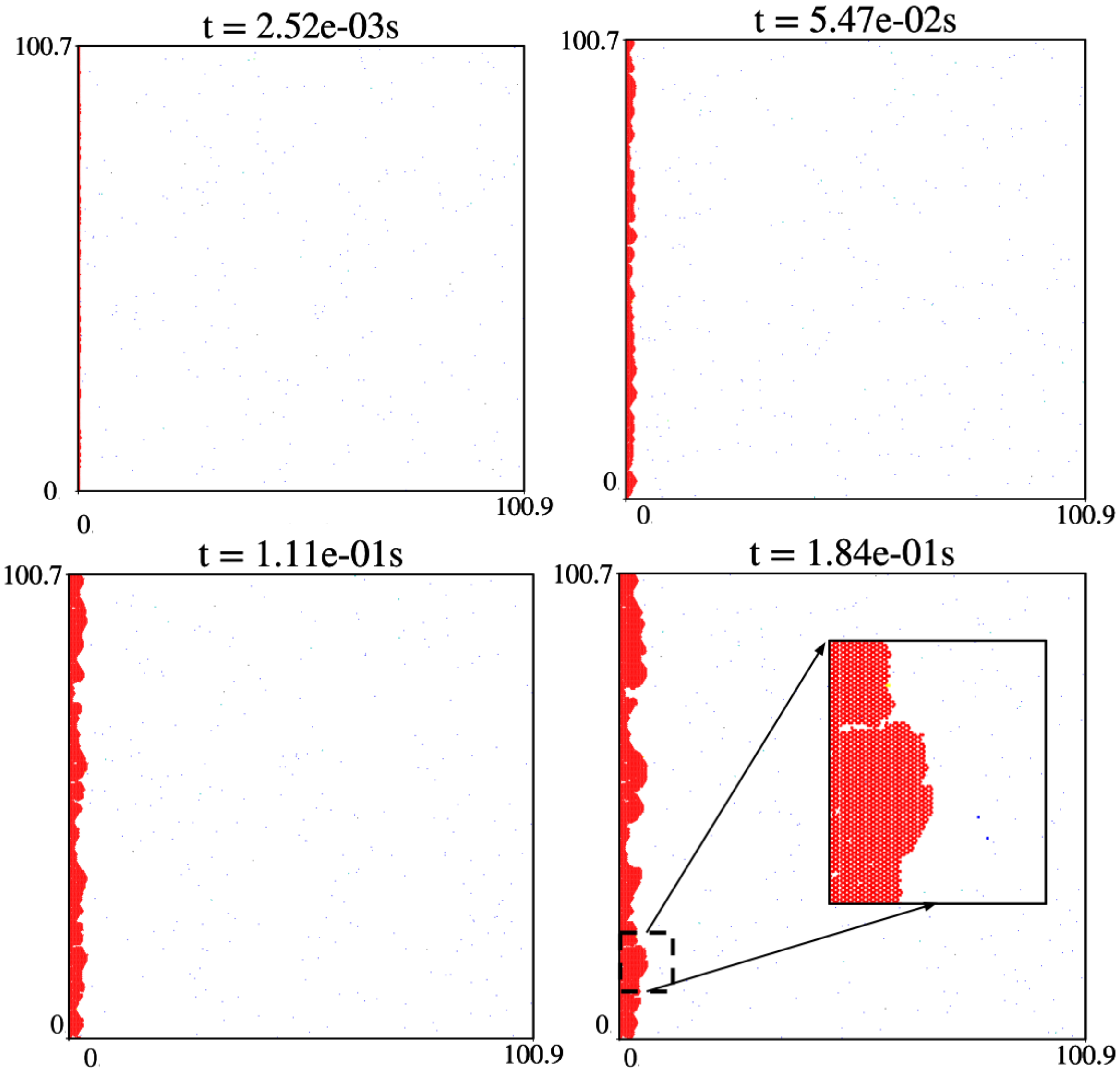

Figure 3.44.: KMC simulation of the CVD graphene growth on Cu(111) surface represented by 100×100 nm^2 lattice for P_{CH_4} = 10 Torr, P_{H_2} = 0.05 Torr, and T=1300K (sample S7 from Table 3.6). Each snapshot has a timestamp and shows different stages of the growth process (in red). The first stage of growth in which hydrogen and carbon-containing species reach the surface via dissociative adsorption of CH_4 and H_2, followed by further decomposition and (de)hydrogenations. As the concentration of species increases over time, around 2×10^{-3} system reaches a steady state and flakes begin to grow from the left hand side, where the initial flake is located. Growth stage at $t=7.30\times10^{-2}$ S and $t=1.87\times10^{-1}$ S where the flake grows with cracks and irregular edges caused by vacancy defects and hydrogenation at the edges are included.

We examined the spatio-temporal evolution of all samples shown in Figures 3.39 to 3.45 and used the flake radius as a measure of time-dependent flake growth during the simulation. The flake radius was defined as the average horizontal distance between the outer layer edges of the flake and the vertical axis on the left side, as depicted schematically in Figure 3.46. The average radius of all samples, along with their pair partial pressures and simulation time, is presented in Table 3.7. The obtained data can be used to calculate the growth rate as the radius per time for each sample.

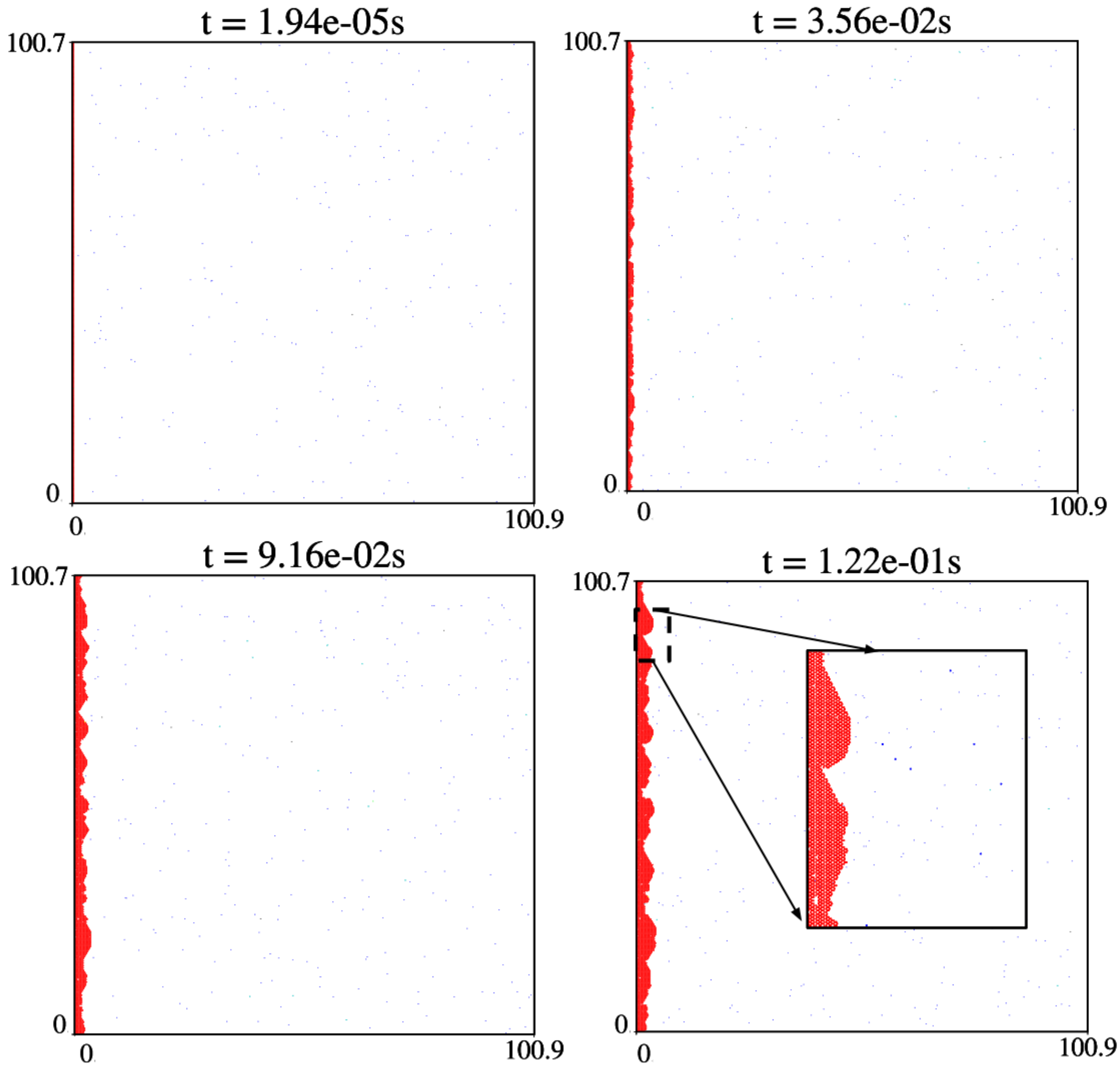

Figure 3.45.: KMC simulation of the CVD graphene growth on Cu(111) surface represented by 100×100 nm^2 lattice for P_{CH_4} = 10 Torr, P_{H_2} = 0.08 Torr, and T=1300K (sample S8 from Table 3.6). Each snapshot has a timestamp and shows different stages of the growth process (in red). The first stage of growth in which hydrogen and carbon-containing species reach the surface via dissociative adsorption of CH_4 and H_2, followed by further decomposition and (de)hydrogenations. As the concentration of species increases over time, around 2×10^{-3} system reaches a steady state and flakes begin to grow from the left hand side, where the initial flake is located. Growth stage at t=7.30×10^{-2} S and t=1.87×10^{-1} S where the flake grows with cracks and irregular edges caused by vacancy defects and hydrogenation at the edges are included.

This suggests that the growth rate (radius per time) of graphene flake can be positively correlated with CH_4 partial pressures. To confirm this relationship, we conducted additional analysis on four samples: S1, S3, S4, and S6. These samples were selected because they were grown using varying CH_4 partial pressures of 100, 60, 30, and 10 Torr, respectively, as specified in Table 3.6.

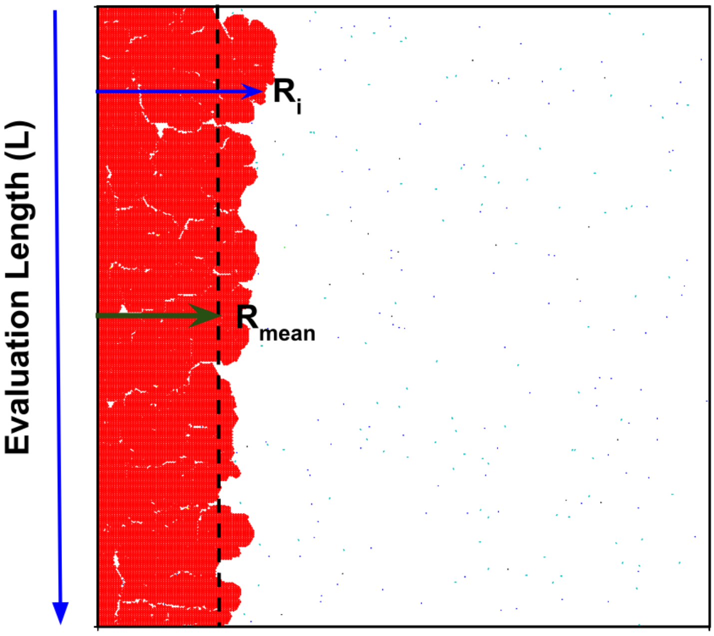

Figure 3.46.: Schematic of the surface with a flake (in red) where the radius (R$_i$), mean radius R$_{mean}$, and evaluation length (L) arr shown.

Table 3.7.: Summary on the average radius (R$_{mean}$), and simulation time for all samples.

Sample	P$_{CH_4}$ (Torr)	P$_{H_2}$ (Torr)	R$_{mean}$ (nm)	time (s)
S1	100	0.01	38.23	0.157
S2	10	0.001	25.95	1.018
S3	60	0.01	30.53	0.2
S4	30	0.01	22.87	0.302
S5	10	0.005	17.29	0.709
S6	10	0.01	12.40	0.523
S7	10	0.05	3.85	0.184
S8	10	0.08	2.86	0.131

During this section of the analysis, we calculated the radius profiles over time for the samples up to 0.157 S of simulation time. As depicted in Figure 3.47, we observed that Sample S1 had the highest average radius values over time. The data indicated that larger graphene flake sizes could be achieved by increasing the partial pressure of CH_4 while maintaining the H_2 partial pressure constant. This result can be explained by the fact that a higher concentration of carbon-containing species increases the number of successful attachments. Our finding is in agreement with previous experimental studies [220, 190, 216, 221]. We also found a linear relationship between the instantaneous growth rate and the CH_4 partial pressure at t=0.157 S, which can be expressed as $R = 2.66 \times P_{CH_4} + 20.38$. This indicates that higher CH_4 partial pressure speeds up graphene growth, as shown in the inset plot of Figure 3.47. However, the growth rate over time decreases due to the limited number of available adsorption sites on the lattice for further dissociative adsorption of precursors. Figure 3.48 displays the growth rate time-dependence profiles for mentioned samples. As demonstrated, the growth rate decreases with time for all samples, and the order of the instantaneous growth rate for all samples is the same.

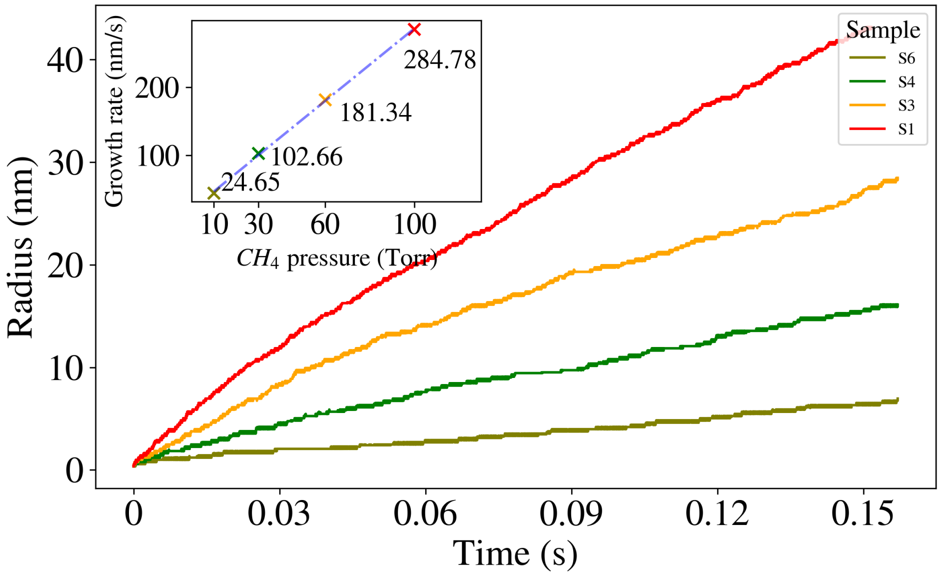

Figure 3.47.: Growth of graphene over time at different CH_4 partial pressures. The change of the flake radius for samples S1 (100 Torr), S3 (60 Torr), S4 (30 Torr) and S6 (10 Torr) is shown with the red, orange, green and olive color, respectively. The KMC simulations up to 0.157 s were performed and the resulting flake radii of approximately 38 nm, 24 nm, 12 nm and 4 nm, respectively, were obtained. **Inset plot**: Growth rate (radius per time) as a function of the CH_4 partial pressure profile at t=0.157 S. The fitted curve on the data is shown in blue dashed lines, indicating a linear relationship between flake radius per time and CH_4 partial pressure.

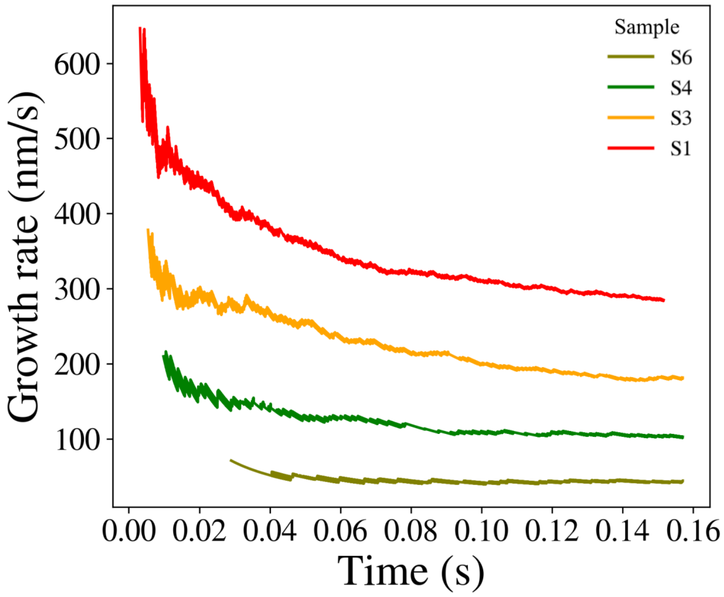

Figure 3.48.: Time series of graphene growth rate for different CH_4 partial pressures. The change of the flake growth rate for samples S1 (100 Torr), S3 (60 Torr), S4 (30 Torr) and S6 (10 Torr) are shown with the red, orange, green and olive color, respectively.

Figure 3.49 illustrates the experimental data from two distinct investigations that demonstrate a consistent understanding of the effect of CH_4 partial pressure on graphene growth.

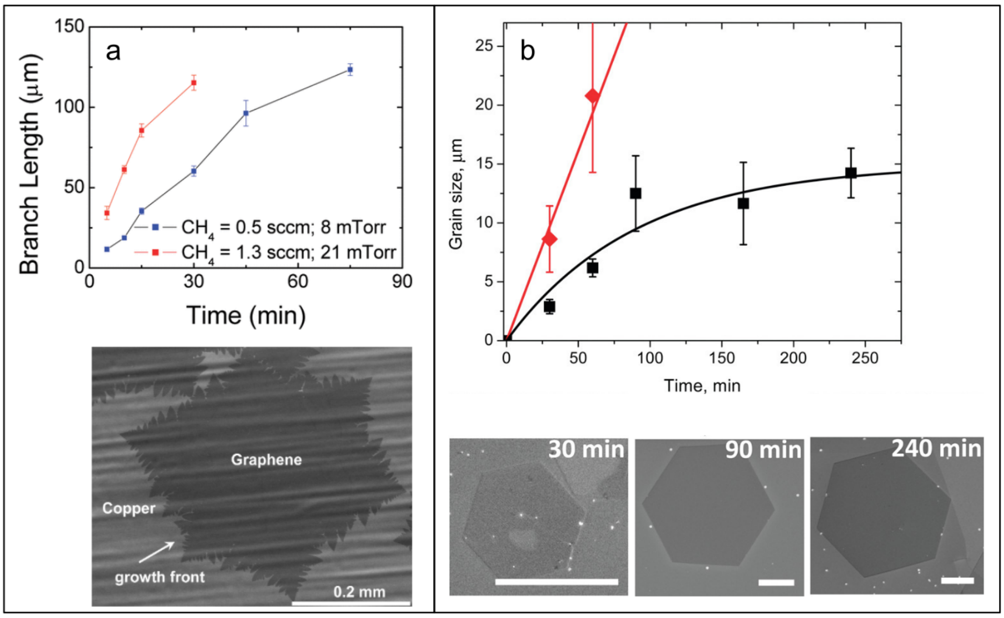

Figure 3.49.: a: At 1035 C graphene growth as a function of time for two methane flow rates and partial pressures while H_2 partial pressure is fixed at 27 mTorr, and SEM images of graphene on copper grown by CVD. Reprinted with permission from Ref([222]). Copyright 2011, American Chemical Society. b: The average size of graphene grains as a function of growth time at 1000 °C on Cu foil for fixed partial pressure of CH_4 (23 mTorr) and 11 and 19 Torr H_2 partial pressure in red and black respectively. SEM images show hexagon size evolution during growth using 19 Torr of H_2 . Scale bars are 3 μm. Reprinted with permission from Ref([223]). Copyright 2011, American Chemical Society

In order to assess the quality of the graphene flakes, we employed two roughness parameters, namely, the average roughness (R_a) and the root-mean-square roughness[224, 225]. The definition of R_a involves the computation of the deviation of R_i from the mean radius (R_{mean}) along the vertical axis over the evaluation length, L:

$$R_a = \frac{1}{L}\sum_{n=1}^{L} |R_i - R_{mean}| \tag{3.7}$$

R_q is also defined as the root-mean-square of the deviation of R_i from the mean radius ($R_m ean$) over the evaluation length, L as follows:

$$R_q = \sqrt{\frac{1}{L}\sum_{n=1}^{L} (R_i - R_{mean})^2} \tag{3.8}$$

Subsequently, we computed the surface average roughness (R_a) and the root-mean-square roughness (R_q) using Equations 3.7 and 3.8, respectively, at the same simulation time. Since the radius of the samples varies with time due to the number of successful attachments, we observed that increasing the CH_4 partial pressure resulted in an elevated surface roughness (as shown in Table 3.8). We believe this may be attributed to the concentration, which could potentially impede the proper attachment of carbon-containing species on the surface.

Table 3.8.: The surface roughness parameters and the average radius R_{mean} for CH_4 partial pressure profile.

Sample	R_{mean} (nm)	R_a (nm)	R_q (nm)
S6	3.88	1.24	1.51
S4	13.14	1.3	1.63
S3	25.14	1.31	1.69
S1	38.51	1.73	2.22

According to a previous study [226], the dissociative adsorption of CH_4 on Cu(111) is less favorable than that of H_2. This leads to a higher concentration of H adatoms compared to carbon-containing species, as observed in simulations (Figure 3.37). Consequently, most simulations indicate a high concentration of H adatoms, particularly in samples with low CH_4 partial pressure, with a concentration of 4×10^{-4}.

3.5.2. The growth mechanism

The subsequent objectives of this investigation comprise discerning the individual contribution of each reaction towards the graphene growth mechanism, as well as elucidating distinct pathways that lead to the growth of graphene. In order to attain these objectives, a total of 55 reactions obtained from DFT, as presented in Table 3.3, have been integrated into the study, including reactions that were previously not explored in the works of Li et al.[200] and Chen et al.[227].

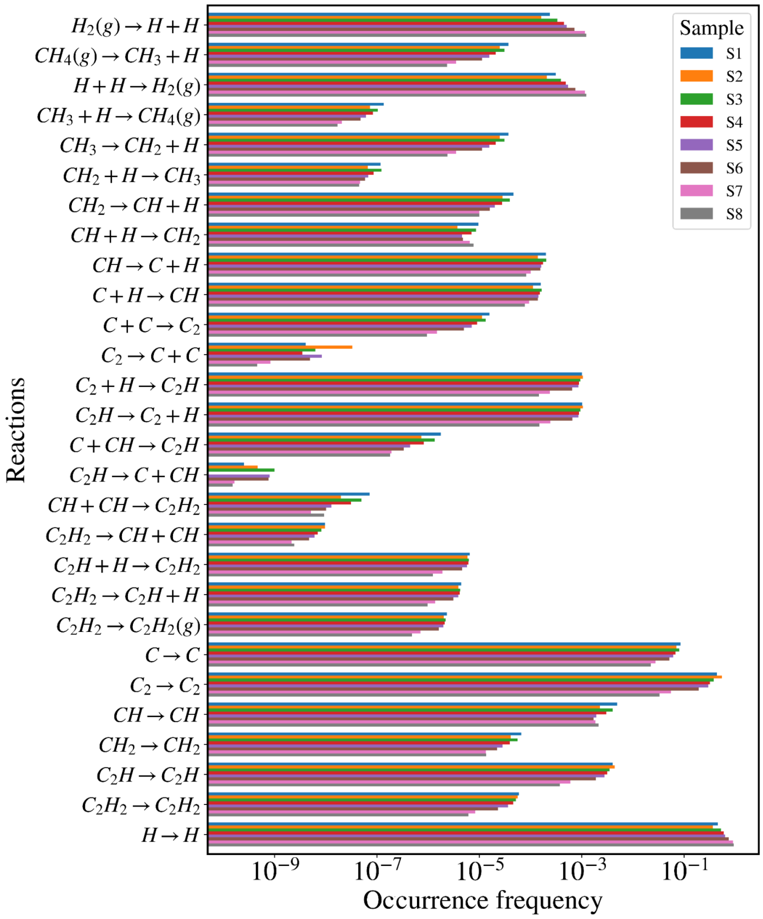

Figure 3.50.: Occurrence frequency of a the first 28 reactions in Table 3.2 (i.e. reaction occurrence per the whole number of reactions) for all samples simulated (listed in Table 3.6).

As the first step, we initiated the analysis by examining the occurrence of reactions in all samples. The occurrence frequency of each specific reaction was defined as the ratio of its occurrence frequency to the total number of occurrences throughout the simulation. The trend of occurrence frequency was found to be consistent across all cases, as evident from Figures 3.50 and 3.51. Nevertheless, minor fluctuations in the prevalence of individual reactions were detected in different partial pressures. These variations are attributable to the influence of partial pressures on the growth mechanism, which has been previously discussed.

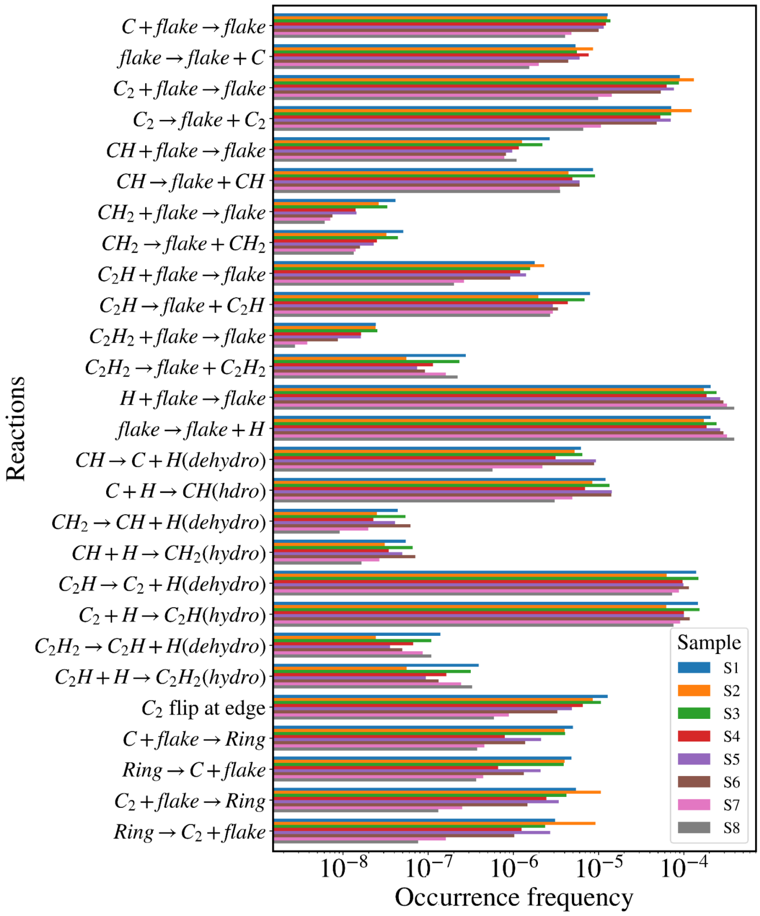

Figure 3.51.: Occurrence frequency of reaction number 29 to 55 in Table 3.2 (i.e. reaction occurrence per the whole number of reactions) for all samples (listed in Table 3.6).

In the next step of our analysis, we directed our focus towards discussing the specific growth pathway by utilizing sample S1 as a representative case, with P_{CH_4} = 100 Torr, P_{H_2} = 0.01 Torr, and T = 1300 K. The reaction occurrence map for this sample, shown in Figure 3.52, illustrates all potential reactions between species through connecting arrows. The direction of the arrows indicates the net contribution direction, with the numerical values on the arrows representing the net contribution (per second per site). The KMC simulation for this sample was conducted for a duration of 0.137 s. H_2 dissociative adsorption and desorption, as well as diffusion of species, are not shown here. The scheme illustrates three primary regions, each comprising distinct groups of reactions. The first group includes reactions between free species, excluding reactions that involve hydrogen adatoms. This group is marked with blue circles in the scheme, while the second and third groups are labeled with green and brown highlights, respectively. The second group encompasses edge attachment reactions, and the third group encompasses growth reactions.

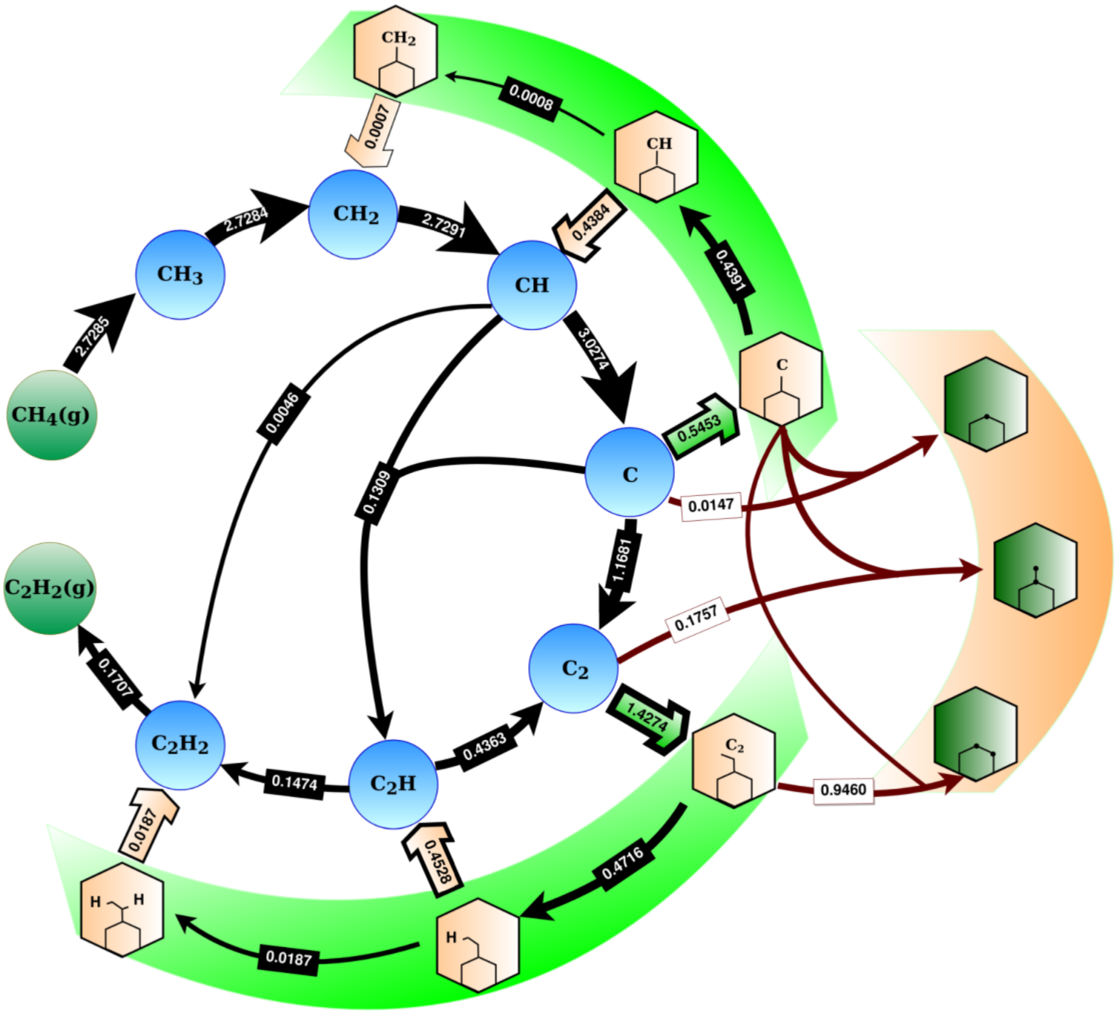

Figure 3.52.: Occurrence map of elementary reactions involved in the graphene growth process on Cu(111) at P_{CH_4} = 100 Torr, P_{H_2} = 0.01 Torr, and T=1300 K conditions (sample S1, see Table 3.6). For 0.138 s, map summarizes the net contributions (per second per site) of the most relevant events over the KMC simulation. Blue and green circles indicate free species on the lattice. Green highlighted regions represent attachment of species to the flake edges, while brown highlighted region shows the hexagon formation via ring closure reactions on the edges. H_2 dissociative adsorption and desorption, as well as diffusion of species, are not shown here. Gas phase species are marked with a "*g*". The possible conversions are shown as the arrows in the direction of the net contribution (forward minus backward occurrences). The numbers on arrows are the net contribution per second per site.

The occurrence map provides a sequence for analyzing the net contribution direction (forward arrows) in detail. Using CH_4 as a precursor, it initially decomposes into CH_3 and CH_2 on the Cu surface, resulting in the formation of CH species (2.7291 events/s/site). Subsequently, CH species can participate in three primary reaction pathways. The first pathway involves decomposition into single carbon atoms (3.0274 events/s/site). The second pathway results in the formation of C_2H species (0.1309 events/s/site), while the third pathway leads to the formation of C_2H_2 species (0.0046 events/s/site). The frequency of each reaction depends on the activation energy barriers of the particular reaction (as shown in Table 3.2) and the concentration of species (as shown in Figure 3.37a). The next most frequent reaction, after the sequence of carbon monomer formation, is the C_2 formation reaction (1.1681 events/s/site) in the free species region. This reaction directly contributes to graphene growth. The carbon monomer also participates in the

C_2H formation reaction (0.1309 events/s/site) and the growth of graphene by attaching to the edge (0.5453 events/s/site) or forming a hexagon (0.0147 events/s/site), as shown in Figure 3.52. In general, the formation of a single carbon atom occurs more frequently than the subsequent C_2 formation (by approximately 721797 times), thereby impacting the concentration of both species during the growth process, considering different pathways from each species (as shown in Figure 3.37).

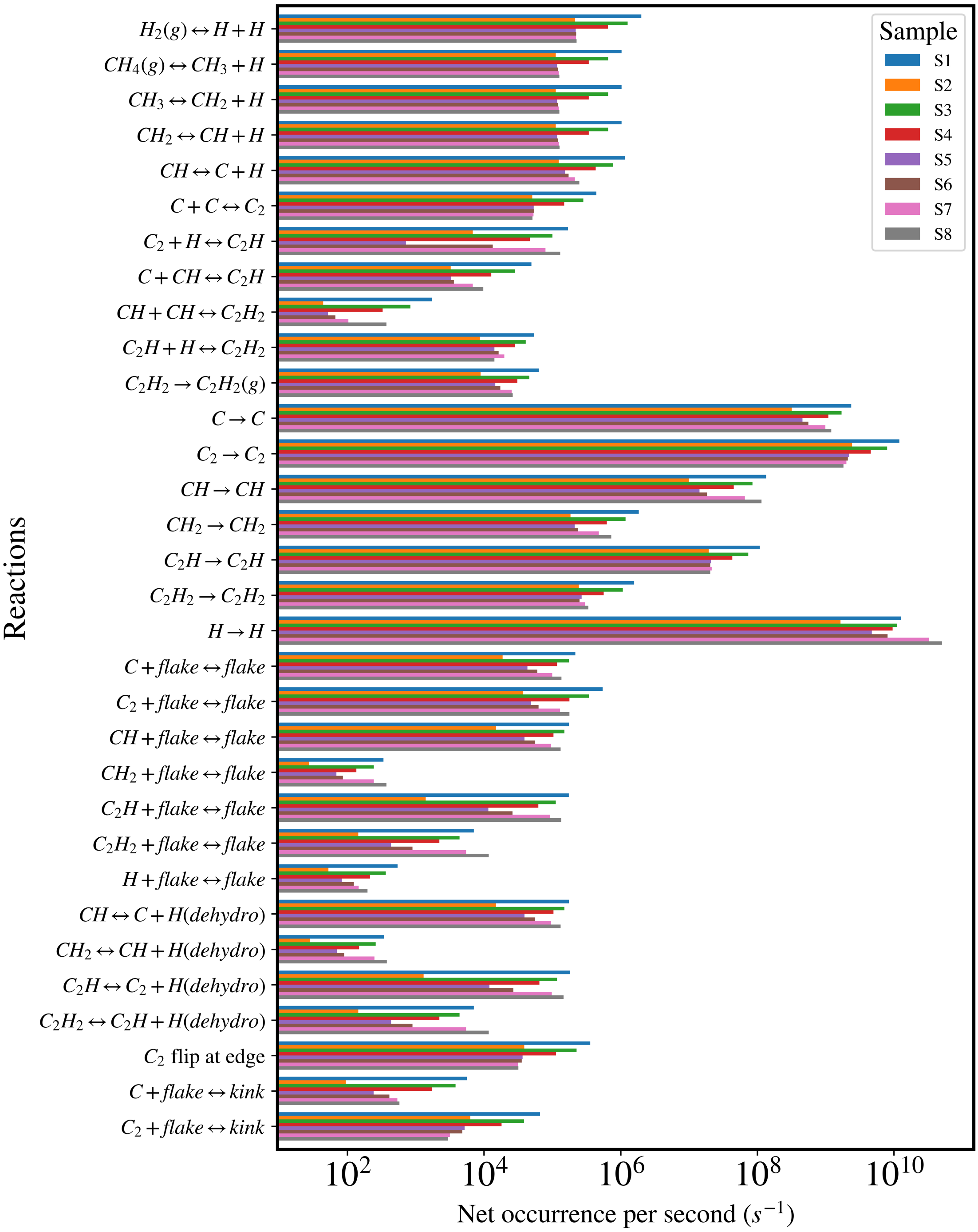

Figure 3.53.: Net occurrence per second for all samples. Numbers are noted in the dominant direction of reactions (positive). Samples are shown in different colors.

Subsequently, the C_2 species undergoes various reactions, including attachment to the

edge with another carbon dimer (1.4274 events/s/site), ring closure reactions (0.1757 events/s/site), and hydrogenation to form C_2H (0.4716 events/s/site). It is worth noting that the contribution of C_2 towards graphene growth is higher than that of the carbon monomer. This highlights the crucial role played by both species in the formation of graphene. Simultaneously, the C_2H species formed decomposes back into C_2 (0.4363 events/s/site), which enhances the content of C_2, and generates C_2H_2 through hydrogenation (0.1474 events/s/site). Finally, C_2H_2 can either desorb from the surface (0.1707 events/s/site) or decompose into CH, while dehydrogenation reactions from the edges also occur (0.0187 events/s). The latter reactions contribute to the final proportion of C_2H_2 desorption.
The net contributions of reactions in the free species region are influenced by reactions occurring on the flake edge, which are highlighted in green in Figure 3.52. The reactions on the edge involve (de)hydrogenation of attached species as well as attachment and detachment of species to the edge (reactions 19 - 29 in Table 3.2). Based on the net contributions, we found that the edge attachments of carbon and its dimer were the most stable, while other attached species were more frequently hydrogenated and detached, as indicated by arrows in Figure 3.52. Furthermore, we observed that the hydrogenation of attached species was more favorable than their dehydrogenation, resulting in a positive net contribution towards hydrogenation at an edge for all attached species (as shown in the green highlighted region in Figure 3.52 and the difference in the occurrence of events). This phenomenon has not been previously reported in the literature. As a consequence, there exists a competition between hydrogenation at the edges and detachment reactions from the edges. The number of events per site in the desorption direction of H_2 is approximately 5.1519 events/s/site. This means that some of the hydrogen adatoms exit the surface, while the remaining species move as free species and participate in other reactions, such as hydrogenation. It is essential to include (de)hydrogenation reactions in the reaction set used in the KMC simulation to investigate the pathways of graphene growth, as the quality of the graphene flake is affected by them. Figure 3.53 provides a detailed analysis of all reactions for samples, presenting a comprehensive representation of all net contributions for the reactions involved. Similarities in reaction pathways towards graphene growth are observed for all samples, as described for sample S1. The net contributions of forming C-containing species, attachment to the edges, and ring closure reactions are higher for samples with higher methane partial pressures (S1, S3, S4 from Table 3.6) than for other samples, due to the higher CH_4 partial pressure.

3.5.3. Hydrogenation reactions

In order to evaluate the effect of (de)hydrogenation on graphene growth, we conducted KMC simulations of samples S1 and S2 at temperatures of 1300 K with and without the (de)hydrogenation reaction set. The two samples had different partial pressures of CH_4 and H_2 (S1 with P_{CH_4} = 100 Torr, P_{H_2} = 0.01 Torr and S2 with P_{CH_4}=10 Torr, P_{H_2}=0.001). We collected data for 0.161 s and 0.936 s of simulation time for samples S1 and S2, respectively, and analyzed three parameters: 1) the ratio of hydrogenated edges to the total number of edges in the flake, 2) the ratio of defects (i.e., vacancies) in the actual flake to a defect-free flake with the same average radius, and 3) the surface roughness and root-mean-square roughness parameters of the graphene flake. Table 3.9 presents the ratio of hydrogenated edges and vacancies for each sample. The results show that the addition of hydrogenation reactions in the simulation of sample S1 leads to approximately 0.96% fewer hydrogenated edges and 2.1% fewer defects (i.e., vacancies) compared to simulations without the (de)hydrogenation reactions. For sample S2, the addition of hydrogenation reactions results in 1.25% more hydrogenated edges and 3.4% more defects (vacancies). This comparison suggests that the quality of graphene is improved in the presence of hydrogenation reactions.

Table 3.9.: The ratio of hydrogenated edges and defects (vacancies) in graphene flake with and without (de)hydrogenation reactions, in percent (samples S1 and S2, respectively). Subscripts 'w' and 'w/o' refer to 'with' and 'without' hydrogenation and dehydrogenation reactions, respectively.

%	$S1_w$	$S1_{w/o}$	$S2_w$	$S2_{w/o}$
Hydrogenated edge	0.44	1.39	0.15	1.38
Vacancy defect	5.7	7.8	6.8	10.2

To analyze the surface roughness of the samples, we used Equations 3.7 and 3.8 to calculate the surface average and mean square roughness values. Additionally, we examined the changes in the radius of the samples over the evaluation length. Figure 3.54 displays the snapshots of the samples under S1 conditions at the same simulation time and presents the roughness profile.

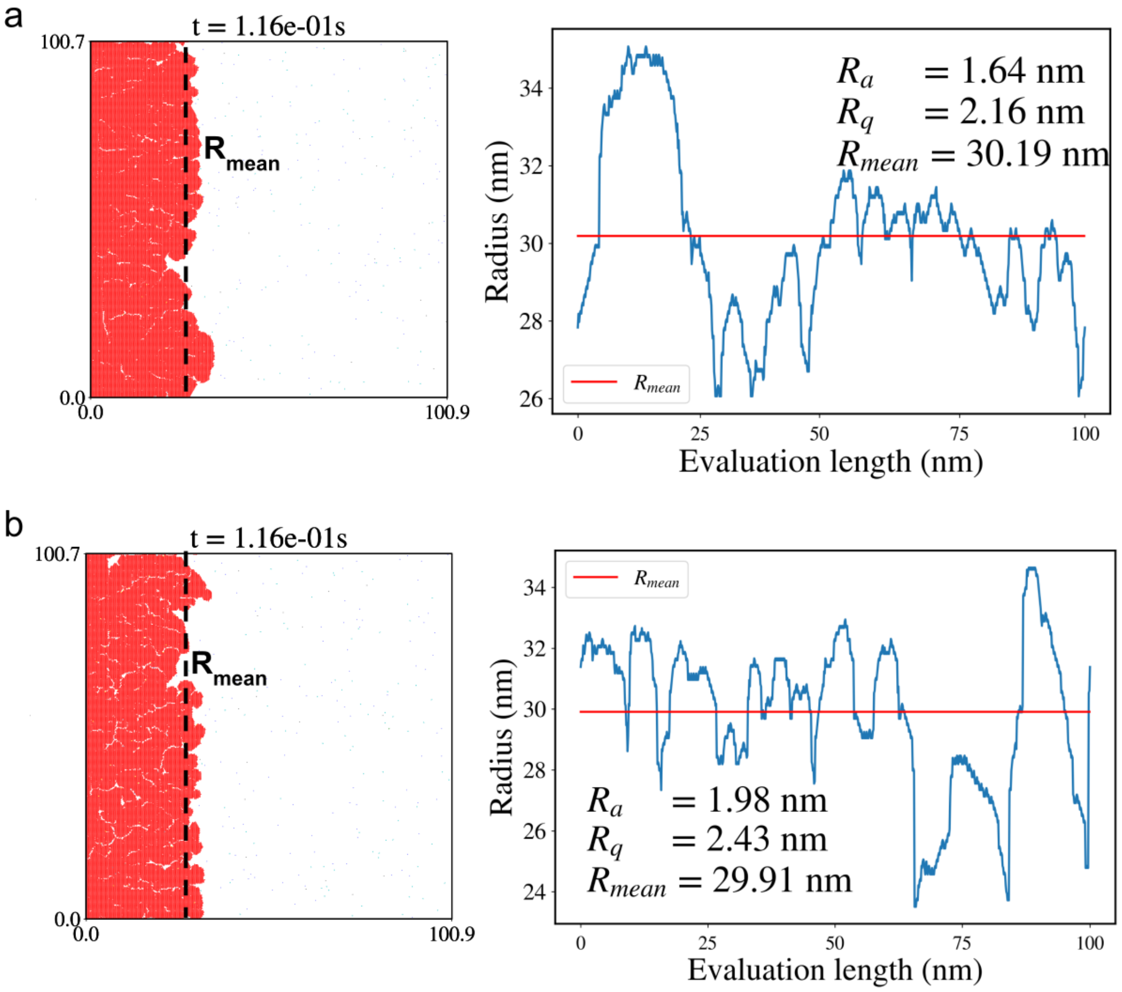

Figure 3.54.: Surface roughness analysis of graphene flake grown in sample S1 (see Table 3.6): a) with and b) without (de)hydrogenation reactions included in the KMC reaction list. The snapshot of the flake at 0.116 s of the simulation (in red) is shown on the left, with a marked mean radius (R_{mean}). On the right, the surface roughness plot as the deviation of radius from the mean radius over evaluation length is shown. The red line represents the mean radius (R_mean), and the blue curve represents the radius over the evaluation length. The average roughness, R_a, the root-mean-square roughness, R_q, and R_{mean} are given in the inset for clarity.

We find that the surface roughness is smaller with added (de)hydrogenation reactions 1.63

nm instead of 1.98 nm). Looking at snapshots in Figure 3.54 a and b, and considering the definition of radius as the distance of each outer layer point from the left axis (see Figure 3.46 for more detail), we characterize the roughness profile as the deviation of radius from the mean radius. The figure indicates how flake radius changes around the mean value. Finally, the visual differences in the grown graphene can be detected by inspecting the simulated layer. At time 0.936 s, sample S2 yielded similar results (see Figure 3.55).Because the partial pressures of CH_4 and H_2 were 10 times lower in this case, it took longer to reach flakes of comparable size. For sample S2, the addition of (de)hydrogenation reactions decreases surface roughness from 2.12 nm to 1.85 nm, simultaneously decreasing the root-mean-square roughness by 0.36 nm. The surface roughness analysis, together with the findings on hydrogenated edges and defects (vacancies) ratios, clearly shows the impact of (de)hydrogenation reactions in the graphene growth, suggesting better quality of the material in the presence of hydrogenation and dehydrogenation on the edges.

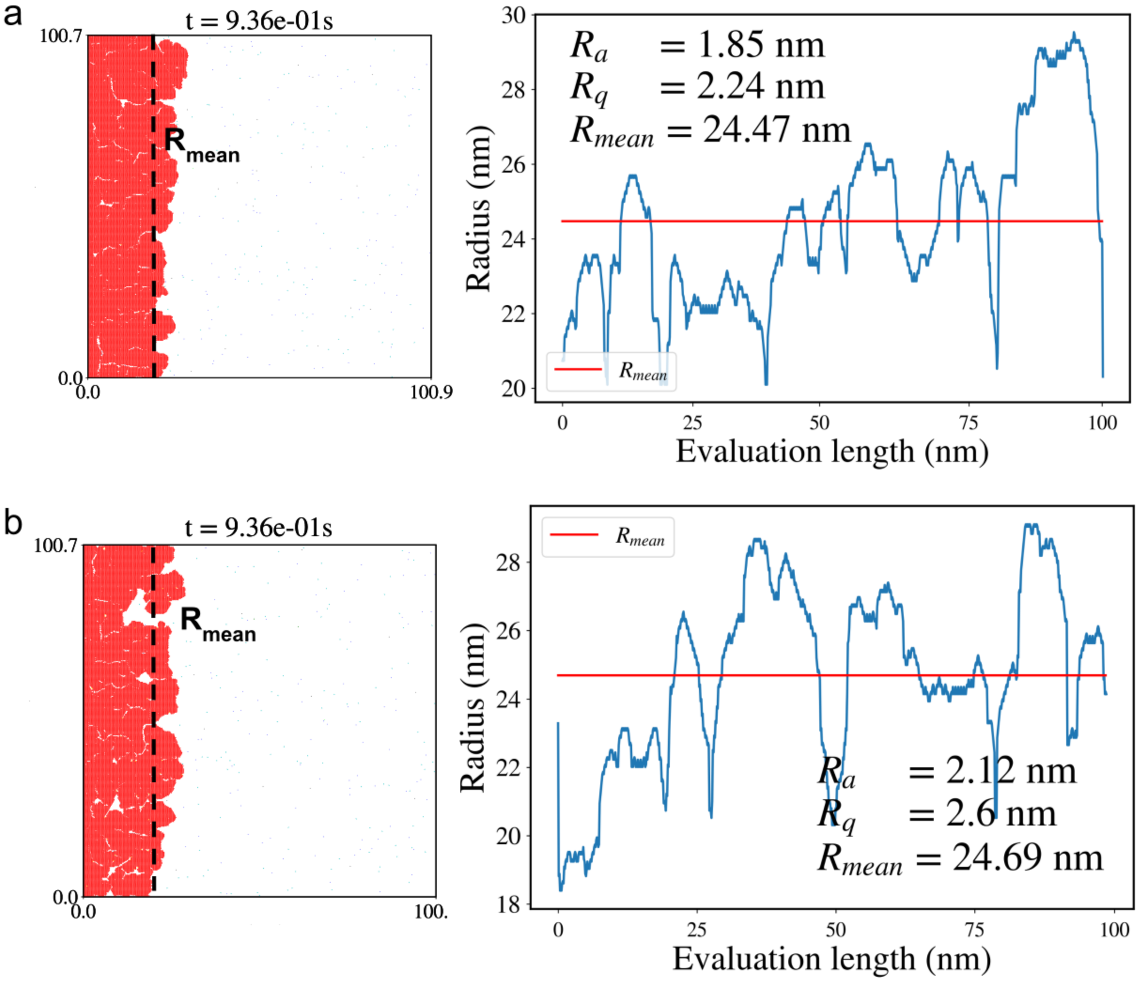

Figure 3.55.: Surface roughness analysis of graphene flake grown in sample S2 (see Table 3.6): a) with and b) without (de)hydrogenation reactions included in the KMC reaction list. The snapshot of the flake at 0.936 s of the simulation (in red) is shown on the left, with a marked mean radius (R_mean). On the right, the surface roughness plot as the deviation of radius from mean radius over evaluation length is shown. The red line represents the mean radius (R_mean), and the blue curve represents the radius over the evaluation length. The average roughness, R_a, the root-mean-square roughness, R_q, and R_{mean} are given in the inset for clarity.

WE defined the ratio of partial pressures of H_2 and CH_4 as $R_p = P_{H2}/P_CH_4$, and calculated this parameter for all samples. The growth rate and radius of the flakes for each sample were plotted against the R$_p$ values, as shown in Figure 3.56. The results indicate that the samples with lower R$_p$ values, namely S1, S3, and S4, which have higher partial pressure of methane, had higher growth rates and larger radii than the other samples. This suggests that these samples required less simulation time to reach the same size as the other samples.

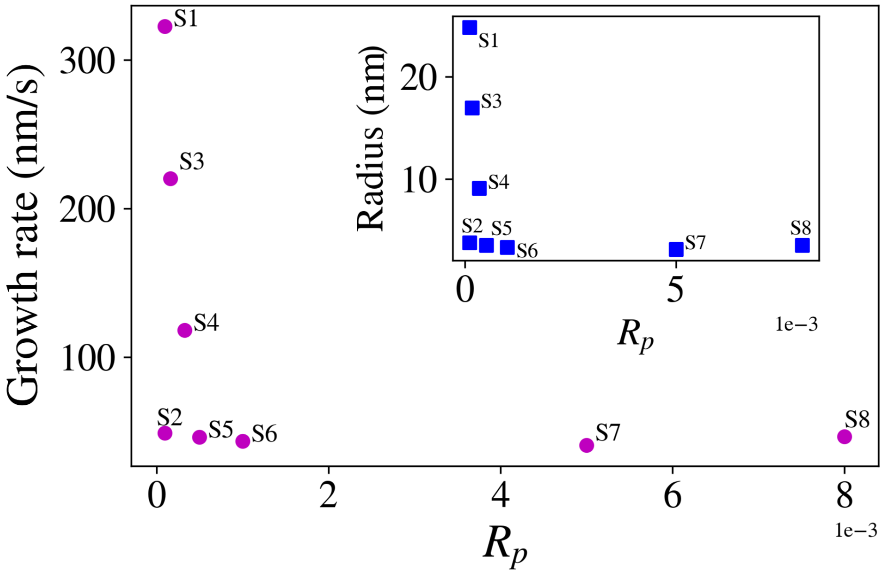

Figure 3.56.: Growth rate parameter and radius of all samples with respect to partial pressure ratio. Samples are marked by their names.

3.6. Conclusions

In this study, we have developed a multiscale model that combines first-principles calculations and the KMC method to investigate graphene chemical vapor deposition (CVD) growth on the Cu(111) surface. The developed model allows for the growth of larger graphene flakes, up to 40 nm, under various CH_4 and H_2 partial pressures and temperatures. This is a significant improvement over previous studies that were only capable of exploring graphene growth and etching with simulated flakes of less than 10 nm[121, 208, 228, 202]. . We have observed that the growth rate (flake radius per time) of all samples depends on the partial pressure of CH_4. In particular, we found that the same ratio of partial pressures of H_2:CH_4 (samples S1 and S2 with H_2:CH_4:10^{-4}) required 10 times higher simulation time to reach the flake size around 26 nm where the CH_4 partial pressure of the sample S1 is 10 times higher. In contrast, the growth rate did not change significantly for the H_2 pressure profile for systems with the same CH_4 partial pressure. The analysis of the CH_4 partial pressure effect on the growth mechanism shows that it acts as the primary CVD control parameter. Increasing the partial pressure of CH_4 (while H_2 partial pressure is fixed) leads to a higher concentration of carbon-containing species on the surface, resulting in a larger graphene flake. We have identified the role of individual reactions during graphene growth and have studied specific pathways of graphene growth. The results show that both the C and C_2 pathways are important for graphene growth, but the C_2 pathway is the dominant feeding species on Cu(111). For the first time, we have demonstrated the impact of hydrogenation and dehydrogenation reactions of species on the graphene edge on the quality of the grown graphene in terms of its surface roughness, hydrogenated sites, and vacancy defects. The developed DFT-based KMC model is based on atomistic reaction parameters and allows for simulation of the growth of nanometer-sized graphene flakes. It provides insights into controlling the growth of graphene in CVD on Cu(111) that may be useful for experimental fabrication of graphene at the relevant temperature and pressure.

4. Developing a Kinetic Monte Carlo model for the growth of Solid Electrolyte Interphase (SEI) in Lithium-Ion Batteries

4.1. Introduction

Lithium-ion batteries (LIBs) have emerged as an effective and reliable technology for energy storage in modern society, and have garnered significant attention due to their safety and efficiency[124, 125, 126]. These batteries can be categorized as either primary (non-rechargeable) or secondary (rechargeable). The typical LIB system consists of two electrodes, the negative electrode (anode) and the positive electrode (cathode), along with a separator and an electrolyte. The anode and cathode electrodes in commercial LIBs are typically composed of active materials combined with a small amount of polymers and conductive carbon additive[229].

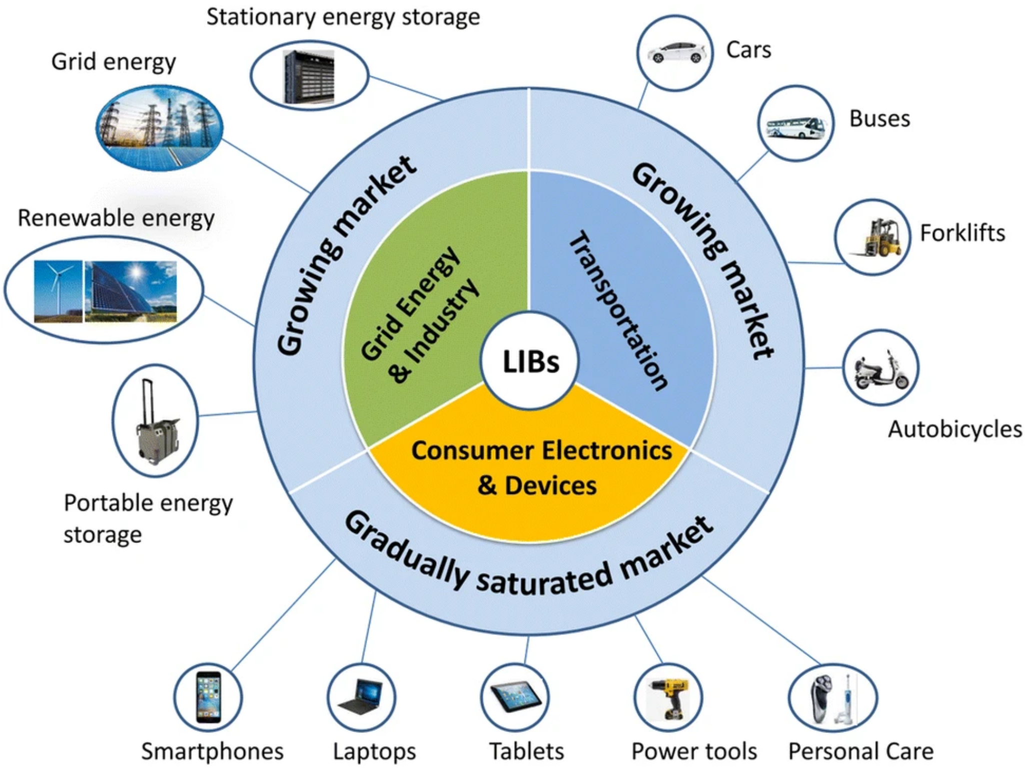

Figure 4.1.: Applications of LIBs in the three main fields as consumer electronics and devices, transportation, as well as grid energy and industry. Reprinted with permission from Ref.[230], 2019, Shanghai University and Periodicals Agency of Shanghai University.

Graphite is the most commonly used material for the anode, while cathode materials are generally metal oxides such as $LiCoO_2$, $LiNiO_2$, $LiMn2O_4$, $LiNiMnCoO_2$, $LiFePO_4$, and $LiNiCoAlO_2$[231]. Electrolytes constitute the third and most important component of LIBs, and can be either a solid polymer or a non-aqueous liquid containing a lithium salt, such as $LiPF_6$, $LiBF_4$, $LiAsF_6$, or $LiClO_4$, dissolved in various solvents such as esters, ethers, or carbonates. The effective voltage of the cell is the difference between the electrochemical potentials of the active materials.

In LIBs, the movement of lithium ions serves as the main mode of charge transfer. These lithium ions can interact with the active materials in the electrodes in three different ways: insertion and de-insertion[232, 233], alloying and de-alloying, and conversion materials. The insertion and de-insertion mechanism, which is also known as intercalation/de-intercalation, is the most commonly used mechanism in commercial applications. This mechanism typically involves transition metal oxide cathodes and graphite anodes. The working principle of a LIB can be explained using Figure 4.2. During the charging cycle, lithium ions are extracted from the cathode (which is the positive electrode) through electrochemical oxidation. These ions then enter the electrolyte and are solvated by the solvent molecules. The solvated lithium ions subsequently migrate to the anode (which is the negative electrode), where they undergo electrochemical reduction. Conversely, during discharging, the lithium ions are extracted from the anode through electrochemical oxidation. The solvated lithium ions then move back to the cathode through migration and enter the cathode through electrochemical reduction. During these processes, electrons flow through an external circuit to the electrode where reduction occurs.

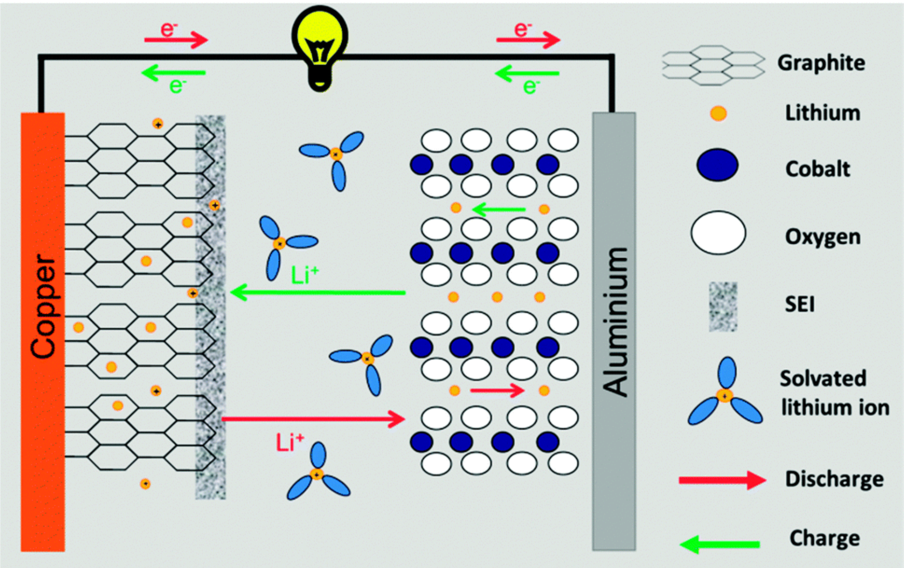

Figure 4.2.: The principle of a lithium ion battery as charge–discharge processes. Graphite (anode), cobalt oxide as cobalt and oxygen (cathode), aluminum, copper foils as current collectors, solid electrolyte interphase (SEI), Li ion, and solvated Li ion are illustrated. Reprinted with permission from Ref.[234], used under Creative Commons CC-BY license.

In LIBs, a solid electrolyte interphase (SEI) is formed at the interface between the negative electrode (anode) and the electrolyte due to the decomposition of the electrolyte. This occurs because the operating potentials of the anode, which are around 0.2V vs. Li^+/Li, fall outside the electrochemical stability window of the electrolyte. To optimize the operation of LIBs, it is crucial to have a deep understanding of the formation, growth, and stability of the SEI layer[235, 236]. Although the reactions at the interfaces are well-understood in terms of the controlling chemistries of the species involved, the mechanism of mesoscale (50

nm) SEI formation and growth remains unknown[237, 238]. The formation of the SEI layer occurs within the first few charging cycles of the battery's operation[127]. The electrolyte used in LIBs typically consists of a lithium salt (such as $LiPF_6$) dissolved in an organic solvent (such as ethylene carbonate (EC)) with an additive[239]. The EC-Li^+ complex is reduced and decomposed on the anode surface in multiple steps, which produces both organic and inorganic SEI components. These products then combine to form the SEI layer. Several studies have focused on the composition and structure of the SEI layer and have demonstrated its critical role in the performance, safety, and lifespan of LIBs[238, 240].
In principle, the process of reduction reactions and the consequent production and aggregation of SEI components, resulting in the formation of a heterogeneous film, could continue indefinitely. However, the growth of SEI up to several layers (with a thickness of hundreds of nanometers) would practically prevent further reduction. This means that the SEI permits the transport of lithium ions while obstructing electrons to prevent further decomposition of the electrolyte and ensure the continuity of electrochemical reactions. The significance of SEI in the lifespan of LIBs is critical, as they are employed in numerous applications. The early-stage inorganic SEI undergoes a dynamic evolution process through autocatalytic hydrolysis of electrolytes, which is initiated by the reduction of trace impurities (e.g., H_2O, HF). This hydrolysis process may result in continuous growth in thickness during cycling, emphasizing the importance of SEI in the long-term performance of LIBs[127, 241, 242, 243][127, 241, 242, 243]. When considering the operation and lifespan of LIBs, the SEI is an essential component. However, despite its importance, the structure, composition, morphology, and growth mechanism of SEI remain unclear and under debate[235, 238, 244]. Recent in-situ technological advancements, such as secondary-ion mass spectroscopy and atomic force microscopy, have allowed for more detailed investigations into the SEI composition and early stage formation[244, 245, 238]. Nevertheless, the application of these techniques to the study of practical battery interfaces, especially over long-term cycling, is still limited due to the high chemical sensitivity of SEI to oxygen and hydrogen and the specific locations of SEI that are not easily accessible using current instruments[246, 247]. The multiscale nature of SEI growth involves different time and length scales.

A significant amount of research has focused on studying the electrochemistry of solvents at the molecular scale to investigate the thermodynamic and kinetic properties at the quantum chemistry level[125, 127]. While these methods have provided insight into various phenomena, such as the positive effects of adding vinylene carbonate (VC) to EC, resulting in better SEI formation[248, 249], the impacts of molecular processes on a larger scale are not well understood. Although molecular dynamics simulations combined with reactive force field methods can study SEI growth on a few nanometer scale[250, 251], their time scale limitations restrict the study's scope of SEI's early-stage formation. For larger time and size scales, many phenomenological models (mostly continuum methods)[252, 253] have been used to explore SEI growth. However, these methods encounter challenges in explaining the apparent paradox of SEI formation growth: electrolyte decomposition requires electrons from the negative electrode (anode). It has been found that the tunneling depth of the electrons into the organic solvent is limited to about 2-3 nanometers[254]. This tunneling depth limitation causes the electrolyte to decompose near the anode surface, where the aggregation of products into an SEI layer is expected to eventually block further SEI formation. This phenomenon, referred to as the "near-shore scenario"[255], can only result in a few nanometers of SEI thickness. Experiments have shown that while inorganic SEI has a similar thickness, organic SEI can grow up to 50-100 nanometers[256, 257]. As continuum models fail to capture the local structure of the SEI, different hypotheses have been proposed to address the SEI growth paradox. One of the approaches is to consider SEI as a porous material, and new layers can grow through the pores of formed SEI layers[258, 130, 259, 260]. However, this method only relocates the SEI formed near the anode to the pores, eventually blocking them and ending further SEI growth at a nanoscale. Other studies have suggested that SEI is electronically conductive, but the microscopic nature of this conduction is unclear due to the insulating nature of the electrolyte products' degradation that forms the organic SEI[259, 261, 262]. Therefore, the SEI's growth mechanism on the mesoscale, which is not yet fully understood, has a significant impact on its properties and mechanical stability, limiting the lifetime, performance, and safety of LIBs. In this chapter, we have developed a comprehensive model to investigate the growth of the SEI in LIBs. The model is based on the specific features of the microscopic processes that lead to SEI formation and employs a bottom-up multiscale approach. We use a DFT-based kinetic Monte Carlo (KMC) method that consists of a list of reaction rates and a protocol capable of handling them. The developed model allows exploring the SEI growth mechanism in a mesoscopic system with molecular resolution using reaction rates obtained from quantum chemical calculations. In order to avoid a systematic uncertainty caused by transferring molecular information to the mesoscale in the result of the simulations at the mesoscopic level, we generate over 50000 sets of parameters (activation energy barriers) to systematically study the spatiotemporal evolution of SEI organic and inorganic components controlled by a series of chemical reactions, diffusion, and aggregation with nanometer resolution while considering kinetic information calculated for specific electrolyte-anode chemistries. We perform KMC simulations for each set of conditions and barriers, resulting in three distinct regions identified by different compositions of organic and inorganic components: inorganic-only, bad, and good SEI regions, where the first region includes samples with mostly organic SEI layers, the second one contains a very thin, porous, and often discontinuous organic layer, and the last region contains a thick, continuous organic layer. Focusing on the last (good SEI) region, we realized that SEI forms via a solution-mediated pathway, in which the SEI precursors nucleate far from the anode surface and then grow rapidly. We analyze the results to identify the key reactions that contribute to the nucleation and growth mechanisms, enabling us to determine the composition and properties of the SEI.

4.2. Reaction network

As an initial step of our investigation, we compile a comprehensive catalog of reactions that participate in the SEI growth process (Table 4.2). It is known that the molecular constituents of the SEI arise from two consecutive electron reduction reactions involving EC molecules that coordinate with Li^+ ions[263, 264]. Considering that EC-Li^+ serves as an active medium for Li diffusion in a solvent-mediated pathway, and the SEI constituents are electronically insulating, the reduction reactions can only transpire in regions near the electrode where free electrons are available, i.e., within a narrow band of approximately 4 nm (layers) from the electrode surface.

$$Electrode\,(surf) + EC - Li^{+} \rightarrow C_2H_4OCOOLi \tag{reaction 1}$$

Following the initial electron reduction reaction of EC molecules coordinated with Li^+ ions, a subsequent reduction reaction occurs near the electrode surface that converts the first reaction product, $C_2H_4OCOOLi$, into an inorganic component of the SEI, Li_2CO_3. This transformation is limited to a narrow region within 4 nm of the anode surface where electrons are available to drive the reaction.

$$Electrode\,(surf) + C_2H_4OCOOLi + Li^{+} \rightarrow Li_2CO_3 + C_2H_4 \uparrow \tag{reaction 2}$$

In the developed model, we neglect the presence of the gas that is generated during the SEI growth process as it diffuses rapidly and exits the simulation box. Once the Li_2CO_3 compound is formed at the anode surface through the second electron reduction reaction, it immediately starts to aggregate. Since the reaction requires the availability of electrons, the formation of a layer of inorganic SEI can only occur within a distance of 4 nm from the anode surface. This implies that any further electron reductions that take place adjacent to the Li_2CO_3 compound can only happen within the vicinity of the anode surface, and not beyond the 4 nm threshold, through the third reaction:

$$Li_2CO_3\ (surf) + EC - Li^+ \rightarrow C_2H_4OCOOLi \qquad \text{(reaction 3)}$$

In addition to Li_2CO_3, the other molecules produced during SEI formation are capable of diffusing in solution, allowing for further reactions to occur between them as outlined in Table 4.2. Specifically, in reaction 4, two $C_2H_4OCOOLi$ molecules react and produce dilithium ethylene dicarbonate (Li_2EDC), which serves as the organic component of the SEI.

$$C_2H_4OCOOLi + C_2H_4OCOOLi \rightarrow Li_2EDC + C_2H_4 \uparrow \qquad \text{(reaction 4)}$$

In order to simulate the formation of SEI through its organic components, we adopt a two-step approach. Firstly, we consider the dimerization of two Li_2EDC molecules, which leads to the formation of a dimeric species (reaction 5). Secondly, we take into account the clustering of three or more Li_2EDC molecules to form a "SEI cluster", which is a significant constituent of the organic SEI (reactions 6, 8, and 10). According to our observations, we have found that the second electron reduction reaction can produce Li_2CO_3 in proximity to the anode surface, even within 4 nm, and also on top of the previously formed Li_2CO_3 when $C_2H_4OCOOLi$ molecules are present in the vicinity.

$$Li_2EDC + Li_2EDC \rightarrow (Li_2EDC)_2 \qquad \text{(reaction 5)}$$

$$(Li_2EDC)_2 + Li_2EDC \rightarrow SEI\ cluster \qquad \text{(reaction 6)}$$

$$Li_2CO_3(surf) + C_2H_4OCOOLi + Li^+ \rightarrow Li_2CO_3 + C_2H_4 \uparrow \qquad \text{(reaction 7)}$$

$$Li_2EDC + SEI\ cluster \rightarrow SEI\ cluster \qquad \text{(reaction 8)}$$

$$(Li_2EDC)_2 + SEI\ cluster \rightarrow SEI\ cluster \qquad \text{(reaction 9)}$$

$$(Li_2EDC)_2 + (Li_2EDC)_2 \rightarrow SEI\ cluster \qquad \text{(reaction 10)}$$

$$SEI\ cluster + SEI\ cluster \rightarrow SEI\ cluster \qquad \text{(reaction 11)}$$

In addition to the eleven irreversible reactions that we have investigated in this study, there are two other types of reactions that we have defined for the movable components in the system. The first type is diffusion, which involves the exchange of sites on the lattice. The second type is the irreversible escape of movable components from the simulation box once they reach the top layer, which we refer to as the absorbing boundary. These additional reactions are listed in Table 4.2 as reactions 12 to 19. Material losses that diffuse across the absorbing boundary account for electrolyte decomposition products that do not form organic or inorganic SEI and can have an impact on the overall mass balance of the battery. Moreover, SEI clusters have the potential to attach to each other and form larger clusters, as demonstrated in reaction 11.

4.3. KMC model implementation

After gathering a list of reactions, the present section outlines the methodology of the model by elucidating the requisite aspects, namely the construction of the lattice, calculation of rates, and implementation of the KMC protocol, in a comprehensive manner.

4.3.1. Lattice configuration and rate used in KMC simulation

4.3.1.1. Lattice construction

As part of the lattice construction process, we create a 2D square lattice with dimensions of 50×50 nm^2, where each molecule is represented by a lattice point. The lattice is designed such that every point is surrounded by at most four neighboring points, as shown in Figure 4.3, with red points representing the species of interest, and blue points representing their neighboring points. It should be noted that the nearest neighboring assumption used in the construction of the lattice applies only to individual lattice points, while clusters or pairs of molecules, as depicted in Figure 4.3, may have different numbers of neighboring points.

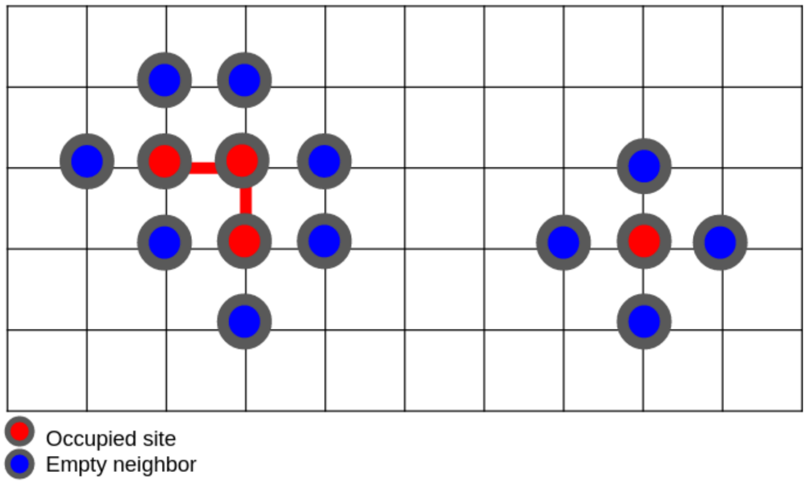

Figure 4.3.: Neighboring role in 2D square lattice. At the right hand side, a single species is in red with four neighbors in blue, and a three-component cluster is in red with seven neighbors marked in blue. Reprinted with permission from Ref.[265], Copyright 2023, Advanced Energy Materials, under the Creative Commons CC-BY-NC license.

As part of the modeling process, we generate a site class by converting each point on the lattice into an object. This object contains various information about the point, such as its coordinate, the molecule that occupies it, and the indices of any neighboring pairs or clusters. Additionally, it includes the indices of its nearest neighbors and its occupation status. A detailed breakdown of this information can be found in Table 4.1.

Table 4.1.: Site class structure. The attributes of the class assigned to each point on the square lattice are listed.

Coordinate	Coordinate of lattice point as a (x, y) pairs.
Molecule	Name of the molecule located at the lattice point (empty for not occupied sites).
Bond	Index of aggregated molecules sites according to the lattice indexing format.
Neighbors	Indices of neighboring sites according to the lattice indexing format.
Status	**True** for occupied site. **False** for empty site.

The site object can be constructed as:

$$(x, y) \Longrightarrow site(Coordinate\,(x, y),\ Molecule,\ Bond,\ Neighbours,\ Status)$$

With this, the square lattice can be converted to a list of site objects, which makes the KMC protocol implementation straightforward.

4.3.1.2. Rates used in KMC simulations

In order to model the formation and growth characteristics of SEI, we compiled a list of reactions, along with their activation barriers and rates, as shown in Table 4.2, which was collected from various literature sources[266, 267, 268]. The activation energy barriers were taken from reported values and not calculated by us since the aim of this study was not to simulate idealistic conditions. Calculating these barriers under different conditions may not provide a perfect reaction barrier that is actually relevant for the system. Due to assumptions made in DFT calculations that may not be true for the system, we opted to randomly generate activation energy barriers based on the literature list (Table 4.2) to explore the parameter space of different conditions (further details on the random generation process will be discussed in section 4.3.2.3 of this chapter). The reaction rate for each reaction was calculated based on the transition state theory (TST)[269].

$$r(E_b,\, T) = ke^{(-E_b/k_B T)} \tag{4.1}$$

where, k is the frequency of atomic vibration, denoted as k, has a value of 6.25×10^{12} s^{-1}, The energy barrier for the reaction is represented by E_b, k_B is the Boltzmann constant, and T is the temperature. The reaction rates are computed using Equation 4.1 with the activation energy barriers provided in the reaction network.

Table 4.2.: All reactions are involved in the KMC simulation to understand the formation and growth of the SEI. The initial rates for the reactions are collected from the literature. The rates for nucleations are chosen based on the successful execution of the KMC simulations. Diffusion rates are chosen based on the modified Wilke-Chang equation. Dimerization and cluster formation are nucleation-driven processes with typical barriers of 0.4 eV and 0.3 eV. Reprinted with permission from Ref.[265], Copyright 2023, Advanced Energy Materials, under the Creative Commons CC-BY-NC license.

4mm

Entry	**Reactants**	**Products**	**Reaction barrier**	**Rate**(s^{-1})
1	Electrode (surf) + EC-Li^+	$C_2H_4OCOOLi$	0.22 eV[266]	1.26×10^9
2	Electrode (surf) + $C_2H_4OCOOLi$ + Li^+	Li_2CO_3 + C_2H_4 ↑	0.5 eV[266]	2.49×10^4
3	Li_2CO_3 (surf) + EC-Li^+	$C_2H_4OCOOLi$	0.22 eV[266]	1.26×10^9
4	$C_2H_4OCOOLi$ + $C_2H_4OCOOLi$	Li_2EDC + C_2H_4 ↑	0.2 eV[267]	2.73×10^9
5	Li_2EDC + Li_2EDC	$(Li_2EDC)_2$	0.4 eV	1.19×10^6
6	$(Li_2EDC)_2$ + Li_2EDC	SEI cluster	0.3 eV	5.7×10^7
7	Li_2CO_3 (surf) + $C_2H_4OCOOLi$ + Li^+	Li_2CO_3 + C_2H_4 ↑	0.5 eV[266]	2.49×10^4
8	Li_2EDC + SEI cluster	SEI cluster	0.3 eV	5.7×10^7
9	$(Li_2EDC)_2$ + SEI cluster	SEI cluster	0.3 eV	5.7×10^7
10	$(Li_2EDC)_2$ + $(Li_2EDC)_2$	SEI Cluster	0.3 eV	5.7×10^7
11	SEI cluster + SEI cluster	SEI cluster	0.3 eV	$5.7\text{-} \times 10^7$
12	$(Li_2EDC)_2$	Diffusion	1/3 diff rate $C_2H_4OCOOLi$	3.01×10^{11}
13	Li_2EDC	Diffusion	1/2.3 diff rate $C_2H_4OCOOLi$	3.9×10^{11}
14	$C_2H_4OCOOLi$	Diffusion	0.05 eV[268]	9.04×10^{11}
15	SEI cluster	Diffusion	0.3 eV[268]	5.7×10^7
16	$C_2H_4OCOOLi$	Out	0.01 eV[268]	4.25×10^{12}
17	$(Li_2EDC)_2$	Out	0.01 eV[268]	4.25×10^{12}
18	SEI cluster	Out	0.01 eV[268]	4.25×10^{12}
19	Li_2EDC	Out	0.01 eV[268]	4.25×10^{12}

Regarding the architecture of the model utilized in this study, we established an event class to generate objects from reactions, comprising the pertinent details of the reaction and data concerning the location on the lattice where the reaction could occur. The attributes of the event class, such as reactants, products, activation energy barrier, rate constant, and local information of the specific reaction, are listed in Table 4.3. We used this class to develop a reference reaction list consisting of 19 event objects for the KMC model.

Table 4.3.: Event object structure.

Reactant	Reaction's reactants
Product	Reaction's products
Barrier	Activation energy barrier of the reaction
Rate	Rate constant of the reaction
Reaction info	All involved species data and the reaction index

According to the Table 4.3, each event object in general can be constructed as:

$$reaction \Longrightarrow event(Reactant,\ Product,\ Barrier,\ Rate,\ Reaction\,info)$$

After creating the lists of reaction and lattice point objects, the subsequent section describes the development of the KMC algorithm.

4.3.2. KMC algorithm development

We developed a 2D KMC method to model the formation and growth of SEI on a nanoscale level over timescales of hundreds of microseconds. KMC algorithms have been widely used to simulate the mesoscopic growth of materials, as explained in Chapter 2. To develop our KMC model, we used site and event classes that were defined in previous sections. We discretized space based on the size of the molecular components, such as Li_2EDC, Li_2CO_3, and $C_2H_4OCOOLi$, which are approximately 1 nanometer in size. We ran simulations on 50×50 nm^2 square lattices, with the negative electrode (anode) and absorbing boundary modeled at the down and up edges, respectively. If any mobile component passes through the absorbing boundary via diffusion and leaves the lattice, it cannot return, indicating an irreversible reaction. Lattice sites represent either a solvent-Li complex (EC-Li^+) or the result of a reaction between adjacent sites, which could be a pair or an agglomeration of three or more molecules, as shown in Table 4.2. We applied the simulation using a rejection-free Kinetic Monte Carlo (rfKMC) model, known as the Bortz-Kalos-Lebowitz (BKL) algorithm[270], which will be explained in more detail in the following section.

4.3.2.1. KMC algorithm

The developed KMC algorithm includes the following steps:

1. Generate the lattice from the list of site objects considering the electrode layer at the bottom and the absorbing layer at the top;
2. Set the simulation time to zero (t=0);
3. Traverse the lattice to collect possible reactions;
4. Calculate the cumulative rate of the collected reaction list using their rates as;

$$k_{tot} = \sum_{p=1}^{n} k_p$$

5. Generate a random number as $r_1 \in [0,1)$ to select q^{th} process that satisfies the following condition;

$$\sum_{p=1}^{q} k_p \geq r_1 k_{tot} \geq \sum_{p=1}^{q-1} k_p$$

6. Execute the selected reaction and update the lattice configuration based on the type of the chosen reaction;
7. Generate a random number $r_2 \in [0,1)$ and advance the system's real time as follows;

$$t \to t - \frac{ln(r_2)}{k_{tot}}$$

8. Iterate the procedure from step 2 to 6 until the system reaches its steady state or until a desired time or step is achieved.

Here, k_p is the rate for the p^{t}h process, r_1 and r_2 are uniformly distributed random numbers in the unit interval, and k_{tot} is the cumulative rate of reactions. A general schematic of the KMC algorithm is shown in Figure 4.4.

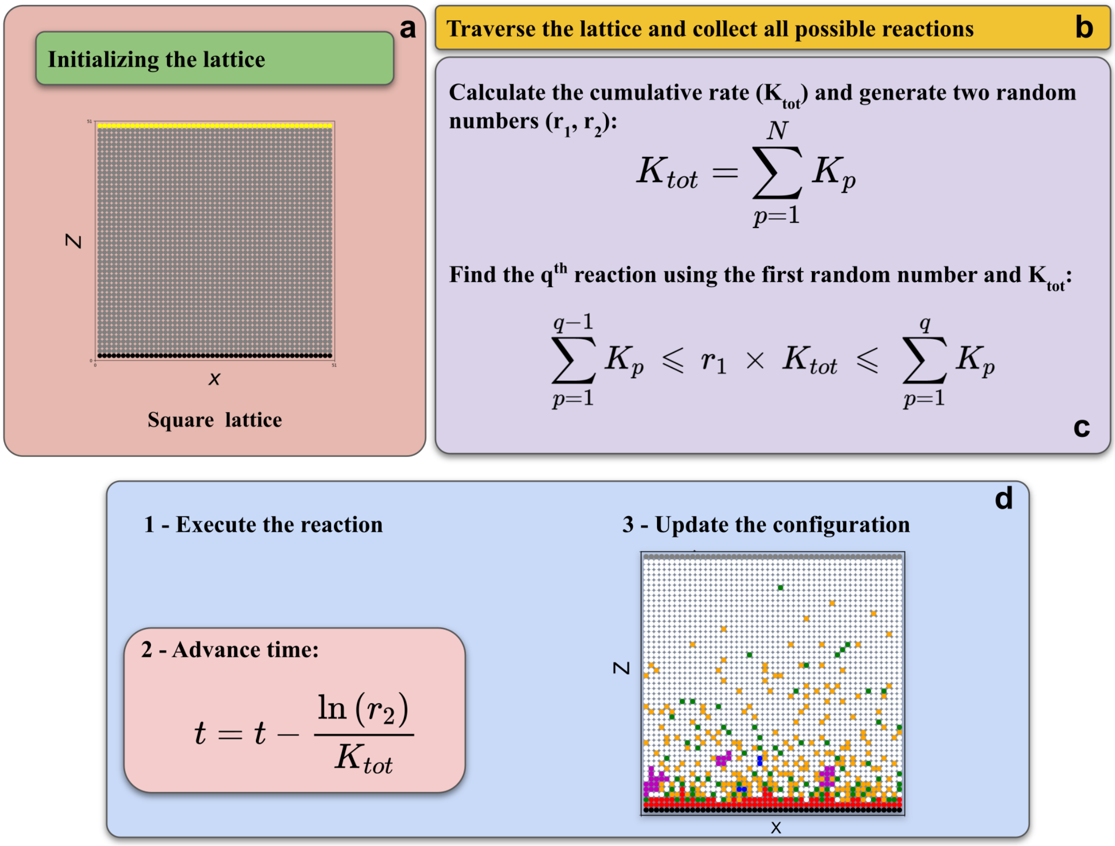

Figure 4.4.: Schematic depiction of the 2D KMC algorithm for the formation and growth of the SEI on the graphite electrode surface. a) initializing the square lattice , b) collecting all possible reactions traversing the lattice, c) generating two random numbers, selecting a reaction following the KMC selection criteria, and 4) executing the selected reaction, updating the simulation time and the lattice configuration. Here, r_1, r_2 are random numbers, K_p is the rate for the p^{th} reaction, and K_{tot} is the cumulative rate over all possible reactions at each step. Reprinted with permission from Ref.[265], Copyright 2023, Advanced Energy Materials, under the Creative Commons CC-BY-NC license.

In the course of KMC simulations, the problem of disparity arises, which is described in detail in Chapter2, section 2.7. This occurs because the reaction list contains several processes with much higher reaction rates than the remaining ones, as seen in Table 4.2. In order to address this issue, we utilized the manual scaling approach among the suggested solutions to modify the original list in Table 4.2, and utilized the modified list to produce samples. Nevertheless, the simulation time is contingent on the reaction rates, and most simulations required up to 30 CPU minutes on a single core. The computational expense of the simulation is influenced by the size of the lattice and the rates. For the same rate list, altering the lattice size from 50×50 nm^2 to 100×100 nm^2 increases CPU time from 30 minutes to several hours.

4.3.2.2. SEI observables

To be able to investigate the impact of activation energy barriers on the growth of SEI and its composition, we have identified three observables that can be computed from the data collected during KMC simulations. The simulation involves different components, which can be distinguished by their specific coloring styles, as shown in the last column of Table 4.2. As a result, the SEI properties can be measured as post-processing parameters, using the final configuration of the system where only organic (purple) and inorganic (red) SEI components remain on the lattice. Figure 4.5 provides an illustration of the final configuration of a KMC simulation, where the black lattice points represent the electrode and the red and purple lattice points represent inorganic and organic SEI components, respectively. The computational approach enables us to investigate the impact of varying activation energy barriers on the SEI growth and composition, using these three observables.

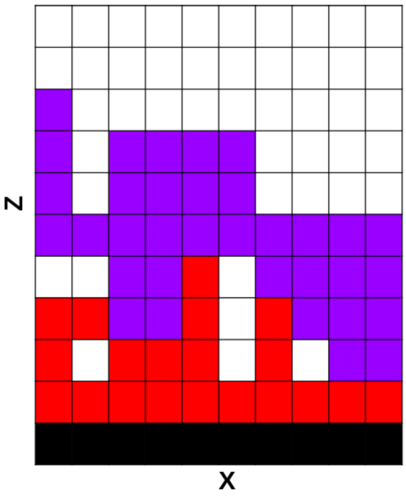

Figure 4.5.: A sketch of the last configuration of a KMC simulation. Electrode and SEI organic and inorganic components are shown in black, purple, and red, respectively. Reprinted with permission from Ref.[265], Copyright 2023, Advanced Energy Materials, under the Creative Commons CC-BY-NC license.

The volume fraction is defined as the fraction of SEI components over layers (Z direction):

$$Volume\,fraction = \sum_{z=1}^{n} SEI(fraction_z) \tag{4.2}$$

Where:

$$SEI(fraction_z) = \frac{The\,number\,of\,organic\,and\,inorganic\,SEI\,at\,layer\,Z}{X\,dimension} \tag{4.3}$$

For the sample configuration volume fraction is 5.4.
The second SEI observable was thickness, which is defined as the SEI average height over the X-axis (electrode) as:

$$Thickness = \frac{\sum_{n=1}^{X\,dim} H_n}{X\ dimension} \tag{4.4}$$

where, H denotes the maximum SEI height at each x on the surface.The thickness of the sample configuration is 6.1.
The last observable, porosity, is defined as the fraction of empty lattice points under the area of (volume fraction × xdim) as:

$$Porosity = \frac{Empty\,lattice\,points}{volume\,fraction \times X\ dimension} \tag{4.5}$$

For the sample configuration, porosity is 0.12.

4.3.2.3. Simulation samples

Following the manual scaling of activation energy barriers for a single simulation, we implemented a sampling technique to generate 50000 samples as lists of activation energy barriers to explore the parameter space for the study's main objective. The statistical method employed in this study was the Latin hypercube sampling (LHS), which enables the sampling of probable collections of parameter values from a multidimensional distribution[271, 272, 273, 274, 275]. The LHS sampling scheme involves dividing the range of each variable into equally probable intervals and placing M sample points to satisfy the Latin hypercube requirements, where M is the number of divisions for each variable. The number of samples required does not increase with the number of dimensions, making this sampling scheme independent of dimensionality. Moreover, random samples can be taken one at a time, making this approach efficient. We used the pyDOE Python package[276] to implement the LHS approach (see Appendix B for more details), and we generated a random activation barrier list for 50000 samples. Each sample comprises a list of activation energy barriers that mimic a broad range of conditions and the assumptions of DFT calculations. We excluded the last four reactions from Table 4.2, which involve escaping the simulation box via passing the absorbing layer, and kept their activation energy fixed for all samples due to their fast reaction rates. However, we included the activation energy barriers of all the other 15 reactions in the sampling approach.

4.4. Results and Discussion

In the developed model, the process space of SEI formation is defined by a set of activation energy barriers, which constitutes a fifteen-dimensional process space vector (PSV). To obtain a list of activation energy barriers, we gathered data from existing literature sources[266, 267, 268]. However, because our model involves certain approximations, there is inherent uncertainty in the parameter values used in the mesoscopic model. Therefore, the initial values presented in Table 4.2 serve as an approximation of the PSV that represents the growth of SEI in any real system. Since the actual PSV for a given system is not known, we employed a sampling method (described in Section 4.3.2.3) to generate PSVs based on the initial values, thereby systematically exploring the PSV space in a domain near the approximate PSV. This approach enables us to investigate the properties and kinetics of the resulting SEI by analyzing the spatio-temporal models generated by each PSV.

4.4.1. SEI growth in a model system

Prior to discussing the potential SEI growth regimes and gaining a deeper understanding of SEI growth, it is beneficial to analyze the spatio-temporal progression of a single PSV to demonstrate the formation and growth of the SEI. Figure 4.6 displays six diverse snapshots of the simulation for a representative PSV (sample number 30407) at various points in the simulation time (rates are outlined in Table4.4). It should be noted that these times are relative and not absolute.

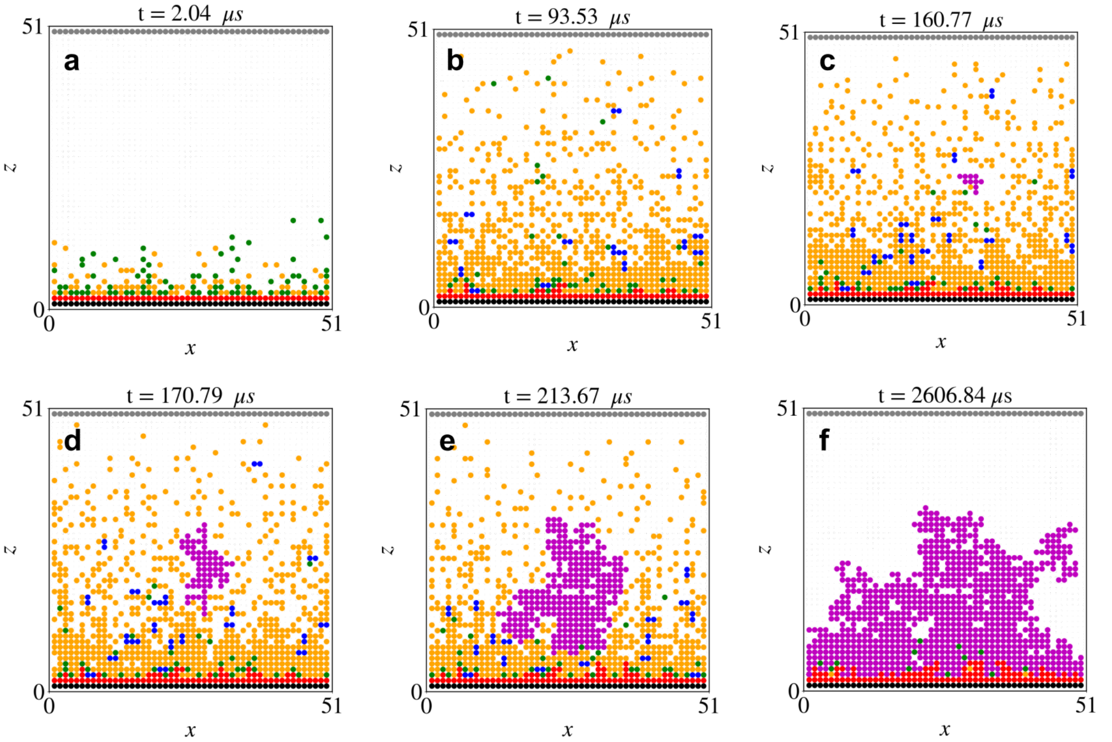

Figure 4.6.: Different KMC simulation snapshots (50 × 50 nm^2) for the representative PSV at the indicated time. In the simulation box, the graphite electrode layer is implemented at the bottom (black), with the absorbing open interface at the top. Initially, all other sites are occupied by EC-Li^+ (white), the precursor for the SEI formation at the start of the simulation. The reaction intermediates and products, namely Li_2CO_3, $C_2H_4OCOOLi$, Li_2EDC, $(Li_2EDC)_2$, and organic SEI clusters are represented by red, green, orange, blue, and purple sites, respectively (see Table 4.2). During the simulation, a) $C_2H_4OCOOLi$ (green) and Li_2EDC (orange) rapidly form a stable inorganic SEI layer (red), and b) Li_2EDC (orange) dimerized to form $(Li_2EDC)_2$ (blue). SEI clusters (purple) start to grow (c-e) away from the electrode presence of $(Li_2EDC)_2$ and Li_2EDC, and the organic SEI is deposited (f) on the inorganic SEI to form porous, immovable SEI. Reprinted with permission from Ref.[265], Copyright 2023, Advanced Energy Materials, under the Creative Commons CC-BY-NC license.

At the commencement of the simulation (4.6 a), the first electron reduction reaction of EC-Li^+ transpires next to the electrode surface (black), generating $C_2H_4OCOOLi$ (green), which is a mobile intermediate component. This intermediate component can either react in proximity to the electrode or diffuse away, enabling it to participate in another reaction. The latter reaction is identified as the "second electron reduction", in which $C_2H_4OCOOLi$ (green) converts to Li_2CO_3 (red) in the presence of electrons supplied by the electrode. The appearance of the inorganic SEI component, Li_2CO_3 (red), is first detected around 2 μs of simulation time in the presence of excess Li^+.

In view of the slow rate of dimerization, the process of Li-EDC (blue) formation occurs at a slow pace. Based on the spatio-temporal panel, a large number of intermediate components, $C_2H_4OCOOLi$ (green), are transformed into Li_2EDC (orange) and a few dimers $(Li_2EDC)_2$ (blue) around 94 μs (Figure 4.6b). Since electron reduction reactions require electrons to occur, all intermediate components ($C_2H_4OCOOLi$ (green)) must be produced close to the electrode and then diffuse around to participate in other possible reactions. Hence, owing to their high diffusion rate, these SEI precursors move far away from the electrode and distribute almost uniformly in the simulation box; some even escape the box through the absorbing boundary at the top. For this PSV, the escape ratio of $C_2H_4OCOOLi$ (green) is 37%, meaning only 63% of the precursors remain inside the simulation box and participate in the nucleation, aggregation, and deposition. Around 160 μs into the simulation for the representative PSV, the first SEI cluster (purple) is observed to form via the aggregation of two dimers ($(Li_2EDC)_2$, blue). Interestingly, the first nucleation event occurs far from the electrode surface, at a distance of approximately 23 nm, indicating that the SEI growth mechanism is likely solution-mediated. The formation of the initial SEI cluster (purple) can occur through two possible reaction mechanisms, namely the aggregation of two $(Li_2EDC)_2$ (blue) dimers or the interaction between one $(Li_2EDC)_2$ (blue) and one Li_2EDC (orange), which can diffuse throughout the simulation box. According to Table 4.4, the difference in reaction rates between these two mechanisms results in the first pathway dominating. Finally, the low concentration of $(Li_2EDC)_2$ (blue) allows for the nucleation of a 3 or 4 component SEI cluster (purple). This SEI cluster (purple) can also diffuse and grows rapidly (within 50 μs of simulation time) in all directions, but mostly in the downward direction (see Figure 4.6c-e).

Table 4.4.: All reactions involved in the KMC simulation to understand the formation and growth of the SEI for the representative PSV. Reprinted with permission from Ref.[265], Copyright 2023, Advanced Energy Materials, under the Creative Commons CC-BY-NC license.

Entry	**Reactants**	**Products**	**Rate**(s^{-1})
1	Electrode (surf) + EC-Li^+	$C_2H_4OCOOLi$	1.15×10^8
2	Electrode (surf) + $C_2H_4OCOOLi$ + Li^+	$Li_2CO_3 + C_2H_4 \uparrow$	4.43×10^7
3	Li_2CO_3 (surf) + EC-Li^+	$C_2H_4OCOOLi$	2.19×10^8
4	$C_2H_4OCOOLi + C_2H_4OCOOLi$	$Li_2EDC + C_2H_4 \uparrow$	6.66×10^7
5	$Li_2EDC + Li_2EDC$	$(Li_2EDC)_2$	4.43×10^3
6	$(Li_2EDC)_2 + Li_2EDC$	SEI cluster	8.6×10^4
7	Li_2CO_3 (surf) + $C_2H_4OCOOLi$ + Li^+	$Li_2CO_3 + C_2H_4 \uparrow$	3.33×10^4
8	Li_2EDC + SEI cluster	SEI cluster	1.32×10^5
9	$(Li_2EDC)_2$ + SEI cluster	SEI cluster	1.33×10^5
10	$(Li_2EDC)_2 + (Li_2EDC)_2$	SEI Cluster	1.29×10^5
11	SEI cluster + SEI cluster	SEI cluster	1.22×10^5
12	$(Li_2EDC)_2$	Diffusion	1.42×10^6
13	Li_2EDC	Diffusion	9.88×10^6
14	$C_2H_4OCOOLi$	Diffusion	8.62×10^6
15	SEI cluster	Diffusion	2.52×10^6
16	$C_2H_4OCOOLi$	Out	4.25×10^{12}
17	$(Li_2EDC)_2$	Out	4.25×10^{12}
18	SEI cluster	Out	4.25×10^{12}
19	Li_2EDC	Out	4.25×10^{12}

The gradient profile of Li_2EDC (orange) over layers, as shown in Figure 4.7, provides an explanation for the observed decrease in SEI growth. The red dashed line represents the height at which the first SEI cluster (purple) nucleates, and the blue points represent the number of Li_2EDC (orange) at each height. The decrease in the number of Li_2EDC over layers is expected to result in a decrease in SEI growth. However, diffusion of both SEI clusters and organic components could potentially enable growth from the top layer during the simulation. The SEI cluster gradually contacts the surface of the inorganic SEI either through downward growth or diffusion, and ultimately becomes a part of a porous and immobile layer of SEI. Eventually, around 2.6 ms (Figure 4.6f), the SEI blocks access to the electrode, and almost all intermediate SEI components have deposited on the electrode surface. The SEI growth stops because the passage to the electrode surface is blocked and no more electrons are available at the outer layers. For the presented PSV, the final SEI structure consists of more organic layers in volume. The slow rate of the second electron reduction and the lack of electrons on the surface of inorganic SEI are the main reasons for the formation of a thin inorganic SEI layer. The simulation result (Figure 4.6f) is consistent with the experimental observations, where a few layers of inorganic SEI form on top of the anode surface, which is covered by a thick layer of organic SEI [277].

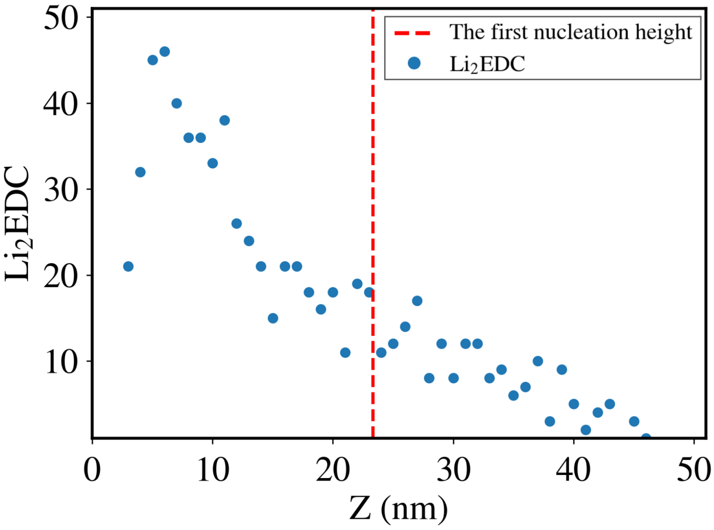

Figure 4.7.: For the representative PSV, the gradient of the Li_2EDC over layers. Blue points present the number of Li_2EDC, and the red dashed line indicates the first nucleation height. Reprinted with permission from Ref.[265], Copyright 2023, Advanced Energy Materials, under the Creative Commons CC-BY-NC license.

In order to obtain a more comprehensive understanding of the concentration changes in different components during the growth of SEI, we present a time series of the concentration profiles of various components, as shown in Figure 4.8. Generally, the concentration evolution allows us to identify when the system reaches a steady state. For the representative PSV, the steady state is reached after approximately 200 μs. Starting with the first and second electron reduction reactions, products such as $C_2H_4OCOOLi$ (green) and Li_2CO_3 (red) are formed within a few microseconds. Li_2EDC (orange) is immediately produced as a result of two $C_2H_4OCOOLi$ (green) reactions, and its concentration reaches a maximum value at approximately 100 μs. The concentration of $C_2H_4OCOOLi$ (green) remains nearly constant during the simulation, as its formation rate is similar to the conversion rate of $C_2H_4OCOOLi$ (green) to Li_2EDC (orange). After a few microseconds, $(Li_2EDC)_2$ (blue) is formed from Li_2EDC (orange) due to its low dimerization rate. The nucleation of the SEI cluster (purple) requires both Li_2EDC (orange) and $(Li_2EDC)_2$ (blue). Once $(Li_2EDC)_2$ (blue) forms as the essential component, it diffuses and eventually nucleates into the first SEI cluster (purple). After the first nucleation, the SEI cluster grows rapidly by consuming Li_2EDC (orange) and reaches a steady state after a few microseconds. Through monitoring the growth mechanism via the concentration profile (Figure 4.8), the simulation reaches a steady state after 200 μs, at which intermediate components are either involved in the formation process or trapped inside the final structure. At this point, all reactions stop, and a stable porous organic SEI has formed on the anode surface.

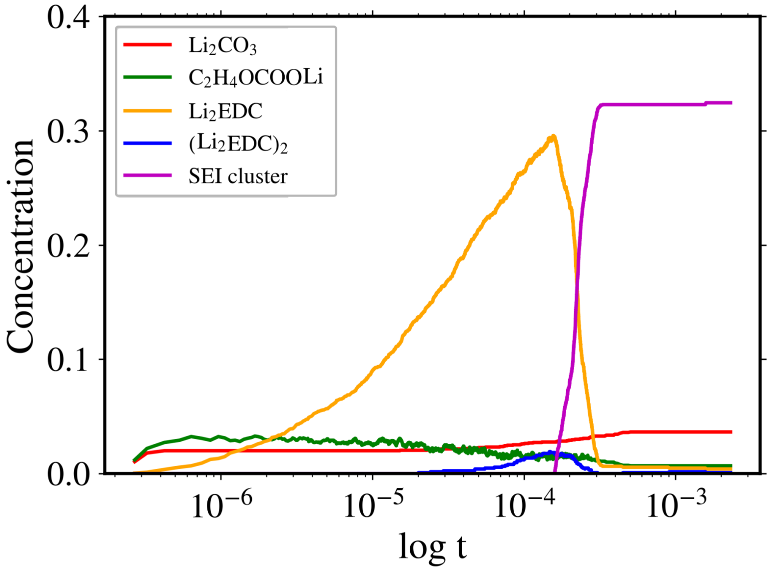

Figure 4.8.: Average concentration of intermediate components and SEI products as a function of time (in seconds) during the spatio-temporal evolution of the reference sample for a given set of reaction rates in the simulation. At the start of the simulation, electron reductions near the electrode produced $C_2H_4OCOOLi$ and Li_2CO_3 components (green and red lines). Both lines rapidly equilibrate (the red line is for the stable inorganic SEI, and the green is for reaching a steady state) with time, and the concentration of Li_2EDC rises rapidly. $(Li_2EDC)_2$ (blue line) begins to form as an essential precursor of the SEI cluster (purple line) after 20 μs. Once the SEI cluster (purple) has been nucleated, it grows rapidly by consuming Li_2EDC (orange) components. As a result, the Li_2EDC concentration falls rapidly, and all concentrations reach a steady state, indicating completion of the SEI formation. Reprinted with permission from Ref.[265], Copyright 2023, Advanced Energy Materials, under the Creative Commons CC-BY-NC license.

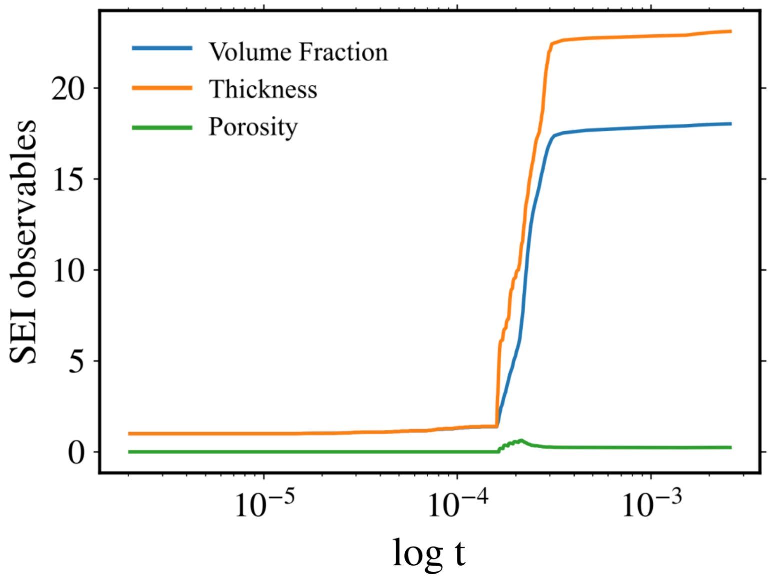

Figure 4.9.: The SEI volume fraction, thickness, and porosity change over time for the representative PSV. Blue, orange, and green colored lines show the SEI volume fraction, thickness, and porosity, respectively. Reprinted with permission from Ref.[265], Copyright 2023, Advanced Energy Materials, under the Creative Commons CC-BY-NC license.

Figure 4.9 displays the evolution of SEI properties over time. Considering their definitions and growth timeline, when the SEI cluster nucleates and begins to grow by consuming Li_2EDC, both the volume fraction and thickness increase rapidly. The difference between these two comes from their definitions: the volume fraction is defined as the compact SEI layers obtained by summing fractions per layer, while the thickness is defined as the average height. Porosity is determined by the structure of the formed SEI layers over time, which does not change significantly.

To gain a more detailed understanding of the individual reactions involved in the SEI formation mechanism of the representative PSV, we have created a multi-panel plot that provides information on the occurrence and duration of each reaction in the KMC simulation (Figure 4.10a). In particular, we have examined the average residence time for each reaction, which is the average time required to complete each step (Figure 4.10b), and the total time spent by each reaction, which is the product of the average residence time and the occurrence of each reaction (Figure 4.10c). The occurrence ratio of each reaction can vary significantly due to differences in reaction rates and product concentrations, with the important reactions during SEI growth being those with a fractional occurrence higher than 200, as indicated by the red dashed line in Figure 4.10. We have identified the electron reduction reactions as the crucial ones that provide the SEI precursors, with the formation of Li_2EDC from two $C_2H_4OCOOLi$ and all the diffusion processes being important reactions. Figure 4.10a indicates that the diffusion of SEI precursors is essential for SEI formation. The SEI precursors produced near the electrode-electrolyte interface diffuse away from the surface, and the $(Li_2EDC)_2$ precursors begin to aggregate at a distance of about 22 nm. Interestingly, reaction number 6, in which Li_2EDC interacts with $(Li_2EDC)_2$ to form SEI clusters, did not occur during the simulation. Instead, the first nucleation occurred via an interaction between two $(Li_2EDC)_2$, and the gradient of Li_2EDC led to downward growth of the formed SEI cluster to form the final structure. The simulation of the representative PSV showed that the SEI formed had a thickness of approximately 23 nm, with a few SEI precursors trapped inside the organic SEI. The porous nature of the formed SEI is reflected by vacant lattice points within the organic SEI. Due to the stochastic growth of the SEI, the resulting SEI surface is rough. These properties, namely thickness, porosity, and roughness, are crucial for the mechanical and electrochemical characteristics of the SEI during battery operation. The final structure of the generated SEI consists of a thin inorganic layer at the electrode surface with almost no defects, while the organic layer is the largest part with a thickness of several nanometers and 29% porosity. During the SEI growth mechanism, mass transport plays a significant role in the nucleation and growth of the SEI. By monitoring the SEI precursors away from the surface during the growth mechanism, it was observed that the SEI organic precursors are formed near the electrode surface and then move away (diffuse) from the surface, leading to nucleation far from the electrode. The organic SEI then grows via the aggregation of SEI precursors in the cluster (nuclei), which is also mobile. Diffusion of SEI precursors results in a considerable loss (37%) of material that escapes the simulation box at the absorbing layer.

Prior to delving into the parameter space analysis of activation energy barriers and SEI observables derived from 50000 simulations in the following section, it is pertinent to acknowledge that the growth of a thick organic SEI layer necessitates a high concentration of mobile SEI components and a nucleation reaction, which may not occur in close proximity to the electrode surface, despite the intricate nature of the reaction network. Once these prerequisites are met, the organic SEI layer grows rapidly atop the electrode surface already coated with an inorganic SEI layer.

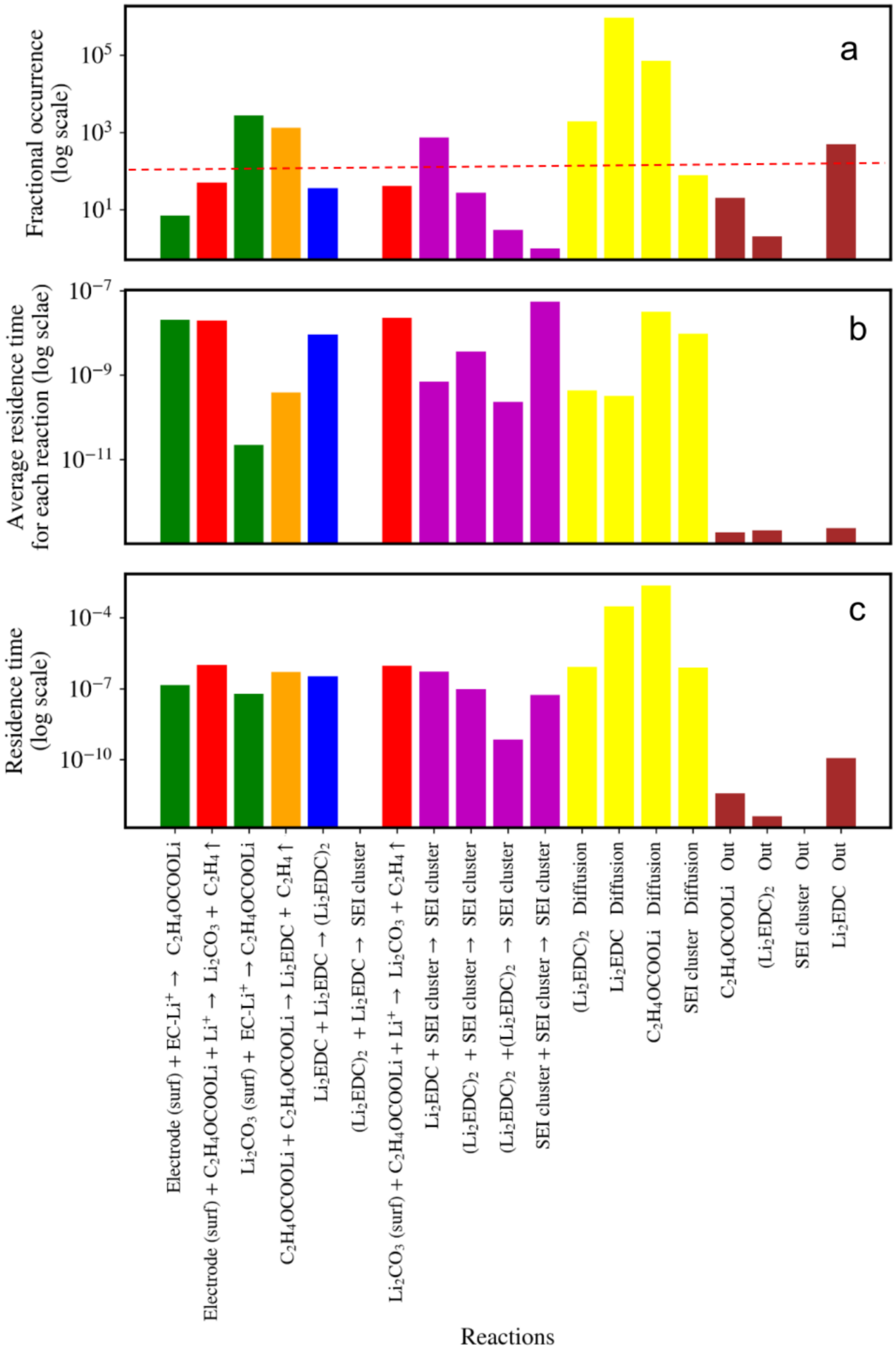

Figure 4.10.: The fractional occurrence and residence time for the reaction in the model for the representative PSV. Here, $C_2H_4OCOOLi$, Li_2CO_3, Li_2EDC, $(Li_2EDC)_2$ and SEI clusters are colored green, red, orange, blue, and purple, respectively. Yellow and brick-red bars represent diffusion within and outside the simulation box, respectively. a) Fractional occurrence of each reaction in the simulation b) The average residence time spent by a particular reaction during the simulation. c) Total residence time spent by each reaction throughout the simulation. Reprinted with permission from Ref.[265], Copyright 2023, Advanced Energy Materials, under the Creative Commons CC-BY-NC license.

4.4.2. Classification of the SEI regimes using machine learning

In the previous section, we presented the SEI growth mechanism for a single simulation of the representative PSV. However, developing a model that can transfer parameters from a lower scale to a more coarse-grained one is a challenging task due to various assumptions required for establishing the model. For instance, transferring electrochemical reaction rates from idealized environments to mesoscale models, such as the established model, can lead to uncertainties. Additionally, assumptions such as uniform molecular sizes used in the model can limit the transfer of parameters between scales. Thus, it may not be possible to specify the parameters for a particular chemistry with certainty. In this study, we adopt an alternative approach. We generate lists of reaction rates for the developed model, covering a wide range of conditions and chemistries. Each PSV in the dataset represents a datapoint in a fifteen-dimensional activation energy barrier parameter space (escape reaction rates are kept constant for all cases), resulting in different SEI properties. To gain a general understanding of the possible growth scenarios, we performed simulations for a dataset of 50000 PSV using a design of experiment method that systematically varied the activation energy barriers to cover the parameter space. We then used the obtained data to calculate SEI properties such as thickness, porosity, and volume fraction.

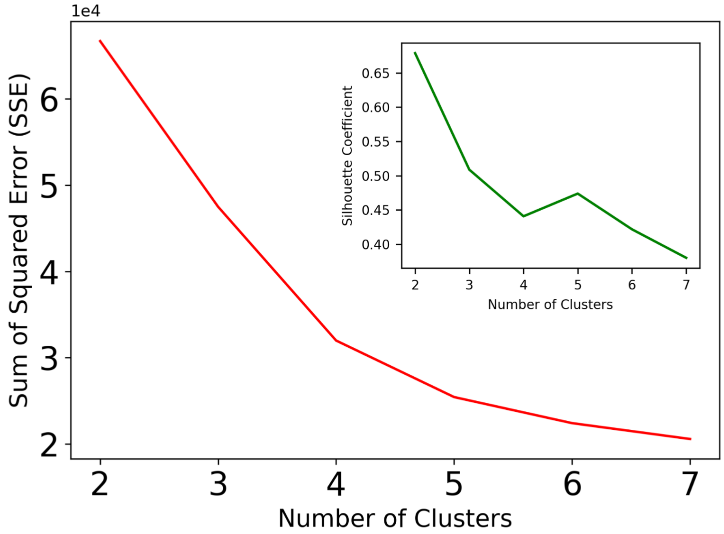

Figure 4.11.: Elbow method, sum of squared errors (outer plot), and silhouette coefficient (separation score) (inset plot) for the dataset scaled with the UMAP method for a sequence of clusters from 2 to 7. Reprinted with permission from Ref.[265], Copyright 2023, Advanced Energy Materials, under the Creative Commons CC-BY-NC license.

Following the post-processing of simulations, we obtain the SEI properties for each PSV, which allows us to construct a dataset comprising a combination of activation energy barriers and post-processing features. To facilitate data representation for high-dimensional datasets, we employ the K-Means clustering method[277, 278] with the Uniform Manifold Approximation and Projection (UMAP) algorithm[279]. The first step in K-Means clustering is to determine the optimal number of clusters from the dataset. To achieve this, we utilize two approaches under the elbow method. This involves fitting a model, such as K-Means, with a range of cluster values starting from 2, and then applying different scoring parameter metrics such as the sum of squared errors (SSE), sum of squared distances from each point to its assigned center, and silhouette score, which is the mean silhouette coefficient (SC) of all samples as the ratio of dispersion between and within clusters. The elbow method[280, 281] is applied to determine the optimal number of clusters when the line

connecting the measures by increasing the number of clusters resembles an arm, and the inflection point on the curve (the elbow) provides an appropriate indication of the optimal number of clusters. We calculate SSE and SC for the K-Means method, and the results suggest three clusters (see Figure 4.11) with the separation score of 0.51 for three clusters. This indicates three regions of the 18-dimensional (15 activation energy barriers and 3 SEI observables) parameter space of the model, where each PSV in the clusters exhibits fundamentally different compositions of the SEI at the end of the simulation.
After determining the optimal number of clusters using the elbow method, we applied the K-Means clustering algorithm to the dataset, which revealed that the simulations in region 1, consisting of 21109 samples, predominantly resulted in inorganic SEI formation. In contrast, simulations in region 2, comprising 13554 samples, showed a combination of organic and inorganic SEI with low thickness and high porosity. Finally, simulations in region 3, consisting of 15337 samples, led to the formation of an organic SEI with a substantial thickness and high density (see Figure 4.12). Based on the SEI characteristics exhibited by each region, we labeled them as "inorganic," "bad," and "good" SEI for regions 1, 2, and 3, respectively.

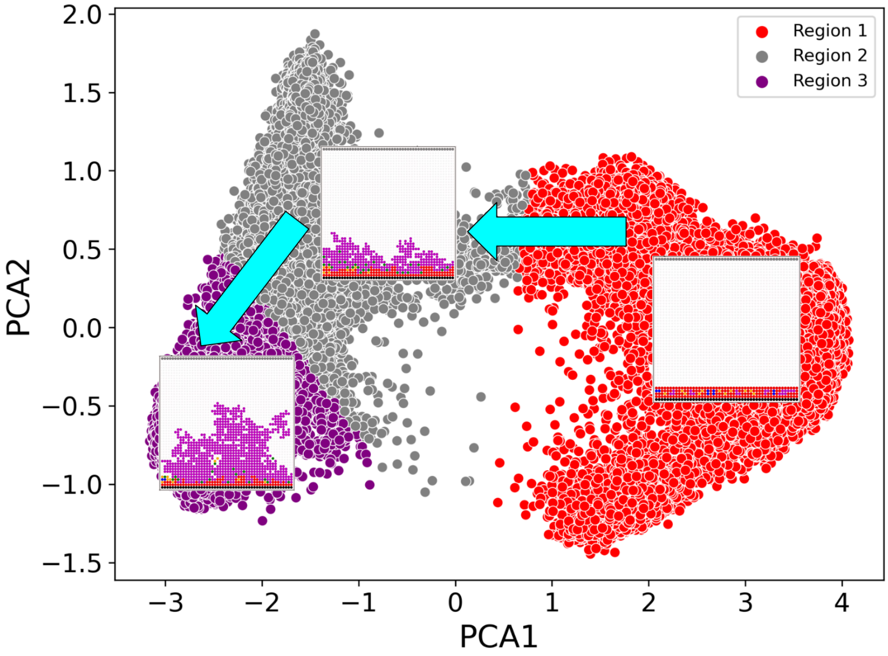

Figure 4.12.: Three different regions of the dataset based on reaction barriers and SEI observables within the parameter space (PSV) along the two most dominant principal components after Principal Component Analysis (PCA) of the clustered dataset comprising (50000 simulations). The PSV labeled in the region colored in red result in trajectories that have mainly inorganic SEI and no organic SEI, the PSV in the gray region result in thin layers of porous organic and less inorganic SEI. PSV in the purple region result in thick, comparatively dense organic SEI and very thin inorganic SEI. Reprinted with permission from Ref.[265], Copyright 2023, Advanced Energy Materials, under the Creative Commons CC-BY-NC license.

The subsequent step in the analysis involves a quantitative examination of the obtained regions by inspecting the SEI observables in these regions. A multi-panel plot of thickness and porosity for each of the three regions is provided in Figure 4.13. The left-hand column shows that the thickness of the SEI increases from region 1 to 3. In region 1, thin inorganic SEI forms in most cases, with a mean thickness of 3.09 nm. The formation of SEI that blocks the region close to the electrode surface (within 4 nm) via fast electron reduction reactions is the main reason for the resulting SEI. In region 2, SEI with almost equal contributions of organic and inorganic parts are observed. The formation of thick SEI is optimal in region 3, where the formed SEI is porous and has a mean thickness of 12.14 nm. In terms of size, these results are not comparable to experimental observations.The PSV in this region follows a well-defined Gaussian distribution for the SEI thickness.

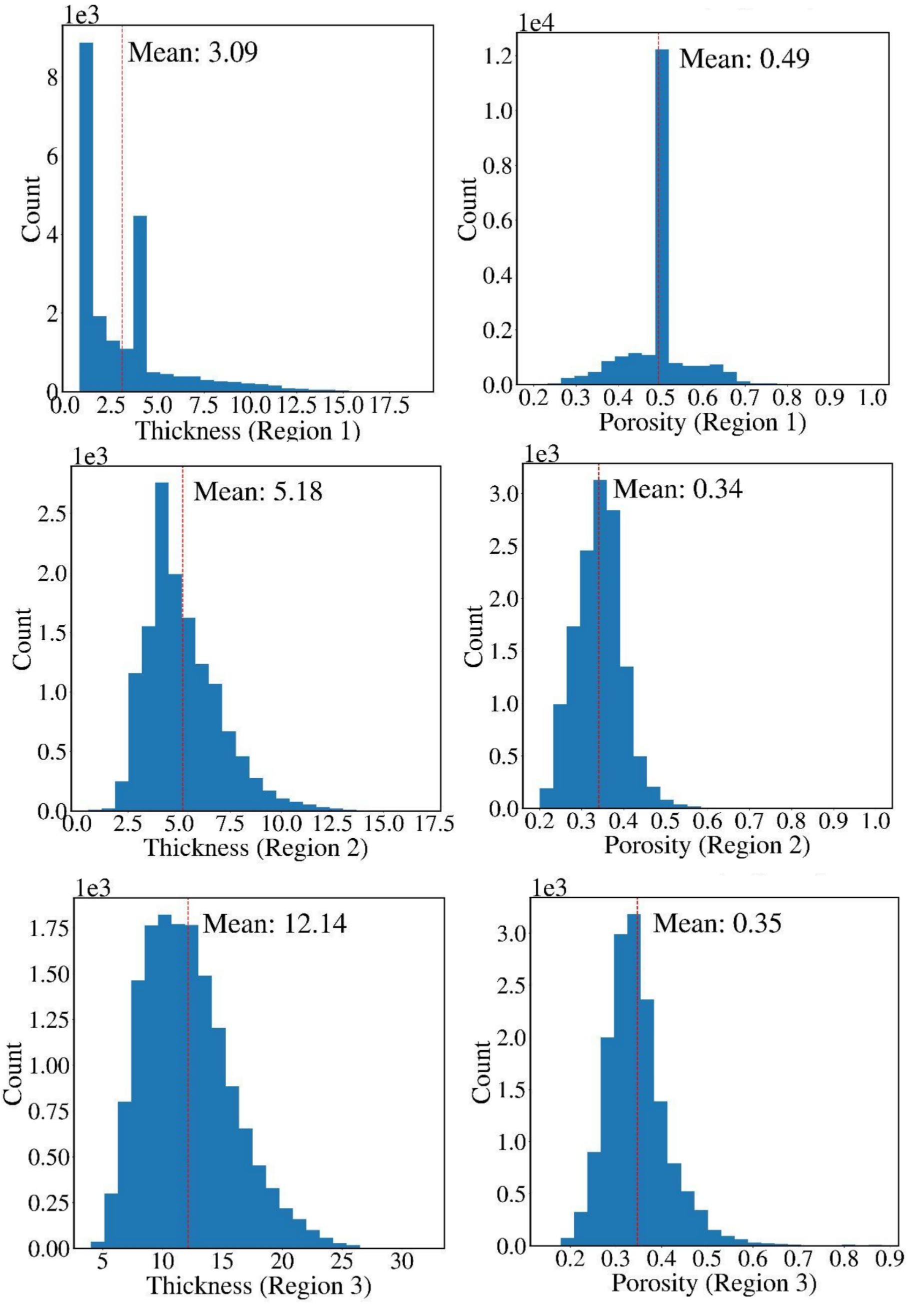

Figure 4.13.: Histograms of a) thickness, and b) porosity of the SEI for the three regions of SEI growth (occurrence in thousands) (see Figure 4.12). Here, the red dotted line shows the mean of the observable in each region. The average thickness of the SEI increases from 3.09 nm to 12.14 nm from region 1 to region 3. In contrast, the porosity is similar for all regions. Reprinted with permission from Ref.[265], Copyright 2023, Advanced Energy Materials, under the Creative Commons CC-BY-NC license.

We propose two types of analyses to gain a deeper understanding of the selected regions: 1) mean fractional occurrences, which represents the mean value of occurrences for each individual reaction across all samples in the region, and 2) escape fraction of mobile components, which is the ratio of SEI mobile precursors that left the simulation box to those that were produced across all samples in the different regions. The mean fractional occurrence plots have error bars indicating the standard deviation of the fractional occurrence of reactions. Small error bars represent frequent fractional occurrences of reactions, whereas large error bars signify the opposite.

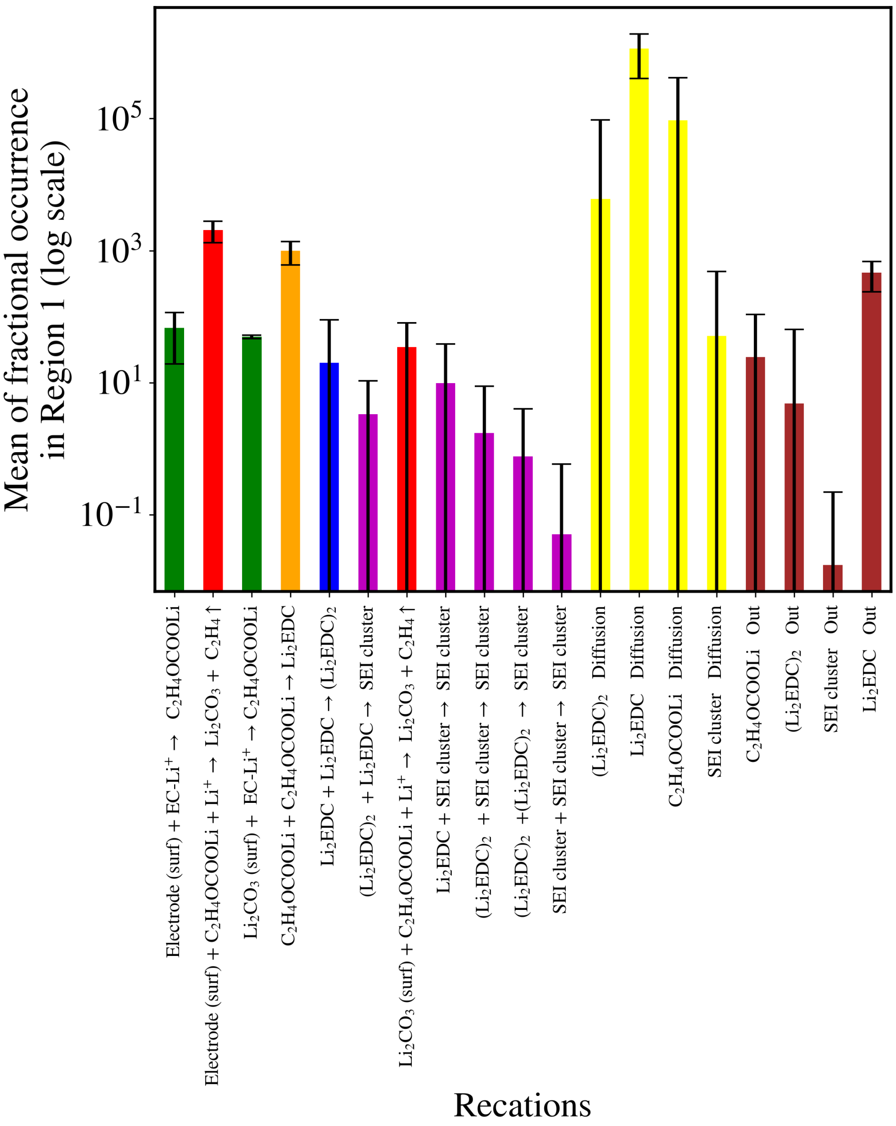

Figure 4.14.: Bar plot for the average fractional occurrence of each reaction in the KMC simulation for region 1 (represents the region for inorganic SEI, see Figure 4.12). The error bar represents the standard deviation of the fractional occurrence of the reactions and diffusions. The small error bars are for the frequent fractional occurrence of the reactions, whereas it is the opposite for large error bars. Reprinted with permission from Ref.[265], Copyright 2023, Advanced Energy Materials, under the Creative Commons CC-BY-NC license.

In Figure 4.14, it can be seen that the first and second electron reductions occur frequently (small error bars), indicating that inorganic SEI formation occurs rapidly close to the electrode in Region 1. In this region, most of the produced Li_2EDC diffuses and escapes the simulation box (small error bar), where around 50% of the produced material escapes, as shown in Figure 4.15. The combination of fast diffusion and inorganic SEI formation may be the primary reasons for the mostly thin inorganic SEI within Region 1. In Region

2, electron reduction reactions also occur frequently (Figure 4.16), but the formation of the SEI cluster on top of the inorganic SEI layer leads to a few layers of organic SEI, resulting in a thin SEI layer composed of both organic and inorganic parts. The escape fractions for this region show that the majority of the produced material was consumed in the SEI formation processes, with approximately 17% escaping the box (Figure 4.17), with $Li_2EDC)_2$ contributing the most of all components. For the "good" SEI region, where thick SEI forms, the mean fractional occurrences of reactions and the escape fractions are shown in Figures 4.20 and 4.18, respectively. Some reactions occur very often with high error bars, i.e., reactions numbers 5, 6, 7, 9, 10, and 11, indicating a difference in reaction rate from one simulation to another. The diffusion of SEI precursors was found to be a frequently occurring reaction during the analysis. Given the crucial role of diffusion rates in the formation of "good" SEI, it is imperative to produce SEI precursors and form layers before they escape the simulation box. Therefore, in region 3, balancing the aforementioned reaction rates leads to the creation of thick SEI layers composed of organic and inorganic parts. In Figure 4.20, reactions with mean fractional occurrences greater than 200 times are indicated by the dashed red line, highlighting their significant role in the SEI formation process. Based on the analyses conducted, the data supports the hypothesis that the transport of precursors, particularly the organic SEI ingredients (Li_2EDC), plays a crucial role in directing the formation of a thick and dense SEI.

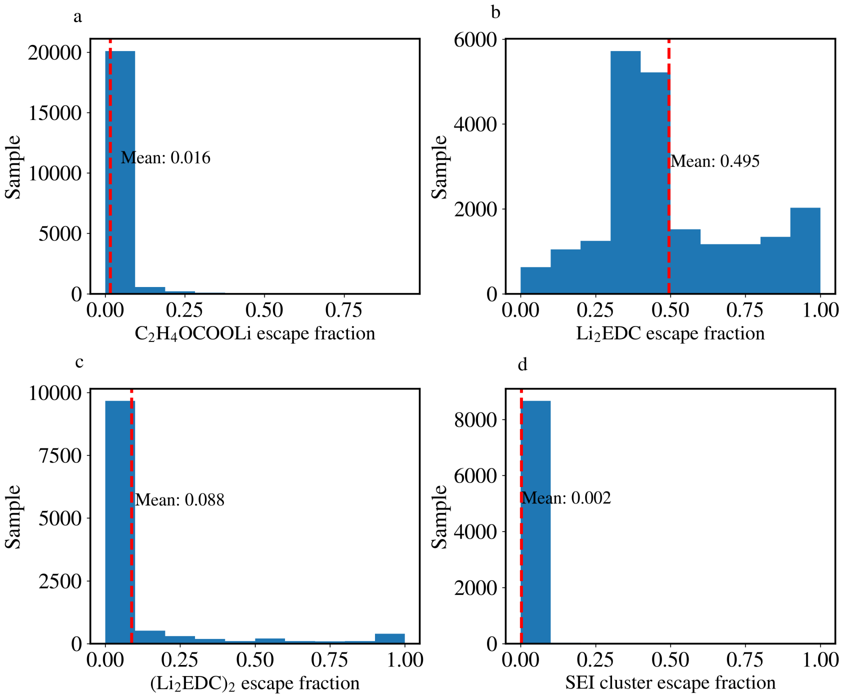

Figure 4.15.: Histograms of organic SEI precursor escape fractions a) $C_2H_4OCOOLi$ clusters, b) Li_2EDC clusters, c) $(Li_2EDC)_2$ clusters, and d) SEI clusters) for region 1. Here, the red dotted line represents the mean escape fraction of the precursors. A low mean value of the escape fraction means that more precursors form the organic SEI. Because competing reactions occur infrequently before nucleation, Li_2EDC has the highest escape fraction of these four precursors. The majority of the Li_2EDC escapes the system before nucleation, resulting in the formation of inorganic SEI in this region. Reprinted with permission from Ref.[265], Copyright 2023, Advanced Energy Materials, under the Creative Commons CC-BY-NC license.

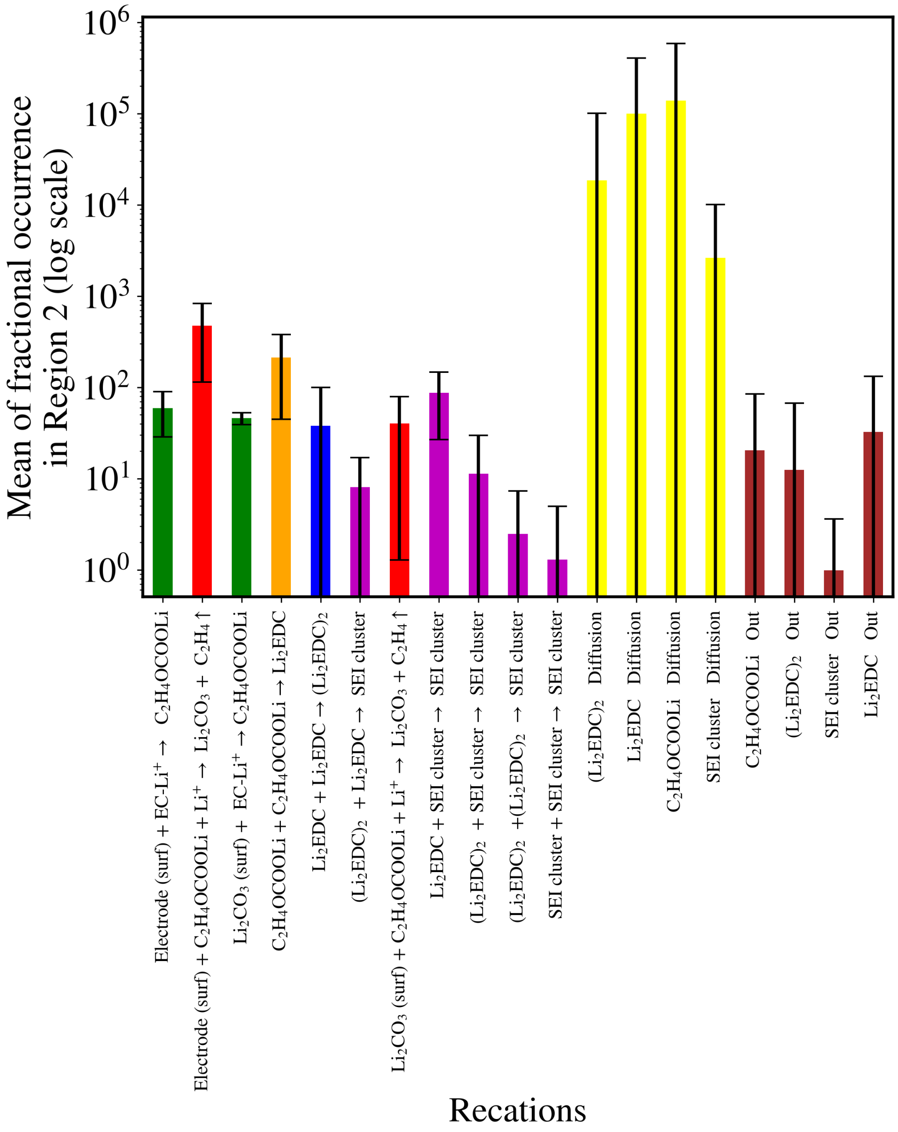

Figure 4.16.: Bar plot for the average fractional occurrence of each reaction in the KMC simulation for region 2 (represents the region for inorganic SEI, see Figure 4.12). The error bar represents the standard deviation of the fractional occurrence of the reactions and diffusions. The small error bars are for the frequent fractional occurrence of the reactions, whereas it is the opposite for large error bars. Reprinted with permission from Ref.[265], Copyright 2023, Advanced Energy Materials, under the Creative Commons CC-BY-NC license.

Upon examining the escape fraction of region 3 in Figure 4.18, it becomes evident that only around 1% of $C_2H_4OCOOLi$ escaped out of the system, meaning that 99% of it was involved in the production of Li_2EDC (refer to 4.18a). The fraction of Li_2EDC that escaped was approximately 22%, which suggests an irreversible loss of SEI precursors before dimerization. On the other hand, for $(Li_2EDC)_2$ and mobile SEI clusters, the escape fraction was around 1% and 0.2%, respectively. This implies that most of the agglomerated SEI components eventually join the organic SEI cluster to form a thick SEI.

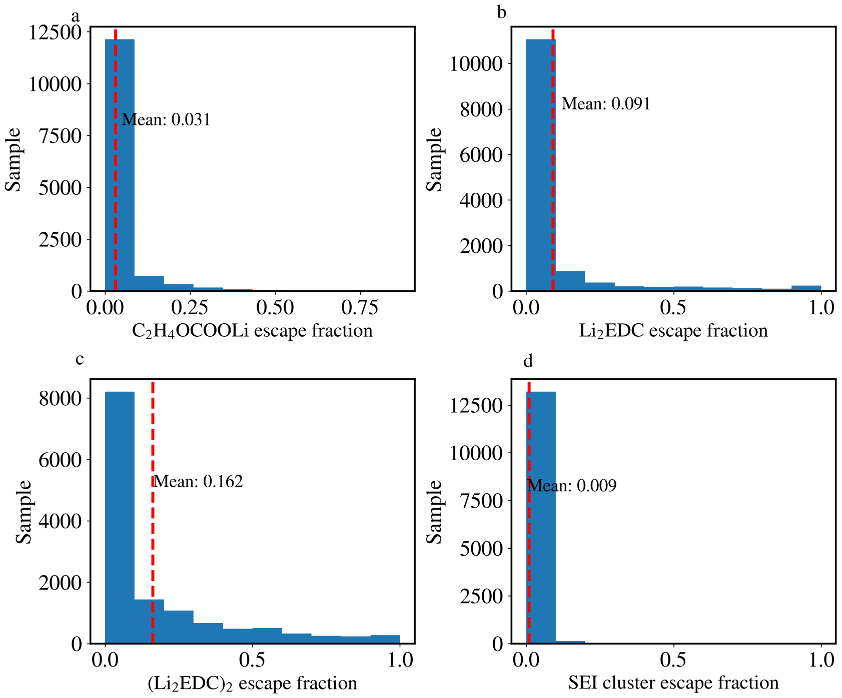

Figure 4.17.: Histograms of organic SEI precursor escape fractions a) $CC_2H_4OCOOLi$, b) Li_2EDC, c) $(Li_2EDC)_2$, and d) SEI clusters) for region 2. Here, the red dotted line represents the mean escape fraction of the precursors. Among mobile species, $(Li_2EDC)_2$ has the highest escape fraction. Reprinted with permission from Ref.[265], Copyright 2023, Advanced Energy Materials, under the Creative Commons CC-BY-NC license.

When comparing Figure 4.20 to Figure 4.10a, it becomes evident that the PSV chosen to elucidate the organic SEI formation process is also the PSV that leads to the formation of "good" SEI. Thus, even though it is not possible to specify the exact reaction rates for the particular system, it can be suggested that the formation of "good" SEI in a model (the general structure developed and discussed here) involves a solution-mediated growth mechanism instead of a surface-mediated growth mechanism.

In order to evaluate how the distance of the first nucleation event from the electrode surface impacts the formation of SEI, we generated a correlation plot between this distance and SEI thickness (Figure 4.19), utilizing data from region 3 of our dataset. The blue line on the plot denotes the linear regression fit of the scattered data points. Considering the effects of SEI cluster diffusion and the gradient of SEI precursors on SEI formation, the linear regression suggests that thick SEI layers are formed when the first nucleation event occurs farther away from the electrode surface. As we follow the blue solid line on the plot towards smaller distances, it becomes evident that the SEI layer becomes thinner as the nucleation event occurs closer to the electrode surface. In addition, nucleation events that occur near the electrode surface may lead to blockage of further SEI growth by covering the electrode surface. The slope of the blue line is less than one, indicating that the shape of the SEI cluster elongates in a direction perpendicular to the surface due to the concentration gradient of the precursors. Based on these observations, we conclude that the thickness of SEI can be predicted by the location of the first nucleation event in the SEI formation mechanism. Rapid nucleation events that occur near the electrode surface lead to the formation of thin SEI layers (region 2).

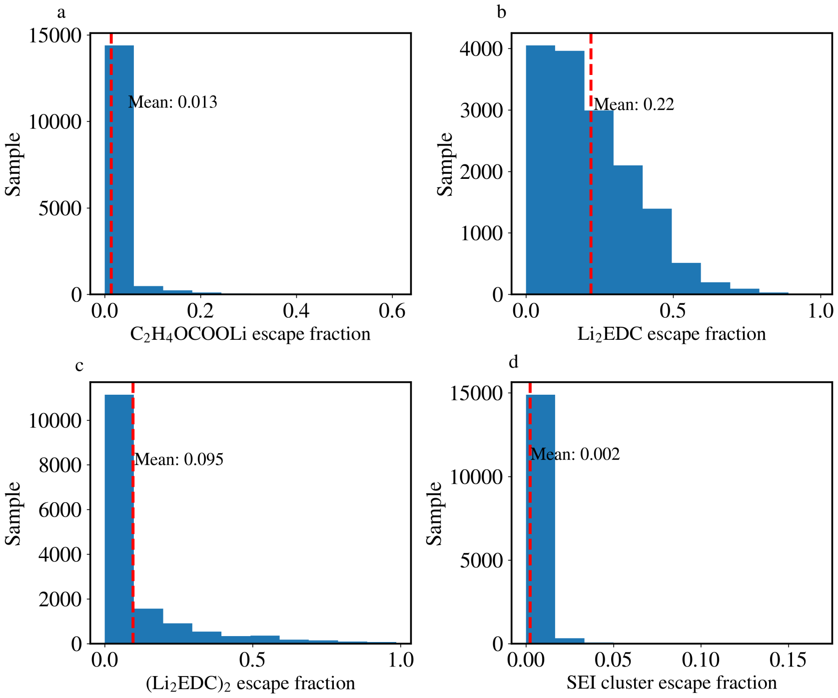

Figure 4.18.: Histograms of the escape fraction of organic SEI precursors a) $C_2H_4OCOOLi$, b) Li_2EDC, c) $(Li_2EDC)_2$, and d) SEI clusters) i.e. the fraction of precursors that diffuse out of the KMC simulation box for region 3 (see 4.12). Here, the red dotted line represents the mean escape fraction of the precursors. A low mean value of the escape fraction means that more precursors form the organic SEI. Li_2EDC has the highest escape fraction among these four precursors because competing reactions occur infrequently before nucleation. Reprinted with permission from Ref.[265], Copyright 2023, Advanced Energy Materials, under the Creative Commons CC-BY-NC license.

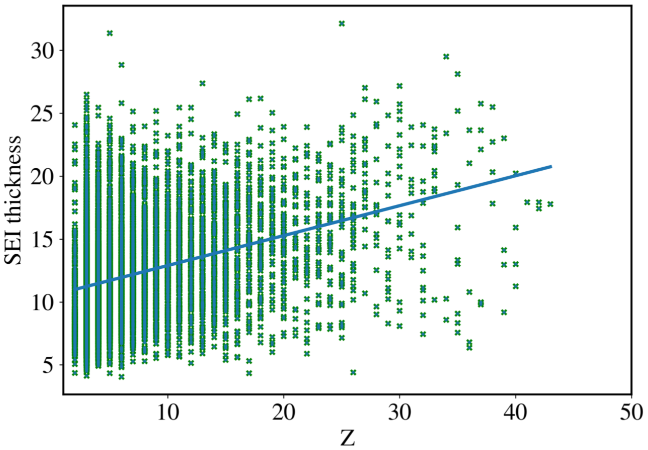

Figure 4.19.: Scatter plot of SEI thickness with respect to the distance (Z) of the first nucleation (formation of a SEI cluster for organic SEI, (purple)) from the electrode for the samples in region 3. The blue solid line represents the linear regression fit, and it shows that the thickness of the SEI increases with distance from the first appearance of the SEI clusters. Thicker SEI developed when the nucleation started far away from the electrode surface, which resulted from the directional growth through aggregation along a concentration gradient. If the nucleation starts near the electrode, then the electrode is rapidly blocked. Reprinted with permission from Ref.[265], Copyright 2023, Advanced Energy Materials, under the Creative Commons CC-BY-NC license.

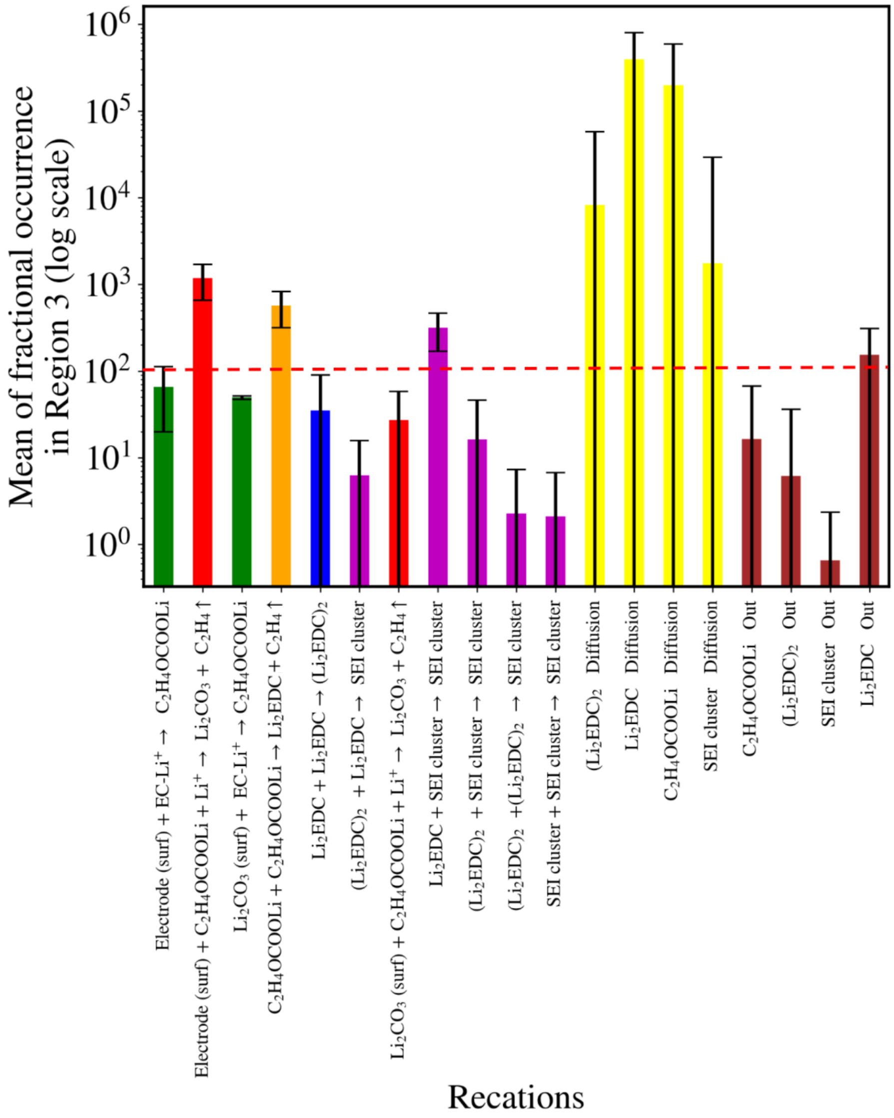

Figure 4.20.: Bar plot for the average fractional occurrence of each reaction in the KMC simulation for region 3 (represents the region for good SEI, see 4.12).The high mean values for diffusions reflect the necessity of a good SEI. The error bar represents the standard deviation of the fractional occurrence of the reactions and diffusions. The small error bars are for the frequent fractional occurrence of the reactions, whereas it is the opposite for large error bars. Reprinted with permission from Ref.[265], Copyright 2023, Advanced Energy Materials, under the Creative Commons CC-BY-NC license.

Based on this observation, a practical principle for controlling SEI thickness can be proposed: controlling the nucleation reaction. The computational limitations of this study necessitated the use of a 50×50 nm^2 lattice, which led to the formation of an SEI with a maximum thickness of 25 nm.

Furthermore, to gain a better understanding of the contribution of different reactions to the formation of "good" SEI in the final region, a correlation matrix plot was generated for activation energy barriers and SEI observables. This plot, depicted in Figure 4.21, considers various reactions, such as the formation of $(Li_2EDC)_2$ and SEI clusters, diffusion of Li_2EDC and SEI clusters, and SEI observables, and displays their correlation.

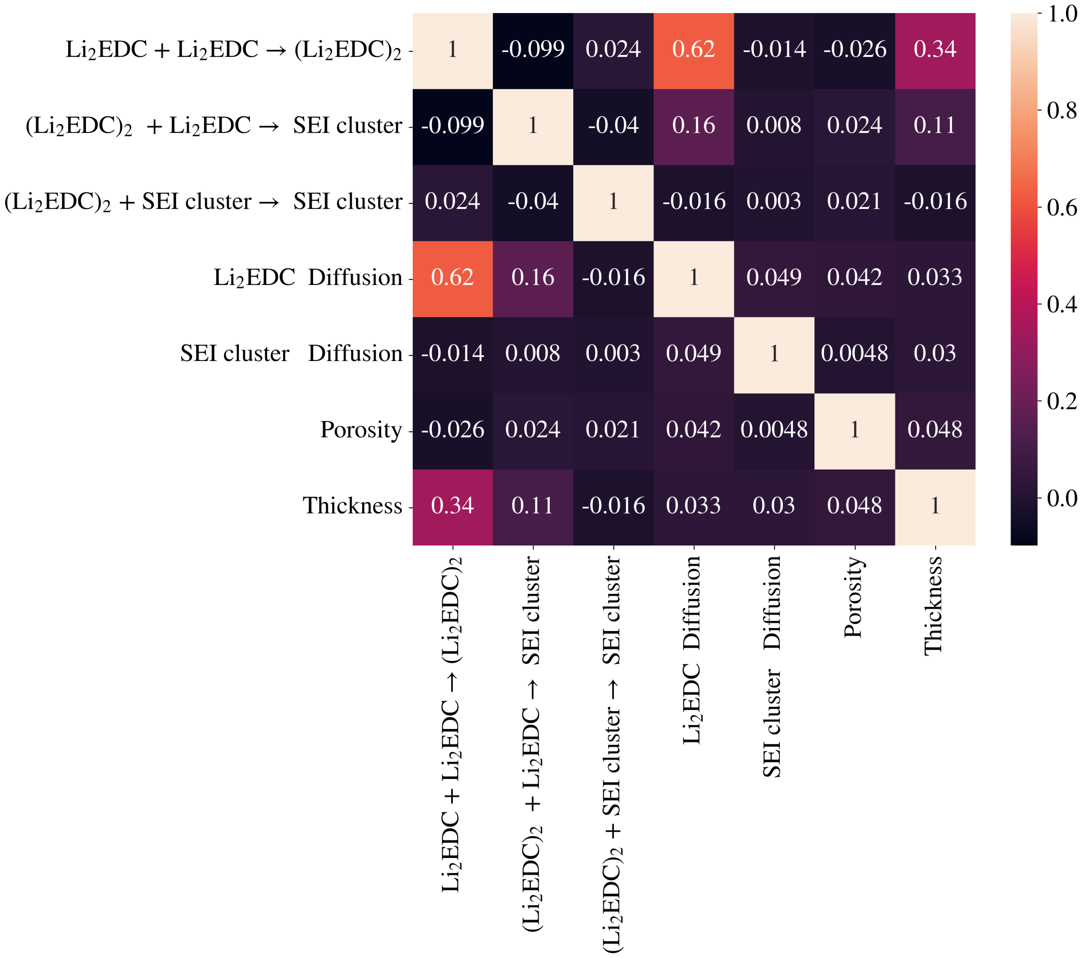

	$Li_2EDC + Li_2EDC \rightarrow (Li_2EDC)_2$	$(Li_2EDC)_2 + Li_2EDC \rightarrow$ SEI cluster	$(Li_2EDC)_2$ + SEI cluster $\rightarrow$ SEI cluster	Li_2EDC Diffusion	SEI cluster Diffusion	Porosity	Thickness
$Li_2EDC + Li_2EDC \rightarrow (Li_2EDC)_2$	1	-0.099	0.024	0.62	-0.014	-0.026	0.34
$(Li_2EDC)_2 + Li_2EDC \rightarrow$ SEI cluster	-0.099	1	-0.04	0.16	0.008	0.024	0.11
$(Li_2EDC)_2$ + SEI cluster $\rightarrow$ SEI cluster	0.024	-0.04	1	-0.016	0.003	0.021	-0.016
Li_2EDC Diffusion	0.62	0.16	-0.016	1	0.049	0.042	0.033
SEI cluster Diffusion	-0.014	0.008	0.003	0.049	1	0.0048	0.03
Porosity	-0.026	0.024	0.021	0.042	0.0048	1	0.048
Thickness	0.34	0.11	-0.016	0.033	0.03	0.048	1

Figure 4.21.: Correlation matrix plot of a few barriers (for reactions 5, 6, 9, 13, and 15) and observables (SEI thickness and porosity), where 0 is for no linear correlation and any positive and negative values indicate the positive and negative linear correlation between two variables, the formation of Li_2EDC is closely related to the diffusion of Li_2EDC and the thickness of the SEI. A correlation plot for all reactions and SEI observables is available in Appendix Section F Figure F.13. Reprinted with permission from Ref.[265], Copyright 2023, Advanced Energy Materials, under the Creative Commons CC-BY-NC license.

Based on the correlation matrix plot shown in Figure 4.21, it can be observed that there exists a significant linear correlation between the diffusion of Li_2EDC and the formation of $(Li_2EDC)_2$. Furthermore, there is a strong positive correlation between the formation of $(Li_2EDC)_2$ and the thickness of SEI formed. This highlights the crucial role played by dimerization in producing the precursor required for the initiation of nucleation and the first organic components in the solution-mediated SEI growth mechanism.

4.5. Effect of exchange between lithiated solvent and the organic SEI

To delve deeper into the various possibilities for the growth of the SEI, which were previously discussed, the developed model is lacking the necessary components that facilitate transport for the pathway that requires electron transport through the organic SEI. Furthermore, we observed no evidence of organic SEI growth through "cracks" or "pores" in the SEI. In order to quantitatively demonstrate the infeasibility of such a mechanism, we performed two additional simulations that would have favored such a situation. In the first simulation, we accelerated the rate of exchange of lithiated solvent with organic components. This created a pathway for the lithiated solvent to react with the anode or inorganic SEI surface through solvent reduction or Li intercalation. Figure 4.22 illustrates the formation of a thin organic SEI located 9 nm from the anode surface, which rapidly expanded inward over a period of 260 μs to become a thick organic SEI. However, the organic SEI eventually fractured and separated into small organic clusters that diffused into the solution, as the lithiated solvent could pass through it. As a result, the organic SEI disintegrated, leaving only the inorganic SEI remains. Since we could not detect any SEI growth using this method, we instead investigated SEI stability. To assess SEI stability, we began with a thick organic SEI that had already formed and then increased the rate of solvent-SEI exchange. Figure 4.23 shows how we observed the organic SEI degrading continuously to a thin layer of less than 3 nm over a period of 4 ms. These simulations led us to the conclusion that a solvent molecule must undergo numerous diffusive events in order to move through a thick SEI and eventually reach the surface, where it may react and create a single new component of the organic SEI. However, each diffusive process has the potential to break the SEI, resulting in significantly faster degradation on average than regeneration.

According to our criterion, we can anticipate two possible outcomes, which are as follows: a "good" SEI may be formed due to the exchange of the lithiated solvent with organic components. Conversely, a "bad SEI" may form when the formed organic SEI interacts with the solvent. To investigate this, we utilize the set of exchange rates from the representative sample presented in our manuscript, which was previously demonstrated to yield a "good" SEI. Subsequently, we integrate additional exchange events to the existing event list in our kinetic Monte Carlo (KMC) model and perform the simulation again to analyze the formation and growth of the SEI.

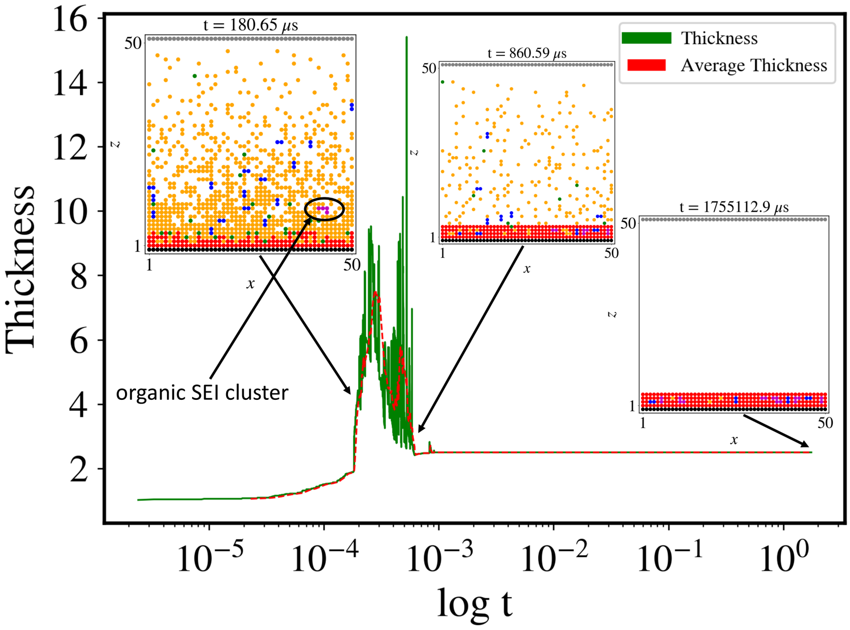

Figure 4.22.: The SEI thickness (nm) as a function of time (in seconds) during the spatio-temporal evolution of the reference sample. At the beginning of the simulation, the solvent reduction process leads to the formation of inorganic SEI. The organic SEI starts to form at 180 μs (9 nm away from the surface, highlighted in the inset image) and the average thickness (red dotted line) rises. However, due to its continuous dissolution, the average thickness of the organic SEI subsequently declines until it is completely dissolved (260 μs). Inset images are snapshots at different time-interval during the simulations. Reprinted with permission from Ref.[265], Copyright 2023, Advanced Energy Materials, under the Creative Commons CC-BY-NC license.

To enhance the lucidity of our findings, we implemented an alternative approach where we introduce the extra event (i.e., the exchange between lithiated solvent and organic SEI) directly after the complete formation of SEI (i.e., after 2.6 ms of simulation, as depicted in Figure 4.6f). As anticipated, our observations demonstrate that the deterioration of SEI surpasses its renewal by a significant margin. This outcome indicates that any battery operating under these conditions would inevitably degrade.

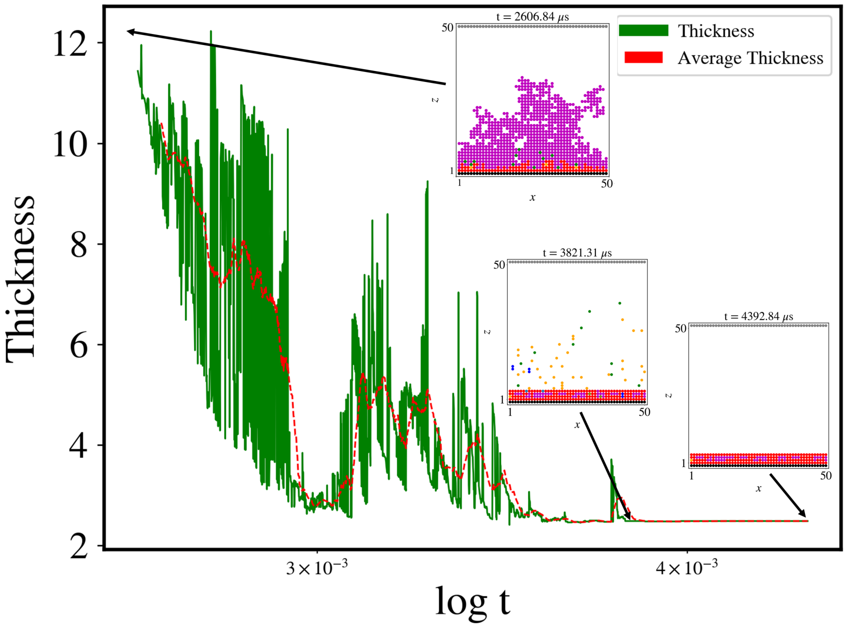

Figure 4.23.: The SEI thickness (nm) as a function of time (in seconds) during the spatio-temporal evolution of the reference sample starting at a preformed SEI. Here the simulation begins at 2.6 ms with the additional events (exchange between lithiated solvent and organic SEI). In this case, already formed organic SEI starts to dissolve and the average SEI thickness declines and reaches a constant value of 3 nm at 4 ms. This result demonstrates that even a thick preexisting organic SEI will be degraded by diffusion events that allow a significant fraction of the solvent to reach the surface. Inset images are snapshots at different time-interval during the simulations. Reprinted with permission from Ref.[265], Copyright 2023, Advanced Energy Materials, under the Creative Commons CC-BY-NC license.

4.6. Conclusions

Although the SEI is widely recognized as a crucial element in liquid electrolyte batteries, its growth mechanism and resulting structure and function remain elusive. The SEI growth models must address a paradoxical situation in which electrons required for electrochemical reactions that degrade the electrolyte into SEI precursors are available only within a few nanometers of the electrode surface, while functional batteries exhibit an organic SEI an order of magnitude thicker. In this research, we proposed a multi-scale model that resolves this paradox by suggesting a solution-mediated pathway for SEI growth. We established a reaction network for microscopic reactions relevant to SEI growth and estimated the initial reaction rates based on literature data. As the transferability of microscopic reaction parameters obtained under idealized assumptions to mesoscopic models with various assumptions is limited, we conducted a design-of-experiment study to explore the relevant parameter space of the reaction model, performing over 50000 model simulations, each corresponding to a specific set of microscopic parameters. The model balances the realism of the represented mechanisms and computational feasibility. Our analysis of the simulations revealed three SEI outcomes: "inorganic," "bad," and "good" SEI.

Our simulations revealed that only parameter sets in a specific region allowed for the growth of a thick and stable SEI that ultimately covered the electrode surface. Surprisingly, we found that the SEI grew through a solution-mediated pathway, which involved a nucleation reaction of SEI precursors taking place far away from the electrode surface, rather than directly on it as most existing models postulate. We observed a positive correlation between the thickness of the SEI and the distance from the electrode where the nucleation reaction occurred. Strikingly, we found that the most stable SEI was grown when the nucleation reaction occurred far from the surface. As a result of this solution-mediated pathway, some of the degraded electrolyte diffused away from the surface and was no longer available for SEI formation. Nonetheless, about 20% of the degraded electrolyte precursors were still available for SEI formation.

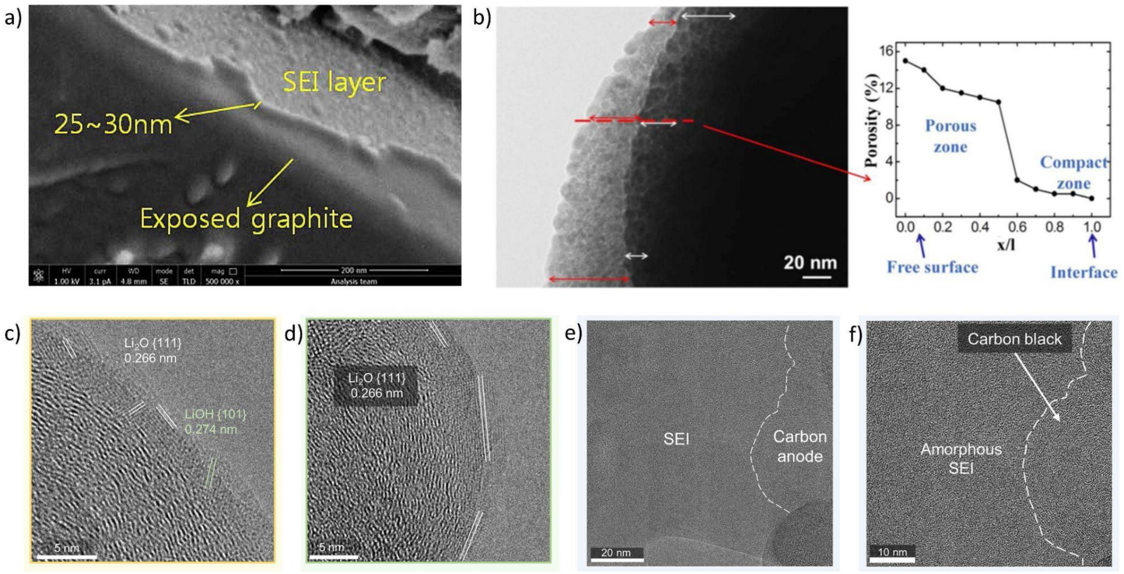

Figure 4.24.: Images of SEI from experiments using advanced techniques (SEM, TEM). (a) XHR-SEM image of the SEI layer on the graphite electrode after 5 minutes of ion etching. Reprinted with permission from Ref.[282] Copyright (2013) Elsevier. (b) The TEM image and the porosity analysis of the SEI layer. Reprinted with permission from Ref.[283] Creative Commons Attribution 4.0 license. (c, d) cryogenic transmission electron microscopy (Cryo-TEM) images of the compact SEI with an approximate thickness of 5 nm. (e, f) cryogenic high-resolution transmission electron microscopy (Cryo-HRTEM) images of the extended SEI interfaced with carbon black. Reprinted with permission from Ref.[284] Copyright 2019, American Chemical Society.

We identified the reaction leading to the formation of $(Li_2EDC)_2$ as an essential prerequisite for the nucleation reaction. This insight into a controllable reaction offers opportunities for designing the properties of the SEI. SEI grown via a solution-mediated pathway will exhibit different electrochemical and mechanical properties from SEI grown in a continuous manner, starting at the electrode and progressing towards the electrolyte. By using the outcome of our simulations, our model presents an opportunity to investigate these properties for functional studies of batteries. The organic SEI, depicted in Figure 4.6f, is much more porous than the inorganic SEI, which has consequences for long-term battery operation. The soft organic SEI is expected to crack with each charging cycle, leading to further degradation of solvent molecules. This process causes the continuous, irreversible consumption of active battery materials and ultimately limits the battery's lifetime. While only a qualitative comparison is presently possible, it is interesting to compare our simulation results with experimental observations. The morphology (thickness and porosity) of an

SEI layer on graphite that is commensurate with the morphology of the SEI in region 3 of our simulation is shown in Figure 4.24a, an extreme high resolution scanning electron microscopy (XHR-SEM) image of the SEI after 5 minutes of ion etching [282].

In both experimental and simulation studies, the morphology of the SEI has been observed to have a size of around 40 nm, consisting of a dense inner zone and a more porous outer zone[283] (Figure 4.24b). This supports the solution-mediated pathway scenario, as the density of SEI precursors decreases with distance from the surface. A surface growth mechanism would not produce the observed discontinuous porosity distribution. Additionally, Figure 4.24(c-f) displays two examples of SEI growth under different conditions[284]. Figures 4.24 (c,d) correspond to a scenario where only the inorganic SEI is growing (region 1 in the SEI landscape), while Figures 4.24 (e,f) correspond to a scenario where substantial SEI growth is observed (region called "good" SEI). Although this comparison is only indicative of possible scenarios at present, it shows that the mesoscopic model discussed in the study can produce SEI morphologies that agree with experimental observations qualitatively. In future work, there will be attempts to establish a more quantitative correspondence between the simulation results and experimental observations. Additionally, the assumptions made in this study will be systematically tested, including whether a three-dimensional model will produce different outcomes. However, the authors expect that the two-dimensional model can still capture the qualitative mechanism of organic SEI growth in LIBs. The model can also be extended to incorporate the presence of electrolyte mixtures and additives, providing a solid foundation for further research into the growth and function of SEI in LIBs. While this study focuses on the SEI growth mechanism, future research can address more complex systems. Two possible avenues include using ab-initio data to parameterize KMC simulations or relying on molecular dynamics simulations as an intermediate model to inform KMC simulations[285]. The mesoscopic model developed in this study can be readily expanded to include the presence of various additives and electrolyte mixtures. The accuracy of the model will be validated through experiments, such as X-ray photoelectron spectroscopy (XPS) and transmission electron microscopy (TEM) to refine the efficient continuum scale models for predicting SEI properties during cycling in LIBs with high accuracy. Although the current study focuses on the general mechanisms underlying SEI growth, future work may investigate more intricate systems. Two approaches can be pursued in this regard. First, ab-initio data from other systems can be directly utilized to parameterize the KMC simulations in some cases. Second, the KMC model can be used as an intermediary to parameterize molecular dynamics simulations on shorter time and length scales[285]. The mesoscopic model can be easily modified to account for the presence of additives and different electrolyte mixtures. As with the original model, experiments such as XPS and TEM results will be used to verify the modified model and input parameters will be used to improve the accuracy of effective continuum scale models for predicting SEI properties during cycling in LIBs.

5. Summary

Mesoscopic science deals with studying systems at intermediate length and time scales, and has emerged as an essential subfield in condensed matter physics, materials science, and biology. It encompasses a vast array of phenomena, including self-assembly, phase transitions, diffusion, and reaction kinetics, all of which occur in systems ranging from a few nanometers to micrometers in size and from picoseconds to microseconds in duration. Despite its importance, mesoscopic science faces significant challenges due to the so-called mesoscale gap, which arises when there is a substantial difference between the length and time scales of the phenomena of interest and those that can be resolved by available theoretical or experimental techniques. This gap presents a significant obstacle to the accurate modeling and simulation of mesoscopic systems. On the one hand, atomistic simulations based on first-principles calculations can provide detailed information about the electronic structure and chemical reactions at the atomic scale. However, these methods are computationally expensive and can only simulate systems with a limited number of atoms and a short simulation time. On the other hand, continuum models, such as finite element or continuum mechanics methods, can simulate macroscopic systems with a large number of atoms and a long simulation time but lack the necessary resolution to capture the details of the microstructure and the underlying physics. To overcome this challenge, researchers have developed various computational methods, such as Kinetic Monte Carlo (KMC) simulation, which allows for the efficient simulation of large systems over long simulation times. KMC simulation is a stochastic method based on the Markovian assumption that the system evolves through a sequence of discrete, randomly occurring events, such as diffusion or chemical reactions. With the advancement of computational power and the development of more sophisticated algorithms, KMC simulations have become increasingly popular and accurate, enabling researchers to study complex mesoscopic systems.

KMC simulations offer a powerful and flexible approach for investigating the growth and properties of graphene-based materials[286, 287]. One of the main areas of application for KMC simulations in graphene research is the study of the growth process itself, considering the effects of different growth conditions, as it is discussed in the third chapter of this thesis. KMC simulations can also be used to investigate defects in graphene, such as vacancies, dislocations[288], and grain boundaries[289]. For instance, KMC simulations can be employed to study the effect of temperature, pressure, and precursor molecules on the formation of defects[290], as well as the impact of different annealing conditions on the healing of defects in graphene[291]. With the growing interest in graphene for various applications, KMC simulations can be used to investigate new applications of graphene-based materials. By predicting the optimal growth conditions and defect configurations, KMC simulations can help to optimize the properties and performance of graphene-based materials in new devices, such as gas sensors[292], electronic devices[293], and energy storage devices[294].

KMC simulations are also a valuable tool for studying various aspects of lithium-ion batteries (LIBs), including electrode materials, electrolytes, additives, solid electrolyte interphases (SEI), and cathode electrolyte interphases (CEI). In the study of electrode materials, KMC simulations are used to model the diffusion of lithium ions within the electrode material[61], which is crucial in determining battery capacity and cycle life[295]. Additionally, KMC simulations can be employed to study the transport of lithium ions in the electrolyte solution and their interaction with the electrode surface[296]. Studying the effects of additives on battery performance and safety by simulating the interactions between additive molecules and electrode surfaces can be another application of such simulation models[297, 298]. The forth chapter of this thesis is dedicated to study the SEI formation in LIBs employing KMC simulation. In the case of CEI, KMC simulations have been used to study the formation and stability of the CEI layer on cathode materials[299]. KMC simulations can also aid in the design of new electrolytes, and additives, and predict their effects on the formation and degradation of the SEI and their influences on the battery performance[300]. These simulations have the potential to significantly improve the design and performance of LIBs by providing insights into the complex electrochemical processes involved in battery operation. Advancements in computational power are anticipated to enhance the accuracy and predictability of KMC simulations, leading to further progress in a research and development areas.

6. Acknowledgements

I would like to express my sincere gratitude to my family and friends for their unwavering support throughout my PhD journey. A special thank you to my wife, Mahdiyeh, who played a pivotal role in changing my life by encouraging me to pursue my dreams in Germany and standing by me through the ups and downs of this challenging path.

I also want to acknowledge my supervisors, particularly Prof. Wenzel, for providing me with the opportunity to work and conduct research in his esteemed group. His guidance, insights, and expertise have been invaluable in shaping my academic and professional growth.

I am deeply grateful for the support and encouragement of my loved ones and colleagues, without whom this achievement would not have been possible.

7. List of publications

Esmaeilpour, M., Jana, S., Li, H., Soleymanibrojeni, M., Wenzel, W. (2023). A Solution-Mediated Pathway for the Growth of the Solid Electrolyte Interphase in Lithium-Ion Batteries. In Advanced Energy Materials (p. 2203966). Wiley. https://doi.org/10.1002/aenm.202203966

Esmaeilpour, Meysam; Bügel, Patrick; Fink, Karin; Studt, Felix; Wenzel, Wolfgang; Kozlowska, Mariana. Multiscale model of CVD growth of graphene on Cu (111) surface. [Submitted in JCTC]

Appendix

A. Evolution of net rate constant with time for AS-KMC and FSR-KMC simulations : Chapter 3

The time-dependent evolution of the net occurrence rate of all the reactions involved (reactions 1 to 18, as shown in Table 3.2) was analyzed for the given simulations. Figures A.1 to A.6 illustrate that the reaction rates change during the simulation and eventually attain a steady state value. It was anticipated that the rates would achieve a steady state value when the species concentrations reach their steady state values, based on the fact that the rate (probability) of reactions can be expressed as the product of the rate constant (provided in Table 3.2) and the species concentrations. The steady-state rate values are presented in Figure 3.34.

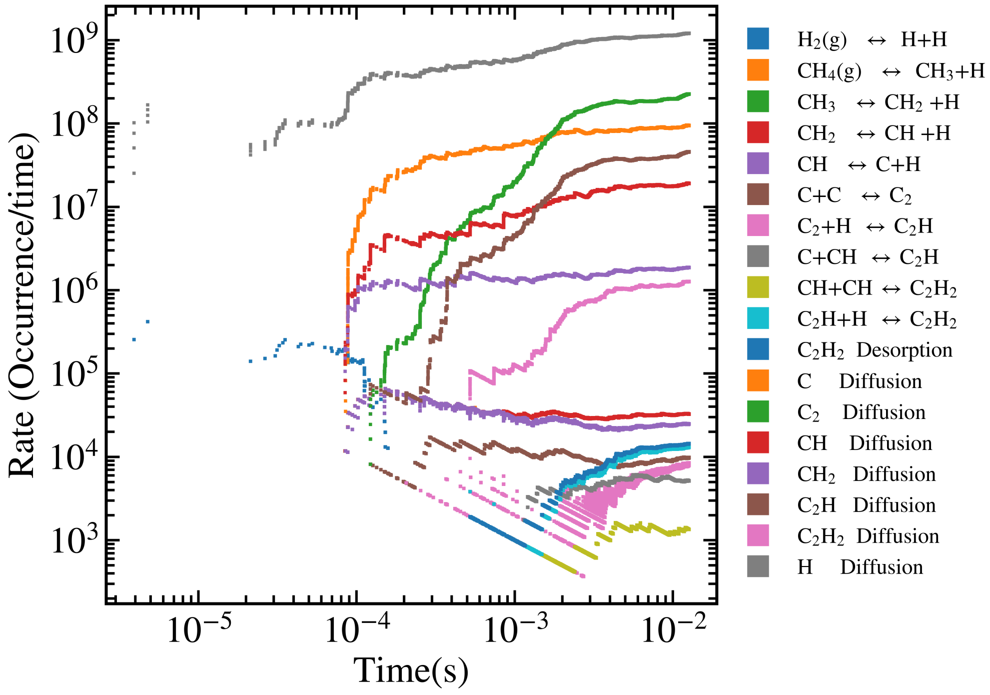

Figure A.1.: Evolution of net rate constant with time for AS-KMC simulation with $\delta = 0.3$. Net rate constant is calculated as forward minus backward occurrence per time.

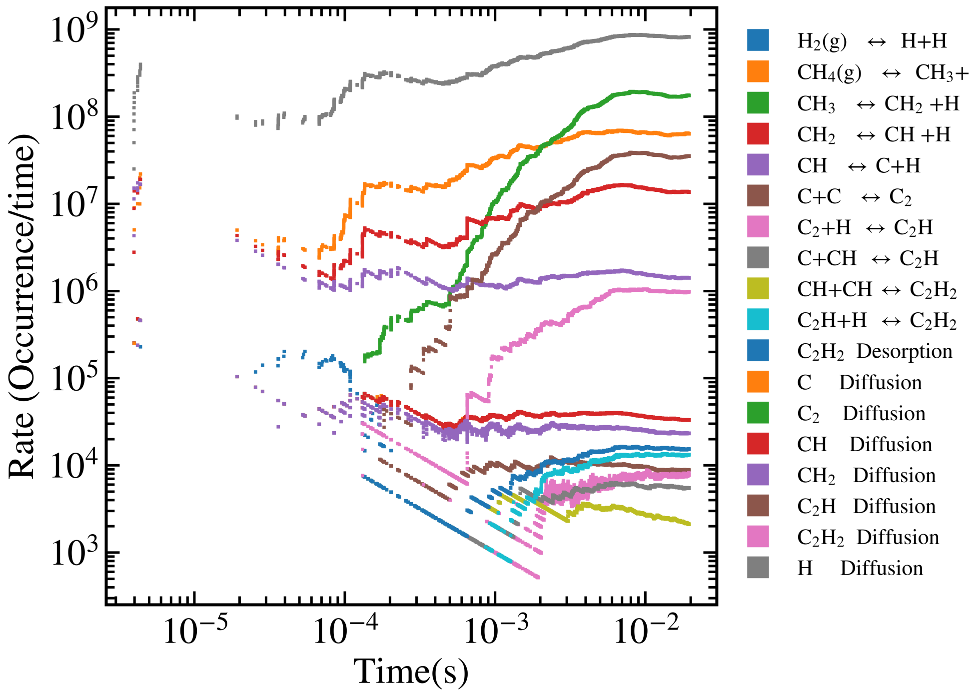

Figure A.2.: Evolution of net rate constant with time for AS-KMC simulation with $\delta = 0.4$. Net rate constant is calculated as forward minus backward occurrence per time.

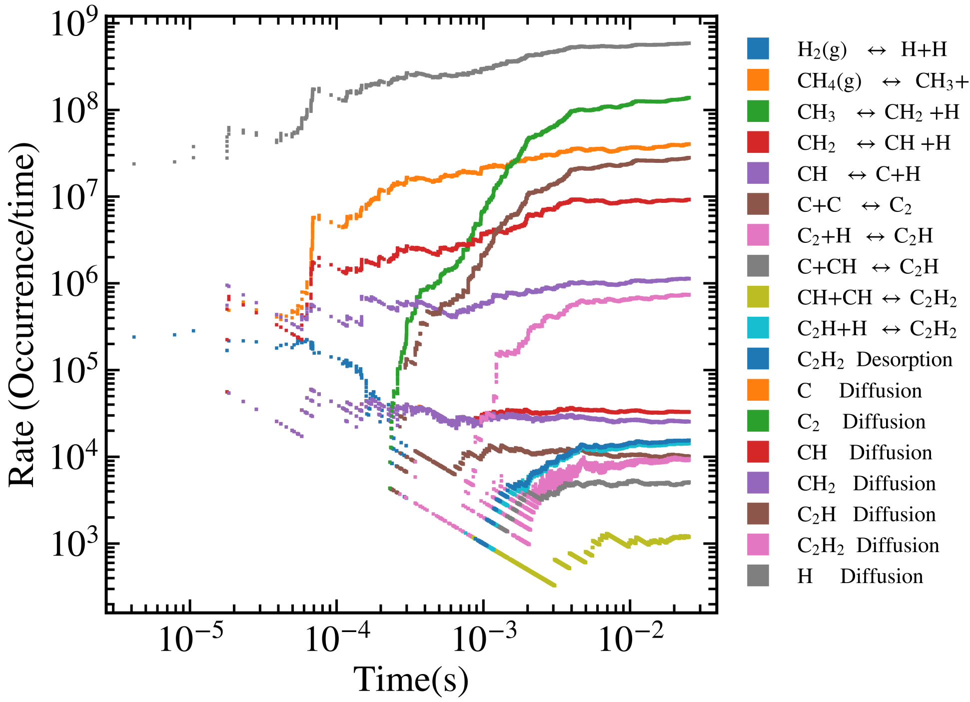

Figure A.3.: Evolution of net rate constant with time for AS-KMC simulation with $\delta = 0.5$. Net rate constant is calculated as forward minus backward occurrence per time.

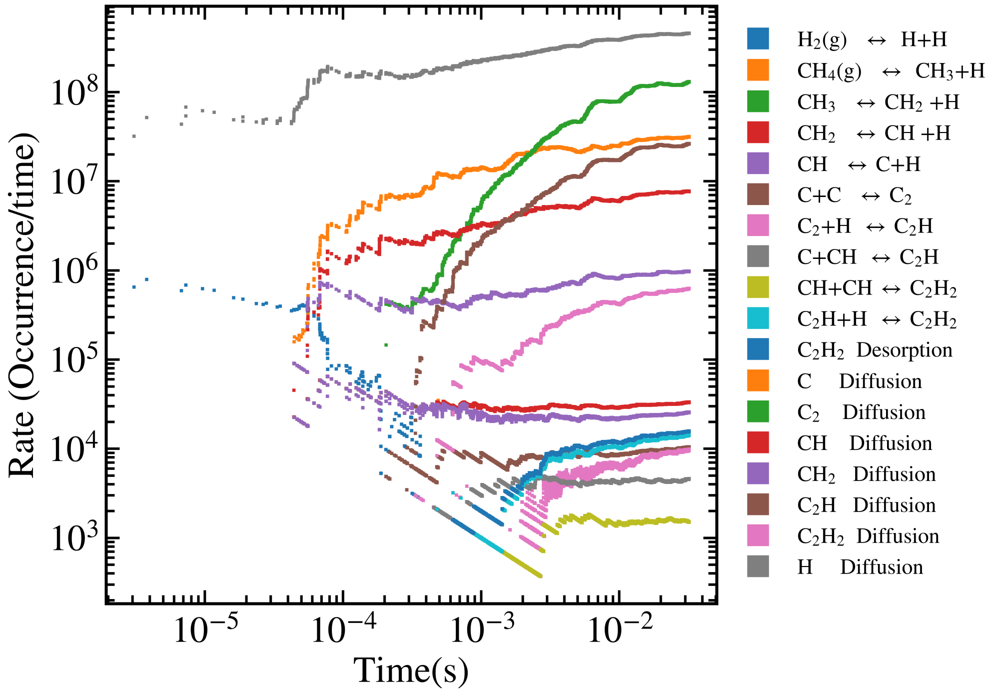

Figure A.4.: Evolution of net rate constant with time for AS-KMC simulation with $\delta =$ 0.6. Net rate constant is calculated as forward minus backward occurrence per time.

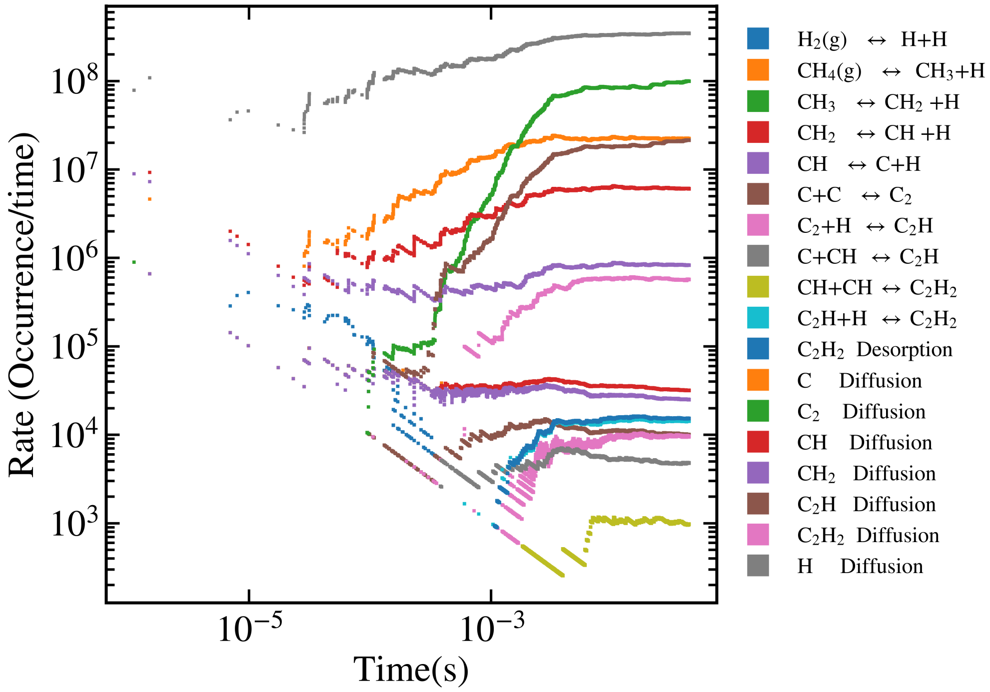

Figure A.5.: Evolution of net rate constant with time for AS-KMC simulation with $\delta =$ 0.7. Net rate constant is calculated as forward minus backward occurrence per time.

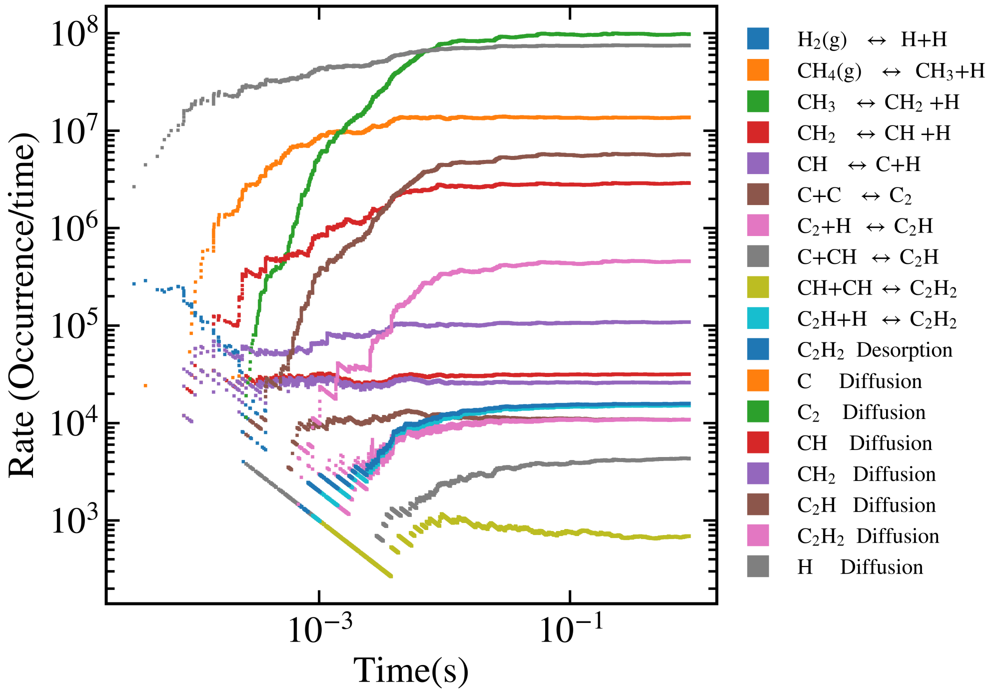

Figure A.6.: Evolution of net rate constant with time for FSR-KMC. Net rate constant is calculated as forward minus backward occurrence per time.

B. Latin-Hypercube (lhs): Chapter 4

We employed the python pyDOE package[276] to generate random barrier lists. In this package, the latin-hypercube designs can be created via the following syntax:

$$lhs(n = 15,\ [samples = 50,000,\ criterion = "correlation"])$$

Where n, samples, and criterion are the number of barriers, the number of samples, and the way this function sample the points (here "correlation" stands for minimizing the maximum correlation coefficient). in general:

- “center” or “c”: center the points within the sampling intervals.
- “maximin” or “m”: maximize the minimum distance between points, but place the point in a randomized location within its interval.
- “centermaximin” or “cm”: same as “maximin”, but centered within the intervals.
- “correlation” or “corr”: minimize the maximum correlation coefficient

The sampling result was a 50000×15 parameter space where each row contains 15 randomly generated activation energy barriers representing the specific sample.

C. Dataset, including barriers and SEI observables: Chapter 4

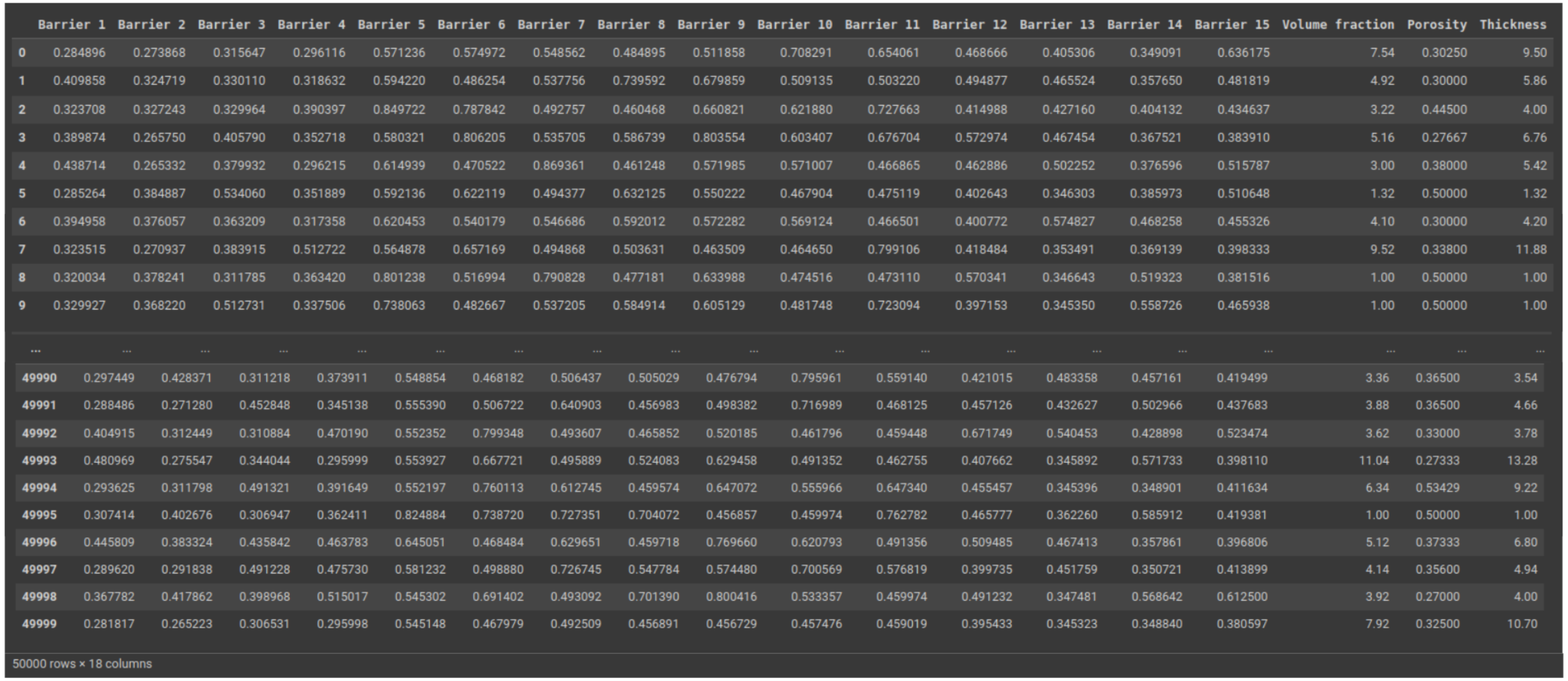

	Barrier 1	Barrier 2	Barrier 3	Barrier 4	Barrier 5	Barrier 6	Barrier 7	Barrier 8	Barrier 9	Barrier 10	Barrier 11	Barrier 12	Barrier 13	Barrier 14	Barrier 15	Volume fraction	Porosity	Thickness
0	0.284896	0.273868	0.315647	0.296116	0.571236	0.574972	0.548562	0.484895	0.511858	0.708291	0.654061	0.468666	0.405306	0.349091	0.636175	7.54	0.30250	9.50
1	0.409858	0.324719	0.330110	0.318632	0.594220	0.486254	0.537756	0.739592	0.679859	0.509135	0.503220	0.494877	0.465524	0.357650	0.481819	4.92	0.30000	5.86
2	0.323708	0.327243	0.329964	0.390397	0.849722	0.787842	0.492757	0.460468	0.660821	0.621880	0.727663	0.414988	0.427160	0.404132	0.434637	3.22	0.44500	4.00
3	0.389874	0.265750	0.405790	0.352718	0.580321	0.806205	0.535705	0.586739	0.803554	0.603407	0.676704	0.572974	0.467454	0.367521	0.383910	5.16	0.27667	6.76
4	0.438714	0.265332	0.379932	0.296215	0.614939	0.470522	0.869361	0.461248	0.571985	0.571007	0.466865	0.462886	0.502252	0.376596	0.515787	3.00	0.38000	5.42
5	0.285264	0.384887	0.534060	0.351889	0.592136	0.622119	0.494377	0.632125	0.550222	0.467904	0.475119	0.402643	0.346303	0.385973	0.510648	1.32	0.50000	1.32
6	0.394958	0.376057	0.363209	0.317358	0.620453	0.540179	0.546686	0.592012	0.572282	0.569124	0.466501	0.400772	0.574827	0.468258	0.455326	4.10	0.30000	4.20
7	0.323515	0.270937	0.383915	0.512722	0.564878	0.657169	0.494868	0.503631	0.463509	0.464650	0.799106	0.418484	0.353491	0.369139	0.398333	9.52	0.33800	11.88
8	0.320034	0.378241	0.311785	0.363420	0.801238	0.516994	0.790828	0.477181	0.633988	0.474516	0.473110	0.570341	0.346643	0.519323	0.381516	1.00	0.50000	1.00
9	0.329927	0.368220	0.512731	0.337506	0.738063	0.482667	0.537205	0.584914	0.605129	0.481748	0.723094	0.397153	0.345350	0.558726	0.465938	1.00	0.50000	1.00
...	...	...	...	...	...	...	...	...	...	...	...	...	...	...	...	...	...	...
49990	0.297449	0.428371	0.311218	0.373911	0.548854	0.468182	0.506437	0.505029	0.476794	0.795961	0.559140	0.421015	0.483358	0.457161	0.419499	3.36	0.36500	3.54
49991	0.288486	0.271280	0.452848	0.345138	0.555390	0.506722	0.640903	0.456983	0.498382	0.716989	0.468125	0.457126	0.432627	0.502966	0.437683	3.88	0.36500	4.66
49992	0.404915	0.312449	0.310884	0.470190	0.552352	0.799348	0.493607	0.465852	0.520185	0.461796	0.459448	0.671749	0.540453	0.428898	0.523474	3.62	0.33000	3.78
49993	0.480969	0.275547	0.344044	0.295999	0.553927	0.667721	0.495889	0.524083	0.629458	0.491352	0.462755	0.407662	0.345892	0.571733	0.398110	11.04	0.27333	13.28
49994	0.293625	0.311798	0.491321	0.391649	0.552197	0.760113	0.612745	0.459574	0.647072	0.555966	0.647340	0.455457	0.345396	0.348901	0.411634	6.34	0.53429	9.22
49995	0.307414	0.402676	0.306947	0.362411	0.824884	0.738720	0.727351	0.704072	0.456857	0.459974	0.762782	0.465777	0.362260	0.585912	0.419381	1.00	0.50000	1.00
49996	0.445809	0.383324	0.435842	0.463783	0.645051	0.468484	0.629651	0.459718	0.769660	0.620793	0.491356	0.509485	0.467413	0.357861	0.396806	5.12	0.37333	6.80
49997	0.289620	0.291838	0.491228	0.475730	0.581232	0.498880	0.726745	0.547784	0.574480	0.700569	0.576819	0.399735	0.451759	0.350721	0.413899	4.14	0.35600	4.94
49998	0.367782	0.417862	0.398968	0.515017	0.545302	0.691402	0.493092	0.701390	0.800416	0.533357	0.459974	0.491232	0.347481	0.568642	0.612500	3.92	0.27000	4.00
49999	0.281817	0.265223	0.306531	0.295998	0.545148	0.467979	0.492509	0.456891	0.456729	0.457476	0.459019	0.395433	0.345323	0.348840	0.380597	7.92	0.32500	10.70

50000 rows × 18 columns

Figure C.7.: A section of dataset as 50,000×18 table including reaction barriers and SEI obervables. To evaluate the formation close to the electrode, only the first 15 reactions are considered.

D. Samples from bad, inorganic, and good SEI regions : Chapter 4

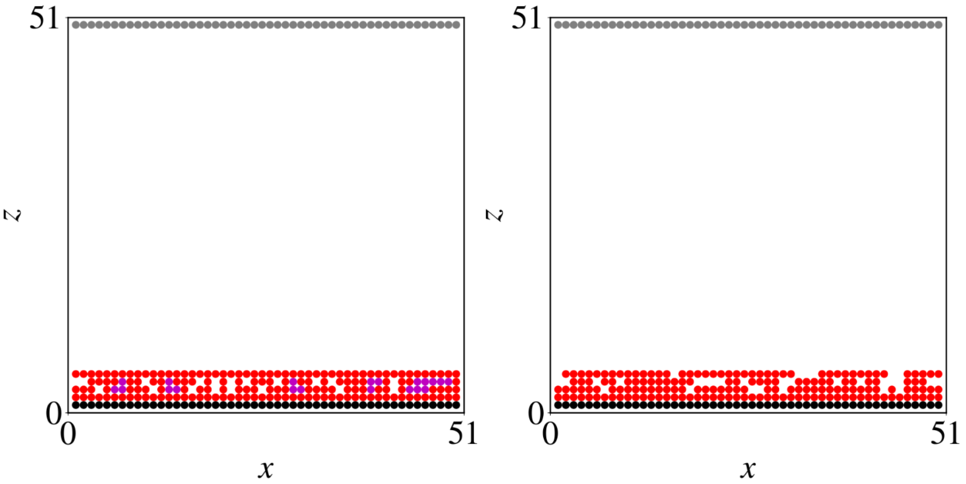

sample 3 sample 66

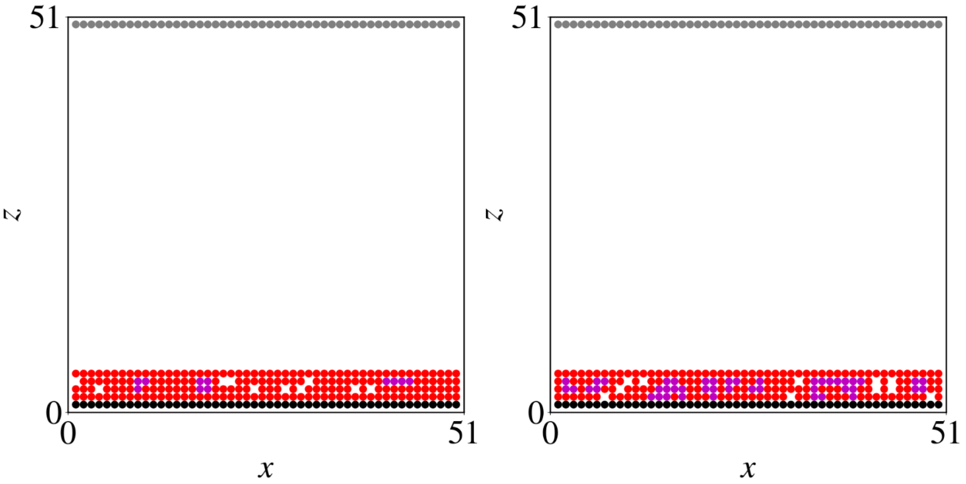

sample 100 sample 107

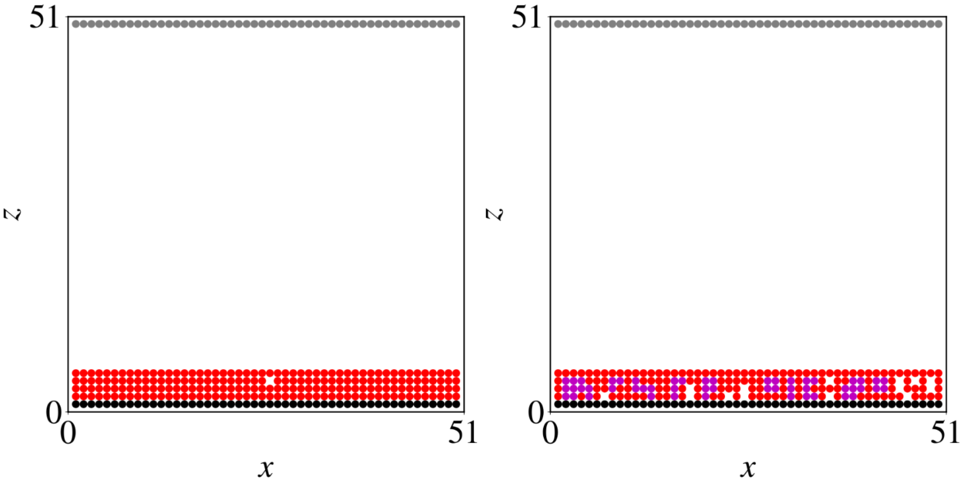

sample 300 sample 337

Figure D.8.: Samples taken from region 1 where inorganic SEI forms (labeled from 50000 dataset). Organic, inorganic SEI components are shown in red and purple respectively.

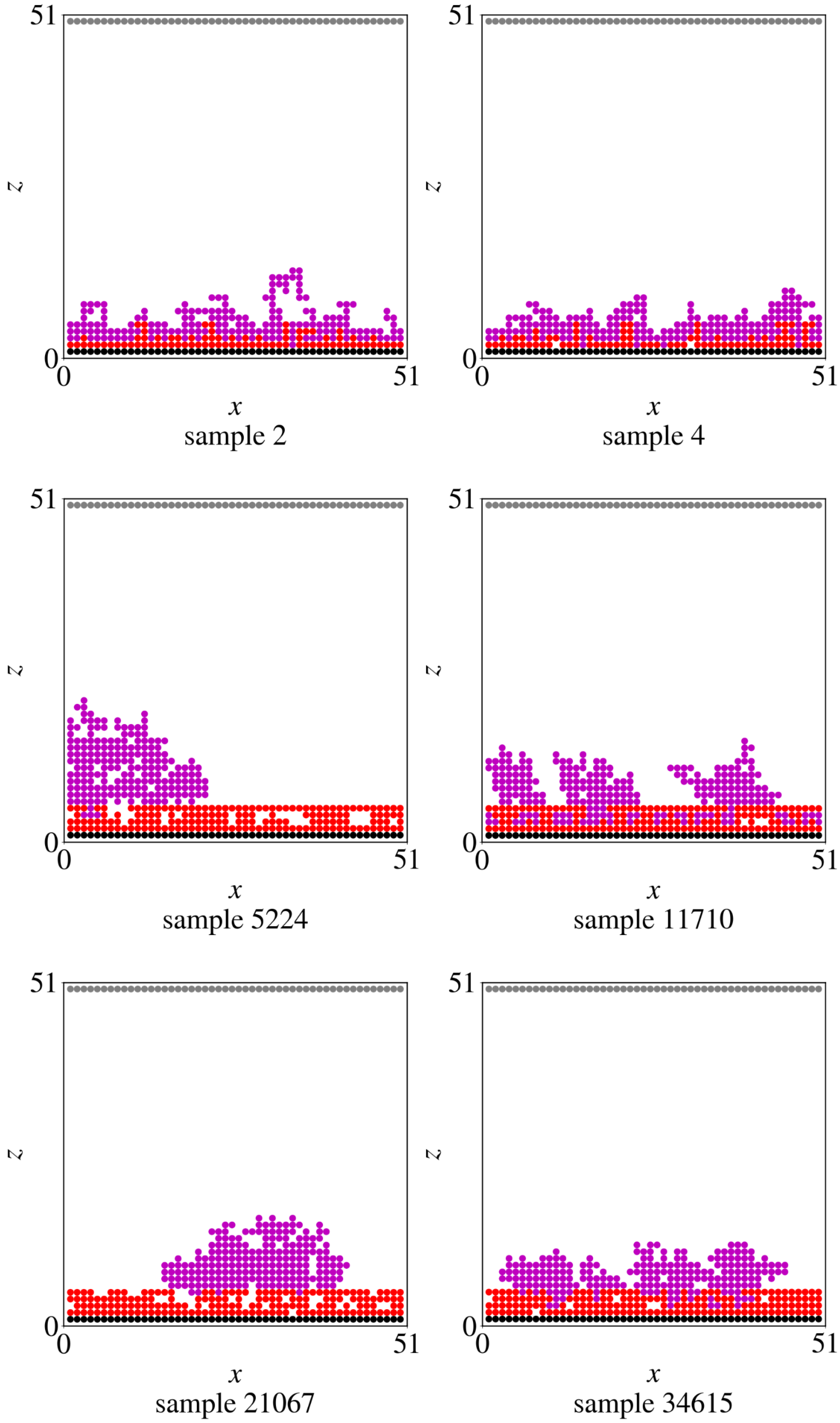

sample 2

sample 4

sample 5224

sample 11710

sample 21067

sample 34615

Figure D.9.: Samples taken from region 2 where bad SEI forms (labeled from 50000 dataset). Organic, inorganic SEI components are shown in red and purple respectively.

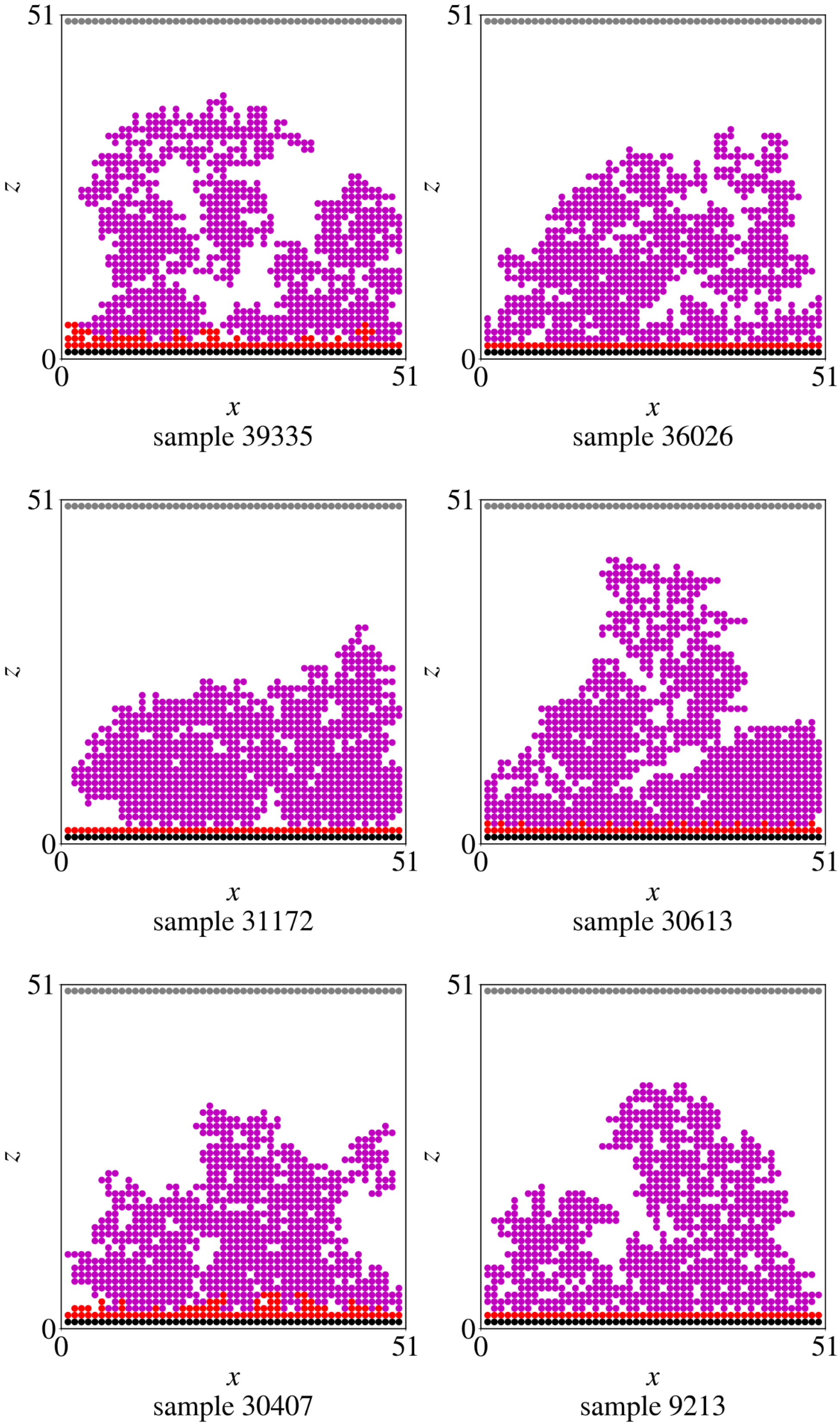

sample 39335

sample 36026

sample 31172

sample 30613

sample 30407

sample 9213

Figure D.10.: Samples taken from region 3 where good SEI forms (labeled from 50000 dataset). Organic, inorganic SEI components are shown in red and purple respectively.

E. Good SEI samples growth multi-panel plots

Two further simulation cases where the SEI nucleation and growth are shown using multi-panel figures E.11 and E.12. Both cases indicate the far nucleation of SEI cluster and downward growth because of the gradient of Li_2EDC on the lattice.

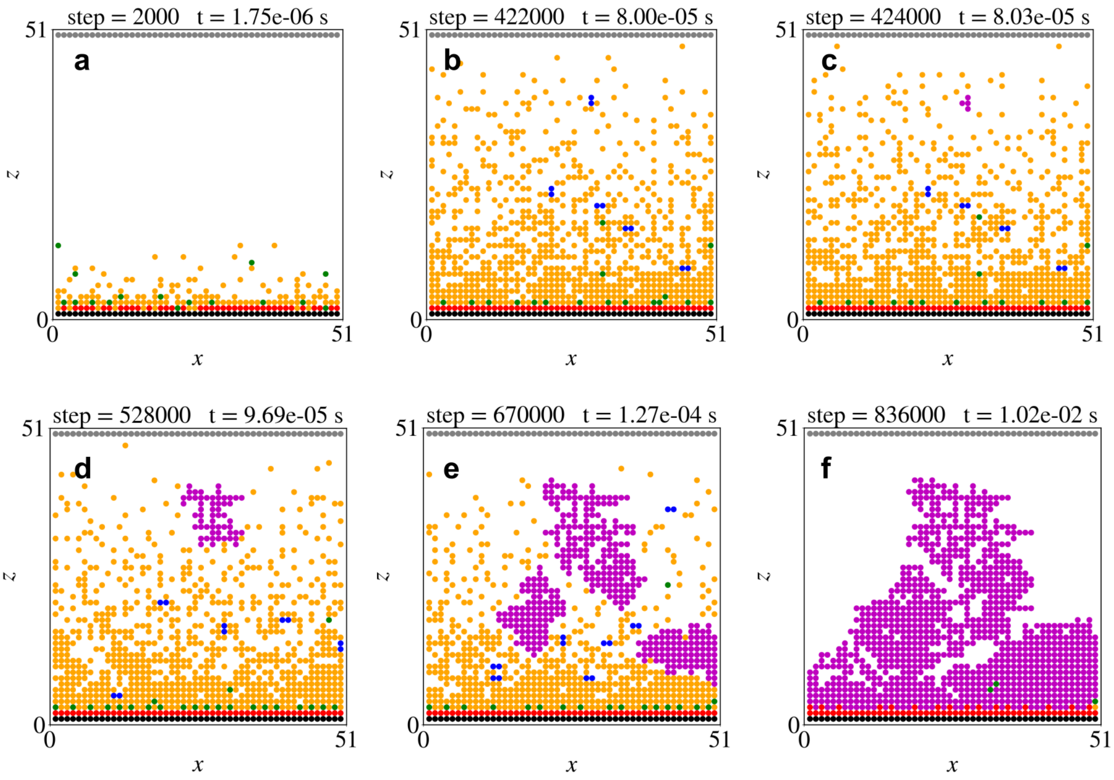

Figure E.11.: Different snapshots of the KMC simulation (50 × 50 nm^2) for the sample 30613 at the indicated time. In the simulation box, the graphite electrode layer is implemented at the bottom (black), the absorbing open interface at the top. Initially, all other sites are occupied by EC-Li^+ (white), the precursor for the SEI formation at the start of the simulation. The reaction intermediates and products, namely Li_2CO_3, $C_2H_4OCOOLi$, Li_2EDC, $(Li_2EDC)_2$, and organic SEI clusters are represented by red, green, orange, blue, and purple sites, respectively (see 4.2). During the simulation, a) $C_2H_4OCOOLi$ (green) and Li_2EDC (orange) form rapidly a stable inorganic SEI layer (red), and b) Li_2EDC (orange) dimerized to form $(Li_2EDC)_2$ (blue). SEI clusters (purple) start to grow (c-e) away from the electrode presence of $(Li_2EDC)_2$ and Li_2EDC, and the organic SEI deposited (f) on the inorganic SEI to form porous immovable SEI.

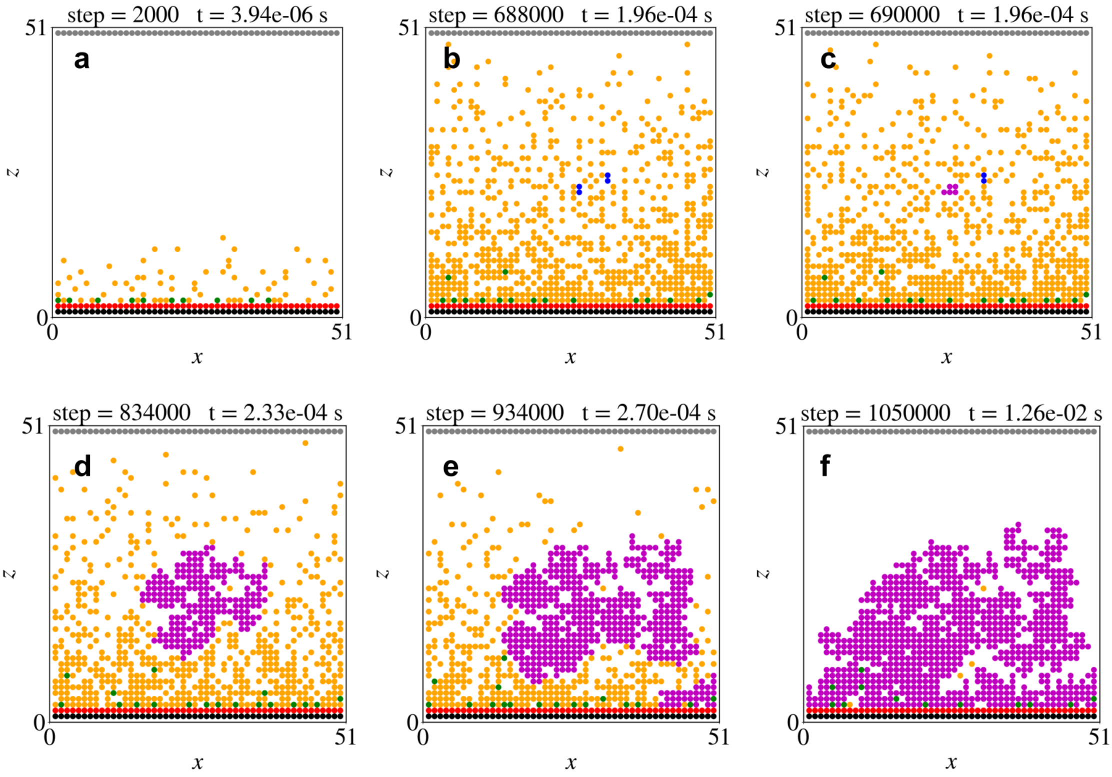

Figure E.12.: Different snapshots of the KMC simulation (50 × 50 nm^2) for the sample 36026 at the indicated time (see SI). In the simulation box, the graphite electrode layer is implemented at the bottom (black), the absorbing open interface at the top. Initially, all other sites are occupied by EC-Li$^+$ (white), the precursor for the SEI formation at the start of the simulation. The reaction intermediates and products, namely Li_2CO_3, $C_2H_4OCOOLi$, Li_2EDC, $(Li_2EDC)_2$, and organic SEI clusters are represented by red, green, orange, blue, and purple sites, respectively (see 4.2). During the simulation, a) $C_2H_4OCOOLi$ (green) and Li_2EDC (orange) form rapidly a stable inorganic SEI layer (red), and b) Li_2EDC (orange) dimerized to form $(Li_2EDC)_2$ (blue). SEI clusters (purple) start to grow (c-e) away from the electrode presence of $(Li_2EDC)_2$ and Li_2EDC, and the organic SEI deposited (f) on the inorganic SEI to form porous immovable SEI.

F. Correlation matrix plot of all barriers and SEI obseravles: Chapter 4

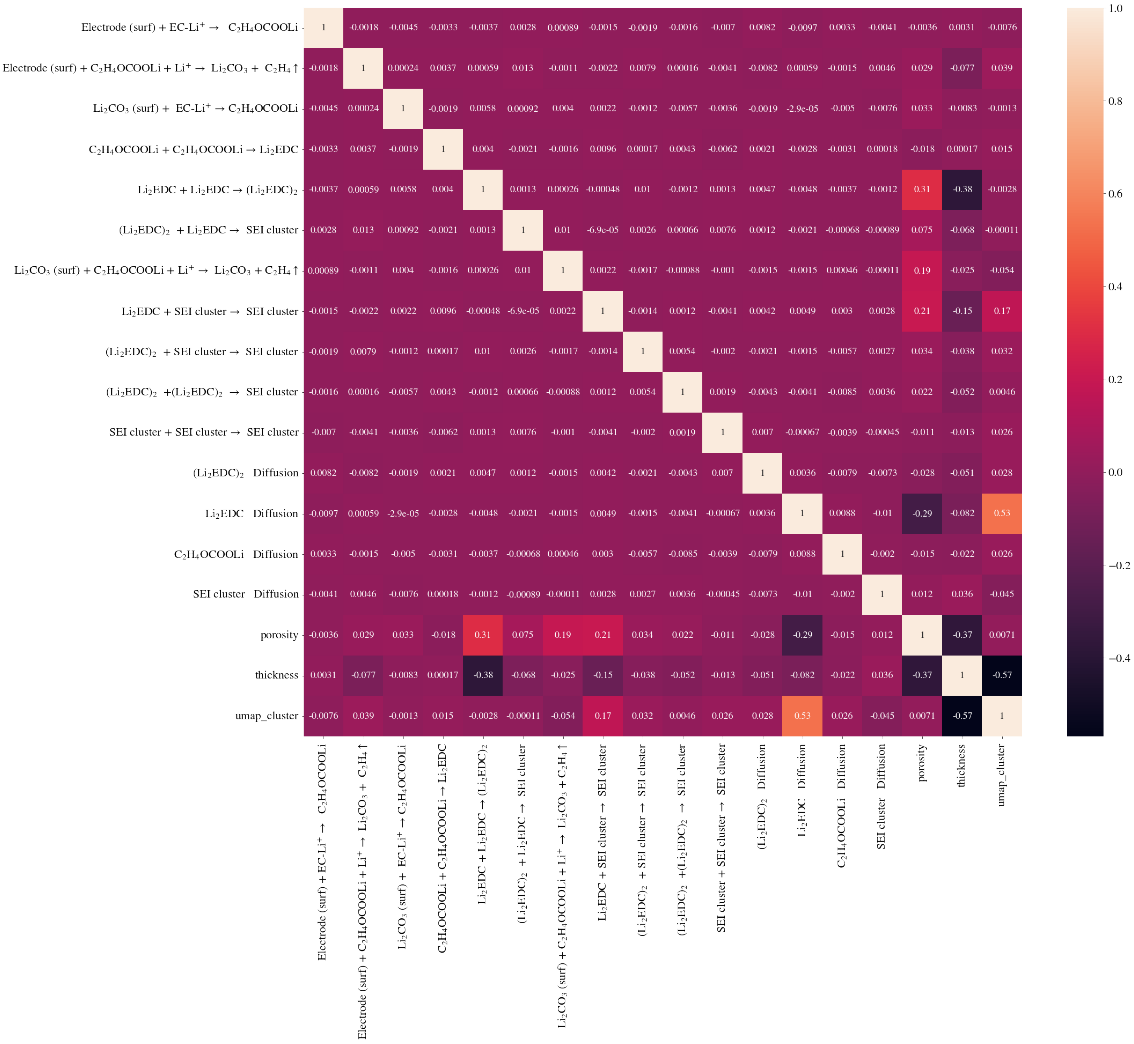

	Electrode (surf) + EC-Li$^+$ → $C_2H_4OCOOLi$	Electrode (surf) + $C_2H_4OCOOLi$ + Li$^+$ → Li_2CO_3 + C_2H_4 ↑	Li_2CO_3 (surf) + EC-Li$^+$ → $C_2H_4OCOOLi$	$C_2H_4OCOOLi$ + $C_2H_4OCOOLi$ → Li_2EDC	Li_2EDC + Li_2EDC → $(Li_2EDC)_2$	$(Li_2EDC)_2$ + Li_2EDC → SEI cluster	Li_2CO_3 (surf) + $C_2H_4OCOOLi$ + Li$^+$ → Li_2CO_3 + C_2H_4 ↑	Li_2EDC + SEI cluster → SEI cluster	$(Li_2EDC)_2$ + SEI cluster → SEI cluster	$(Li_2EDC)_2$ +$(Li_2EDC)_2$ → SEI cluster	SEI cluster + SEI cluster → SEI cluster	$(Li_2EDC)_2$ Diffusion	Li_2EDC Diffusion	$C_2H_4OCOOLi$ Diffusion	SEI cluster Diffusion	porosity	thickness	umap_cluster
Electrode (surf) + EC-Li$^+$ → $C_2H_4OCOOLi$	1	-0.0018	-0.0045	-0.0033	-0.0037	0.0028	0.00089	-0.0015	-0.0019	-0.0016	-0.007	0.0082	-0.0097	0.0033	-0.0041	-0.0036	0.0031	-0.0076
Electrode (surf) + $C_2H_4OCOOLi$ + Li$^+$ → Li_2CO_3 + C_2H_4 ↑	-0.0018	1	0.00024	0.0037	0.00059	0.013	-0.0011	-0.0022	0.0079	0.00016	-0.0041	-0.0082	0.00059	-0.0015	0.0046	0.029	-0.077	0.039
Li_2CO_3 (surf) + EC-Li$^+$ → $C_2H_4OCOOLi$	-0.0045	0.00024	1	-0.0019	0.0058	0.00092	0.004	0.0022	-0.0012	-0.0057	-0.0036	-0.0019	-2.9e-05	-0.005	-0.0076	0.033	-0.0083	-0.0013
$C_2H_4OCOOLi$ + $C_2H_4OCOOLi$ → Li_2EDC	-0.0033	0.0037	-0.0019	1	0.004	-0.0021	-0.0016	0.0096	0.00017	0.0043	-0.0062	0.0021	-0.0028	-0.0031	0.00018	-0.018	0.00017	0.015
Li_2EDC + Li_2EDC → $(Li_2EDC)_2$	-0.0037	0.00059	0.0058	0.004	1	0.0013	0.00026	-0.00048	0.01	-0.0012	0.0013	0.0047	-0.0048	-0.0037	-0.0012	0.31	-0.38	-0.0028
$(Li_2EDC)_2$ + Li_2EDC → SEI cluster	0.0028	0.013	0.00092	-0.0021	0.0013	1	0.01	-6.9e-05	0.0026	0.00066	0.0076	0.0012	-0.0021	-0.00068	-0.00089	0.075	-0.068	-0.00011
Li_2CO_3 (surf) + $C_2H_4OCOOLi$ + Li$^+$ → Li_2CO_3 + C_2H_4 ↑	0.00089	-0.0011	0.004	-0.0016	0.00026	0.01	1	0.0022	-0.0017	-0.00088	-0.001	-0.0015	-0.0015	0.00046	-0.00011	0.19	-0.025	-0.054
Li_2EDC + SEI cluster → SEI cluster	-0.0015	-0.0022	0.0022	0.0096	-0.00048	-6.9e-05	0.0022	1	-0.0014	0.0012	-0.0041	0.0042	0.0049	0.003	0.0028	0.21	-0.15	0.17
$(Li_2EDC)_2$ + SEI cluster → SEI cluster	-0.0019	0.0079	-0.0012	0.00017	0.01	0.0026	-0.0017	-0.0014	1	0.0054	-0.002	-0.0021	-0.0015	-0.0057	0.0027	0.034	-0.038	0.032
$(Li_2EDC)_2$ +$(Li_2EDC)_2$ → SEI cluster	-0.0016	0.00016	-0.0057	0.0043	-0.0012	0.00066	-0.00088	0.0012	0.0054	1	0.0019	-0.0043	-0.0041	-0.0085	0.0036	0.022	-0.052	0.0046
SEI cluster + SEI cluster → SEI cluster	-0.007	-0.0041	-0.0036	-0.0062	0.0013	0.0076	-0.001	-0.0041	-0.002	0.0019	1	0.007	-0.00067	-0.0039	-0.00045	-0.011	-0.013	0.026
$(Li_2EDC)_2$ Diffusion	0.0082	-0.0082	-0.0019	0.0021	0.0047	0.0012	-0.0015	0.0042	-0.0021	-0.0043	0.007	1	0.0036	-0.0079	-0.0073	-0.028	-0.051	0.028
Li_2EDC Diffusion	-0.0097	0.00059	-2.9e-05	-0.0028	-0.0048	-0.0021	-0.0015	0.0049	-0.0015	-0.0041	-0.00067	0.0036	1	0.0088	-0.01	-0.29	-0.082	0.53
$C_2H_4OCOOLi$ Diffusion	0.0033	-0.0015	-0.005	-0.0031	-0.0037	-0.00068	0.00046	0.003	-0.0057	-0.0085	-0.0039	-0.0079	0.0088	1	-0.002	-0.015	-0.022	0.026
SEI cluster Diffusion	-0.0041	0.0046	-0.0076	0.00018	-0.0012	-0.00089	-0.00011	0.0028	0.0027	0.0036	-0.00045	-0.0073	-0.01	-0.002	1	0.012	0.036	-0.045
porosity	-0.0036	0.029	0.033	-0.018	0.31	0.075	0.19	0.21	0.034	0.022	-0.011	-0.028	-0.29	-0.015	0.012	1	-0.37	0.0071
thickness	0.0031	-0.077	-0.0083	0.00017	-0.38	-0.068	-0.025	-0.15	-0.038	-0.052	-0.013	-0.051	-0.082	-0.022	0.036	-0.37	1	-0.57
umap_cluster	-0.0076	0.039	-0.0013	0.015	-0.0028	-0.00011	-0.054	0.17	0.032	0.0046	0.026	0.028	0.53	0.026	-0.045	0.0071	-0.57	1

Figure F.13.: Correlation matrix plot of all barriers (except escape ones) and observables (SEI thickness and porosity) where 0 is for no linear correlation, and any positive and negative values indicate the positive and negative linear correlation between two variables.

Bibliography

[1] Richard A Kerr. A frontal attack on a paradigm of meteorology: researchers are grappling with how to bring the 70-year-old concept of weather fronts and storms into the modern age. *Science*, 254(5038):1591–1592, 1991.

[2] Philippe Thunis and R Bornstein. Hierarchy of mesoscale flow assumptions and equations. *Journal of atmospheric sciences*, 53(3):380–397, 1996.

[3] M Rieth. Handbook of theoretical and computational nanotechnology: 10 volumes. volume 1. basic concepts, nanomachines, and medical nanodevices= s tay công ngh nanô/nano lỳ thuyt và đin toán: 10 tp. tp 1. nhng khái nim c bn, máy nanô và thit b nanô y t, 2006.

[4] Leo P Kouwenhoven, Charles M Marcus, Paul L McEuen, Seigo Tarucha, Robert M Westervelt, and Ned S Wingreen. Electron transport in quantum dots. *Mesoscopic electron transport*, pages 105–214, 1997.

[5] Jacob Fish. *Multiscale methods: bridging the scales in science and engineering.* Oxford University Press on Demand, 2010.

[6] Theodoros E Karakasidis and CA Charitidis. Multiscale modeling in nanomaterials science. *Materials Science and Engineering: C*, 27(5-8):1082–1089, 2007.

[7] Gary S Ayton, Will G Noid, and Gregory A Voth. Multiscale modeling of biomolecular systems: in serial and in parallel. *Current opinion in structural biology*, 17(2):192–198, 2007.

[8] Valentina Tozzini. Multiscale modeling of proteins. *Accounts of chemical research*, 43(2):220–230, 2010.

[9] John C Dallon. Multiscale modeling of cellular systems in biology. *Current opinion in colloid & interface science*, 15(1-2):24–31, 2010.

[10] CWJ Beenakker and Henk van Houten. Quantum transport in semiconductor nanostructures. In *Solid state physics*, volume 44, pages 1–228. Elsevier, 1991.

[11] Arieh Aviram and Mark A Ratner. Molecular rectifiers. *Chemical physics letters*, 29(2):277–283, 1974.

[12] Supriyo Datta. *Electronic transport in mesoscopic systems.* Cambridge university press, 1997.

[13] Yoseph Imry. *Introduction to mesoscopic physics.* Number 2. Oxford University Press on Demand, 2002.

[14] Eric Akkermans and Gilles Montambaux. *Mesoscopic physics of electrons and photons.* Cambridge university press, 2007.

[15] Antti-Pekka Jauho, Ned S Wingreen, and Yigal Meir. Time-dependent transport in interacting and noninteracting resonant-tunneling systems. *Physical Review B*, 50(8):5528, 1994.

[16] Wenlai Huang, Jinghai Li, and Peter P Edwards. Mesoscience: exploring the common principle at mesoscales. *National Science Review*, 5(3):321–326, August 2017.

[17] D ben Avraham. Cellular automata modeling of physical systems. *JOURNAL OF STATISTICAL PHYSICS*, 97(5/6):1031–1032, 1999.

[18] TS Gates, GM Odegard, SJV Frankland, and TC Clancy. Computational materials: multi-scale modeling and simulation of nanostructured materials. *Composites Science and Technology*, 65(15-16):2416–2434, 2005.

[19] Harry A Atwater and Albert Polman. Plasmonics for improved photovoltaic devices. *Nature materials*, 9(3):205–213, 2010.

[20] Joseph O Dada and Pedro Mendes. Multi-scale modelling and simulation in systems biology. *Integrative Biology*, 3(2):86–96, 2011.

[21] Qi-Qi Yang, Rui-Tong Liu, Chao Huang, Yi-Fan Huang, Lin-Feng Gao, Bing Sun, Zhi-Peng Huang, Lei Zhang, Chen-Xia Hu, Ze-Qi Zhang, et al. 2d bismuthene fabricated via acid-intercalated exfoliation showing strong nonlinear near-infrared responses for mode-locking lasers. *Nanoscale*, 10(45):21106–21115, 2018.

[22] Gerd Binnig, Calvin F Quate, and Ch Gerber. Atomic force microscope. *Physical review letters*, 56(9):930, 1986.

[23] Vladimir I Fal'ko and KB Efetov. Statistics of wave functions in mesoscopic systems. *Journal of Mathematical Physics*, 37(10):4935–4967, 1996.

[24] Branislav K Nikolić. Statistical properties of eigenstates in three-dimensional mesoscopic systems with off-diagonal or diagonal disorder. *Physical Review B*, 64(1):014203, 2001.

[25] Peter Kuchment. Differential and pseudo-differential operators on graphs as models of mesoscopic systems. *Analysis and Applications—ISAAC 2001*, pages 7–30, 2003.

[26] MP Allen and DJ Tildesley. Computer simulation of liquids oxford university press oxford 385. 1987.

[27] William L Jorgensen, Jayaraman Chandrasekhar, Jeffry D Madura, Roger W Impey, and Michael L Klein. Comparison of simple potential functions for simulating liquid water. *The Journal of chemical physics*, 79(2):926–935, 1983.

[28] Robert Byron Bird, Charles F Curtiss, Robert C Armstrong, and Ole Hassager. *Dynamics of polymeric liquids, volume 2: Kinetic theory.* Wiley, 1987.

[29] Todd M Squires and Stephen R Quake. Microfluidics: Fluid physics at the nanoliter scale. *Reviews of modern physics*, 77(3):977, 2005.

[30] Hongmei Liu, Zhixiang Gao, Yongqiang Kang, and Yunlong Shi. Monte carlo simulation of electrons transport in quantum dot infrared photodetector. *Journal of Computational and Theoretical Nanoscience*, 12(10):3735–3738, 2015.

[31] Ya M Blanter and Markus Büttiker. Shot noise in mesoscopic conductors. *Physics reports*, 336(1-2):1–166, 2000.

[32] Gerald D Mahan. *Many-particle physics.* Springer Science & Business Media, 2000.

[33] Jianzhong Wu. Density functional theory for chemical engineering: From capillarity to soft materials. *AIChE journal*, 52(3):1169–1193, 2006.

[34] Mingguang Li, Haitao Yu, Jianhua Wang, Xiaohe Xia, and Jinjian Chen. A multiscale coupling approach between discrete element method and finite difference method for dynamic analysis. *International Journal for Numerical Methods in Engineering*, 102(1):1–21, 2015.

[35] Albert Solernou, Benjamin S Hanson, Robin A Richardson, Robert Welch, Daniel J Read, Oliver G Harlen, and Sarah A Harris. Fluctuating finite element analysis (ffea): A continuum mechanics software tool for mesoscale simulation of biomolecules. *PLoS computational biology*, 14(3):e1005897, 2018.

[36] Oussama Zobiri, Abdelmalek Atia, and Müslüm Arıcı. Study of robin condition influence on phonon nano-heat conduction using meso-scale method in mosfet and soi-mosfet devices. *Materials Today Communications*, 26:102031, 2021.

[37] Carlo WJ Beenakker. Random-matrix theory of quantum transport. *Reviews of modern physics*, 69(3):731, 1997.

[38] Maurizio Fermeglia and Sabrina Pricl. Multiscale modeling for polymer systems@articlekerr1991frontal, title=A frontal attack on a paradigm of meteorology: researchers are grappling with how to bring the 70-year-old concept of weather fronts and storms into the modern age, author=Kerr, Richard A, journal=Science, volume=254, number=5038, pages=1591–1592, year=1991, publisher=American Association for the Advancement of Science of industrial interest. *Progress in Organic Coatings*, 58(2-3):187–199, 2007.

[39] Adam Hospital, Josep Ramon Goñi, Modesto Orozco, and Josep L Gelpí. Molecular dynamics simulations: advances and applications. *Advances and applications in bioinformatics and chemistry*, pages 37–47, 2015.

[40] HJC Berendsen and WF Van Gunsteren. Molecular dynamics with constraints. *The physics of superionic conductors and electrode materials*, pages 221–240, 1983.

[41] Carlos A Felippa. Introduction to finite element methods. *University of Colorado*, 885, 2004.

[42] Sharon C Glotzer and Wolfgang Paul. Molecular and mesoscale simulation methods for polymer materials. *Annual Review of Materials Research*, 32(1):401–436, 2002.

[43] Peter D Yeh and Alexander Alexeev. Mesoscale modelling of environmentally responsive hydrogels: emerging applications. *Chemical Communications*, 51(50):10083–10095, 2015.

[44] Bernard Brogliato, Rogelio Lozano, Bernhard Maschke, Olav Egeland, et al. Dissipative systems analysis and control. *Theory and Applications*, 2:2–5, 2007.

[45] Zachary Grant Mills, Wenbin Mao, and Alexander Alexeev. Mesoscale modeling: solving complex flows in biology and biotechnology. *Trends in biotechnology*, 31(7):426–434, 2013.

[46] Risto M Nieminen. From atomistic simulation towards multiscale modelling of materials. *Journal of Physics: Condensed Matter*, 14(11):2859, 2002.

[47] Fang-Zhou Yao, Qibin Yuan, Qing Wang, and Hong Wang. Multiscale structural engineering of dielectric ceramics for energy storage applications: from bulk to thin films. *Nanoscale*, 12(33):17165–17184, 2020.

[48] A.B. Bortz, M.H. Kalos, and J.L. Lebowitz. A new algorithm for monte carlo simulation of ising spin systems. *Journal of Computational Physics*, 17(1):10–18, 1975.

[49] Arthur F Voter. Introduction to the kinetic monte carlo method. In *Radiation effects in solids*, pages 1–23. Springer, 2007.

[50] Peifeng Zhang, Xiaoping Zheng, and Deyan He. Kinetic monte carlo simulation of thin film growth. *Science in China (Series G)*, 46:610–618, 2003.

[51] Corbett C Battaile, David J Srolovitz, and JE Butler. A kinetic monte carlo method for the atomic-scale simulation of chemical vapor deposition: application to diamond. *Journal of applied physics*, 82(12):6293–6300, 1997.

[52] Shiyun Ruan and Christopher A Schuh. Kinetic monte carlo simulations of nanocrystalline film deposition. *Journal of Applied Physics*, 107(7):073512, 2010.

[53] Biswajit Das and Gautam Gangopadhyay. Stochastic theory of interfacial enzyme kinetics: A kinetic monte carlo study. *Chemical Physics*, 393(1):58–64, 2012.

[54] Dezső Boda, David D Busath, Bob Eisenberg, Douglas Henderson, and Wolfgang Nonner. Monte carlo simulations of ion selectivity in a biological na channel: Charge–space competition. *Physical Chemistry Chemical Physics*, 4(20):5154–5160, 2002.

[55] Barry Z Shang and Jhih-Wei Chu. Kinetic modeling at single-molecule resolution elucidates the mechanisms of cellulase synergy. *Acs Catalysis*, 4(7):2216–2225, 2014.

[56] Marius Stan. Discovery and design of nuclear fuels. *Materials Today*, 12(11):20–28, November 2009.

[57] Xiao Wang Zhou, Richard A Karnesky, Nancy Yang, and Joshua K Yee. Kinetic monte carlo simulations of structural evolution during anneal of additively manufactured materials. *Computational Materials Science*, 179:109605, 2020.

[58] Ping Wu, Wenhua Zhang, Zhenyu Li, and Jinglong Yang. Mechanisms of graphene growth on metal surfaces: theoretical perspectives. *Small*, 10(11):2136–2150, 2014.

[59] Hamed Moradmand Jalali. Kinetic study of photodegradation of methylene blue over p25-graphene and p25-cnt nanocomposites using monte carlo simulation. *Russian Journal of Physical Chemistry A*, 91:1337–1344, 2017.

[60] Fridolin Röder, Richard D Braatz, and Ulrike Krewer. Multi-scale modeling of solid electrolyte interface formation in lithium-ion batteries. In *Computer Aided Chemical Engineering*, volume 38, pages 157–162. Elsevier, 2016.

[61] Ravi N Methekar, Paul WC Northrop, Kejia Chen, Richard D Braatz, and Venkat R Subramanian. Kinetic monte carlo simulation of surface heterogeneity in graphite anodes for lithium-ion batteries: passive layer formation. *Journal of The Electrochemical Society*, 158(4):A363, 2011.

[62] Philip Richard Wallace. The band theory of graphite. *Physical review*, 71(9):622, 1947.

[63] K. S. Novoselov, A. K. Geim, S. V. Morozov, D. Jiang, Y. Zhang, S. V. Dubonos, I. V. Grigorieva, and A. A. Firsov. Electric field effect in atomically thin carbon films. *Science*, 306(5696):666–669, 2004.

[64] Deji Akinwande, Christopher J. Brennan, J. Scott Bunch, Philip Egberts, Jonathan R. Felts, Huajian Gao, Rui Huang, Joon-Seok Kim, Teng Li, Yao Li, Kenneth M. Liechti, Nanshu Lu, Harold S. Park, Evan J. Reed, Peng Wang, Boris I. Yakobson, Teng Zhang, Yong-Wei Zhang, Yao Zhou, and Yong Zhu. A review on mechanics and mechanical properties of 2d materials—graphene and beyond. *Extreme Mechanics Letters*, 13:42–77, 2017.

[65] Sheneve Z. Butler, Shawna M. Hollen, Linyou Cao, Yi Cui, Jay A. Gupta, Humberto R. Gutiérrez, Tony F. Heinz, Seung Sae Hong, Jiaxing Huang, Ariel F. Ismach, Ezekiel Johnston-Halperin, Masaru Kuno, Vladimir V. Plashnitsa, Richard D. Robinson, Rodney S. Ruoff, Sayeef Salahuddin, Jie Shan, Li Shi, Michael G. Spencer, Mauricio Terrones, Wolfgang Windl, and Joshua E. Goldberger. Progress, challenges, and opportunities in two-dimensional materials beyond graphene. *ACS Nano*, 7(4):2898–2926, 2013. PMID: 23464873.

[66] Qing Hua Wang, Kourosh Kalantar-Zadeh, Andras Kis, Jonathan N. Coleman, and Michael S. Strano. Electronics and optoelectronics of two-dimensional transition metal dichalcogenides. *Nature Nanotechnology*, 7(11):699–712, Nov 2012.

[67] Pengzhan Sun, Kunlin Wang, and Hongwei Zhu. Recent developments in graphene-based membranes: Structure, mass-transport mechanism and potential applications. *Advanced Materials*, 28(12):2287–2310, 2016.

[68] Rubén Mas-Ballesté, Cristina Gómez-Navarro, Julio Gómez-Herrero, and Félix Zamora. 2d materials: to graphene and beyond. *Nanoscale*, 3:20–30, 2011.

[69] Changgu Lee, Xiaoding Wei, Jeffrey W. Kysar, and James Hone. Measurement of the elastic properties and intrinsic strength of monolayer graphene. *Science*, 321(5887):385–388, 2008.

[70] K.I. Bolotin, K.J. Sikes, Z. Jiang, M. Klima, G. Fudenberg, J. Hone, P. Kim, and H.L. Stormer. Ultrahigh electron mobility in suspended graphene. *Solid State Communications*, 146(9):351–355, 2008.

[71] Alexander A. Balandin, Suchismita Ghosh, Wenzhong Bao, Irene Calizo, Desalegne Teweldebrhan, Feng Miao, and Chun Ning Lau. Superior thermal conductivity of single-layer graphene. *Nano Letters*, 8(3):902–907, 2008. PMID: 18284217.

[72] R. R. Nair, P. Blake, A. N. Grigorenko, K. S. Novoselov, T. J. Booth, T. Stauber, N. M. R. Peres, and A. K. Geim. Fine structure constant defines visual transparency of graphene. *Science*, 320(5881):1308–1308, 2008.

[73] Feng Wang, Yuanbo Zhang, Chuanshan Tian, Caglar Girit, Alex Zettl, Michael Crommie, and Y. Ron Shen. Gate-variable optical transitions in graphene. *Science*, 320(5873):206–209, 2008.

[74] Yu-Ming Lin, Keith A Jenkins, Alberto Valdes-Garcia, Joshua P Small, Damon B Farmer, and Phaedon Avouris. Operation of graphene transistors at gigahertz frequencies. *Nano letters*, 9(1):422–426, 2009.

[75] Yanqing Wu, Yu-ming Lin, Ageeth A Bol, Keith A Jenkins, Fengnian Xia, Damon B Farmer, Yu Zhu, and Phaedon Avouris. High-frequency, scaled graphene transistors on diamond-like carbon. *Nature*, 472(7341):74–78, 2011.

[76] Y-M Lin, Christos Dimitrakopoulos, Keith A Jenkins, Damon B Farmer, H-Y Chiu, Alfred Grill, and Ph Avouris. 100-ghz transistors from wafer-scale epitaxial graphene. *Science*, 327(5966):662–662, 2010.

[77] Houk Jang, Yong Ju Park, Xiang Chen, Tanmoy Das, Min-Seok Kim, and Jong-Hyun Ahn. Graphene-based flexible and stretchable electronics. *Advanced Materials*, 28(22):4184–4202, 2016.

[78] Keun Soo Kim, Yue Zhao, Houk Jang, Sang Yoon Lee, Jong Min Kim, Kwang S Kim, Jong-Hyun Ahn, Philip Kim, Jae-Young Choi, and Byung Hee Hong. Large-scale pattern growth of graphene films for stretchable transparent electrodes. *nature*, 457(7230):706–710, 2009.

[79] Marco Furchi, Alexander Urich, Andreas Pospischil, Govinda Lilley, Karl Unterrainer, Hermann Detz, Pavel Klang, Aaron Maxwell Andrews, Werner Schrenk, Gottfried Strasser, et al. Microcavity-integrated graphene photodetector. *Nano letters*, 12(6):2773–2777, 2012.

[80] Xuetao Gan, Ren-Jye Shiue, Yuanda Gao, Inanc Meric, Tony F Heinz, Kenneth Shepard, James Hone, Solomon Assefa, and Dirk Englund. Chip-integrated ultrafast graphene photodetector with high responsivity. *Nature photonics*, 7(11):883–887, 2013.

[81] Marco Furchi, Alexander Urich, Andreas Pospischil, Govinda Lilley, Karl Unterrainer, Hermann Detz, Pavel Klang, Aaron Maxwell Andrews, Werner Schrenk, Gottfried Strasser, et al. Microcavity-integrated graphene photodetector. *Nano letters*, 12(6):2773–2777, 2012.

[82] Haegyeom Kim, Kyu-Young Park, Jihyun Hong, and Kisuk Kang. All-graphene-battery: bridging the gap between supercapacitors and lithium ion batteries. *Scientific reports*, 4(1):1–8, 2014.

[83] Maher F El-Kady, Veronica Strong, Sergey Dubin, and Richard B Kaner. Laser scribing of high-performance and flexible graphene-based electrochemical capacitors. *Science*, 335(6074):1326–1330, 2012.

[84] Jeremy T Robinson, F Keith Perkins, Eric S Snow, Zhongqing Wei, and Paul E Sheehan. Reduced graphene oxide molecular sensors. *Nano letters*, 8(10):3137–3140, 2008.

[85] Jesse D. Fowler, Matthew J. Allen, Vincent C. Tung, Yang Yang, Richard B. Kaner, and Bruce H. Weiller. Practical chemical sensors from chemically derived graphene. *ACS Nano*, 3(2):301–306, 2009. PMID: 19236064.

[86] F Traversi, C Raillon, SM Benameur, K Liu, S Khlybov, M Tosun, D Krasnozhon, A Kis, and A Radenovic. Detecting the translocation of dna through a nanopore using graphene nanoribbons. *Nature nanotechnology*, 8(12):939–945, 2013.

[87] Grégory F Schneider, Stefan W Kowalczyk, Victor E Calado, Grégory Pandraud, Henny W Zandbergen, Lieven MK Vandersypen, and Cees Dekker. Dna translocation through graphene nanopores. *Nano letters*, 10(8):3163–3167, 2010.

[88] Grégory F Schneider, Stefan W Kowalczyk, Victor E Calado, Grégory Pandraud, Henny W Zandbergen, Lieven MK Vandersypen, and Cees Dekker. Dna translocation through graphene nanopores. *Nano letters*, 10(8):3163–3167, 2010.

[89] Jingquan Liu, Liang Cui, and Dusan Losic. Graphene and graphene oxide as new nanocarriers for drug delivery applications. *Acta biomaterialia*, 9(12):9243–9257, 2013.

[90] Xiaoming Sun, Zhuang Liu, Kevin Welsher, Joshua Tucker Robinson, Andrew Goodwin, Sasa Zaric, and Hongjie Dai. Nano-graphene oxide for cellular imaging and drug delivery. *Nano research*, 1(3):203–212, 2008.

[91] Jingquan Liu, Liang Cui, and Dusan Losic. Graphene and graphene oxide as new nanocarriers for drug delivery applications. *Acta biomaterialia*, 9(12):9243–9257, 2013.

[92] Sasha Stankovich, Dmitriy A Dikin, Geoffrey HB Dommett, Kevin M Kohlhaas, Eric J Zimney, Eric A Stach, Richard D Piner, SonBinh T Nguyen, and Rodney S Ruoff. Graphene-based composite materials. *nature*, 442(7100):282–286, 2006.

[93] Nicolas Mounet, Marco Gibertini, Philippe Schwaller, Davide Campi, Andrius Merkys, Antimo Marrazzo, Thibault Sohier, Ivano Eligio Castelli, Andrea Cepellotti, Giovanni Pizzi, et al. Two-dimensional materials from high-throughput computational exfoliation of experimentally known compounds. *Nature nanotechnology*, 13(3):246–252, 2018.

[94] Per Joensen, RF Frindt, and S Roy Morrison. Single-layer mos2. *Materials research bulletin*, 21(4):457–461, 1986.

[95] MT Paffett, RJ Simonson, P Papin, and RT Paine. Borazine adsorption and decomposition at pt (111) and ru (001) surfaces. *Surface Science*, 232(3):286–296, 1990.

[96] MT Paffett, RJ Simonson, P Papin, and RT Paine. Borazine adsorption and decomposition at pt (111) and ru (001) surfaces. *Surface Science*, 232(3):286–296, 1990.

[97] Han Liu, Adam T Neal, Zhen Zhu, Zhe Luo, Xianfan Xu, David Tománek, and Peide D Ye. Phosphorene: an unexplored 2d semiconductor with a high hole mobility. *ACS nano*, 8(4):4033–4041, 2014.

[98] Baojie Feng, Jin Zhang, Qing Zhong, Wenbin Li, Shuai Li, Hui Li, Peng Cheng, Sheng Meng, Lan Chen, and Kehui Wu. Experimental realization of two-dimensional boron sheets. *Nature chemistry*, 8(6):563–568, 2016.

[99] Andrew J. Mannix, Xiang-Feng Zhou, Brian Kiraly, Joshua D. Wood, Diego Alducin, Benjamin D. Myers, Xiaolong Liu, Brandon L. Fisher, Ulises Santiago, Jeffrey R. Guest, Miguel Jose Yacaman, Arturo Ponce, Artem R. Oganov, Mark C. Hersam, and Nathan P. Guisinger. Synthesis of borophenes: Anisotropic, two-dimensional boron polymorphs. *Science*, 350(6267):1513–1516, 2015.

[100] Baojie Feng, Zijing Ding, Sheng Meng, Yugui Yao, Xiaoyue He, Peng Cheng, Lan Chen, and Kehui Wu. Evidence of silicene in honeycomb structures of silicon on ag (111). *Nano letters*, 12(7):3507–3511, 2012.

[101] ME Dávila, Lede Xian, Seymur Cahangirov, Angel Rubio, and Guy Le Lay. Germanene: a novel two-dimensional germanium allotrope akin to graphene and silicene. *New Journal of Physics*, 16(9):095002, 2014.

[102] Feng-feng Zhu, Wei-jiong Chen, Yong Xu, Chun-lei Gao, Dan-dan Guan, Can-hua Liu, Dong Qian, Shou-Cheng Zhang, and Jin-feng Jia. Epitaxial growth of two-dimensional stanene. *Nature materials*, 14(10):1020–1025, 2015.

[103] Jianping Ji, Xiufeng Song, Jizi Liu, Zhong Yan, Chengxue Huo, Shengli Zhang, Meng Su, Lei Liao, Wenhui Wang, Zhenhua Ni, et al. Two-dimensional antimonene single crystals grown by van der waals epitaxy. *Nature communications*, 7(1):1–9, 2016.

[104] T Nagao, JT Sadowski, Mineo Saito, S Yaginuma, Y Fujikawa, T Kogure, T Ohno, Y Hasegawa, S Hasegawa, and T Sakurai. Nanofilm allotrope and phase transformation of ultrathin bi film on s i (111)- 7× 7. *Physical review letters*, 93(10):105501, 2004.

[105] Zhili Zhu, Xiaolin Cai, Seho Yi, Jinglei Chen, Yawei Dai, Chunyao Niu, Zhengxiao Guo, Maohai Xie, Feng Liu, Jun-Hyung Cho, et al. Multivalency-driven formation of te-based monolayer materials: a combined first-principles and experimental study. *Physical review letters*, 119(10):106101, 2017.

[106] Mohammad Mansoob Khan. Introduction and fundamentals of chalcogenides and chalcogenides-based nanomaterials. In *Chalcogenide-based nanomaterials as photocatalysts*, pages 1–6. Elsevier, 2021.

[107] Zhiming Shi, Zhuhua Zhang, Alex Kutana, and Boris I Yakobson. Predicting two-dimensional silicon carbide monolayers. *ACS nano*, 9(10):9802–9809, 2015.

[108] Zhuhua Zhang, Xiaofei Liu, Boris I Yakobson, and Wanlin Guo. Two-dimensional tetragonal tic monolayer sheet and nanoribbons. *Journal of the American Chemical Society*, 134(47):19326–19329, 2012.

[109] Zixin Xiong, Lei Zhong, Haotian Wang, and Xiaoyan Li. Structural defects, mechanical behaviors, and properties of two-dimensional materials. *Materials*, 14(5), 2021.

[110] Tingting Wang, Huide Wang, Zongkui Kou, Weiyuan Liang, Xiaoling Luo, Francis Verpoort, Yu-Jia Zeng, and Han Zhang. Xenes as an emerging 2d monoelemental family: Fundamental electrochemistry and energy applications. *Advanced Functional Materials*, 30(36):2002885, 2020.

[111] Farjana Haque, Torben Daeneke, Kourosh Kalantar-Zadeh, and Jian Zhen Ou. Two-dimensional transition metal oxide and chalcogenide-based photocatalysts. *Nano-Micro Letters*, 10(2):1–27, 2018.

[112] Min Yi and Zhigang Shen. A review on mechanical exfoliation for the scalable production of graphene. *Journal of Materials Chemistry A*, 3(22):11700–11715, 2015.

[113] Jonathan N. Coleman, Mustafa Lotya, Arlene O'Neill, Shane D. Bergin, Paul J. King, Umar Khan, Karen Young, Alexandre Gaucher, Sukanta De, Ronan J. Smith, Igor V. Shvets, Sunil K. Arora, George Stanton, Hye-Young Kim, Kangho Lee, Gyu Tae Kim, Georg S. Duesberg, Toby Hallam, John J. Boland, Jing Jing Wang, John F. Donegan, Jaime C. Grunlan, Gregory Moriarty, Aleksey Shmeliov, Rebecca J. Nicholls, James M. Perkins, Eleanor M. Grieveson, Koenraad Theuwissen, David W. McComb, Peter D. Nellist, and Valeria Nicolosi. Two-dimensional nanosheets produced by liquid exfoliation of layered materials. *Science*, 331(6017):568–571, 2011.

[114] Zhengyang Cai, Bilu Liu, Xiaolong Zou, and Hui-Ming Cheng. Chemical vapor deposition growth and applications of two-dimensional materials and their heterostructures. *Chemical Reviews*, 118(13):6091–6133, 2018. PMID: 29384374.

[115] Gregg S. B. McKee and Kenneth S. Vecchio. Thermogravimetric analysis of synthesis variation effects on cvd generated multiwalled carbon nanotubes. *The Journal of Physical Chemistry B*, 110(3):1179–1186, 2006. PMID: 16471661.

[116] P Hohenberg and WJPR Kohn. Density functional theory (dft). *Phys. Rev*, 136(1964):B864, 1964.

[117] Walter Kohn and Lu Jeu Sham. Self-consistent equations including exchange and correlation effects. *Physical review*, 140(4A):A1133, 1965.

[118] John C Slater and George F Koster. Simplified lcao method for the periodic potential problem. *Physical review*, 94(6):1498, 1954.

[119] BJ Alder, DM Gass, and TE Wainwright. Studies in molecular dynamics. viii. the transport coefficients for a hard-sphere fluid. *The Journal of Chemical Physics*, 53(10):3813–3826, 1970.

[120] Nicholas Metropolis, Arianna W Rosenbluth, Marshall N Rosenbluth, Augusta H Teller, and Edward Teller. Equation of state calculations by fast computing machines. *The journal of chemical physics*, 21(6):1087–1092, 1953.

[121] Simone Taioli. Computational study of graphene growth on copper by first-principles and kinetic monte carlo calculations. *Journal of molecular modeling*, 20(7):1–13, 2014.

[122] Sumit Beniwal, James Hooper, Daniel P Miller, Paulo S Costa, Gang Chen, Shih-Yuan Liu, Peter A Dowben, E Charles H Sykes, Eva Zurek, and Axel Enders. Graphene-like boron–carbon–nitrogen monolayers. *ACS nano*, 11(3):2486–2493, 2017.

[123] Robert Vajtai, Bingqing Wei, Yung Joon Jung, Anyuan Cao, Sujit K Biswas, Ganapathiraman Ramanath, and Pulickel M Ajayan. Building and testing organized architectures of carbon nanotubes. *IEEE transactions on nanotechnology*, 2(4):355–361, 2003.

[124] Daniele Stampatori, Pier Paolo Raimondi, and Michel Noussan. Li-ion batteries: A review of a key technology for transport decarbonization. *Energies*, 13(10):2638, 2020.

[125] Junxiong Wu, Muhammad Ihsan-Ul-Haq, Yuming Chen, and Jang-Kyo Kim. Understanding solid electrolyte interphases: advanced characterization techniques and theoretical simulations. *Nano Energy*, 89:106489, 2021.

[126] Lijing Xie, Cheng Tang, Zhihong Bi, Mingxin Song, Yafeng Fan, Chong Yan, Xiaoming Li, Fangyuan Su, Qiang Zhang, and Chengmeng Chen. Hard carbon anodes for next-generation li-ion batteries: Review and perspective. *Advanced Energy Materials*, 11(38):2101650, 2021.

[127] Aiping Wang, Sanket Kadam, Hong Li, Siqi Shi, and Yue Qi. Review on modeling of the anode solid electrolyte interphase (sei) for lithium-ion batteries. *npj Computational Materials*, 4(1):1–26, 2018.

[128] Colin A Vincent. Lithium batteries: a 50-year perspective, 1959–2009. *Solid State Ionics*, 134(1-2):159–167, 2000.

[129] E Peled, D Golodnttsky, G Ardel, C Menachem, D Bar Tow, and V Eshkenazy. The role of sei in lithium and lithium ion batteries. *MRS Online Proceedings Library (OPL)*, 393:209, 1995.

[130] Matthew B Pinson and Martin Z Bazant. Theory of sei formation in rechargeable batteries: capacity fade, accelerated aging and lifetime prediction. *Journal of the Electrochemical Society*, 160(2):A243, 2012.

[131] D Alliata, R Kötz, P Novák, and H Siegenthaler. Electrochemical spm investigation of the solid electrolyte interphase film formed on hopg electrodes. *Electrochemistry communications*, 2(6):436–440, 2000.

[132] RIR Blyth, Hilmi Buqa, FP Netzer, MG Ramsey, JO Besenhard, Peter Golob, and Martin Winter. Xps studies of graphite electrode materials for lithium ion batteries. *Applied Surface Science*, 167(1-2):99–106, 2000.

[133] Martin Winter, R Imhof, F Joho, and Petr Novák. Ftir and dems investigations on the electroreduction of chloroethylene carbonate-based electrolyte solutions for lithium-ion cells. *Journal of power sources*, 81:818–823, 1999.

[134] Hong Li, Xuejie Huang, and Liquan Chen. Electrochemical impedance spectroscopy study of sno and nano-sno anodes in lithium rechargeable batteries. *Journal of Power Sources*, 81:340–345, 1999.

[135] Yifeng Wang. *Nuclear magnetic resonance studies of solid state lithium ion battery materials*. City University of New York, 1999.

[136] Agnès Claye and John E Fischer. Short-range order in disordered carbons: where does the li go? *Electrochimica acta*, 45(1-2):107–120, 1999.

[137] Dmitry Bedrov, Oleg Borodin, and Justin B. Hooper. Lisup/sup transport and mechanical properties of model solid electrolyte interphases (SEI): Insight from atomistic molecular dynamics simulations. *The Journal of Physical Chemistry C*, 121(30):16098–16109, July 2017.

[138] Lars von Kolzenberg, Arnulf Latz, and Birger Horstmann. Solid-electrolyte interphase during battery cycling: Theory of growth regimes. 2020.

[139] Michail Stamatakis. Kinetic modelling of heterogeneous catalytic systems. *Journal of Physics: Condensed Matter*, 27(1):013001, 2014.

[140] Corbett C Battaile and David J Srolovitz. Kinetic monte carlo simulation of chemical vapor deposition. *Annual Review of Materials Research*, 32(1):297–319, 2002.

[141] J Dai, WD Seider, and T Sinno. Lattice kinetic monte carlo simulations of defect evolution in crystals at elevated temperature. *Molecular Simulation*, 32(3-4):305–314, 2006.

[142] Matthew H Flamm, Scott L Diamond, and Talid Sinno. Lattice kinetic monte carlo simulations of convective-diffusive systems. *The Journal of chemical physics*, 130(9):094904, 2009.

[143] Xue Yang and Ahmed Hassanein. Kinetic monte carlo simulation of hydrogen diffusion on tungsten reconstructed (0 0 1) surface. *Fusion Engineering and Design*, 89(11):2545–2549, 2014.

[144] Matthew T Darby, Simone Piccinin, and Michail Stamatakis. First principles-based kinetic monte carlo simulation in catalysis. *Physics of Surface, Interface and Cluster Catalysis*, 2:1–38, 2016.

[145] Peter Kratzer. Monte carlo and kinetic monte carlo methods. *arXiv preprint arXiv:0904.2556*, 2009.

[146] Nicholas Metropolis, Arianna W Rosenbluth, Marshall N Rosenbluth, Augusta H Teller, and Edward Teller. Equation of state calculations by fast computing machines. *The journal of chemical physics*, 21(6):1087–1092, 1953.

[147] Art B Owen. Monte carlo theory, methods and examples. pages 3–40, 2013.

[148] FM Bulnes, VD Pereyra, and JL Riccardo. Collective surface diffusion: n-fold way kinetic monte carlo simulation. *Physical Review E*, 58(1):86, 1998.

[149] Van Kampen N. *he Master Equation. In: Stochastic Processes in Physics and Chemistry.* Elsevier, 2007.

[150] Panagiotis D. Kolokathis and Doros N. Theodorou. On solving the master equation in spatially periodic systems. *The Journal of Chemical Physics*, 137(3):034112, jul 2012.

[151] René Marcelin. *Contribution a l'etude de la cinetique physico-chimique.* Number 4. Gauthier-Villars et cie., 1914.

[152] Peter Hänggi, Peter Talkner, and Michal Borkovec. Reaction-rate theory: fifty years after kramers. *Reviews of modern physics*, 62(2):251, 1990.

[153] McQuarrie DA. *Classical Statistical Mechanics. In: Statistical Mechanics.* Harper and Row, 1973.

[154] Christopher J Cramer. *Essentials of computational chemistry.* John Wiley & Sons, Nashville, TN, 2 edition, apr 2013.

[155] Antonius Petrus Johannes Jansen. *An introduction to kinetic Monte Carlo simulations of surface reactions*, volume 856. Springer, 2012.

[156] Tim P. Schulze. Efficient kinetic monte carlo simulation. *Journal of Computational Physics*, 227(4):2455–2462, 2008.

[157] Hamza M. Ruzayqat and Tim P. Schulze. A rejection scheme for off-lattice kinetic monte carlo simulation. *Journal of Chemical Theory and Computation*, 14(1):48–54, December 2017.

[158] A. P. J. Jansen. An introduction to monte carlo simulations of surface reactions, 2008.

[159] Abhijit Chatterjee and Dionisios G Vlachos. An overview of spatial microscopic and accelerated kinetic monte carlo methods. *Journal of computer-aided materials design*, 14(2):253–308, 2007.

[160] JJ Lukkien, JPL Segers, PAJ Hilbers, RJ Gelten, and APJ Jansen. Efficient monte carlo methods for the simulation of catalytic surface reactions. *Physical Review E*, 58(2):2598, 1998.

[161] A.P.J. Jansen. Monte carlo simulations of chemical reactions on a surface with time-dependent reaction-rate constants. *Computer Physics Communications*, 86(1-2):1–12, April 1995.

[162] Kristen A. Fichthorn and W. H. Weinberg. Theoretical foundations of dynamical monte carlo simulations. *The Journal of Chemical Physics*, 95(2):1090–1096, July 1991.

[163] Daniel T. Gillespie. Approximate accelerated stochastic simulation of chemically reacting systems. *The Journal of Chemical Physics*, 115(4):1716–1733, July 2001.

[164] Eric L. Haseltine and James B. Rawlings. Approximate simulation of coupled fast and slow reactions for stochastic chemical kinetics. *The Journal of Chemical Physics*, 117(15):6959–6969, October 2002.

[165] Howard Salis and Yiannis Kaznessis. Accurate hybrid stochastic simulation of a system of coupled chemical or biochemical reactions. *The Journal of Chemical Physics*, 122(5):054103, February 2005.

[166] Michael Rieger, Jutta Rogal, and Karsten Reuter. Effect of surface nanostructure on temperature programmed reaction spectroscopy: First-principles kinetic monte carlo simulations of CO oxidation atmml:math xmlns:mml="http://www.w3.org/1998/math/MathML" display="inline"mml:msubmml:miRuO/mml:mimml:mn2/mml:mn/mml:msubmml:mo stretchy="false"(/mml:momml:mn110/mml:mnmml:mo stretchy="false")/mml:mo/mml:math. *Physical Review Letters*, 100(1), January 2008.

[167] Simone Piccinin and Michail Stamatakis. CO oxidation on pd(111): A first-principles-based kinetic monte carlo study. *ACS Catalysis*, 4(7):2143–2152, June 2014.

[168] Juan M. Lorenzi, Sebastian Matera, and Karsten Reuter. Synergistic inhibition of oxide formation in oxidation catalysis: A first-principles kinetic monte carlo study of NO CO oxidation at pd(100). *ACS Catalysis*, 6(8):5191–5197, July 2016.

[169] Mikkel Jørgensen and Henrik Grönbeck. Scaling relations and kinetic monte carlo simulations to bridge the materials gap in heterogeneous catalysis. *ACS Catalysis*, 7(8):5054–5061, July 2017.

[170] Abhijit Chatterjee and Arthur F. Voter. Accurate acceleration of kinetic monte carlo simulations through the modification of rate constants. *The Journal of Chemical Physics*, 132(19):194101, May 2010.

[171] Eric C. Dybeck, Craig P. Plaisance, and Matthew Neurock. Generalized temporal acceleration scheme for kinetic monte carlo simulations of surface catalytic processes by scaling the rates of fast reactions. *Journal of Chemical Theory and Computation*, 13(4):1525–1538, March 2017.

[172] M. Núñez, T. Robie, and D. G. Vlachos. Acceleration and sensitivity analysis of lattice kinetic monte carlo simulations using parallel processing and rate constant rescaling. *The Journal of Chemical Physics*, 147(16):164103, October 2017.

[173] Max J. Hoffmann and Thomas Bligaard. A lattice kinetic monte carlo solver for first-principles microkinetic trend studies. *Journal of Chemical Theory and Computation*, 14(3):1583–1593, 2018. PMID: 29357239.

[174] Xiao-Ming Cao, Zheng-Jiang Shao, and P. Hu. A fast species redistribution approach to accelerate the kinetic monte carlo simulation for heterogeneous catalysis. *Phys. Chem. Chem. Phys.*, 22:7348–7364, 2020.

[175] Deji Akinwande, Li Tao, Qingkai Yu, Xiaojing Lou, Peng Peng, and Duygu Kuzum. Large-area graphene electrodes: Using cvd to facilitate applications in commercial touchscreens, flexible nanoelectronics, and neural interfaces. *IEEE Nanotechnology Magazine*, 9(3):6–14, 2015.

[176] Mengyao Zhong, Dikai Xu, Xuegong Yu, Kun Huang, Xuemei Liu, Yiming Qu, Yang Xu, and Deren Yang. Interface coupling in graphene/fluorographene heterostructure for high-performance graphene/silicon solar cells. *Nano Energy*, 28:12–18, 2016.

[177] Graphene applications & uses. `https://www.graphenea.com/pages/graphene-uses-applications`.

[178] Keith R. Paton, Eswaraiah Varrla, Claudia Backes, Ronan J. Smith, Umar Khan, Arlene O'Neill, Conor Boland, Mustafa Lotya, Oana M. Istrate, Paul King, Tom Higgins, Sebastian Barwich, Peter May, Pawel Puczkarski, Iftikhar Ahmed, Matthias Moebius, Henrik Pettersson, Edmund Long, João Coelho, Sean E. O'Brien, Eva K. McGuire, Beatriz Mendoza Sanchez, Georg S. Duesberg, Niall McEvoy, Timothy J. Pennycook, Clive Downing, Alison Crossley, Valeria Nicolosi, and Jonathan N. Coleman. Scalable production of large quantities of defect-free few-layer graphene by shear exfoliation in liquids. *Nature Materials*, 13(6):624–630, Jun 2014.

[179] Rad Sadri, K. Zangeneh Kamali, M. Hosseini, Nashrul Zubir, S. N. Kazi, Goodarz Ahmadi, Mahidzal Dahari, N. M. Huang, and A. M. Golsheikh. Experimental study on thermo-physical and rheological properties of stable and green reduced graphene oxide nanofluids: Hydrothermal assisted technique. *Journal of Dispersion Science and Technology*, 38(9):1302–1310, 2017.

[180] Amartya Chakrabarti, Jun Lu, Jennifer C. Skrabutenas, Tao Xu, Zhili Xiao, John A. Maguire, and Narayan S. Hosmane. Conversion of carbon dioxide to few-layer graphene. *J. Mater. Chem.*, 21:9491–9493, 2011.

[181] Wei Liu, Hong Li, Chuan Xu, Yasin Khatami, and Kaustav Banerjee. Synthesis of high-quality monolayer and bilayer graphene on copper using chemical vapor deposition. *Carbon*, 49(13):4122–4130, 2011.

[182] C Melero, R Rincón, J Muñoz, G Zhang, S Sun, A Perez, O Royuela, C González-Gago, and M D Calzada. Scalable graphene production from ethanol decomposition by microwave argon plasma torch. *Plasma Physics and Controlled Fusion*, 60(1):014009, 2017.

[183] Francesco Bonaccorso, Antonio Lombardo, Tawfique Hasan, Zhipei Sun, Luigi Colombo, and Andrea C. Ferrari. Production and processing of graphene and 2d crystals. *Materials Today*, 15(12):564–589, 2012.

[184] R. Raccichini, A. Varzi, S. Passerini, and B. Scrosati. The role of graphene for electrochemical energy storage. *Nature Materials*, 14(3):271–279, 2015.

[185] K. S. Novoselov, V. I. Fal`ko, L. Colombo, P. R. Gellert, M. G. Schwab, and K. Kim. A roadmap for graphene. *Nature*, 490(7419):192–200, 2012.

[186] Yanyan Xu, Huizhe Cao, Yanqin Xue, Biao Li, and Weihua Cai. Liquid-phase exfoliation of graphene: An overview on exfoliation media, techniques, and challenges. *Nanomaterials*, 8(11):942, November 2018.

[187] Ron Mertens. General graphene launched its new high-capacity cvd graphene roll-to-roll production line, 2021. [Online; posted 21-October-2021, accessed 21-February-2022].

[188] Byoungdo Lee, Weishen Chu, and Wei Li. Effects of Process Parameters on Graphene Growth Via Low-Pressure Chemical Vapor Deposition. *Journal of Micro and Nano-Manufacturing*, 8(3), 10 2020. 031005.

[189] Norlida Ramli, Nazrul Anuar Nayan, Hing Wah Lee, and Saat Shukri Embong. Analysis of the effect of growth parameters on graphene synthesized by chemical vapor deposition. *Journal of Nanoelectronics and Optoelectronics*, 10:50–55, 2015.

[190] Roberto Muñoz and Cristina Gómez-Aleixandre. Review of cvd synthesis of graphene. *Chemical Vapor Deposition*, 19(10-11-12):297–322, 2013.

[191] Shuaishuai Xu, Lipeng Zhang, Bin Wang, and Rodney S. Ruoff. Chemical vapor deposition of graphene on thin-metal films. *Cell Reports Physical Science*, 2(3):100372, 2021.

[192] Joseph Lyding, Joshua Wood, and Eric Pop. Growing better graphene by finding the best copper surface. *SPIE Newsroom*, March 2012.

[193] L. Zhao, K.T. Rim, H. Zhou, R. He, T.F. Heinz, A. Pinczuk, G.W. Flynn, and A.N. Pasupathy. Influence of copper crystal surface on the cvd growth of large area monolayer graphene. *Solid State Communications*, 151(7):509–513, 2011.

[194] Maryam Saeed, Yousef Alshammari, Shereen A. Majeed, and Eissa Al-Nasrallah. Chemical vapour deposition of graphene-synthesis, characterisation, and applications: A review. *Molecules*, 25(17), 2020.

[195] Aaesha Alnuaimi, Ibraheem Almansouri, Irfan Saadat, and Ammar Nayfeh. Toward fast growth of large area high quality graphene using a cold-wall cvd reactor. *RSC Adv.*, 7:51951–51957, 2017.

[196] Choon-Ming Seah, Siang-Piao Chai, and Abdul Rahman Mohamed. Mechanisms of graphene growth by chemical vapour deposition on transition metals. *Carbon*, 70:1–21, 2014.

[197] Kasra Momeni, Yanzhou Ji, Kehao Zhang, Joshua A. Robinson, and Long-Qing Chen. Multiscale framework for simulation-guided growth of 2d materials. *npj 2D Materials and Applications*, 2(1):27, Sep 2018.

[198] Mie Andersen, Juan Santiago Cingolani, and Karsten Reuter. Ab initio thermodynamics of hydrocarbons relevant to graphene growth at solid and liquid cu surfaces. *The Journal of Physical Chemistry C*, 123(36):22299–22310, August 2019.

[199] Lan Zhang, Yongchao Zhu, Wenrui Teng, Tian Xia, Yan Rong, Na Li, and Huizhong Ma. A molecular dynamics simulation of the graphene growth on cu(1 1 1) surface. *Computational Materials Science*, 130:10–15, April 2017.

[200] Pai Li, Zhenyu Li, and Jinlong Yang. Dominant kinetic pathways of graphene growth in chemical vapor deposition: The role of hydrogen. *The Journal of Physical Chemistry C*, 121(46):25949–25955, Nov 2017.

[201] Zongyang Qiu, Pai Li, Zhenyu Li, and Jinlong Yang. Atomistic simulations of graphene growth: From kinetics to mechanism. *Accounts of Chemical Research*, 51(3):728–735, Mar 2018.

[202] Shuai Chen, Junfeng Gao, Bharathi M Srinivasan, Gang Zhang, Viacheslav Sorkin, Ramanarayan Hariharaputran, and Yong-Wei Zhang. An all-atom kinetic monte carlo model for chemical vapor deposition growth of graphene on cu(1 1 1) substrate. *Journal of Physics: Condensed Matter*, 32(15):155401, jan 2020.

[203] P. Gaillard, T. Chanier, L. Henrard, P. Moskovkin, and S. Lucas. Multiscale simulations of the early stages of the growth of graphene on copper. *Surface Science*, 637-638:11–18, 2015.

[204] Jichen Dong, Leining Zhang, and Feng Ding. Kinetics of graphene and 2d materials growth. *Advanced Materials*, 31(9):1801583, 2019.

[205] Ilya Popov, Patrick Bügel, Mariana Kozlowska, Karin Fink, Felix Studt, and Dmitry I. Sharapa. Analytical model of CVD growth of graphene on cu(111) surface. *Nanomaterials*, 12(17):2963, August 2022.

[206] Ping Wu, Yue Zhang, Ping Cui, Zhenyu Li, Jinlong Yang, and Zhenyu Zhang. Carbon dimers as the dominant feeding species in epitaxial growth and morphological phase transition of graphene on different cu substrates. 114(21):216102.

[207] Xiao Kong, Jianing Zhuang, Liyan Zhu, and Feng Ding. The complementary graphene growth and etching revealed by large-scale kinetic monte carlo simulation. *npj Computational Materials*, 7(1):14, Jan 2021.

[208] Huijun Jiang and Zhonghuai Hou. Large-scale epitaxial growth kinetics of graphene: a kinetic monte carlo study. *The Journal of Chemical Physics*, 143(8):084109, 2015.

[209] Shaama Mallikarjun Sharada, Thomas Bligaard, Alan C. Luntz, Geert-Jan Kroes, and Jens K. Nørskov. Sbh10: A benchmark database of barrier heights on transition metal surfaces. *The Journal of Physical Chemistry C*, 121(36):19807–19815, 2017.

[210] Xiaohua Yang, Gaixia Zhang, Jai Prakash, Zhangsen Chen, Marc Gauthier, and Shuhui Sun. Chemical vapour deposition of graphene: Layer control, the transfer process, characterisation, and related applications. *International Reviews in Physical Chemistry*, 38(2):149–199, 2019.

[211] Congqin Miao, Churan Zheng, Owen Liang, and Ya-Hong Xie. Chemical vapor deposition of graphene. *Physics and applications of graphene-experiments*, page 2011, 2011.

[212] Maria Sarno, Gabriella Rossi, Claudia Cirillo, and Loredana Incarnato. Cold wall chemical vapor deposition graphene-based conductive tunable film barrier. *Industrial & Engineering Chemistry Research*, 57(14):4895–4906, 2018.

[213] Menglin Li, Donghua Liu, Dacheng Wei, Xuefen Song, Dapeng Wei, and Andrew Thye Shen Wee. Controllable synthesis of graphene by plasma-enhanced chemical vapor deposition and its related applications. *Advanced Science*, 3(11):1600003, 2016.

[214] Mariana Fraga and Rodrigo Pessoa. Progresses in synthesis and application of SiC films: From CVD to ALD and from MEMS to NEMS. *Micromachines*, 11(9):799, August 2020.

[215] C. Tsakonas, A.C. Manikas, M. Andersen, M. Dimitropoulos, K. Reuter, and C. Galiotis. In situ kinetic studies of cvd graphene growth by reflection spectroscopy. *Chemical Engineering Journal*, 421:129434, 2021.

[216] Indu Sharma, Girija Shankar Papanai, Sharon Jyotika Paul, and Bipin Kumar Gupta. Partial pressure assisted growth of single-layer graphene grown by low-pressure chemical vapor deposition: Implications for high-performance graphene fet devices. *ACS Omega*, 5(35), Sep 2020.

[217] Athanasia K. Balerba, Alexis Kotanidis, Angelos Paraskeuas, Martha Gialampouki, José Julio Gutiérrez Moreno, Dimitrios G. Papageorgiou, Georgios A. Evangelakis, and Christina E. Lekka. Chapter 9 - graphene nano-flakes on cu low-index surfaces by density functional theory and molecular dynamics simulations. In Panagiotis Grammatikopoulos, editor, *Computational Modelling of Nanomaterials*, volume 17 of *Frontiers of Nanoscience*, pages 141–159. Elsevier, 2020.

[218] Eric R. Bittner. Chemical dynamics in the condensed phases: Relaxation, transfer, and reactions in condensed molecular systems. *Journal of the American Chemical Society*, 128(51):17156–17157, 2006.

[219] P. Bügel. *Quantenchemische Untersuchungen zu Wachstumsprozessen an Oberflächen im Rahmen der chemischen Gasphasenabscheidung (Unpublished doctoral dissertation)*. PhD thesis, Karlsruhe Institute of Technology (KIT), 2022.

[220] Xuesong Li, Carl W. Magnuson, Archana Venugopal, Jinho An, Ji Won Suk, Boyang Han, Mark Borysiak, Weiwei Cai, Aruna Velamakanni, Yanwu Zhu, Lianfeng Fu, Eric M. Vogel, Edgar Voelkl, Luigi Colombo, and Rodney S. Ruoff. Graphene films with large domain size by a two-step chemical vapor deposition process. *Nano Letters*, 10(11):4328–4334, Nov 2010.

[221] Sreekar Bhaviripudi, Xiaoting Jia, Mildred S. Dresselhaus, and Jing Kong. Role of kinetic factors in chemical vapor deposition synthesis of uniform large area graphene using copper catalyst. *Nano Letters*, 10(10):4128–4133, Oct 2010.

[222] Xuesong Li, Carl W. Magnuson, Archana Venugopal, Rudolf M. Tromp, James B. Hannon, Eric M. Vogel, Luigi Colombo, and Rodney S. Ruoff. Large-area graphene single crystals grown by low-pressure chemical vapor deposition of methane on copper. *Journal of the American Chemical Society*, 133(9):2816–2819, Mar 2011.

[223] Ivan Vlassiouk, Murari Regmi, Pasquale Fulvio, Sheng Dai, Panos Datskos, Gyula Eres, and Sergei Smirnov. Role of hydrogen in chemical vapor deposition growth of large single-crystal graphene. *ACS Nano*, 5(7):6069–6076, July 2011.

[224] T.R. Thomas. Characterization of surface roughness. *Precision Engineering*, 3(2):97–104, April 1981.

[225] E.S. Gadelmawla, M.M. Koura, T.M.A. Maksoud, I.M. Elewa, and H.H. Soliman. Roughness parameters. *Journal of Materials Processing Technology*, 123(1):133–145, April 2002.

[226] Wenhua Zhang, Ping Wu, Zhenyu Li, and Jinlong Yang. First-principles thermodynamics of graphene growth on cu surfaces. *The Journal of Physical Chemistry C*, 115(36):17782–17787, 2011.

[227] Shuai Chen, Junfeng Gao, Bharathi M Srinivasan, Gang Zhang, Viacheslav Sorkin, Ramanarayan Hariharaputran, and Yong-Wei Zhang. Unveiling the competitive role of etching in graphene growth during chemical vapor deposition. *2D Materials*, 6(1):015031, dec 2018.

[228] Shuai Chen, Junfeng Gao, Bharathi M Srinivasan, Gang Zhang, Viacheslav Sorkin, Ramanarayan Hariharaputran, and Yong-Wei Zhang. A kinetic monte carlo model for the growth and etching of graphene during chemical vapor deposition. *Carbon*, 146:399–405, 2019.

[229] Naoki Nitta and Gleb Yushin. High-capacity anode materials for lithium-ion batteries: Choice of elements and structures for active particles. *Particle &amp Particle Systems Characterization*, 31(3):317–336, October 2013.

[230] Yuanli Ding, Zachary P. Cano, Aiping Yu, Jun Lu, and Zhongwei Chen. Automotive li-ion batteries: Current status and future perspectives. *Electrochemical Energy Reviews*, 2(1):1–28, January 2019.

[231] Umair Gulzar, Subrahmanyam Goriparti, Ermanno Miele, Tao Li, Giulia Maidecchi, Andrea Toma, Francesco De Angelis, Claudio Capiglia, and Remo Proietti Zaccaria. Next-generation textiles: from embedded supercapacitors to lithium ion batteries. *J. Mater. Chem. A*, 4:16771–16800, 2016.

[232] Bruno Scrosati. Recent advances in lithium ion battery materials. *Electrochimica Acta*, 45(15):2461–2466, 2000.

[233] Jordi Cabana, Laure Monconduit, Dominique Larcher, and M. Rosa Palacín. Beyond intercalation-based li-ion batteries: The state of the art and challenges of electrode materials reacting through conversion reactions. *Advanced Materials*, 22(35):E170–E192, August 2010.

[234] E. Ventosa and W. Schuhmann. Scanning electrochemical microscopy of li-ion batteries. *Physical Chemistry Chemical Physics*, 17(43):28441–28450, 2015.

[235] Martin Winter. The solid electrolyte interphase–the most important and the least understood solid electrolyte in rechargeable li batteries. *Zeitschrift für physikalische Chemie*, 223(10-11):1395–1406, 2009.

[236] John B Goodenough and Youngsik Kim. Challenges for rechargeable li batteries. *Chemistry of materials*, 22(3):587–603, 2010.

[237] Luning Wang, Anjali Menakath, Fudong Han, Yi Wang, Peter Y Zavalij, Karen J Gaskell, Oleg Borodin, Dinu Iuga, Steven P Brown, Chunsheng Wang, et al. Identifying the components of the solid–electrolyte interphase in li-ion batteries. *Nature chemistry*, 11(9):789–796, 2019.

[238] Tongchao Liu, Lingpiao Lin, Xuanxuan Bi, Leilei Tian, Kai Yang, Jiajie Liu, Maofan Li, Zonghai Chen, Jun Lu, Khalil Amine, et al. In situ quantification of interphasial chemistry in li-ion battery. *Nature nanotechnology*, 14(1):50–56, 2019.

[239] Samuel A Delp, Oleg Borodin, Marco Olguin, Claire G Eisner, Joshua L Allen, and T Richard Jow. Importance of reduction and oxidation stability of high voltage electrolytes and additives. *Electrochimica Acta*, 209:498–510, 2016.

[240] Satu Kristiina Heiskanen, Jongjung Kim, and Brett L Lucht. Generation and evolution of the solid electrolyte interphase of lithium-ion batteries. *Joule*, 3(10):2322–2333, 2019.

[241] Birger Horstmann, Fabian Single, and Arnulf Latz. Review on multi-scale models of solid-electrolyte interphase formation. *Current Opinion in Electrochemistry*, 13:61–69, 2019.

[242] Yue Gao, Zhifei Yan, Jennifer L Gray, Xin He, Daiwei Wang, Tianhang Chen, Qingquan Huang, Yuguang C Li, Haiying Wang, Seong H Kim, et al. Polymer–inorganic solid–electrolyte interphase for stable lithium metal batteries under lean electrolyte conditions. *Nature materials*, 18(4):384–389, 2019.

[243] Paul G. Kitz, Petr Novák, and Erik J. Berg. Influence of water contamination on the SEI formation in li-ion cells: An operando EQCM-d study. *ACS Applied Materials &amp Interfaces*, 12(13):15934–15942, March 2020.

[244] Dongqing Liu, Zulipiya Shadike, Ruoqian Lin, Kun Qian, Hai Li, Kaikai Li, Shuwei Wang, Qipeng Yu, Ming Liu, Swapna Ganapathy, et al. Review of recent development of in situ/operando characterization techniques for lithium battery research. *Advanced Materials*, 31(28):1806620, 2019.

[245] Zhenyu Zhang, Keenan Smith, Rhodri Jervis, Paul R Shearing, Thomas S Miller, and Daniel JL Brett. Operando electrochemical atomic force microscopy of solid–electrolyte interphase formation on graphite anodes: the evolution of sei morphology and mechanical properties. *ACS applied materials & interfaces*, 12(31):35132–35141, 2020.

[246] Aimin Ge, Da Zhou, Ken-ichi Inoue, Yanxia Chen, and Shen Ye. Role of oxygen in surface structures of the solid-electrolyte interphase investigated by sum frequency generation vibrational spectroscopy. *The Journal of Physical Chemistry C*, 124(32):17538–17547, 2020.

[247] Sara Malmgren, Katarzyna Ciosek, Rebecka Lindblad, Stefan Plogmaker, Julius Kühn, Håkan Rensmo, Kristina Edström, and Maria Hahlin. Consequences of air exposure on the lithiated graphite sei. *Electrochimica Acta*, 105:83–91, 2013.

[248] Keisuke Ushirogata, Keitaro Sodeyama, Yukihiro Okuno, and Yoshitaka Tateyama. Additive effect on reductive decomposition and binding of carbonate-based solvent toward solid electrolyte interphase formation in lithium-ion battery. *Journal of the American Chemical Society*, 135(32):11967–11974, 2013.

[249] Norio Takenaka, Yuichi Suzuki, Hirofumi Sakai, and Masataka Nagaoka. On electrolyte-dependent formation of solid electrolyte interphase film in lithium-ion batteries: strong sensitivity to small structural difference of electrolyte molecules. *The Journal of Physical Chemistry C*, 118(20):10874–10882, 2014.

[250] Lorena Alzate-Vargas, Samuel M Blau, Evan Walter Clark Spotte-Smith, Srikanth Allu, Kristin A Persson, and Jean-Luc Fattebert. Insight into sei growth in li-ion batteries using molecular dynamics and accelerated chemical reactions. *The Journal of Physical Chemistry C*, 125(34):18588–18596, 2021.

[251] Samuel Bertolini and Perla B Balbuena. Buildup of the solid electrolyte interphase on lithium-metal anodes: reactive molecular dynamics study. *The Journal of Physical Chemistry C*, 122(20):10783–10791, 2018.

[252] John L. Christensen and John. Newman. A mathematical model for the lithium-ion negative electrode solid electrolyte interphase. *Journal of The Electrochemical Society*, 151, 2003.

[253] Lars von Kolzenberg, Arnulf Latz, and Birger Horstmann. Solid–electrolyte interphase during battery cycling: Theory of growth regimes. *ChemSusChem*, 13(15):3901–3910, 2020.

[254] Jay R Winkler and Harry B Gray. Long-range electron tunneling. *Journal of the American Chemical Society*, 136(8):2930–2939, 2014.

[255] Keisuke Ushirogata, Keitaro Sodeyama, Zdenek Futera, Yoshitaka Tateyama, and Yukihiro Okuno. Near-shore aggregation mechanism of electrolyte decomposition products to explain solid electrolyte interphase formation. *Journal of The Electrochemical Society*, 162(14):A2670, 2015.

[256] Anna M Andersson, A Henningson, Hans Siegbahn, Ulf Jansson, and Kristina Edström. Electrochemically lithiated graphite characterised by photoelectron spectroscopy. *Journal of Power Sources*, 119:522–527, 2003.

[257] Mengyun Nie, Daniel P Abraham, Yanjing Chen, Arijit Bose, and Brett L Lucht. Silicon solid electrolyte interphase (sei) of lithium ion battery characterized by microscopy and spectroscopy. *The Journal of Physical Chemistry C*, 117(26):13403–13412, 2013.

[258] Harry J Ploehn, Premanand Ramadass, and Ralph E White. Solvent diffusion model for aging of lithium-ion battery cells. *Journal of The Electrochemical Society*, 151(3):A456, 2004.

[259] Maureen Tang, Sida Lu, and John Newman. Experimental and theoretical investigation of solid-electrolyte-interphase formation mechanisms on glassy carbon. *Journal of the Electrochemical Society*, 159(11):A1775, 2012.

[260] Fabian Single, Birger Horstmann, and Arnulf Latz. Revealing sei morphology: in-depth analysis of a modeling approach. *Journal of the electrochemical society*, 164(11):E3132, 2017.

[261] MICHEL Broussely, S Herreyre, Ph Biensan, P Kasztejna, K Nechev, and RJ Staniewicz. Aging mechanism in li ion cells and calendar life predictions. *Journal of Power Sources*, 97:13–21, 2001.

[262] John Christensen and John Newman. A mathematical model for the lithium-ion negative electrode solid electrolyte interphase. *Journal of The Electrochemical Society*, 151(11):A1977, 2004.

[263] Yixuan Wang, Shinichiro Nakamura, Makoto Ue, and Perla B Balbuena. Theoretical studies to understand surface chemistry on carbon anodes for lithium-ion batteries: reduction mechanisms of ethylene carbonate. *Journal of the American Chemical Society*, 123(47):11708–11718, 2001.

[264] Tom Eriksson, Anna M Andersson, Andrea G Bishop, Cecilia Gejke, Torbjörn Gustafsson, and John O Thomas. Surface analysis of limn2 o 4 electrodes in carbonate-based electrolytes. *Journal of the Electrochemical Society*, 149(1):A69, 2001.

[265] Meysam Esmaeilpour, Saibal Jana, Hongjiao Li, Mohammad Soleymanibrojeni, and Wolfgang Wenzel. A solution-mediated pathway for the growth of the solid electrolyte interphase in lithium-ion batteries. *Advanced Energy Materials*, n/a(n/a):2203966.

[266] Keisuke Ushirogata, Keitaro Sodeyama, Yukihiro Okuno, and Yoshitaka Tateyama. Additive effect on reductive decomposition and binding of carbonate-based solvent toward solid electrolyte interphase formation in lithium-ion battery. *Journal of the American Chemical Society*, 135(32):11967–11974, 2013.

[267] Yixuan Wang, Shinichiro Nakamura, Makoto Ue, and Perla B Balbuena. Theoretical studies to understand surface chemistry on carbon anodes for lithium-ion batteries: reduction mechanisms of ethylene carbonate. *Journal of the American Chemical Society*, 123(47):11708–11718, 2001.

[268] Kanji Miyabe and Ryo Isogai. Estimation of molecular diffusivity in liquid phase systems by the wilke–chang equation. *Journal of Chromatography A*, 1218(38):6639–6645, 2011.

[269] Eric R. Bittner. Chemical dynamics in the condensed phases: relaxation, transfer, and reactions in condensed molecular systems by abraham nitzan (tel aviv university). oxford university press: oxford, new york. 2006. xxii 720 pp. $89.50. ISBN 0-19-852979-1. *Journal of the American Chemical Society*, 128(51):17156–17157, November 2006.

[270] Alfred B Bortz, Malvin H Kalos, and Joel L Lebowitz. A new algorithm for monte carlo simulation of ising spin systems. *Journal of Computational Physics*, 17(1):10–18, 1975.

[271] Michael Stein. Large sample properties of simulations using latin hypercube sampling. *Technometrics*, 29(2):143–151, 1987.

[272] M. D. McKay, R. J. Beckman, and W. J. Conover. A comparison of three methods for selecting values of input variables in the analysis of output from a computer code. *Technometrics*, 21(2):239, May 1979.

[273] Michael D. McKay. Latin hypercube sampling as a tool in uncertainty analysis of computer models. In *Proceedings of the 24th conference on Winter simulation - WSC '92*. ACM Press, 1992.

[274] Ronald L. Iman. scpl/scpatin hypercube sampling, September 2014.

[275] A. Olsson, G. Sandberg, and O. Dahlblom. On latin hypercube sampling for structural reliability analysis. *Structural Safety*, 25(1):47–68, January 2003.

[276] Randomized designs - pydoe 0.3.6 documentation. (n.d.).

[277] Stuart Lloyd. Least squares quantization in pcm. *IEEE transactions on information theory*, 28(2):129–137, 1982.

[278] Shie Mannor, Xin Jin, Jiawei Han, Xin Jin, Jiawei Han, Xin Jin, Jiawei Han, and Xinhua Zhang. K-means clustering. In *Encyclopedia of Machine Learning*, pages 563–564. Springer US, 2011.

[279] Leland McInnes, John Healy, and James Melville. Umap: Uniform manifold approximation and projection for dimension reduction. *arXiv preprint arXiv:1802.03426*, 2018.

[280] M A Syakur, B K Khotimah, E M S Rochman, and B D Satoto. Integration k-means clustering method and elbow method for identification of the best customer profile cluster. *IOP Conference Series: Materials Science and Engineering*, 336:012017, April 2018.

[281] Dhendra Marutho, Sunarna Hendra Handaka, Ekaprana Wijaya, and Muljono. The determination of cluster number at k-mean using elbow method and purity evaluation on headline news. In *2018 International Seminar on Application for Technology of Information and Communication*. IEEE, September 2018.

[282] Seon-Hong Lee, Ho-Gon You, Kyu-Suk Han, Jake Kim, In-Ho Jung, and Joo-Han Song. A new approach to surface properties of solid electrolyte interphase on a graphite negative electrode. *Journal of Power Sources*, 247:307–313, February 2014.

[283] Pengjian Guan, Lin Liu, and Xianke Lin. Simulation and experiment on solid electrolyte interphase (SEI) morphology evolution and lithium-ion diffusion. *Journal of The Electrochemical Society*, 162(9):A1798–A1808, 2015.

[284] William Huang, Peter M. Attia, Hansen Wang, Sara E. Renfrew, Norman Jin, Supratim Das, Zewen Zhang, David T. Boyle, Yuzhang Li, Martin Z. Bazant, Bryan D. McCloskey, William C. Chueh, and Yi Cui. Evolution of the solid–electrolyte interphase on carbonaceous anodes visualized by atomic-resolution cryogenic electron microscopy. *Nano Letters*, 19(8):5140–5148, July 2019.

[285] Joseph W. Abbott and Felix Hanke. Kinetically corrected monte carlo–molecular dynamics simulations of solid electrolyte interphase growth. *Journal of Chemical Theory and Computation*, 18(2):925–934, 2022.

[286] Ioannis Deretzis, Filippo Giannazzo, Giuseppe G. N. Angilella, Luca Parisi, and Antonino La Magna. Atom by atom simulations of nano-materials processing. In *2016 IEEE Nanotechnology Materials and Devices Conference (NMDC)*, pages 1–2, 2016.

[287] Soumyadeep Basak and Gopinath Packirisamy. Graphene-based nanomaterials for biomedical, catalytic, and energy applications. *ChemistrySelect*, 6(36):9669–9683, 2021.

[288] Thomas Trevethan, Christopher D. Latham, Malcolm I. Heggie, Patrick R. Briddon, and Mark J. Rayson. Vacancy diffusion and coalescence in graphene directed by defect strain fields. *Nanoscale*, 6(5):2978–2986, 2014.

[289] Jianing Zhuang, Ruiqi Zhao, Jichen Dong, Tianying Yan, and Feng Ding. Evolution of domains and grain boundaries in graphene: a kinetic monte carlo simulation. *Physical Chemistry Chemical Physics*, 18(4):2932–2939, 2016.

[290] Sharon Edward and Harley Johnson. Atomistic multi-lattice kinetic monte carlo (kmc) modeling of hyperthermal oxidation of multi-layer graphene. In *AIAA SCITECH 2022 Forum*, page 1610, 2022.

[291] I. Deretzis and A. La Magna. Simulating structural transitions with kinetic monte carlo: The case of epitaxial graphene on SiC. *Physical Review E*, 93(3), March 2016.

[292] Wenjing Yuan and Gaoquan Shi. Graphene-based gas sensors. *Journal of Materials Chemistry A*, 1(35):10078–10091, 2013.

[293] Tae-Hee Han, Hobeom Kim, Sung-Joo Kwon, and Tae-Woo Lee. Graphene-based flexible electronic devices. *Materials Science and Engineering: R: Reports*, 118:1–43, 2017.

[294] Jixin Zhu, Dan Yang, Zongyou Yin, Qingyu Yan, and Hua Zhang. Graphene and graphene-based materials for energy storage applications. *Small*, 10(17):3480–3498, 2014.

[295] Siby Thomas, Eun Bi Nam, and Sang Uck Lee. Atomistic dynamics investigation of the thermomechanical properties and li diffusion kinetics in ψ-graphene for lib anode material. *ACS applied materials & interfaces*, 10(42):36240–36248, 2018.

[296] Edgardo Maximiliano Gavilán-Arriazu, MP Mercer, DE Barraco, Harry Ernst Hoster, and Ezequiel Pedro M Leiva. Kinetic monte carlo simulations applied to li-ion and post li-ion batteries: a key link in the multi-scale chain. *Progress in Energy*, 3(4):042001, 2021.

[297] Feng Hao, Zhixiao Liu, Perla B Balbuena, and Partha P Mukherjee. Mesoscale elucidation of solid electrolyte interphase layer formation in li-ion battery anode. *The Journal of Physical Chemistry C*, 121(47):26233–26240, 2017.

[298] Zhixiao Liu and Partha P Mukherjee. Microstructure evolution in lithium-ion battery electrode processing. *Journal of The Electrochemical Society*, 161(8):E3248, 2014.

[299] Lucy M Morgan, Mazharul M Islam, Hui Yang, Kieran O'Regan, Anisha N Patel, Abir Ghosh, Emma Kendrick, Monica Marinescu, Gregory J Offer, Benjamin J Morgan, et al. From atoms to cells: Multiscale modeling of lini x mn y co z o2 cathodes for li-ion batteries. *ACS Energy Letters*, 7(1):108–122, 2021.

[300] Arghya Bhowmik, Ivano E Castelli, Juan Maria Garcia-Lastra, Peter Bjørn Jørgensen, Ole Winther, and Tejs Vegge. A perspective on inverse design of battery interphases using multi-scale modelling, experiments and generative deep learning. *Energy Storage Materials*, 21:446–456, 2019.